STRATIFIED VOLUME DIFFRACTIVE OPTICAL ELEMENTS

by

DIANA MARIE CHAMBERS

A DISSERTATION

Submitted in partial fulfillment of the requirements
For the degree of Doctor of Philosophy in
The Department of Physics
Of
The School of Graduate Studies
Of
The University of Alabama in Huntsville

HUNTSVILLE, ALABAMA

2000

DISSERTATION APPROVAL FORM

Submitted by Diana M. Chambers in partial fulfillment of the requirements for the degree of Doctor of Philosophy in Physics.

Accepted on behalf of the Faculty of the School of Graduate Studies by the dissertation committee:

Committee Chair

Department Chair

College Dean

Graduate Dean

ABSTRACT

School of Graduate Studies
The University of Alabama in Huntsville

Degree Doctor of Philosophy College/Dept Science/Physics

Name of Candidate Diana Marie Chambers

Title Stratified Volume Diffractive Optical Elements

Gratings with high diffraction efficiency into a single order find use in applications ranging from optical interconnects to beam steering. Such gratings have been realized with volume holographic, blazed, and diffractive optical techniques. However, each of these methods has limitations that restrict the range of applications in which they can be used. In this work an alternate, novel approach and method for creating high efficiency gratings has been developed. These new gratings are named stratified volume diffractive optical elements (SVDOE's). In this approach diffractive optic techniques are used to create an optical structure that emulates volume grating behavior.

An SVDOE consists of binary gratings interleaved with homogeneous layers in a multi-layer, stratified grating structure. The ridges of the binary gratings form fringe planes analogous to those of a volume hologram. The modulation and diffraction of an incident beam, which occur concurrently in a volume grating, are achieved sequentially by the grating layers and the homogeneous layers, respectively. The layers in this type of structure must be fabricated individually, which introduces the capability to laterally shift the binary grating layers relative to one another to create a grating with slanted fringe planes. This allows an element to be designed with high diffraction efficiency into the first order for any arbitrary angle of incidence.

A systematic design process has been developed for SVDOE's. Optimum modulation depth of the SVDOE is determined analytically and the number of grating layers along with the thickness of homogeneous layers is determined by numerical simulation. A rigorous electromagnetic simulation of the diffraction properties of multi-layer grating structures, based on the Rigorous Coupled-Wave Analysis (RCWA) algorithm, was developed and applied to SVDOE performance prediction.

Fabrication of an SVDOE structure presents unique challenges. Microfabrication combined with planarization techniques can be employed to address individual layers of the device. However, a novel approach for aligning adjacent binary grating layers is required to create a functional element. Such an alignment approach is developed in this work and applied to the fabrication of demonstration elements. These fabricated SVDOE's are then tested and their performance is shown to agree well with theoretical predictions.

Abstract Approval: Committee Chair ______________________________

(Date)

Department Chair ______________________________

Graduate Dean ______________________________

ACKNOWLEDGEMENTS

The completion of this work would not have been possible without the assistance of a number of people. First, I would like to thank Dr. Greg Nordin for his suggestion of the research topic and for his guidance throughout its duration. Dr. Nordin's presence as a mentor and as a friend has been a tremendous inspiration. I would also like to thank the other members of my committee, Drs. Mustafa Abushagur, John Dimmock, Don Gregory, and Lloyd Hillman, for their helpful comments and suggestions.

This work was made possible by funding from two technology development programs at NASA Marshall Space Flight Center. Specifically, the coherent doppler wind lidar program, led by Dr. Michael J. Kavaya, and the diffractive optics program, led by Dr. Helen Cole.

My colleagues at UAH have made many contributions to this work. Successful fabrication of the diffractive optical elements described here is largely a result of the diligent efforts of Seunghyun Kim. Jeff Meier, Lou Deguzman, and Arthur Ellis have provided a great deal of assistance to both Seunghyun Kim and myself with microfabrication and micro-optical evaluation processes. Hui Liu tested many diffractive elements. Daniel Crumbley, Aimee Dorman, and Seth Knight assisted with thin-film depositions.

My family has also made many contributions which enabled me to complete this work. My parents, Dr. Don Duncan and Sarah Duncan, always encouraged me to pursue education and provided their support in innumerable ways to ensure my success in that endeavor. My sons, Clark and Garrett, were very patient and provided perspective in my daily life simply by being themselves. Finally, this work would not have been possible without the support of my husband, Burt Chambers. Burt provided tangible support by assisting in preparing this dissertation and by participating in many technical discussions. More importantly though, he provided the encouragement, the reassurance, and the strength that I needed to see this through. Thank you.

TABLE OF CONTENTS

Page

LIST OF FIGURES

LIST OF TABLES

LIST OF SYMBOLS

Symbol	Definition
a_ℓ , b_ℓ , f_ℓ , f'_ℓ , g_ℓ , g'_ℓ	Matrices, representing subsets of matrix products
A_ℓ	$K_x{}^2 - E_\ell$
$A_{\ell,1}$	Matrix, represents I for homogeneous layer, W_ℓ for grating layer
$A_{\ell,2}$	Matrix, represents Γ_ℓ for homogeneous layer, V_ℓ for grating layer
$A_{\ell,11}$, $A_{\ell,12}$	Matrix, represents F_c or $F_s\Omega_\ell$ for homogeneous layer, V_{ss} or V_{sp} for grating layer
$A_{\ell,21}$, $A_{\ell,22}$	Matrix, represents $F_c\Gamma_\ell$ or F_s for homogeneous layer, W_{ss} or W_{sp} for grating layer
$A_{\ell,31}$, $A_{\ell,32}$	Matrix, represents F_c or $F_s\Gamma_\ell$ for homogeneous layer, W_{ps} or W_{pp} for grating layer
$A_{\ell,41}$, $A_{\ell,42}$	Matrix, represents $F_c\Omega_\ell$ or F_s for homogeneous layer, V_{ps} or V_{pp} for grating layer
$A'_{\ell,(\#\#)}$	Matrix, represents subset of matrix product
B_ℓ	$K_x E_\ell^{-1} K_x - I$
c	Speed of light
$c_{\ell,m}{}^+$, $c_{\ell,m}{}^-$	Unknown constants to be calculated
c_R , c_S	Obliquity factors in coupling coefficient
C_ℓ^+ , C_ℓ^-	Matrices of unknown constants

d_{AR}	Thickness of anti-reflective grating
d_b	Combined thickness of a grating layer and a homogeneous layer
d_g	Thickness of a binary grating layer
d_h	Depth of each homogenous layer within an SVDOE
d_ℓ	Thickness of L^{th} layer (along z) in SVDOE
d_p	Thickness of p^{th} layer (along z) in SVDOE
d_1	Thickness of first layer (along z) in SVDOE
DE_{ri} , DE_{ti}	Diffraction efficiency of reflected/transmitted i-th diffraction order
D_g	Modulation thickness in SVDOE
$D_{g,max}$	SVDOE Modulation thickness for maximum diffraction efficiency
D_ℓ	Sum of SVDOE layer thicknesses from 1 to ℓ
$D_{\ell,1}$	Matrix, represents P_ℓ for homogeneous layer, C_ℓ^+ for grating layer
$D_{\ell,2}$	Matrix, represents Q_ℓ for homogeneous layer, C_ℓ^- for grating layer
$D_{\ell,1}$, $D_{\ell,2}$	Matrix, represents $C_{\ell,1}^+$, $C_{\ell,2}^+$ in conical diffraction algorithm
$D_{\ell,3}$, $D_{\ell,4}$	Matrix, represents $C_{\ell,1}^-$, $C_{\ell,2}^-$ in conical diffraction algorithm
D_L	Total thickness of SVDOE layers
E	Electric field amplitude
$\vec{E}$	Electric field vector
$\vec{E}_{inc}$	Electric field vector incident on SVDOE
$E_{inc,y}$	Electric field incident on SVDOE in y-direction
E_I , E_{II}	Electric field amplitude in Region I/Region II

$\vec{E}_{I}$, $\vec{E}_{II}$	Electric field vector in Region I/Region II
$E_{I,y}$, $E_{II,y}$	Electric field in Region I/Region II in y-direction
E_{ℓ}	Matrix of permittivity harmonic components
$E_{\ell,gx}$, $E_{\ell,gy}$, $E_{\ell,gz}$	Electric field in grating layer
$\vec{E}_{\ell,g}$	Electric field vector in an SVDOE grating layer
F_c	Diagonal matrix with elements $\cos\phi_i$
F_s	Diagonal matrix with elements $\sin\phi_i$
G_{ℓ}	Diagonal matrix with elements $\exp(-k_0\gamma d)$
H	Magnetic field amplitude
$\vec{H}$	Magnetic field vector
$H_{inc,y}$	Magnetic field incident on SVDOE in y-direction
$H_{\ell,gx}$, $H_{\ell,gy}$, $H_{\ell,gz}$	Magnetic field in grating layer
$\vec{H}_{\ell,g}$	Magnetic field vector in an SVDOE grating layer
i	Designation for a diffracted order number
I	Identity matrix
j	Square root of negative one
J_{ℓ}	$K_y E_{\ell} K_y - I$
k	Propagation number in a medium
k_x	Wavevector x-component
k_{xi}	Wavevector of i-th diffracted order, x-component
k_y	Wavevector y-component
k_0	Propagation number in free space

k_I	Wavevector of wave incident onto SVDOE
k_{II}	Wavevector of wave transmitted through SVDOE
$k_{I,zi}$, $k_{II,zi}$	Wavevector of i-th diffracted order in Region I/Region II, z-component
$\vec{K}$	Grating vector
K_x	Diagonal matrix with elements k_{xi} / k_0
K_y	Diagonal matrix with elements k_y / k_0
ℓ	Designation for SVDOE layer number
n	Refractive index of a medium
n_g	Refractive index of grating grooves
n_h	Harmonic component of Fourier expansion of refractive index
$n_{\ell,h}$	Harmonic component of Fourier expansion of refractive index
n_r	Refractive index of grating ridges
n_s	Refractive index of substrate
n_0	Average refractive index of a medium with sinusoidal index modulation
n_I	Refractive index in incident region
n_{II}	Refractive index in transmitted region
n_{AR}	Refractive index of ridges in anti-reflective grating
o_2, o_3	Offsets of second and third grating layers
P_ℓ	Matrix of electric field amplitude in homogeneous layer, $+z$ direction
PE	Electric field amplitude in a homogeneous layer, $+z$ direction
PM	Magnetic field amplitude in a homogeneous layer, $+z$ direction
$q_{\ell,m}$	Positive square root of eigenvalues of matrix A_ℓ

Q_ℓ	Matrix of electric field amplitude in homogeneous layer, $-z$ direction
Q'_ℓ	Diagonal matrix with elements $q_{\ell,m}$
QE	Electric field amplitude in a homogeneous layer, $-z$ direction
QM	Magnetic field amplitude in a homogeneous layer, $-z$ direction
$\vec{r}$	Position vector
R_i	Amplitude of electric field of i-th backward diffracted wave
R	Matrix with elements R_i
R_s	Amplitude of reflected electric field normal to diffraction plane
R_p	Amplitude of reflected magnetic field normal to diffraction plane
$S_{\ell,xi}$, $S_{\ell,yi}$, $S_{\ell,zi}$	Space harmonics of tangential electric field
T_i	Amplitude of electric field of i-th forward diffracted wave
T	Matrix with elements T_i
T_s	Amplitude of transmitted electric field normal to diffraction plane
T_p	Amplitude of transmitted magnetic field normal to diffraction plane
TM	Transverse magnetic field polarization mode
TE	Transverse electric field polarization mode
$\hat{u}$	Unit vector giving k direction
$U_{\ell,xi}$, $U_{\ell,yi}$, $U_{\ell,zi}$	Amplitude of pace harmonics of magnetic field
$v_{\ell,i,m}$	Elements of matrix $V_\ell = W_\ell Q_\ell$
V_ℓ	Matrix $W_\ell Q_\ell$
V_{ss}, V_{sp}, V_{ps}, V_{pp}	Matrices representing products and sums of eigenvalues/eigenvectors
V_{11}, V_{12}, V_{21}, V_{22}	Matrices representing products and sums of eigenvalues/eigenvectors

$w_{\ell,i,m}$	Elements of eigenvector matrix W_ℓ
w_r	Width of a grating ridge
W_ℓ	Eigenvector matrix of A_ℓ
W_{ss}, W_{sp}, W_{ps}, W_{pp}	Matrices representing products and sums of eigenvalues/eigenvectors
x	Rectangular coordinate perpendicular to grating ridges
X_ℓ	Diagonal matrix with elements $\exp\left(-k_0 q_m d\right)$
XX_ℓ	Matrix, represents G_ℓ for homogeneous layer, X_ℓ for grating layer
$XX_{\ell,1}$	Matrix, represents G_ℓ for homogeneous layer, $X_{\ell,1}$ for grating layer
$XX_{\ell,2}$	Matrix, represents G_ℓ for homogeneous layer, $X_{\ell,2}$ for grating layer
X_1	Diagonal matrix with elements $\exp\left(-k_0 q_{1,m} d\right)$
X_2	Diagonal matrix with elements $\exp\left(-k_0 q_{2,m} d\right)$
y	Rectangular coordinate along grating ridges within SVDOE
Y_I	Diagonal matrix with elements $k_{I,zi} / k_0$
Y_{II}	Diagonal matrix with elements $k_{II,zi} / k_0$
z	Rectangular coordinate normal to SVDOE surface
Z_I	Diagonal matrix with elements $k_{I,zi} / \left(k_0 n_I^2\right)$
Z_{II}	Diagonal matrix with elements $k_{II,zi} / \left(k_0 n_{II}^2\right)$
$\gamma_{\ell,i}$	$j\left[n_\ell^2 - \left(\frac{k_{xi}}{k_0}\right)^2\right]^{1/2}$
Γ_ℓ	Diagonal matrix with elements γ_ℓ
$\delta_{i,0}$	Kronecker delta function
Δn	Refractive index difference between grating ridge and groove materials

Δn_{amp}	Amplitude of the sinusoidal refractive index modulation
Δn_h	Amplitude of the h^{th} harmonic component of the refractive index
Δn_1	Amplitude of the first harmonic component of the refractive index
ε	Permittivity of a medium
ε_0	Permittivity of free space
ε_0	Average permittivity of a medium with sinusoidal modulation
ε_1	Amplitude of permittivity modulation of a medium
ε_h , $\varepsilon_{\ell,h}$	Amplitude of h^{th} harmonic component of permittivity modulation
θ	Incidence angle of wave on SVDOE
θ_B	Bragg angle
θ_{0p}	Incidence angle where p^{th} diffraction efficiency peak is predicted
κ	Coupling coefficient for volume holography
κ_{SVDOE}	Coupling coefficient for SVDOE
λ_0	Freespace wavelength
Λ	Grating period
μ_0	Permeability of free space
π	Physical constant pi
ϕ	Azimuthal angle of wave incident on SVDOE
φ	Angle between grating vector and inward surface normal
φ_i	Inclination angle of i-th propagating diffraction order
χ	Modulation parameter in volume holography
χ_{SVDOE}	Modulation parameter for SVDOE
ψ	Polarization angle, 90° = TE, 0° = TM

ω	Angular optical frequency
Ω_ℓ	Diagonal matrix with elements $\frac{\gamma}{n^2}$

Chapter 1

INTRODUCTION

Gratings with high diffraction efficiency into a single order find use in a multitude of applications ranging from optical interconnects to beam steering. Such gratings have been realized with volume holographic, blazed, and diffractive optical techniques [1], [2], [3], [4], [5], [6], [7], [8], [9]. However, each of these methods has limitations that restrict the range of applications in which they can be used. For example, high efficiency volume holographic gratings require an appropriate combination of thickness and permittivity modulation throughout the bulk of the material. Possible combinations of these parameters are limited by the physical properties of currently available materials, thus restricting the range of potential applications. Similarly, fabrication considerations place constraints on the minimum achievable period for blazed gratings and multi-phase level diffractive optic gratings, hence limiting the applications in which they can be used. Likewise, high diffraction efficiency can be achieved with deep binary gratings, but only for specific incidence angles. In this work an alternate, novel approach and method for creating high-efficiency gratings has been developed. These new gratings are named stratified volume diffractive optical elements (SVDOE's). In this approach diffractive optic techniques are used to create an optical structure that emulates volume grating behavior. This idea is an extension of concepts derived in previous work on stratified volume holographic optical elements (SVHOE's) in which holographic recording materials available only as thin films are combined to create an element with diffraction efficiency approaching that of a traditional volume holographic optical element [10], [11], [12].

In this current effort the diffraction properties of SVDOE's are examined and their potential use as a beam scanning element are illustrated for application in a space-based coherent wind LIght Detection And Ranging (lidar) system [13]. This application specifies a transmissive scanner element with a *normally* incident input beam and an exiting beam deflected at a fixed angle from the optical axis. A conical scan pattern would be produced by rotating the scanner element about its optical axis. The wavelength of the incident beam for the lidar application is approximately 2μm and the required deflection angle is 30 degrees. Additional requirements include insensitivity to polarization orientation, minimal disruption of the transmitted wavefront (due to the heterodyne detection system), low mass, and the ability to withstand launch and space environments.

The scanner function can in principle be achieved with a rotating prism. However, mass and satellite stability considerations make a thin holographic or diffractive element attractive. For either option, a grating period of approximately 4μm is required. This is small enough that fabrication of either appropriate high-efficiency blazed or multi-phase-level diffractive optical gratings is prohibitively difficult. Moreover, bulk or stratified volume holographic approaches appear impractical due to materials limitations at 2μm and the need to maintain adequate wavefront quality. The requirement for normal incidence operation likewise eliminates the use of deep binary gratings. In contrast to these traditional approaches, the SVDOE concept has the potential to satisfy lidar beam scanner requirements.

Fabrication of the stratified structure of an SVDOE presents unique challenges. Standard microfabrication techniques combined with emerging planarization techniques can be employed to address individual layers of the device. However, a novel approach is required to link these techniques to create a functional element. Such an approach is developed in this work and applied to the fabrication of demonstration elements. These elements are then tested and their performance is shown to agree well with theoretical predictions based on structure parameters measured by examination with a scanning electron microscope (SEM).

The motivation for developing SVDOE's is addressed in Chapter 2. It begins with a description of the lidar instrument and its requirements for a scanning element. It then proceeds with a discussion of current grating technologies, particularly their limitations relative to meeting the lidar scanner requirements.

The SVDOE structure is introduced in Chapter 3 along with the rigorous coupled wave analysis (RCWA) method chosen to model it. The RCWA is then used to illustrate the diffraction properties of SVDOE's as a function of modulation strength, refractive index difference, homogeneous layer thickness, and incidence angle of the input beam. These properties are compared and contrasted to those of traditional gratings. The similarity of SVDOE behavior to volume holographic gratings is exploited to derive an expression for optimum modulation thickness in an SVDOE.

Chapter 4 develops a systematic design process for a complete SVDOE structure. The process is illustrated by establishing a set of SVDOE designs parameterized by representative material properties (refractive index) and the number of grating layers within the structure. One design from within the set is chosen as a proof-of-concept element and its performance is studied in detail, including tolerance to fabrication errors.

Chapter 5 applied the design process developed in Chapter 4 to arrive at detailed designs for two elements that will proceed to a fabrication phase. Materials selections for the elements are given along with their optical properties. Performance studies of the elements based on their fabrication tolerances indicate the need for an alignment scheme with greater precision than that which is available on the photolithographic mask aligner used for this work. The theory of such a high-precision alignment scheme is presented in Chapter 6 along with the equipment modifications needed for its implementation.

Chapter 7 provides detailed discussion of SVDOE fabrication processes. These include thin-film deposition of grating layers, patterning of grating layers with photolithographic and reactive ion etching processes, and planarization with homogeneous layers. The alignment process is also described here. Chapter 8 provides similar discussions for each of the processes involved in evaluating SVDOE performance. Included here are structural parameter measurement, alignment assessment, and diffraction properties.

Chapter 9 and Chapter 10 discuss implementation and outcome of the fabrication and evaluation processes for the two SVDOE designs fabricated in this work. Chapter 11 summarizes the accomplishments made here and makes recommendations for future research.

Chapter 2

BACKGROUND

To establish a background for development of the SVDOE concept, the specific instrument requiring such a device, a wind-measurement lidar, will be discussed. Current grating technologies will also be discussed. The requirements of the lidar system are such that existing grating technologies cannot be levied to create its scanning element.

2.1 Lidar instrument description

The system is a monostatic configuration with polarization as the discriminator between transmitted and received beams. The detection process is heterodyne, or coherent, detection in keeping with the label of 'coherent' wind lidar. The degree of matching for wavefront shape and polarization between the reference and signal beams, or heterodyne efficiency, is directly proportional to signal-to-noise ratio (SNR) in coherent detection and is thus critical to efficient instrument operation. The operating wavelength of the instrument is 2.06μm, which is produced by a Tm,Ho:YLF laser. Diameter of the transmit/receive beam is 25cm. The beam is deflected 30º from the optical axis and scanned 360º in azimuth as illustrated in Figure 2.1. The backscatter target is atmospheric aerosols, which produce a weak return signal in comparison with a solid target. As a result, the efficiency of each component is important in order to maintain SNR at a detectable level. The overall instrument package should be as compact as possible to meet accommodation restrictions for the space shuttle program.

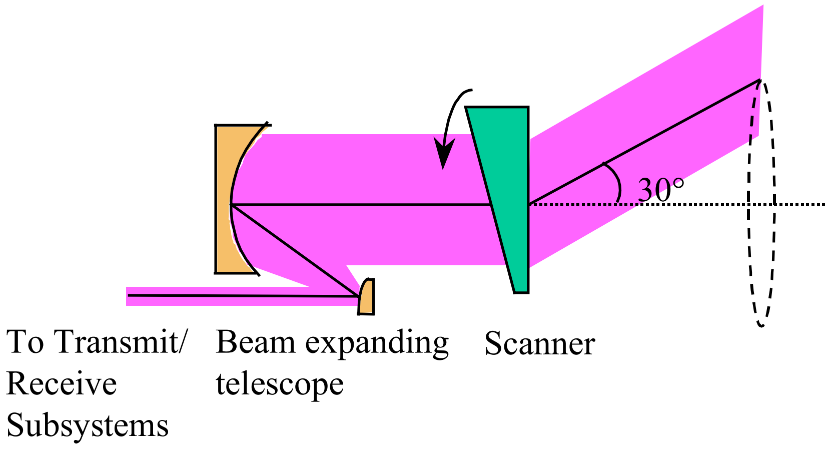

Figure 2.1 Illustration of lidar scanning configuration with existing prism scanning element.

2.2 Scanner requirements

The lidar instrument configuration outlined above implies performance and configuration requirements for the scanning subsystem. The first requirement is that the scanner operate as a transmissive element rather than as a rotating telescope so that the instrument package is compact. The most compact configuration requires that the scanner element be used at normal incidence as shown in Figure 2.2. Efficiency of the element is the next consideration. Since the beam will make a double pass through the scanner element and aerosol backscatter is a weak signal return, transmission efficiency is critical to system performance. For a grating scanner element this translates into a diffraction efficiency of approximately 95%. Matching between the reference and signal beams requires that the scanner cause minimal disruptions to the wavefront shape and beam polarization. For example, an error of 0.1 waves (rms) across the scanner aperture results in an approximately 30% degradation in heterodyne efficiency [14]. A beam deflection angle of 30º in combination with an operating wavelength of 2.06µm dictates that the period of a grating used for this application should be approximately 4µm.

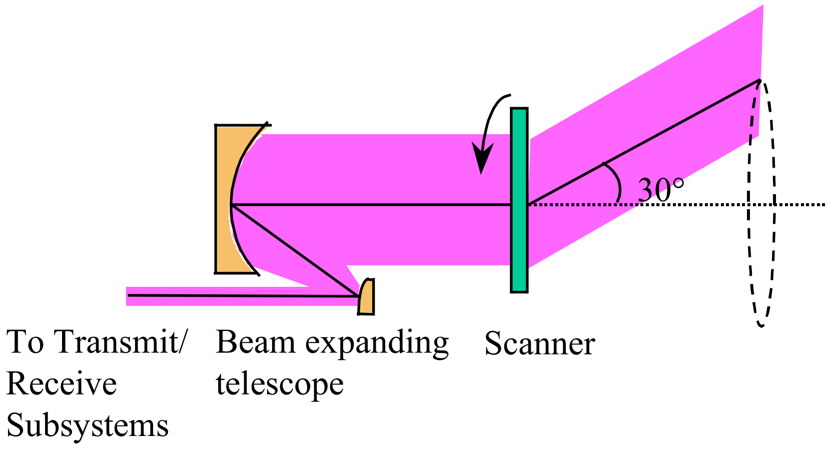

Figure 2.2 Illustration of proposed lidar scanning configuration with prism scanning element replaced by a grating on a symmetric substrate.

2.3 Current grating technologies

The two primary approaches for producing high efficiency gratings, diffractive optic and volume holographic, have been mentioned above. Diffractive optics encompass mechanical, lithographic and direct-write methods for implementing a grating profile in a substrate or thin film. Volume holography typically involves exposure of a photosensitive material to an interference pattern to induce a desired permittivity modulation. A third method of modulating the index of an element is by electro-optic tuning in either bulk or liquid crystal materials. This produces the same effect as a diffractive optic grating, but is dynamic since the modulation is controlled electronically. Each of these techniques will be discussed below, along with the difficulties they encounter in meeting the requirements imposed by the coherent wind lidar instrument.

2.3.1 Diffractive optic gratings

The ideal diffractive optic option is a blazed profile grating, which can yield ~100% efficiency in the desired order. Much attention has been given to the fabrication of analog profiles which are good approximations to the ideal blazed profile. Alternatively, multi-level approximations to the blazed profile may be produced using lithographic etch techniques developed for the electronics industry.

2.3.1.1 Analog profiles

Analog profiles approximating the ideal, blazed profile can be produced by mechanical and direct-write methods [2]. Mechanical methods involve direct shaping of the substrate surface by either ruling or diamond turning. Single-point diamond turning can produce elements with the highest efficiencies, approaching 99%, and feature sizes on the order of a few microns. However, it introduces turning marks in the surface that cause scattering of incident light, which can be significant at visible wavelengths. This implies that the element must be used in the infrared or replicated in a material which shrinks during processing, such as sol-gel, so as to minimize the effect of the turning marks. With minimum feature size remaining at a few microns, diamond turning is not a viable option for producing the grating needed for the coherent wind lidar instrument.

Arbitrary diffractive patterns, rather than the restricted patterns available with diamond machining, can be created using alternative techniques. The two basic methods available are directly writing into a photoresist or substrate with a variable intensity source and gray-scale lithography. One direct-write method is electron-beam lithography. Here an electron beam undergoes deflection within a small area, or subfield, while the energy and/or the shape of the beam is varied to write a pattern. The substrate is translated with respect to the beam to write the entire optical area in a series of subfields. The feature sizes produced with an electron-beam can be on the order of 0.1μm. Difficulties encountered in this process are distortion at the edge of a subfield, abutment of subfields and mechanical runout or registration errors at the limitations of the translation stages. Another method of patterning photoresist is single-point laser writing. In this method a laser beam is scanned across the resist while its intensity is varied to produce the desired profile by controlling exposure of the resist. A laser-writer beam can be 1μm or less, which is inadequate to produce a high-efficiency blazed grating with the 4μm period needed here. Also, maintaining stability during the lengthy writing process for an element with clear aperture of 25cm is not possible with either electron-beam or laser-writer systems at this time.

Excimer laser ablation has recently been developed as a method for directly machining a profile into a material. Again, the substrate is translated with respect to the laser source to write a profile across the element area. Control of the beam characteristics such as shape and fluence and altering the number of pulses applied to a particular region produces an arbitrary profile. Since the entire element area must be processed, this method suffers the same difficulties outlined above in meeting requirements for a large diameter optical element.

Gray-scale lithography has been pursued by producing gray-scale masks using halftones, sliding imagers and electron beam exposure of high-energy beam-sensitive glass (HEBS). The first two gray-scale mask methods produced gratings of 70% and 84% efficiency, respectively, but with feature sizes of 100 microns and greater [3], [4]. Feature sizes reported with the HEBS glass are between 5 and 10 microns using contact lithography [5]. These feature sizes are inadequate for the grating required by the coherent wind lidar instrument.

2.3.1.2 Binary profiles

The typical method for approximating a blazed profile with lithographic techniques is a binary, or multilevel, stepped profile as shown in Figure 2.3. The efficiency of a binary approximation at deflecting light into the desired order is dependent on the number of levels used with 16-32 required to approach 99%. With a period of 4μm as required by the lidar scanner, feature sizes of the levels would be 0.25 microns or below. While features of this size are attainable using current lithographic techniques, generating a multi-level blazed grating with those features would be extremely difficult due to process limitations such as resolution of the binary masks, accuracy of mask registration to the substrate and control of etching parameters.

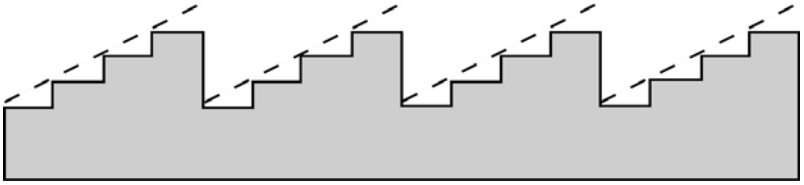

Figure 2.3 Illustration of a diffractive optic, or surface relief, approach to achieving a high-efficiency grating. The dashed line represents an ideal analog profile while the solid line represents a binary approximation.

A new technique for producing slanted surface-relief binary gratings has recently been published [6]. This method attempts to obtain the performance of a volume grating with surface-relief fabrication by slanting the profile of a binary grating at the Bragg angle. The slanted profile is achieved by creating a binary mask in photoresist with a standard lithographic technique then inclining the substrate at the desired slant angle during patterning in a reactive etch process. The theoretical efficiency for such a grating was calculated to be as high as 97%. Experimental verification of a design for a grating with 48% efficiency was within 2% of the theoretical prediction. A limitation of this approach when originally published was that the dimensions of the substrate must be small enough to be compatible with a standard reactive etching chamber when it is slanted at the required profile angle. Thus, the diameter of the element required for the coherent wind lidar instrument eliminates this technique. Researchers at Lawrence Livermore National Laboratory (LLNL) have very recently extended the diameter of the optic that can be produced using this method by employing ion milling, as shown in Figure 2.4, rather than reactive ion etching [15] through collaboration with NASA/MSFC.

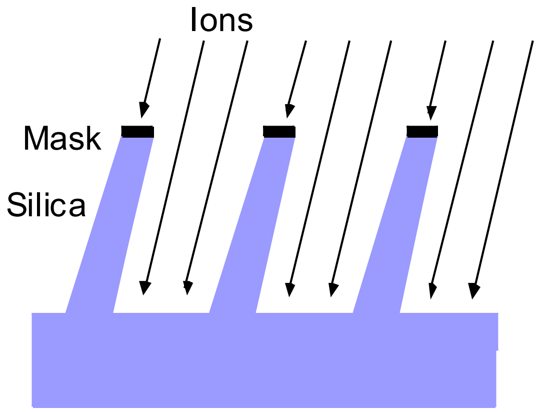

Figure 2.4 Illustration of patterning a slanted groove grating by ion milling.

Another approach that has been explored for approximating the linear phase shift of a blazed grating using binary techniques is to create an effective-index medium using high spatial frequency binary features within the grating period [7], [8]. The binary features are uniform in height and their width is subwavelength, typically submicron. The effective refractive index of the medium is controlled by varying the width of the binary ridges, their position or both. The advantage of this technique is that only a single lithographic step is required. However, the highest diffraction efficiency reported for a grating design at normal incidence was 72% [8], which is lower than that required for the lidar scanner. Also, the deflection angle for this grating was relatively shallow, approximately 5º, compared to the requirements considered here, yet the feature sizes were on the order of one tenth of the operating wavelength. To obtain the 30 degree deflection angle desired for this application the feature sizes would be below 0.1 micron, which is very difficult to achieve at this time, particularly over a large area such as a scanning element.

Diffraction efficiency approaching 100% can also be achieved with simple 50% duty cycle binary gratings as illustrated in Figure 2.5 [9]. The period of these gratings is on the order of a wavelength and the depth is usually at least twice, often many times, greater than the period. This aspect ratio can present a fabrication challenge. Also, obtaining high efficiency requires incidence at the Bragg angle or within a small angular deviation of that angle, which is contrary to the requirement for creating a compact optical system.

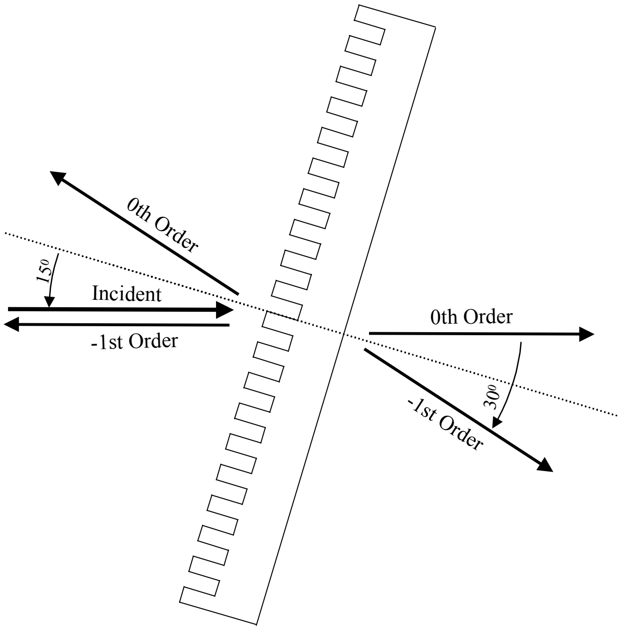

Figure 2.5 Illustration of achieving high efficiency with a binary grating. The grating must be placed at an angle to the beam, specifically the Bragg angle.

2.3.2 Holographic gratings

Holographic gratings are produced by exposing photosensitive material to an interference pattern, which induces a modulation in refractive index of the material as depicted in Figure 2.6. This figure depicts fringe planes which are slanted with respect to the grating surface in order to shift the preferred incidence angle. The resulting grating exhibits properties of a volume grating, providing the material thickness is chosen properly. Volume holograms can theoretically deflect an incident beam with an efficiency approaching 100% [16].

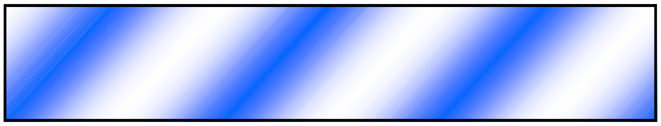

Figure 2.6 Depiction of refractive index modulation in a holographic grating. The dark areas represent higher refractive index than the light areas. The refractive index modulation is typically sinusoidal in amplitude.

Examples of typical non-crystalline permanent holographic recording materials are dichromated materials and photopolymers. One disadvantage of these materials is their sensitivity to the environment. As a result, the material must be protected between two substrates, implying more mass than a comparable grating implemented in surface relief. Disadvantages particular to dichromated materials are the difficulty encountered in reliably reproducing results and the complexity of the procedures needed for their preparation. These problems are compounded as material thickness and beam diameter increase, both of which are conditions for the coherent lidar scanner. Photopolymers are available in sheets of varying thickness; however, the range of thicknesses available does not extend into the region required for the 30 degree deflection angle needed for this application. Also, the chemical formulation of photopolymer sheets is most often optimized for operation at visible wavelengths [17], [18], [19], [20]. One source reports favorable performance using photopolymer sheets at a wavelength of 824nm [21]. However, work under contract to NASA/MSFC to evaluate their performance at the

2.06μm wavelength required for this application indicated that the index modulation, and consequently the diffraction efficiency, was greatly reduced at this wavelength [22].

The observed wavefront quality from holographic elements is another area of concern. There is very little published information concerning measurement of wavefront after passing through holographic gratings. One source cites two waves of irregularity for a holographic grating fabricated using dichromated gelatin (DCG) operating with 83% efficiency at a wavelength of 0.843μm [23]. An experimental DCG holographic grating was fabricated by another research group for evaluation as a possible scanner element for the coherent lidar system considered here [22]. The wavefront transmitted by this holographic element was examined for this work and measured two waves of peak-to-valley aberration. Nonuniformity of the element limited wavefront measurement to an approximately one-inch diameter area in the center of the element's four-inch diameter. The efficiency of diffraction into the first order was also measured and found to be 50% at a wavelength of 2.06μm.

2.3.3 Electro-optic gratings

Binary approximations to gratings can be created in either bulk or liquid crystals by exploiting the electro-optic effect [24], [25], [26]. Strip electrodes are applied to one surface of the material (or protective plate) and voltages are applied between the electrodes and a ground plane on the other surface. The refractive index of the material is proportional to the applied voltage so, by controlling the voltages, stepped index profiles can be created which have variable deflection angle and efficiency. Just as with a surface relief binary grating approximation, many index levels must be used in order to obtain an efficiency approaching 100%. Difficulties associated with implementing those levels on this type of device include electrode spacing, addressibility of the number of electrodes required, electric field fringing effects and the index modulation achievable with a given material. Obtaining the 30° deflection angle required for the coherent lidar application does not appear possible with electro-optic gratings at this time.

Chapter 3

THEORETICAL APPROACH

It has been established that there are applications, in particular the lidar scanner discussed here, that cannot be addressed by current grating technologies. A new approach has been conceptualized, the SVDOE, that has potential to meet these needs. This chapter will describe what is meant by SVDOE and discuss behavior characteristic of such a multi-level element. The structure of an SVDOE will be presented first, followed by a discussion of extensions to existing modeling approaches that are necessary to accommodate its unique form. The discussion will continue by presenting diffraction properties of SVDOE's and by both comparing and contrasting those with properties of traditional volume gratings. Mathematical expressions describing SVDOE behavior are developed en route, again, within the context of a volume grating.

3.1 Grating and coordinate system definitions

Before proceeding with a description of SVDOE's, nomenclature used for binary gratings and the coordinate system used in this work will be defined. Figure 3.1 is an illustration of a binary grating. It consists of alternating rectangular regions of high refractive index, n_r, which are shown in gray, and regions of low refractive index, n_g, which are left blank in the figure. The high-refractive-index regions are referred to as grating ridges and the low-refractive-index regions are referred to as grating grooves. All grating ridges are assumed to be of equal width, w_r, and all grating grooves are also assumed to be of equal width. A grating period, Λ, is defined as the total width of one grating ridge and one grating groove. The ratio of the ridge width to the grating period, w_r/Λ, is typically referred to as the fill factor of the grating. The thickness of the grating, d_g, is defined as the distance from the top of a grating ridge to the bottom of a groove.

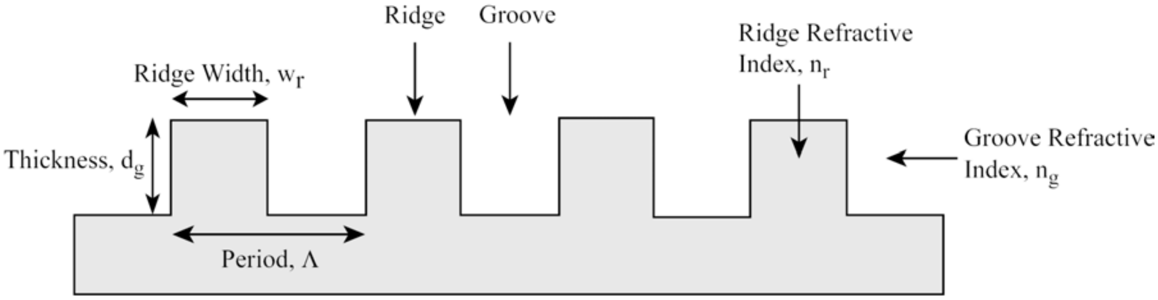

Figure 3.1 Illustration of a binary grating with definitions of grating terms.

The coordinate system used in this work is illustrated in Figure 3.2. A right-handed system is defined with the x-direction perpendicular to the grating grooves, the y-direction parallel to the grooves, and the z-direction normal to the grating plane. A linearly polarized electromagnetic wave with wave-vector, k, is incident on the grating at an arbitrary angle of incidence, θ, with an azimuthal angle, ϕ. The plane of incidence is formed by the wave-vector and the z-axis. For the case of planar diffraction ($\phi = 0$) the incident polarization may be decomposed into a TE- ($\psi = 90°$) and a TM-polarization ($\psi = 0°$) problem, which may be solved independently. For that case, all the forward- and backward-diffracted orders lie in the plane of incidence, or the x-z plane. For the more general case of three-dimensional diffraction ($\phi \neq 0$), or conical diffraction, the diffracted wave-vectors lie on the surface of a cone and the perpendicular and parallel components of the fields are coupled and must be solved simultaneously. The grating is bounded in the incident region, or Region I, by a medium with refractive index n_I and in the exiting, or transmitted, region (Region II) by a medium with refractive index n_{II}.

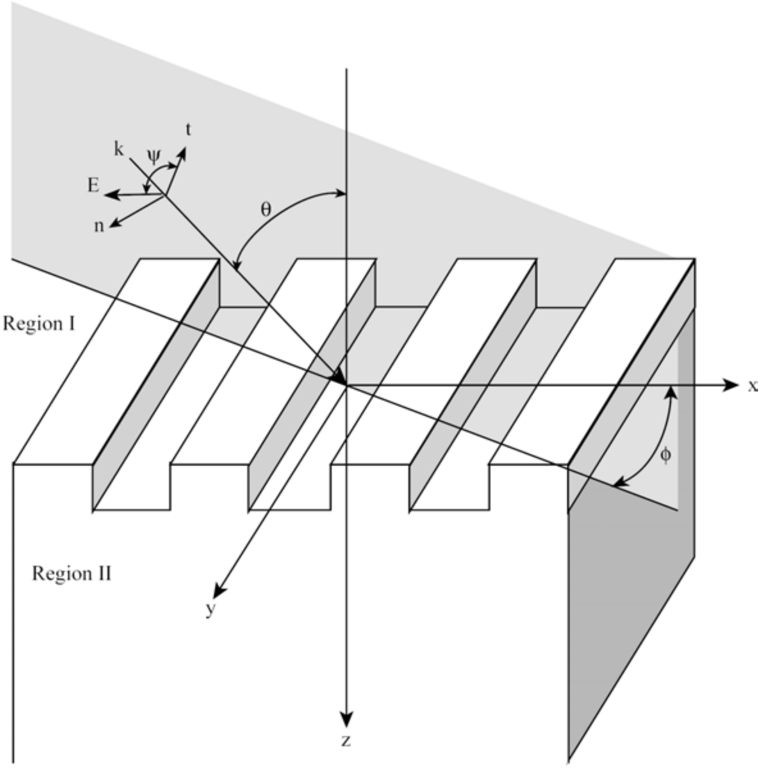

Figure 3.2 Coordinate system illustration.

3.2 SVDOE structure

The SVDOE structure consists of binary grating layers interleaved with homogeneous layers as illustrated in Figure 3.3. An incident wave impinges on the SVDOE from Region I then transmits through the element and exits at an angle in Region II. The incident wave in this figure is shown normal to the SVDOE rather than at an angle. Ridges in the grating layers are composed of a high refractive index material whereas the grooves and homogeneous layers utilize a material with a low refractive index, just as in Figure 3.1. The thickness of each layer is denoted by d_ℓ, where ℓ is the layer number within the structure, ranging from 1 to L. The binary grating layers modulate a wavefront as it passes through the structure and the homogeneous layers allow diffraction to occur. While the individual binary grating layers are relatively thin, incorporation of diffraction via the homogeneous layers permits an SVDOE to attain diffraction efficiencies comparable to a volume holographic element in which modulation and diffraction are spatially coincident throughout the medium.

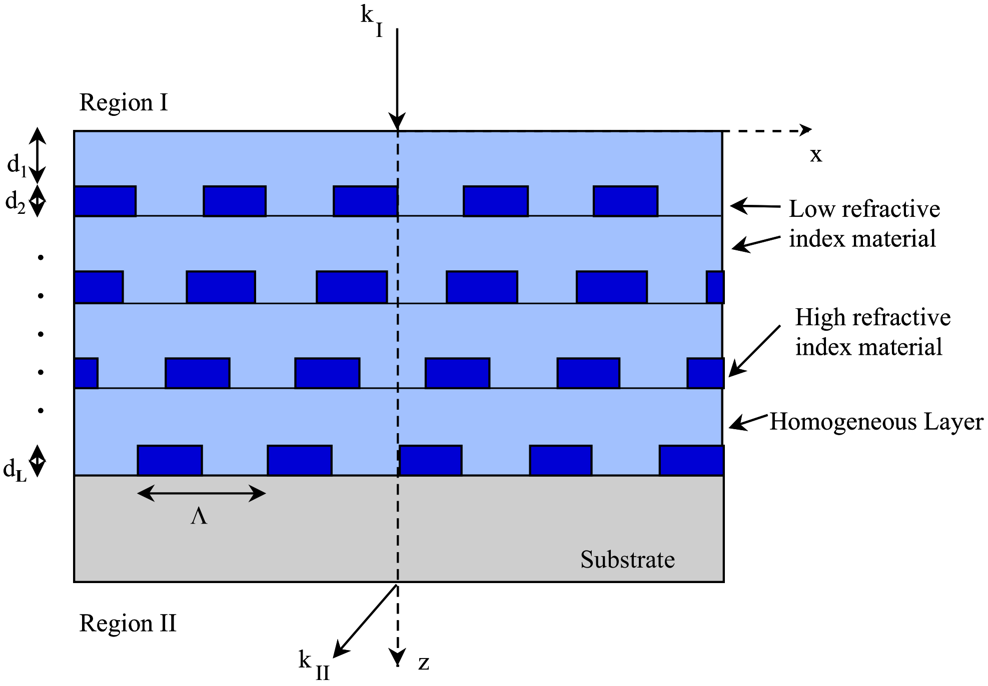

Figure 3.3 Schematic illustration of the stratified volume diffractive optic element (SVDOE) structure. Binary grating layers are interleaved with homogeneous layers to achieve high efficiency. The gratings are shifted relative to one another, much like standard fringes in a volume grating, as a means to control the preferred incidence angle.

Since the layers in this type of structure must be fabricated sequentially, the binary grating layers can be laterally shifted relative to one another (as illustrated in Figure 3.3) to create a stratified diffractive optic structure analogous to a volume grating with slanted fringes. This allows an element to be designed with high diffraction efficiency into the first order for any arbitrary angle of incidence (including normal incidence as is required by the lidar beam scanner application).

3.3 Simulation methodology

Several analysis methods based on scalar theory have previously been applied to the simulation of a holographic element (SVHOE) performance [10], [11], [12], [27]. However, depending on the choice of materials, the grating structure discussed above can include a relatively large refractive index difference between the materials in the grating layer. For the specific example application considered here, there is also a small period to wavelength ratio (e.g., < 10). Accurate prediction of diffraction efficiency under these conditions requires a rigorous electromagnetic diffraction theory. Rigorous coupled-wave analysis (RCWA) as formulated by Moharam, et al. [28], [29] was chosen to model the behavior of these stratified structures. This algorithm was selected from among many other rigorous electromagnetic modeling approaches [30], [31], [32], [33], [34], [35] since it maintains its intuitive description of diffraction within the structure.

3.3.1 Historical development of RCWA

The formulation of RCWA presented by Moharam, et al. has evolved into an efficient and stable implementation for general multi-layer structures from its inception for single-layer, planar gratings. The algorithm for planar gratings [36] was presented in a matrix form, based on the method of state variables, such that it could be easily implemented on a computer and solved using eigenfunction and eigenvalue library routines. Analysis of several grating configurations illustrated agreement with rigorous modal theory and with approximate theories for both the modal and coupled-wave approaches. An additional benefit of this implementation was increased accuracy and the ability to analyze more general grating structures because of its rigorous nature.

Following the initial formulation of RCWA as a state-variables representation, it was then applied to the analysis of surface relief gratings [37]. Arbitrary grating profiles were analyzed by dividing the grating into a large number of thin layers parallel to the substrate and treating each in sequence. For each thin layer the relative permittivity was expanded as a Fourier series and then the rigorous coupled-wave equations were solved in that layer. Applying electromagnetic boundary conditions at the interface between each layer ensured accurate analysis of the grating system. Comparison with other rigorous methods for sinusoidal surface relief profiles showed excellent agreement for diffraction efficiencies while maintaining greater accuracy in conservation of power, indicating both the accuracy and stability of the algorithm for multi-layer systems.

A subsequent formulation of RCWA for single, binary gratings introduced simplifications to the coupled-wave equations which enhanced computational efficiency and reduced computer memory requirements while maintaining its rigorous approach [28]. Numerical overflow in the application of electromagnetic boundary conditions was eliminated by a normalization process which ensured that arguments of exponential functions were always negative. The stability of this approach was illustrated by calculation of diffraction efficiencies for gratings with depths of up to fifty times the incident wavelength.

These improvements for single layer binary gratings were applied to an RCWA formulation for analysis of multi-layer surface-relief gratings. However, numerical instabilities could still arise from the approach used in enforcing the electromagnetic boundary conditions at successive interfaces. The source of these instabilities, namely evanescent fields, was thoroughly discussed by Moharam, et al. and a solution involving an enhanced transmittance matrix approach was developed [29]. The capabilities of the enhanced transmittance matrix algorithm were illustrated by analyzing a 16-level asymmetric grating for periods of one and ten times the incident wavelength and for depths of up to fifty times the incident wavelength. Diffraction efficiency for each of the grating configurations was calculated for planar diffraction in both TE and TM polarizations and for conical diffraction. In all cases the conservation of power was accurate to within 1 part in 10^{10} and the solution converged with an increasing number of field harmonics, thus meeting the stated criteria for numerical stability [29].

3.3.2 Extension of RCWA to accommodate SVDOE structure

The RCWA implementation discussed above for analyzing multi-layer gratings using the enhanced transmittance matrix approach was chosen as the starting point for an extended algorithm to accommodate the unique, layered structure of SVDOE's. That algorithm will be outlined in this section with full mathematical details for planar diffraction, both TE and TM polarization, presented in Appendix A and for conical diffraction in Appendix B. The algorithm begins by establishing space harmonic expansions for the fields in a homogeneous, or uniform, layer similar to the space harmonic expansions in a grating layer. Then, using the matrix structure generated from applying electromagnetic boundary conditions for a binary grating as a basis, an identical matrix structure is enforced when matching boundary conditions for uniform layers. Given the identical matrix structure for all layer types, the sequence of grating and uniform layers may be completely arbitrary. Shifting the grating layers to mimic slanted fringes is accommodated in the Fourier expansion of the relative permittivity for each grating layer. Since this is applied independently to each grating layer, the lateral position of any grating layer is completely independent of the position of other grating layers. Material properties, including both refractive index and dispersion, may be defined for the grooves and the ridges of each grating layer independently as well as for each homogeneous layer independently. The only assumption made in this algorithm is that all grating layers have identical period.

The re-formulation of the coupled-wave equations as published by Li [38] to improve convergence for TM polarization and conical diffraction have been included in this algorithm implementation. Previous RCWA formulations [28], [29] have indicated that more terms are required in the harmonic expansions to obtain convergence for these cases than for TE polarization.

The computational implementation of RCWA with extensions for SVDOE's is listed in Appendix C. It is typically executed from within a graphical user interface (GUI), which is not listed here. Both the extended RCWA and the GUI were developed entirely during the course of this project.

Verification of the algorithm implementation was conducted according to the same criteria applied by Moharam, et al. [28], [29], specifically conservation of power to within one part in 10^{10} and convergence with increasing number of space harmonics. Several grating profiles studied in the previous references, such as deep binary gratings and multi-layer sawtooth configurations, were analyzed and found to agree with published results and also to meet the conservation and convergence criteria [28], [29], [36]. A nine-layer resonant grating configuration consisting of a binary grating layer surrounded by high/low quarter-wave stacks was also studied since it contained both binary and uniform layers, similar to an SVDOE. The transmittance of the filter as a function of wavelength compared exactly to the published curve of the same function [39]. An SVDOE structure consisting of five grating layers separated by uniform layers was then studied. As is shown in Figure 3.4, convergence occurred within a very small number of retained space harmonics (<20) for both TE and TM polarizations. For all number of space harmonics, the residual error in the conservation of power was on the order of 10^{-14}.

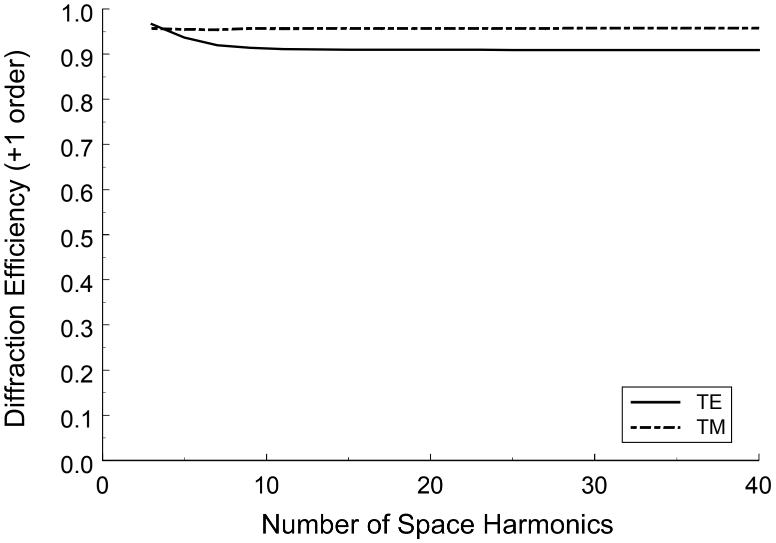

Figure 3.4 Convergence of the first order diffraction efficiency of an SVDOE with five grating layers plotted as a function of the number of space-harmonics, corresponding to the number of diffracted orders, retained in the calculation. $\lambda_0 = 2.06\mu m$, $\theta = \theta_B = 9.885°$, $n_I = 1.5$, $n_{II} = 1.5$, $n_r = 2.0$, $n_g = 1.5$, $d_g = 0.638\mu m$, $d_h = 4.6\mu m$. Readout beam is positioned at Bragg incidence; there is no relative offset between grating layers.

3.4 Diffraction properties

Similar to the holographic based SVHOE's, the stratified structure of SVDOE's introduces diffraction properties that are unique compared to the behavior of traditional volume holographic or diffractive optic gratings. These properties are illustrated in this section by examining the diffraction efficiency of SVDOE's as a function of the total grating layer thickness, the homogeneous layer thickness and the incidence angle of the readout beam.

In a conventional grating the diffraction efficiency increases with increasing modulation thickness until it reaches a peak value. As the modulation thickness continues to increase the grating becomes overmodulated and the diffraction efficiency decreases. The behavior of

SVDOE's in similar circumstances is considered by defining a structure with constant homogeneous layer thickness and varying grating layer thickness. The readout beam is positioned at Bragg incidence with the grating layers aligned such that they have no lateral offset relative to each other, as illustrated in Figure 3.5. Figure 3.6 shows the +1 order diffraction behavior for SVDOE's consisting of 3, 5 and 7 grating layers as a function of the product ΔnD_g, which characterizes the modulation of the grating. Here Δn is the refractive index difference between the ridge and groove materials and D_g is the total grating layer thickness in each structure. For this case illustrated in Figure 3.6, $\Delta n = 0.1$. The homogeneous layers are assumed to have a refractive index identical to the grating grooves. The diffraction efficiency follows the expected behavior in Figure 3.6 which shows the first period of an approximately sinusoidal dependence of the diffraction efficiency on the product ΔnD_g. The peak diffraction efficiency is achieved for the same value of ΔnD_g, regardless of the number of grating layers.

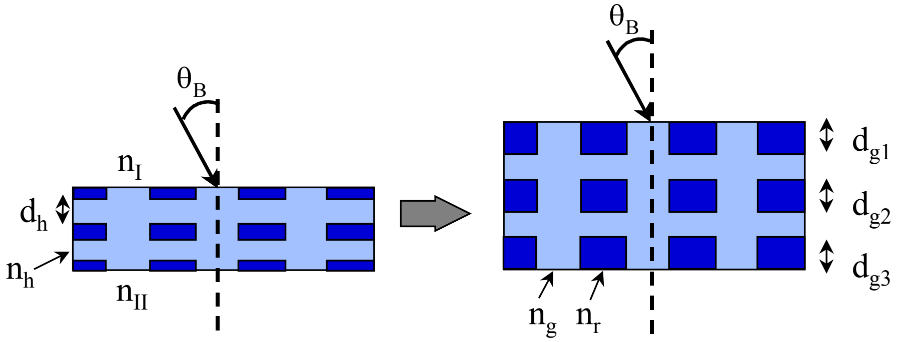

Definitions: $\Delta n = n_r - n_g$

$D_g = \sum_N d_{gN}$

Figure 3.5 Illustration of process for examining diffraction efficiency behavior as SVDOE modulation thickness is increased. Readout beam is positioned at Bragg incidence; there is no relative offset between grating layers.

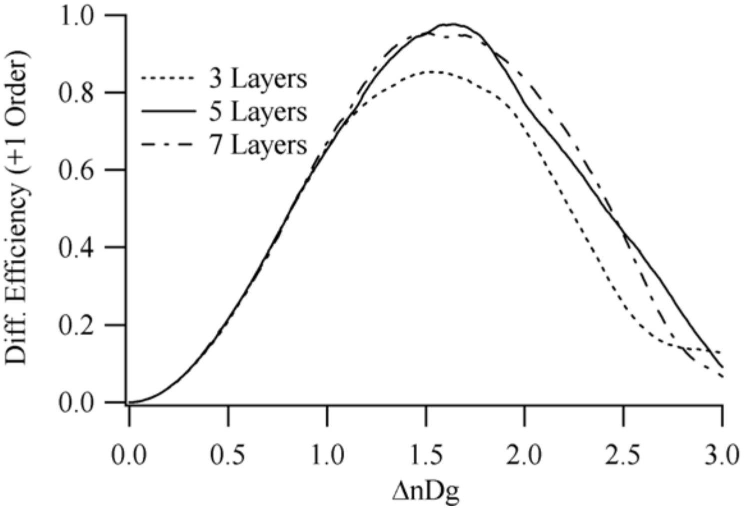

Figure 3.6 Diffraction efficiency of three-, five-, and seven-layer SVDOE's as a function of total modulation (Δn=0.1). $\lambda_0 = 2.06\mu m$, $\theta = \theta_B = 9.885°$, $n_I = 1.5$, $n_{II} = 1.5$, $n_r = 1.6$, $n_g = 1.5$. Readout beam is positioned at Bragg incidence; there is no relative offset between grating layers.

To further examine this behavior, another set of SVDOE's is considered under the same conditions, but with Δn=0.5. Typical results are shown in Figure 3.7. Although there is now significant structure in the curves, the same general trends apply. In particular, note that the peak diffraction efficiency for each curve still occurs near a value of $\Delta nD_g \cong 1.5\mu m$. The variations in the curve from a sinusoidal shape are due to interference from multiple reflections at the grating layers. As one would therefore expect, the structure in the curves changes substantially for small changes in the homogeneous layer thickness.

This assertion is verified by re-examining the set of SVDOE's with $\Delta n = 0.5$ after inserting anti-reflection layers at the interfaces between grating and homogeneous layers. This

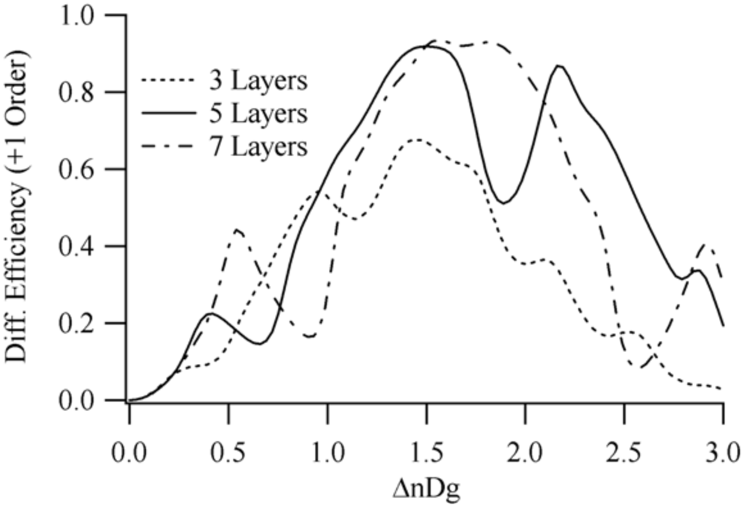

Figure 3.7 Diffraction efficiency of three-, five-, and seven-layer SVDOE's as a function of total modulation (Δn=0.5). $\lambda_0 = 2.06\mu m$, $\theta = \theta_B = 9.885°$, $n_I = 1.5$, $n_{II} = 1.5$, $n_r = 2.0$, $n_g = 1.5$. Readout beam is positioned at Bragg incidence; there is no relative offset between grating layers.

structure is illustrated in Figure 3.8. The refractive index of the anti-reflection layer, n_{AR}, and its thickness, d_{AR}, are calculated using the standard relations [40]

$$n_{AR} = \sqrt{n_r n_g}\,, \tag{3.1}$$

$$d_{AR} = \frac{1}{n_{AR}}\frac{\lambda_0}{4}\,. \tag{3.2}$$

For this particular structure, $n_{AR} = 1.732$, and $d_{AR} = 0.29\,\mu m$. Figure 3.9 shows the +1 order diffraction efficiency behavior for the SVDOE in Figure 3.8. These curves once again follow the expected sinusoidal dependence and, most notably, the structure has been removed. The return to well-behaved diffraction behavior with the addition of anti-reflection layers confirms that Fresnel reflections at the interfaces between SVDOE layers are responsible for variations in the diffraction efficiency with layer thickness changes.

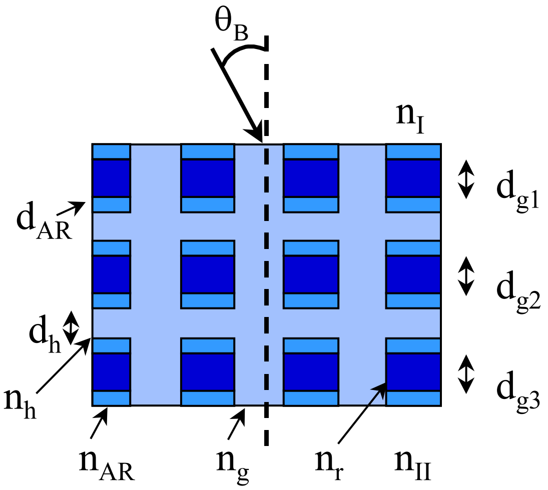

Figure 3.8 SVDOE with anti-reflection at interfaces between grating and homogeneous layers. Readout beam is positioned at Bragg incidence; there is no relative offset between grating layers.

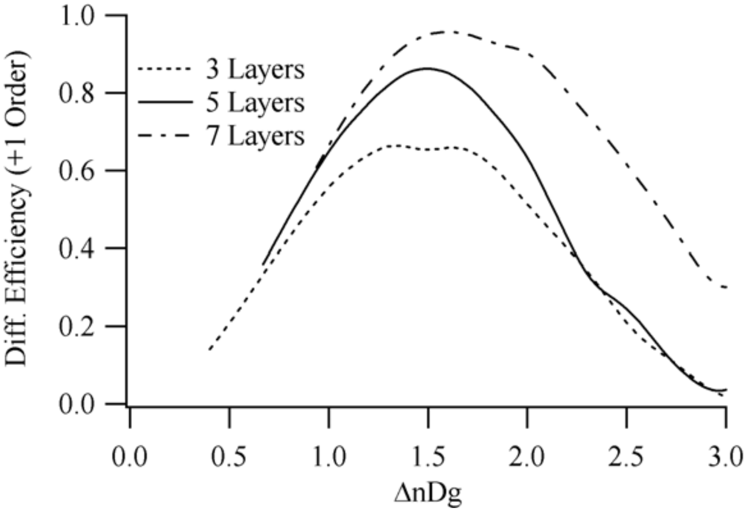

Figure 3.9 Diffraction efficiency of three-, five-, and seven-layer SVDOE's, with anti-reflection layers embedded in the structure, as a function of total modulation (Δn=0.5). $\lambda_0 = 2.06\mu m$, $\theta = \theta_B = 9.885°$, $n_I = 1.5$, $n_{II} = 1.5$, $n_r = 2.0$, $n_g = 1.5$. Readout beam is positioned at Bragg incidence; there is no relative offset between grating layers.

The same type of behavior seen in Figure 3.6 was reported for SVHOE's [11] (which assumed small grating refractive index modulation). In this case the parameter used for characterizing the trend was proportional to the coupling coefficient, κ, discussed in the context of a modulation parameter in volume holography by Kogelnik [41] as shown in

$$\chi = \frac{\kappa D_g}{\sqrt{c_R c_S}} = \frac{\pi \Delta n_{amp} D_g}{\lambda_0 \sqrt{c_R c_S}}, \tag{3.3}$$

where $\kappa = \frac{\pi}{\lambda_0} \Delta n_{amp}$ in which Δn_{amp} represents the amplitude of the sinusoidal refractive index modulation, λ_0 is the freespace wavelength, D_g is the modulation thickness and c_R and c_S are given by

$$\begin{aligned} c_R &= \cos\theta \\ c_S &= \cos\theta - \frac{\lambda_0}{n\Lambda}\cos\varphi \end{aligned}. \tag{3.4}$$

The angle θ is the incidence angle while φ is the angle that the grating vector, which is oriented perpendicular to the fringe planes, makes with the inward surface normal. Also, Λ represents the grating period. This geometry for a volume hologram is shown in Figure 3.10.

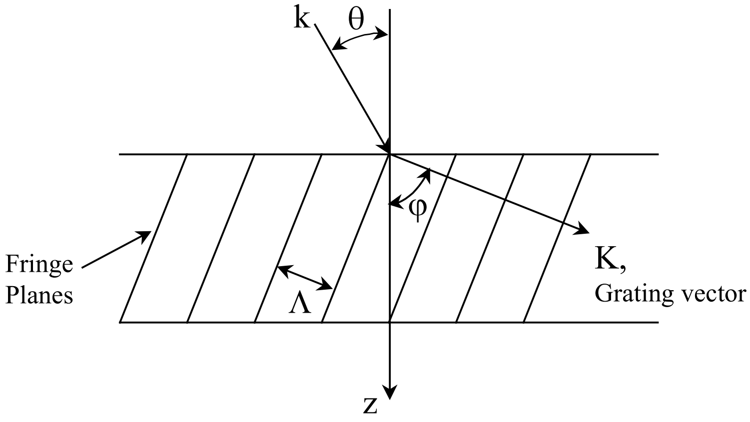

Figure 3.10 Illustration of geometry for a volume hologram.

The expression for the modulation parameter given in Equation (3.3) can be derived, following the example given in Kogelnik [41] and in Collier, et al. [16], by beginning with the wave equation as shown in Equation (3.5) and examining the propagation number as given in Equation (3.6)

$$\nabla^2\vec{E} + k^2\vec{E} = 0\,, \tag{3.5}$$

$$k^2 = \frac{\omega^2}{c^2}\varepsilon\,, \tag{3.6}$$

where ω is the angular optical frequency, c is the speed of light in a vacuum and their ratio is the propagation number in free space, k_0, as shown in

$$\frac{\omega}{c} = k_0 = \frac{2\pi}{\lambda_0}\,, \tag{3.7}$$

where λ_0 is the wavelength of light in free space. Also, ε is the permittivity of the medium, which has a sinusoidal form for holographic materials, as given by

$$\varepsilon = \varepsilon_0 + \varepsilon_1 \cos\vec{K}\bullet\vec{r}\,, \tag{3.8}$$

where $\vec{K}$ is the grating vector, which is perpendicular to the fringe planes and $\vec{r}$ is the orientation of the fringe planes. Also, ε_0 is the average permittivity of the medium and ε_1 is the amplitude of the permittivity modulation. Substituting from Equations (3.7) and (3.8) into the expression for the propagation number, (3.6), yields an expression for the propagation number in terms of the permittivity which, after some rearranging of the terms, may be written

$$\begin{aligned}
k^2 &= \frac{\omega^2}{c^2}\left(\varepsilon_0 + \varepsilon_1\cos\vec{K}\bullet\vec{r}\right) \\
&= {k_0}^2\left(\varepsilon_0 + \varepsilon_1\cos\vec{K}\bullet\vec{r}\right) \\
&= k_0\sqrt{\varepsilon_0}\left(k_0\sqrt{\varepsilon_0} + k_0\frac{\varepsilon_1}{\sqrt{\varepsilon_0}}\cos\vec{K}\bullet\vec{r}\right) \quad . \\
&= k_0\sqrt{\varepsilon_0}\left(k_0\sqrt{\varepsilon_0} + 2k_0\frac{\varepsilon_1}{2\sqrt{\varepsilon_0}}\cos\vec{K}\bullet\vec{r}\right)
\end{aligned} \tag{3.9}$$

The sinusoidal term may then be written in terms of exponentials, which introduces a factor of one-half,

$$k^2 = k_0\sqrt{\varepsilon_0}\left(k_0\sqrt{\varepsilon_0} + 2k_0\frac{\varepsilon_1}{2\sqrt{\varepsilon_0}}\frac{1}{2}\left(e^{i\vec{K}\bullet\vec{r}} + e^{-i\vec{K}\bullet\vec{r}}\right)\right). \tag{3.10}$$

The term $k_0\frac{\varepsilon_1}{2\sqrt{\varepsilon_0}}\frac{1}{2}e^{i\vec{K}\bullet\vec{r}}$ in Equation (3.10) represents coupling to the +1 order and the constants in front of the exponential represent the coupling coefficient, κ. It is preferred to write the coupling coefficient as a function of refractive index rather than permittivity. The relationship between the two quantities is

$$n^2 = \varepsilon\,, \tag{3.11}$$

where n is the refractive index of the medium. Both sides of Equation (3.11) may be written as a sinusoidal modulation

$$\left(n_0 + \Delta n_{amp}\cos\vec{K}\cdot\vec{r}\right)^2 = \varepsilon_0 + \varepsilon_1\cos\vec{K}\cdot\vec{r}\,, \tag{3.12}$$

where n_0 is the average refractive index and Δn_{amp} is the amplitude of the sinusoidal refractive index modulation. Squaring the left-hand-side of Equation (3.12) gives the expression

$$n_0{}^2 + 2n_0\Delta n_{amp}\cos\vec{K}\cdot\vec{r} + \Delta n_{amp}{}^2\cos^2\vec{K}\cdot\vec{r} = \varepsilon_0 + \varepsilon_1\cos\vec{K}\cdot\vec{r}\,. \tag{3.13}$$

For most holographic materials, the index modulation is much less than the average refractive index, as indicated by

$$\Delta n_{amp} << n_0\,, \tag{3.14}$$

and the $\cos^2$ term can be neglected. The other two terms may then be set equal to each other giving the expressions

$$n_0{}^2 = \varepsilon_0 \qquad \text{and} \qquad 2n_0\Delta n_{amp} = \varepsilon_1\,. \tag{3.15}$$

Rearranging the terms then yields expressions for the average refractive index and the index modulation in terms of the permittivity

$$n_0 = \sqrt{\varepsilon_0} \qquad \text{and} \qquad \Delta n_{amp} = \frac{\varepsilon_1}{2\sqrt{\varepsilon_0}}. \tag{3.16}$$

Returning to Equation (3.10) and the coupling coefficient, the second term from (3.16) can be substituted there to give an expression for the coupling coefficient in terms of the refractive index modulation

$$\kappa = \frac{1}{2} k_0 \frac{\varepsilon_1}{2\sqrt{\varepsilon_0}} = \frac{1}{2} k_0 \Delta n_{amp} = \frac{\pi}{\lambda_0} \Delta n_{amp}, \tag{3.17}$$

which leads directly to the expression for the modulation parameter for volume holographic elements as given in Equation (3.3).

The significance of the coupling coefficient is that it represents the degree of coupling between the zeroth and first diffracted orders as they propagate through the bulk material. For Bragg incidence readout of volume gratings, the +1 order diffraction efficiency is well-known to be given by $\sin^2 \chi$, and hence it reaches a maximum value when $\chi = \pi/2$ [41]. This relationship can be used to determine the optimum modulation thickness for a given sinusoidal refractive index modulation, Δn_{amp}.

A similar relationship was established for SVDOE's in this work by realizing that the rectangular permittivity profile of the binary gratings may be expressed as a sum of sinusoidal permittivity profiles, rather than a single sinusoidal profile, through a Fourier series expansion as shown in

$$\varepsilon = \varepsilon_0 + \sum_{\substack{h=-\infty \\ h\neq 0}}^{h=\infty} \varepsilon_h \exp\left(jh\vec{K} \cdot \vec{r} \right), \tag{3.18}$$

in which ε_0 is the average permittivity of the profile and ε_h is the amplitude of the h^{th} harmonic component of the permittivity. This expression for the permittivity can be substituted into the propagation number expression, as was done previously for the sinusoidal profile, and the terms can be rearranged as

$$k^2 = \frac{\omega^2}{c^2}\varepsilon, \tag{3.19}$$

$$k^2 = \frac{\omega^2}{c^2}\left[\varepsilon_0 + \sum_{\substack{h=-\infty \\ h\neq 0}}^{h=\infty} \varepsilon_h \exp\left(jh\vec{K}\cdot\vec{r}\right)\right], \tag{3.20}$$

$$k^2 = k_0\sqrt{\varepsilon_0}\left[k_0\sqrt{\varepsilon_0} + 2k_0 \frac{1}{2\sqrt{\varepsilon_0}} \sum_{\substack{h=-\infty \\ h\neq 0}}^{h=\infty} \varepsilon_h \exp\left(jh\vec{K}\cdot\vec{r}\right)\right], \tag{3.21}$$

where the first-order exponential term represents coupling to the +1 order, meaning that the coupling coefficient for SVDOE's is

$$\kappa_{SVDOE} = k_0 \frac{\varepsilon_1}{2\sqrt{\varepsilon_0}}. \tag{3.22}$$

Note that this coupling coefficient does not contain a factor of $\frac{1}{2}$ that was present in κ, the holographic coupling coefficient. This results from the fact that the permittivity for the case of SVDOE's was expressed initially as an exponential term rather than as a sinusoidal. In the case of sinusoidal modulation, the conversion to exponential terms to distinguish the coupling between the zero and the +1 order introduced the factor of one-half.

Again, it is preferable to write the coupling coefficient and modulation parameter in terms of the refractive index rather than the permittivity. The refractive index profile is expressed as a Fourier series expansion, similar to the permittivity, as shown in

$$n\left(\vec{r}\right) = n_0 + \left[\sum_{\substack{h=-\infty \\ h\neq 0}}^{h=\infty} \Delta n_h \exp\left(jh\vec{K}\cdot\vec{r}\right)\right], \tag{3.23}$$

in which n_0 is the average refractive index of the profile and Δn_h is the amplitude of the hth harmonic component of the refractive index. The first order term is the relevant term for first order coupling so, once again, the refractive index terms may be written as a function of the permittivity terms as given by

$$n_0 = \sqrt{\varepsilon_0} \qquad \text{and} \qquad \Delta n_1 = \frac{\varepsilon_1}{2\sqrt{\varepsilon_0}} . \tag{3.24}$$

The second term from Equation (3.24) can be substituted into the coupling coefficient

$$\begin{aligned} \kappa_{\text{SVDOE}} &= k_0 \frac{\varepsilon_1}{2\sqrt{\varepsilon_0}} = k_0 \Delta n_1 \\ \kappa_{\text{SVDOE}} &= \frac{2\pi}{\lambda_0} \Delta n_1 \end{aligned} . \tag{3.25}$$

This derivation has assumed a lossless dielectric medium.

A modulation parameter may therefore be expressed for SVDOE's by using the amplitude of the first harmonic component of the refractive index, which then leads to the relation

$$\chi_{\text{SVDOE}} = \frac{2\pi |\Delta n_1| D_g}{\lambda_0 \sqrt{c_R c_S}} \tag{3.26}$$

in which the factor of two arises from the exponential expression of the harmonic rather than the sinusoidal expression typical of holographic materials. The SVDOE diffraction efficiency dependence on κ is therefore $\sin^2\left(\kappa_{\text{SVDOE}}\right)$ so that a peak value of diffraction efficiency is again reached when the argument is equal to $\pi/2$. Calculation of Δn_1 in terms of the refractive index difference between grating ridge and groove materials, Δn, leads to $\Delta n_1 = \Delta n/\pi$. Setting Equation (3.26) equal to $\pi/2$ and solving for D_g yields the following expression for the total grating thickness that achieves the maximum diffraction efficiency

$$D_{g,\max} = \pi \frac{\lambda_0}{4\Delta n} \sqrt{c_R c_S} . \tag{3.27}$$

Note that calculating $\Delta n D_{g,\max}$ using Equation (3.27) for the cases shown Figure 3.6 and Figure 3.7 leads to a value of 1.51μm, which is consistent with what is observed in the figures.

Having established the dependence of SVDOE diffraction efficiency on total grating thickness, SVDOE behavior is examined as a function of homogeneous layer thickness. For the following simulation results five grating layers are assumed with a total grating thickness such that $\chi_{SVDOE} = \pi/2$ for each value of Δn. Figure 3.11 shows the diffraction efficiency behavior as the thickness of the homogeneous layer between each grating layer is increased for the case of incidence at the Bragg angle. The +1 order diffraction efficiency is plotted as a function of the sum of a single grating layer thickness and a single homogeneous layer thickness. Note that the curves are periodic for both Δn =0.1 and 0.5. Previous work in SVHOE's [11] has shown the same type of periodic behavior of the diffraction efficiency as a function of the sum of the

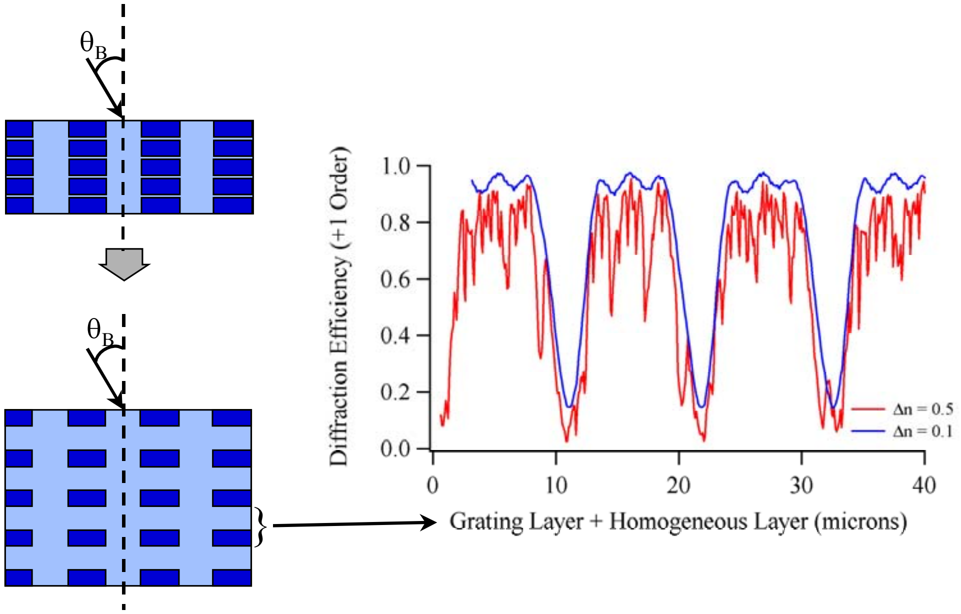

Figure 3.11 Diffraction efficiency of a five layer SVDOE as a function of the thickness of one period in the SVDOE structure (i.e., the sum of a single grating layer thickness and a single homogeneous layer thickness). $\lambda_0 = 2.06\mu m$, $\theta = \theta_B = 9.885°$, $n_I = 1.5$, $n_{II} = 1.5$, $n_g = 1.5$. For $\Delta n=0.1$, $n_r = 1.6$, $d_g = 3.139\mu m$; for $\Delta n=0.5$, $n_r = 2.0$, $d_g = 0.638\mu m$.

homogeneous and grating layer thickness. Also note in Figure 3.11 that the curve for $\Delta n = 0.1$ is smoothly varying whereas the case $\Delta n = 0.5$ exhibits rapid fluctuations due, again, to interference from multiple reflections from the grating layers [42].

Finally, in Figure 3.12 the +1 order diffraction efficiency of SVDOE's is examined as a function of the readout beam incidence angle. A structure consisting of five grating layers with $\Delta n = 0.5$ is assumed. Note that the angular sensitivity exhibits high diffraction efficiency for distinct incidence angles, similar to the behavior of SVHOE's [10], [11], [12]. However, there are several differences. First, previous SVHOE work [11] assumed the validity of the small angle approximation in the derivation of the incidence angles at which high diffraction efficiency should occur. This led to a strictly periodic angular sensitivity. For the case considered here, this approximation is not valid. When it is removed from the derivation of Nordin, et al., one obtains

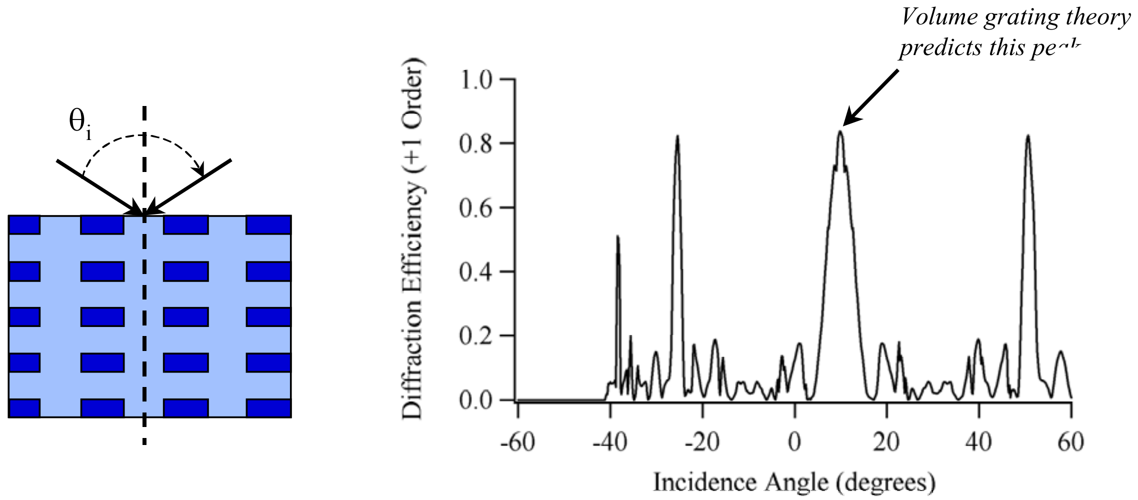

Figure 3.12 Angular selectivity of a five layer SVDOE with $\Delta n = 0.5$. Note that for $\theta_{inc} < -41$ degrees, the +1 order is evanescent and hence the diffraction efficiency is zero. $\lambda_0 = 2.06\mu m$, $n_I = 1.5$, $n_{II} = 1.5$, $n_r = 2.0$, $n_g = 1.5$, $d_g = 0.638\mu m$, $d_h = 4.9\mu m$.

the following transcendental equation for the angles, θ_{0p}, where high diffraction efficiency should occur:

$$\cos\theta_{0p} = \sqrt{1-\left(\sin\theta_{0p} - \frac{\lambda_0}{n\Lambda}\right)^2} - \frac{p\lambda_0}{d_b n} \tag{3.28}$$

in which d_b is the combined thickness of a single grating layer and a single homogeneous layer and p is an integer (… -2, -1, 0, 1, 2 …) distinguishing discrete incidence angles associated with diffraction peaks, e.g., $p=0$ represents Bragg incidence. The location of the diffraction peaks that occur in Figure 3.12 is accurately predicted by the above equation.

A second set of differences relative to previously reported SVHOE behavior is due to interference between multiple reflections generated by the large refractive index difference in the grating layers. For example, one of the expected diffraction peaks shown in Figure 3.12 (near –38°) has reduced diffraction efficiency compared to the other peaks. This turns out to be a sensitive function of the homogeneous layer thickness when Δn is large. In addition, the sidelobe structure between the main diffraction peaks in Figure 3.12 does not exhibit N-2 sidelobes as is normally typical for SVHOE's [10], [11], [12]. For the case of SVDOE's, N-2 sidelobes have only been observed when Δn is on the order of 10^{-2} or less, and hence there are minimal reflections between grating layers.

Chapter 4

DESIGN TECHNIQUE AND EXAMPLE

A systematic design process for SVDOE's has been developed based on the diffraction properties discussed in the previous section. The necessary parameters for a complete design include selection of materials (and hence refractive indices), grating period (which is presumably set by the application), thickness of the grating layers, thickness of the homogeneous layers, and the offset required between adjacent grating layers to achieve high diffraction efficiency at the desired incidence angle. For purposes of this work, the grating grooves and homogeneous layers are presumed to be composed of the same material and thus have the same refractive index.

4.1 Systematic design process

As discussed in Chapter 3, the total grating thickness for an SVDOE may be calculated using Equation (3.27) once the grating layer refractive index difference is known. Likewise, the grating layer offsets for a given incidence angle can be calculated by determining the slant angle for fringes in an equivalent volume grating. The number of grating layers and the homogeneous layer thickness needed to meet a particular diffraction efficiency requirement must be determined numerically with RCWA. This can be accomplished with the following procedure.

1. Divide the total grating thickness into a small number of grating layers.
2. Numerically determine the +1 order diffraction efficiency as a function of the homogeneous layer thickness as shown in Figure 3.11 for the desired input beam incidence angle. To achieve high diffraction efficiency, the grating layers must be

appropriately offset as described above for each homogeneous layer thickness value used in the simulation.

3. From the resultant curve, determine a homogeneous layer thickness that gives high diffraction efficiency.
4. If this diffraction efficiency is not large enough, return to Step 1 and increment the number of grating layers and repeat Steps 2-3 until a design is achieved that meets the desired diffraction efficiency requirement.
5. Determine the fabrication feasibility of the resultant design and evaluate its robustness relative to likely fabrication-dependent parameter variations.

4.2 Parametric design study using lidar scanner element requirements

The above design process was applied to the lidar beam scanner application discussed in Chapter 2. The specific wavelength of 2.06μm was chosen since that wavelength was under consideration during initial instrument planning. Candidate homogeneous layer and grating groove materials are expected to have a refractive index of approximately 1.5. Since there are a number of material choices for the grating ridges that have suitable transmission properties at 2.06 μm, designs were evaluated with grating ridge refractive indices of 1.6, 1.75, and 2.0, yielding Δn values of 0.1, 0.25, and 0.5, respectively. For each Δn, the total grating thickness was calculated with Equation 3.5. The grating period was chosen to be 4 μm.

Figure 4.1 illustrates the results of applying Steps 1-4 as outlined above for each value of Δn. The diffraction efficiency is shown as a function of the number of grating layers parameterized by Δn. For each point in the graph, the homogeneous layer determined in Step 3 was selected as the smallest layer thickness that yielded the maximum achievable diffraction efficiency. Also, since the scanner element must operate at normal incidence, the grating ridges were shifted by the Bragg angle. Note that the peak diffraction efficiency for the case of two binary grating layers was between 65 and 75% while the case of three layers increased to about 90%, regardless of the Δn value. The case of five grating layers was dependent on Δn, yielding a peak efficiency ranging from 92%-96%.

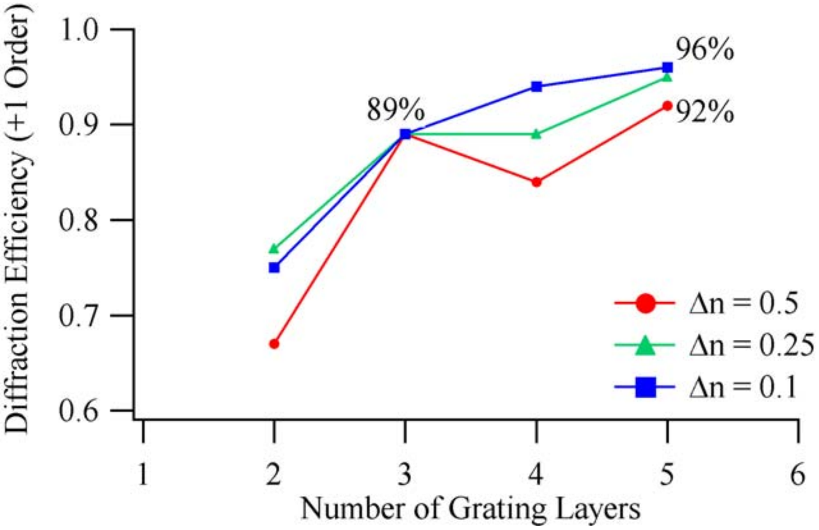

Figure 4.1 Diffraction efficiency as a function of number of grating layers. $\lambda_0 = 2.06\mu m$, $\theta = 0°$, $n_I = 1.5$, $n_{II} = 1.5$, $n_g = 1.5$. For $\Delta n=0.5$, $n_r = 2.0$; for $\Delta n=0.25$, $n_r = 1.75$; and for $\Delta n=0.1$, $n_r = 1.6$.

A diffraction efficiency of approximately 90% was adequate for a first demonstration device. Since an element with three layers requires fewer fabrication steps than one with five layers, the focus of this work was on a three grating layer design. Likewise, fabrication issues dictate selection of the grating ridge material such that $\Delta n = 0.5$ since this leads to physically thinner grating layers. This in turn implies a reduced grating ridge aspect ratio (i.e., grating thickness divided by the ridge width), which is more easily fabricated than larger aspect ratio features.

Geometric specifications for the three grating layer structure with $\Delta n = 0.5$, designed for normal incidence, are illustrated in Figure 4.2. The SVDOE is implemented on a substrate that also has a refractive index of 1.5. Each grating layer is 1.046μm thick, the homogeneous layers are each 4.300μm thick, and the offset increment between adjacent grating layers is 0.931μm. A cover layer is shown on top of the SVDOE to protect the features on the uppermost grating. The RCWA prediction of diffraction efficiency in the first diffracted order for a beam normally incident is 89.1%. The beam exits the element at 31 degrees in air, which is acceptable for the lidar application.

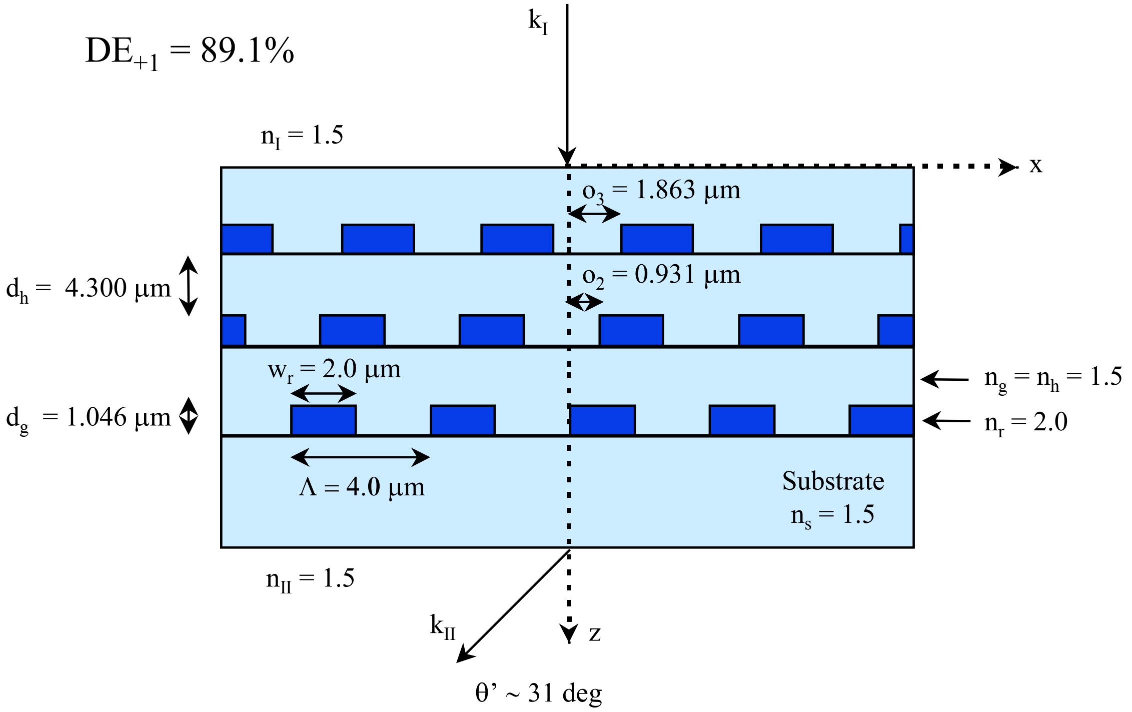

Figure 4.2 Specifications for example design of a lidar scanner element.

4.3 Predicted performance of example lidar scanner element

The lidar scanner element will be rotated about its optical axis to effect a conical scan pattern of the exiting beam. Since the input beam will be circularly polarized, rotation of the element implies its diffraction efficiency must be insensitive to polarization of the incident beam. Figure 4.3 shows the +1 order diffraction efficiency as a function of the input beam incidence angle for the three grating layer structure. Note that the efficiency remains greater than 85% in a region of +/- 1 degree about normal incidence for both TE and TM polarization. The broad peak about normal incidence provides misalignment tolerance when the element is placed in the lidar system. Figure 4.4 shows the +1 order diffraction efficiency as a function of polarization angle of the incident beam. The diffraction efficiency is a smooth, monotonic function between the two bounding values of TE and TM polarization.

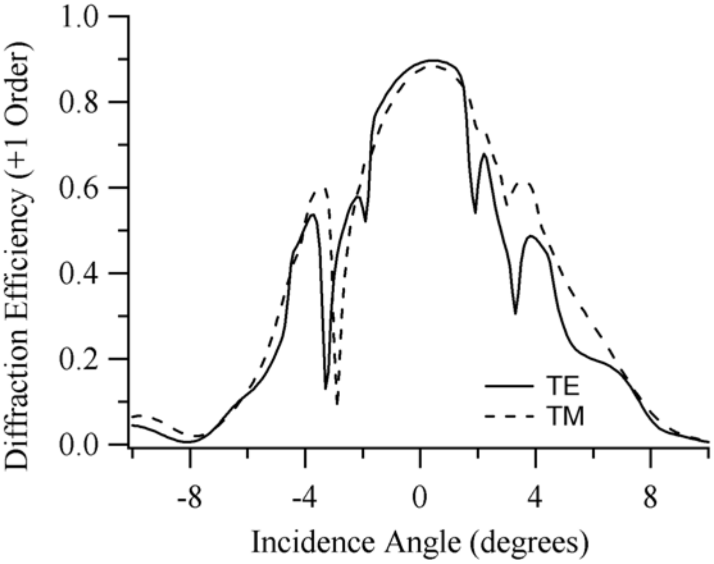

Figure 4.3 Diffraction efficiency as a function of incidence angle for both TE and TM polarizations. Three grating layers, $\lambda_0 = 2.06\mu m$, $n_I = 1.5$, $n_{II} = 1.5$, $n_r = 2.0$, $n_g = 1.5$, $d_g = 1.046\mu m$, $d_h = 4.300\mu m$.

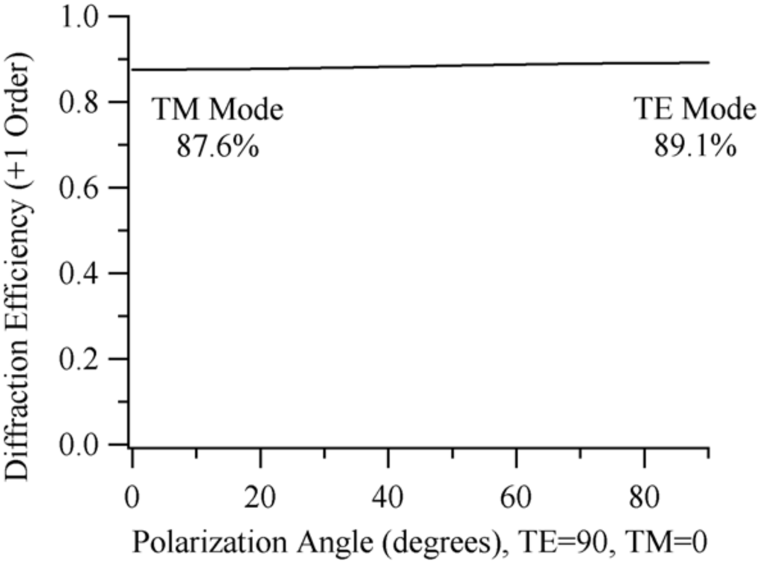

Figure 4.4 Diffraction efficiency as a function of polarization angle for a readout beam at normal incidence. Three grating layers, $\lambda_0 = 2.06\mu m$, $n_I = 1.5$, $n_{II} = 1.5$, $n_r = 2.0$, $n_g = 1.5$, $d_g = 1.046\mu m$, $d_h = 4.300\mu m$.

The implementation of RCWA developed for this work yields an expression for the electric and magnetic fields as they traverse the SVDOE structure. Figure 4.5 is a representation of the total electric field, i.e., the sum of all diffracted orders exterior to the grating and all space harmonics within the grating, in the three-layer example lidar scanner element design considered here. The solid black lines show the profiles of the three binary grating layers. The grating ridges are oriented toward the left of the figure. The areas between the grating profiles are homogeneous layers. The numbers along the lower and left edges of the figure are longitudinal and transverse distance, respectively, in microns.

A plane wave enters the SVDOE at normal incidence from the left of Figure 4.5. Small interference effects between the incident and reflected waves can be seen in the incident region. As the wavefronts pass through the first grating layer they are slightly disrupted while passing through the second grating layer causes them to become completely fractured. The third grating layer connects a lagging wavefront with a leading wavefront to effect the redirection of the beam to the desired deflection angle. The exiting medium in this figure is the substrate, with refractive index of 1.5.

It is instructive to consider individual orders of the electric field rather than the total field shown inFigure 4.5. In Figure 4.6 the electric field of the 0th diffracted order, also the incident beam, is shown. The field magnitude is its full, normalized value in the incident region. It is decreased slightly by each or the first two grating layers and almost completely extinguished as it passes through the third grating layers. It is very weak in the exiting region, as expected for this SVDOE. A similar representation of the +1 order electric field is shown in Figure 4.7. This time the field is very weak in the incident region, as expected. The field magnitude increases at each grating layer and is at its full value in the exiting region.

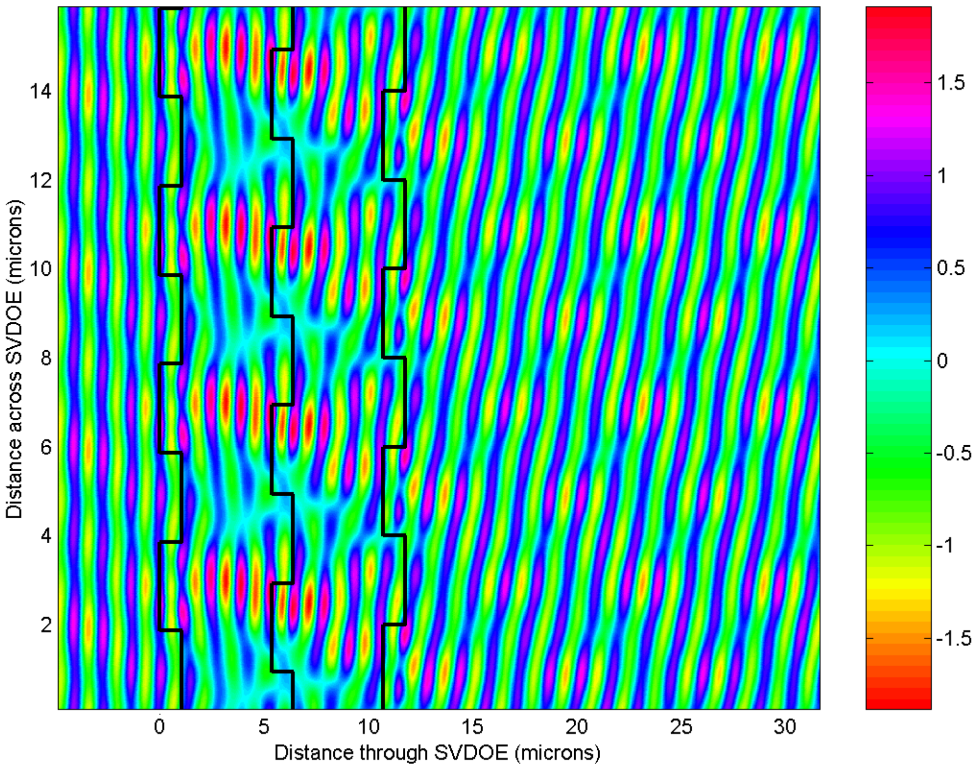

Figure 4.5 RCWA representation of the total electric field as it traverses the SVDOE example lidar scanner. The readout beam is incident normal to the grating from the left of the figure. Three grating layers, $\lambda_0 = 2.06\mu m$, $\theta = 0°$, $n_I = 1.5$, $n_{II} = 1.5$, $n_r = 2.0$, $n_g = 1.5$, $d_g = 1.046\mu m$, $d_h = 4.300\mu m$, TE polarization.

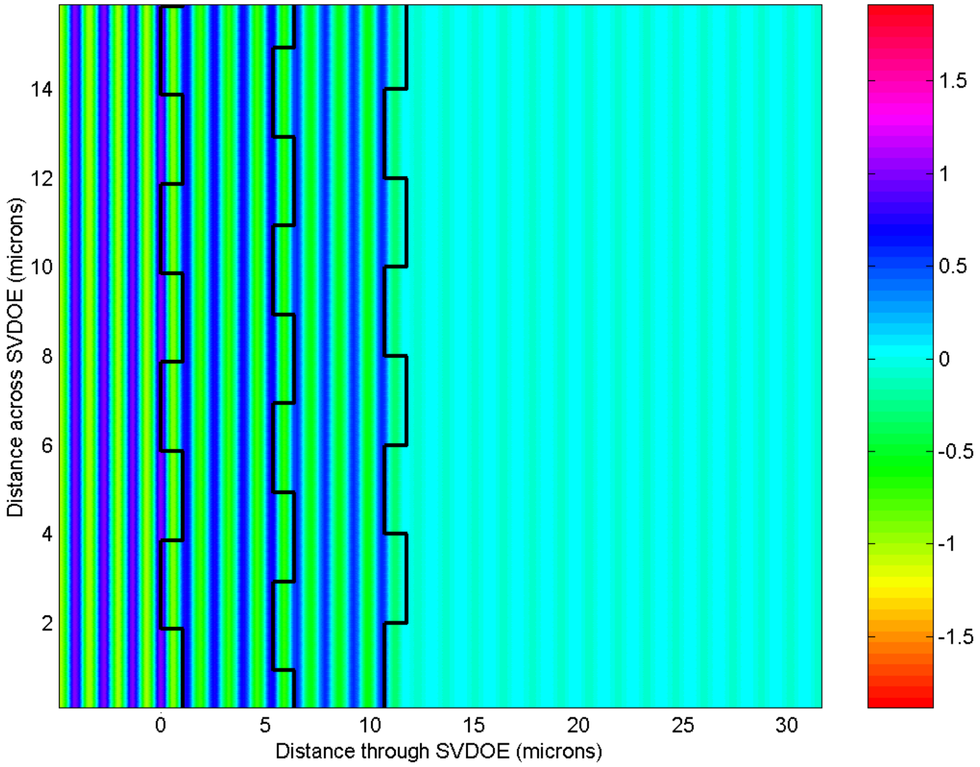

Figure 4.6 RCWA representation of 0^{th} order electric field as it traverses the SVDOE example lidar scanner. The readout beam is incident normal to the grating from the left of the figure. Three grating layers, $\lambda_0 = 2.06\mu m$, $\theta = 0°$, $n_I = 1.5$, $n_{II} = 1.5$, $n_r = 2.0$, $n_g = 1.5$, $d_g = 1.046\mu m$, $d_h = 4.300\mu m$, TE polarization.

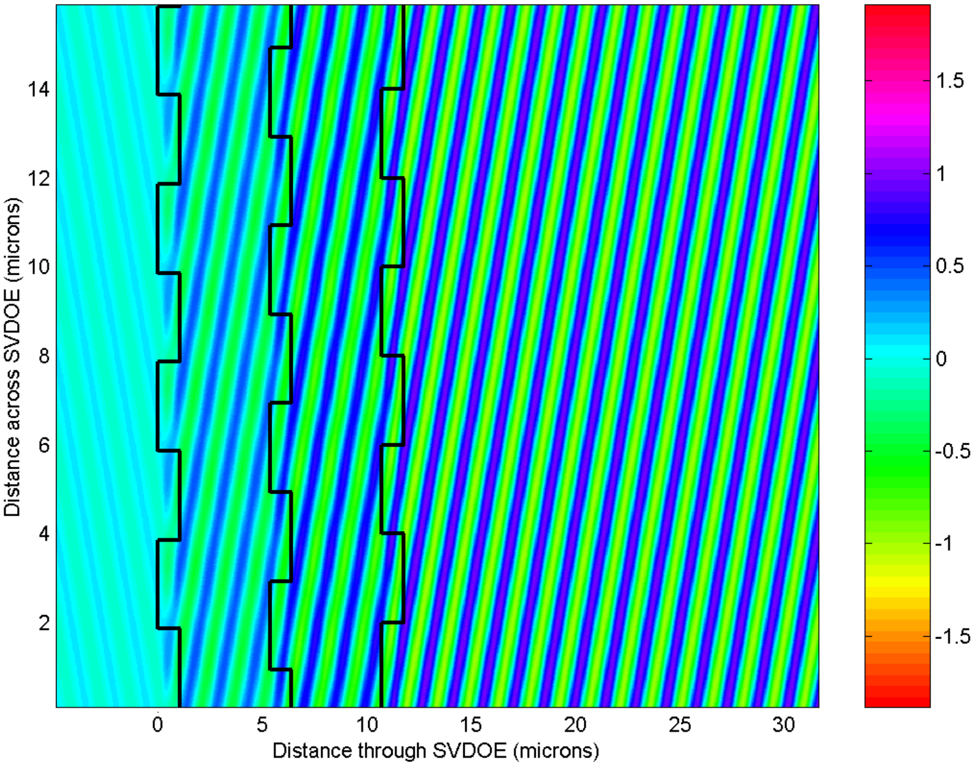

Figure 4.7 RCWA representation of +1 order electric field as it traverses the SVDOE example lidar scanner. The readout beam is incident normal to the grating from the left of the figure. Three grating layers, $\lambda_0 = 2.06\mu m$, $\theta = 0°$, $n_I = 1.5$, $n_{II} = 1.5$, $n_r = 2.0$, $n_g = 1.5$, $d_g = 1.046\mu m$, $d_h = 4.300\mu m$, TE polarization.

4.4 Tolerance to fabrication errors

Anticipated challenges in fabricating an SVDOE include accurate alignment of the grating layers to achieve the desired layer-to-layer offset and deposition of the homogeneous layers with the desired thickness. To assess the tolerances required for these parameters during fabrication, a statistical study of the effects of zero-mean Gaussian random deviations of each parameter from the design values was performed. The effect of these variations on diffraction efficiency of the three grating layer prototype lidar scanner element is shown in Figure 4.8 and Figure 4.9. In all cases the solid line in the plots represents the average diffraction efficiency as a function of the standard deviation of the additive random Gaussian variation for the variable being studied while the dotted line is the standard deviation of the diffraction efficiency. Figure 4.8 presents the statistics for the grating parameters, namely offset, ridge width, and thickness. In order to maintain the diffraction efficiency within 5% of its maximum value, or ~85%, each of these parameters must be maintained to within 50-100nm of their design value. Figure 4.9 is similar to the previous figure, but is based on variation of homogeneous layer thicknesses. From this figure it is apparent that the tolerance on homogeneous layer thickness is not as critical to maintain a high diffraction efficiency.

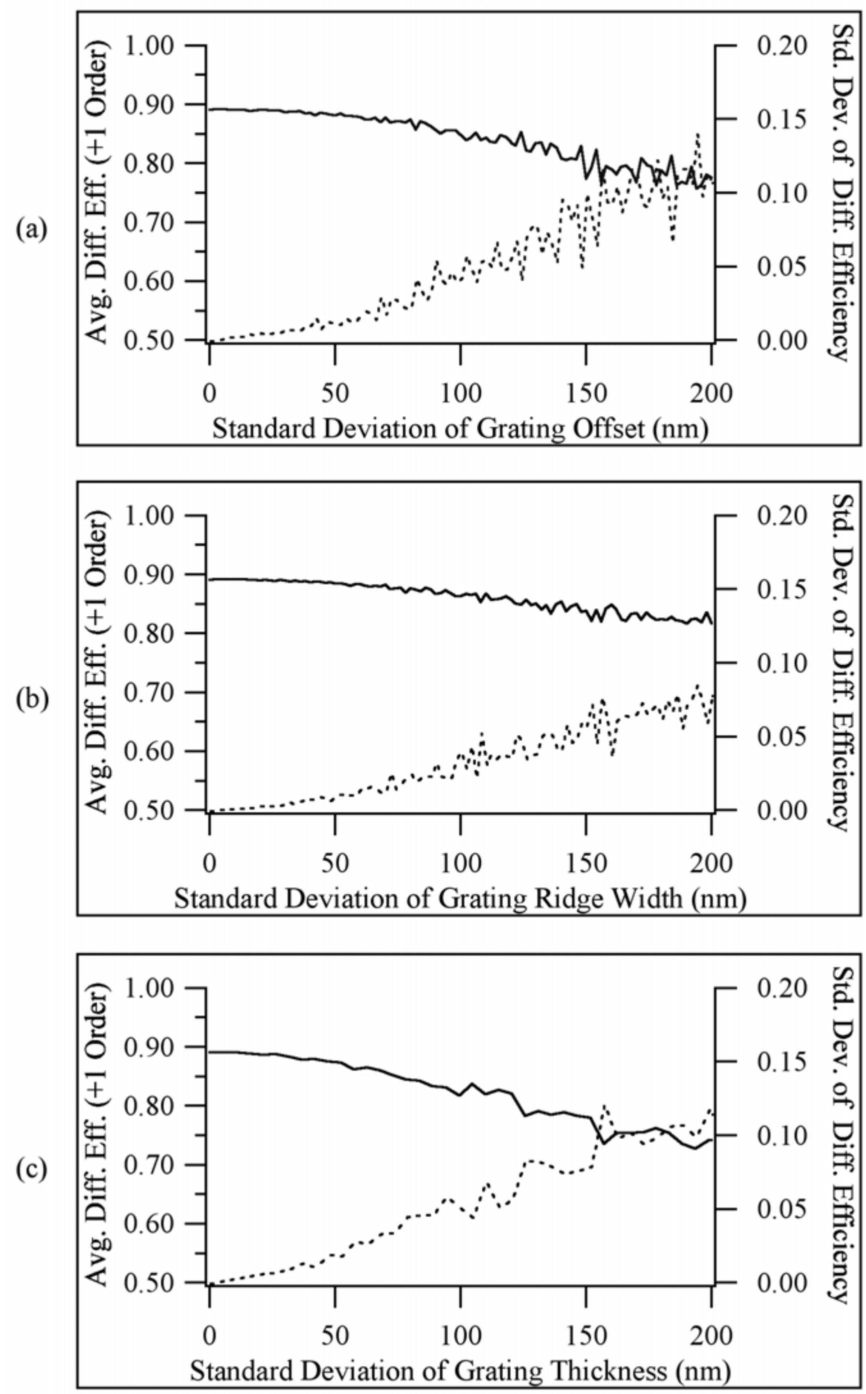

Figure 4.8 Effect of statistical variation of (a) grating offset, (b) ridge width, and (c) grating thickness, on the diffraction efficiency of the example lidar scanner. Three grating layers, $\lambda_0 = 2.06\mu m$, $\theta = 0°$, $n_I = 1.5$, $n_{II} = 1.5$, $n_r = 2.0$, $n_g = 1.5$, $d_g = 1.046\mu m$, $d_h = 4.300\mu m$.

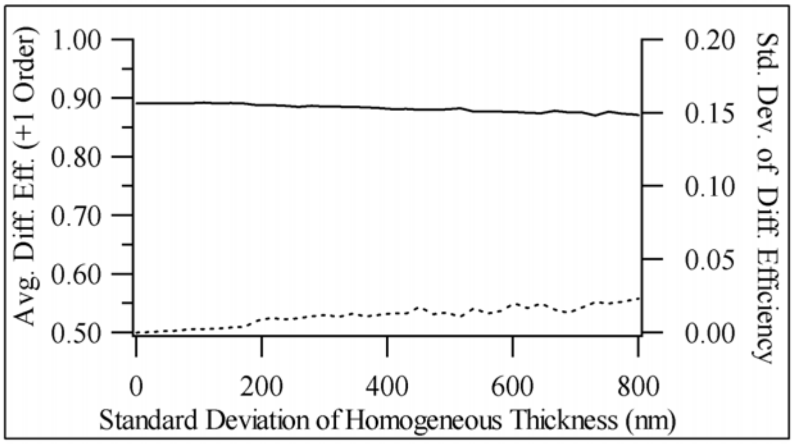

Figure 4.9 Effect of statistical variation of homogeneous layer thickness on the diffraction efficiency of the example lidar scanner. Three grating layers, $\lambda_0 = 2.06\mu m$, $\theta = 0°$, $n_I = 1.5$, $n_{II} = 1.5$, $n_r = 2.0$, $n_g = 1.5$, $d_g = 1.046\mu m$, $d_h = 4.300\mu m$.

Chapter 5

DESIGNS FOR LIDAR SCANNER DEMONSTRATION ELEMENTS

The SVDOE designs presented in Chapter 4 were parameterized based on a range of hypothetical material choices. Recall that a 3-layer design predicted a diffraction efficiency of approximately 89%, while increasing to 4-and 5-layer designs only improved the efficiency to between 92% and 96%. For an initial proof of concept device 89% is an acceptable goal, so a 3-layer design was chosen as the target for such a device. Fabrication of a 3-layer element is also easier than one with more layers, while still demonstrating the lithography and alignment techniques. Of the 3-layer designs presented earlier, the design with $\Delta n = 0.5$ resulted in grating layers which would be easier to fabricate than those of the other designs since they are physically thinner. Hence, the design for $\Delta n = 0.5$ was chosen as a target for an initial effort.

This chapter discusses proceeding from hypothetical designs to designs using specific materials. Rationale for individual materials is provided along with the properties of those materials. Discussion of parameters and predicted performance for a 3-layer element is included as are those for a 2-layer element, which is a first step in developing required fabrication processes and verifying actual performance with simulation.

The designs presented here are for a wavelength of 2.05μm rather than the 2.06μm used in earlier parametric designs. This is the result of a design change in the lidar instrument intended as the recipient of this element and, consequently, a change in the laser that will be provided for testing elements fabricated during this project.

5.1 Materials and properties

The initial material choice to be made for a scanner element is that of the substrate. For this wavelength and application, fused silica proves to be a satisfactory choice. Fused silica has high transmission at 2.05μm and is readily available in many sizes and thicknesses. Its transmission of light in the visible region is of benefit not only to the fabrication alignment process considered here, but also to preliminary instrument alignment and pointing in a lidar system. Additional considerations from a lidar instrument perspective are its lower cost when compared to traditional infrared materials such as silicon and germanium and its ability to be fabricated and polished at high quality in large diameter pieces, which can be difficult for other infrared materials.

To achieve a design with $\Delta n = 0.5$, the grating layer material should have a refractive index value greater than or equal to two. For a high-efficiency element, the absorption should be zero at 2.05μm. The material must also be able to be deposited in a thin film and etched in a Fluorine chemistry so that it is compatible with fabrication equipment available at the University of Alabama in Huntsville (UAH). It should be robust so that the initial grating layers can tolerate processing for subsequent homogeneous and grating layers without sustaining damage. Another consideration is that the material chosen and the fabrication processes developed for the prototype be capable of being scaled up and still meet the environmental requirements for an operational lidar. One of the most common high-refractive-index materials, titanium dioxide (TiO_2), meets all of these specifications and, consequently, was used in this work.

The homogeneous layer material should have a refractive index value approximately equal to 1.5. Since it is assumed that this material will be applied directly over a grating layer, it must be capable of filling the grating grooves completely and then forming a planar layer above the grating, preferably without chemical mechanical polishing. Likewise, it must robust enough to withstand processing for further grating and homogeneous layers without sustaining damage.

Photopolymers have previously been used for this type of application, but are often soluble in the same developing chemicals used for photoresist. However, a relatively new photopolymer, SU-8, is capable of forming damage-resistant layers and was used here.

Silicon dioxide (SiO_2) deposited as a thin film is used as an etch barrier between homogeneous layers and subsequent grating layers. This material was chosen because its refractive index is approximately equal to 1.5, just as SU-8, yet its etch rate is similar to TiO_2.

Accurate refractive index values for each of these materials are critical to developing designs which will perform as intended once fabricated. Published values are not necessarily meaningful since they are typically measured for bulk material rather than for thin films. Also, specific deposition parameters can affect the index value. To ensure accurate knowledge of refractive index at the 2.05μm wavelength for materials deposited at UAH, thin films of each material were prepared using the same method as the final device and then sent to J.A. Woollam, Inc., for measurement using their Infrared Variable Angle Spectroscopic Ellipsometer (IR-VASE) [43]. Refractive index values at 2.05μm are given in Table 5.1. In addition to these materials, examples of the substrates that would be used were also measured to verify their bulk refractive index [44]. A fused silica substrate was measured since that is the target substrate; its refractive index was found to be 1.438. Another substrate, soda lime glass, was also measured since that material will be used during fabrication process development due to its lower cost. Its refractive index was found to be 1.499.

Table 5.1 Measured Refractive Index of SVDOE materials at 2.05μm

Material	**Refractive Index at 2.05μm**
TiO2	2.285
SU-8	1.576
SiO2	1.526
Fused silica	1.438
Soda lime glass	1.499

With materials and refractive indices known, it is possible to arrive at a set of designs for a lidar prototype scanner parameterized by the number of grating layers. This is shown in Figure 5.1. Notice that, even though the refractive index difference is relatively large (0.709), the anomaly seen in Figure 4.1 where the diffraction efficiency decreased as the design changed from three to four grating layers (for large index difference) is not seen here. This indicates that the performance of an SVDOE is a highly sensitive function of the combination of refractive index difference and layer thickness. The designs shown in Figure 5.1 for two and three grating layers will be carried forward through fabrication and evaluation. Details of their design parameters and tolerances are provided in subsequent sections of this chapter.

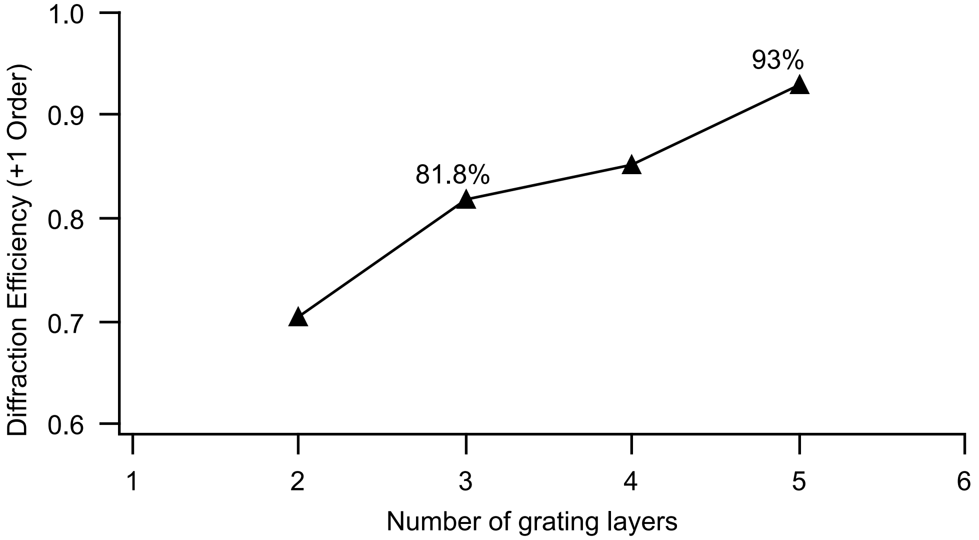

Figure 5.1 Maximum diffraction efficiency using measured refractive index values parameterized by number of grating layers. Three grating layers, $\lambda_0 = 2.05\mu m$, $\theta = 0°$, $n_I = 1.0$, $n_{II} = 1.0$, $n_r = 2.285$, $n_g = 1.576$.

5.2 Prototype design details

The desired structure parameters are determined through the process described in Chapter 4 using a combination of derived expressions for modulation calculation and RCWA for determination of homogeneous thickness and performance analysis. The statistics are also calculated with RCWA and will provide insight into sensitivity of the design to layer parameters. The two designs presented in this section include a finite cover layer thickness as opposed to the designs of Chapter 4 which assumed the element was immersed in a material with refractive index of 1.5. Note that the thickness of the cover layer is different from the other layers. It is optimized separately and acts as an anti-reflective layer.

5.2.1 Two-layer prototype

The design parameters for a two-layer prototype are given in Figure 5.2. Its peak diffraction efficiency in the +1 order is 70.4% with grating layers that are 1.105μm thick and with a relative offset between the layers of 1.154μm. The homogeneous layer is 5.9μm thick and the cover layer is 2.9μm thick. Figure 5.3 shows sensitivity of the design to grating layer parameters. Examination of the graphs confirms that efficiency is most sensitive to grating layer thickness, with a variation of 45-50nm causing a decrease of approximately 5%. The same 5% reduction would require either the offset or ridge width to vary by 0.1μm. Similar analyses for the homogeneous layer and cover layer thicknesses are shown in Figure 5.4. A variation of 75-80nm for either layer thickness would produce a 5% efficiency reduction.

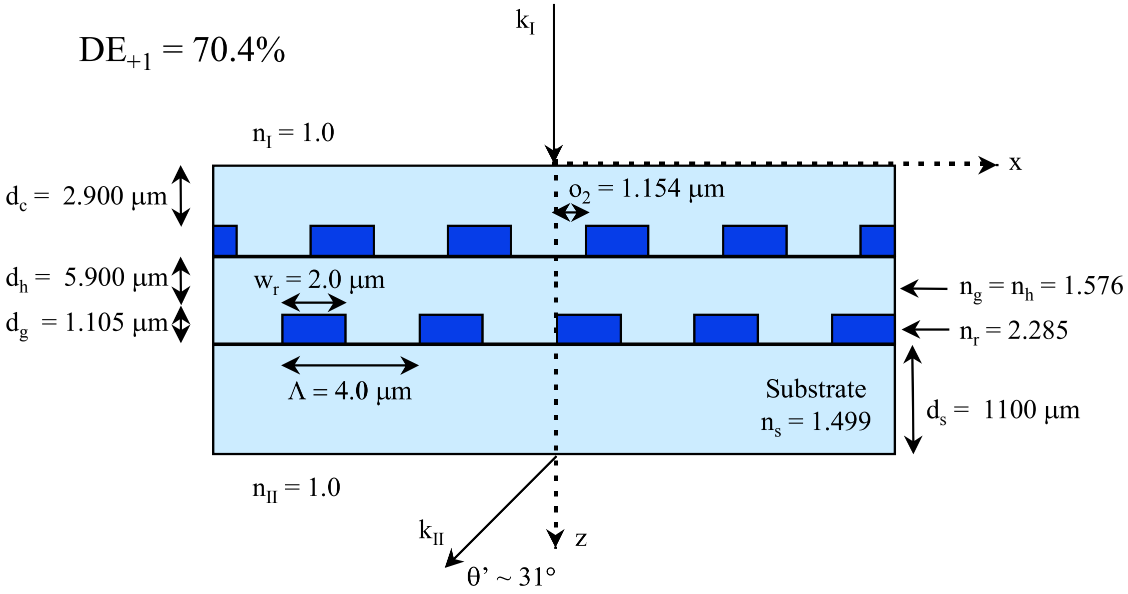

Figure 5.2 Design structural parameters for a two-layer prototype using measured refractive index values.

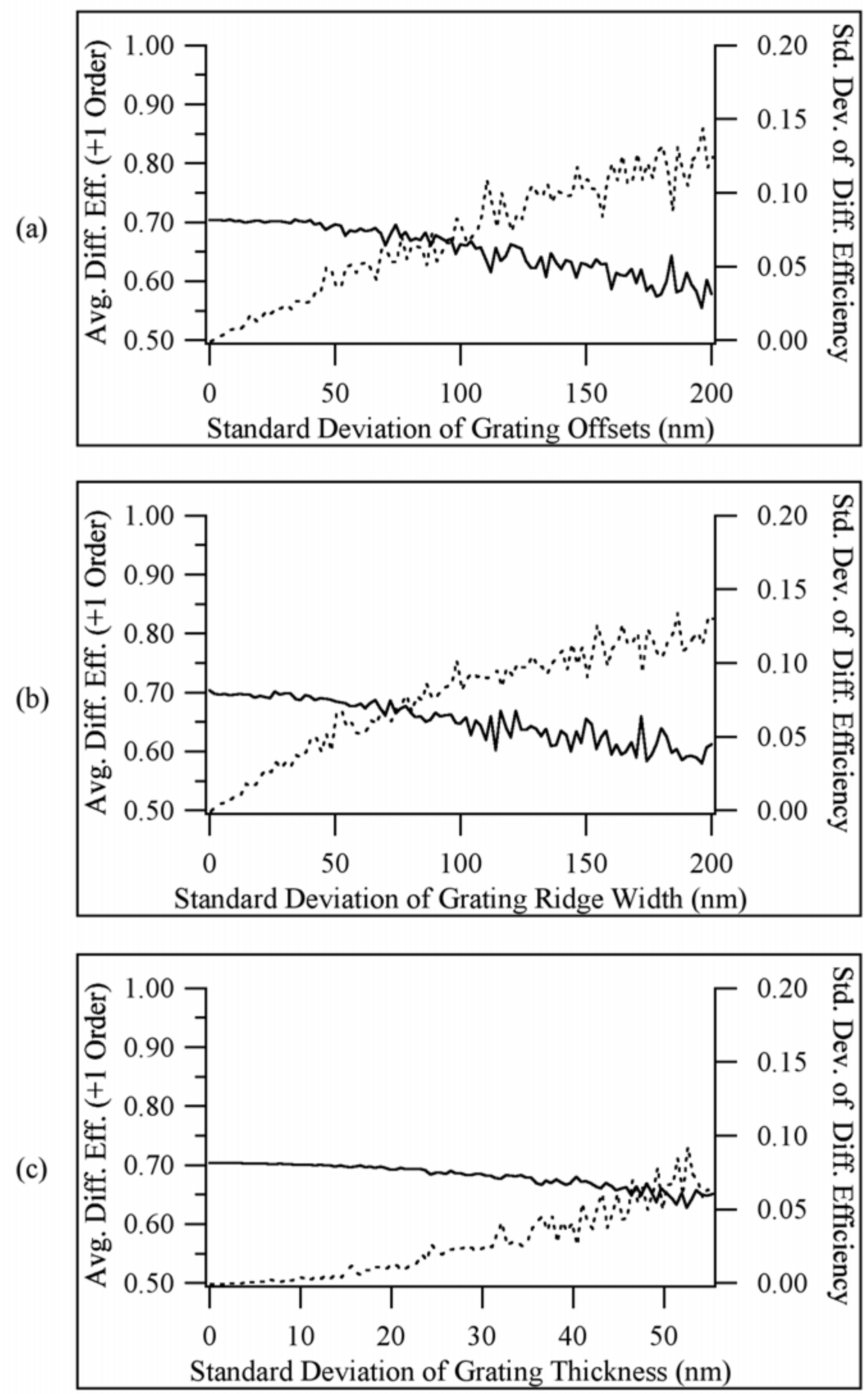

Figure 5.3 Effect of statistical variation of (a) grating offset, (b) ridge width, and (c) grating thickness on the diffraction efficiency of the two-layer prototype scanner element; $\lambda_0 = 2.05\mu m$, $\theta = 0°$, $n_I = 1.0$, $n_{II} = 1.0$, $n_r = 2.285$, $n_g = 1.576$, $d_g = 1.105\mu m$, $d_h = 5.9\mu m$, $d_c = 2.9\mu m$.

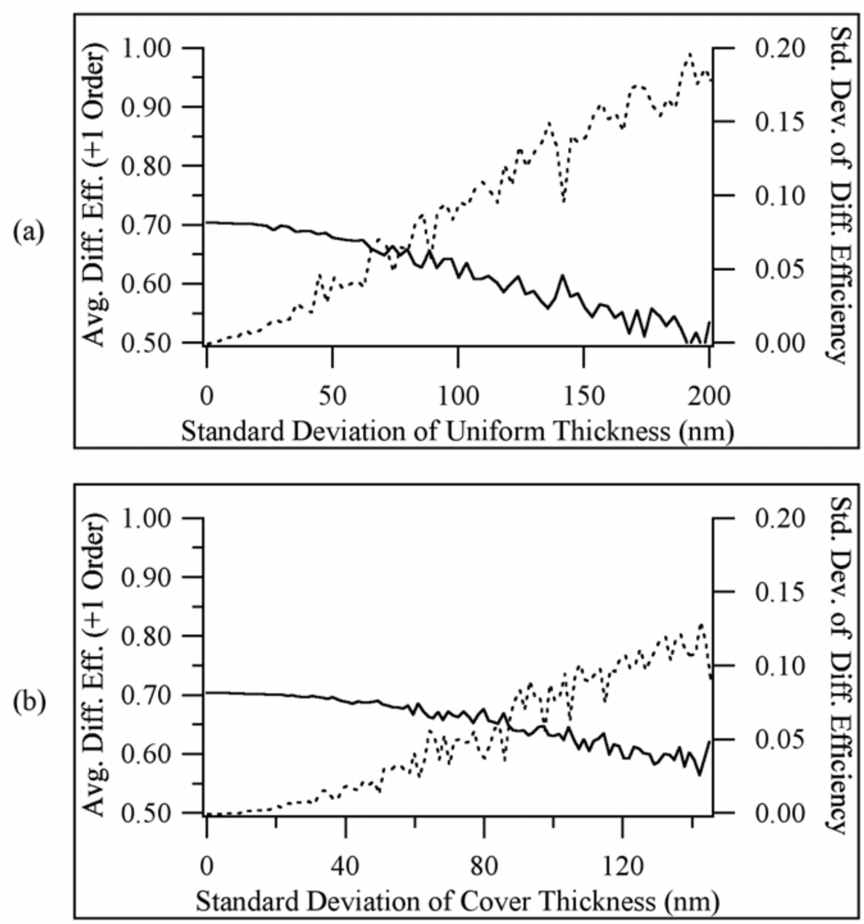

Figure 5.4 Effect of statistical variation of (a) homogeneous layer thickness and (b) cover layer thickness on the diffraction efficiency of the two-layer prototype scanner element; $\lambda_0 = 2.05\mu m$, $\theta = 0°$, $n_I = 1.0$, $n_{II} = 1.0$, $n_r = 2.285$, $n_g = 1.576$, $d_g = 1.105\mu m$, $d_h = 5.9\mu m$, $d_c = 2.9\mu m$.

5.2.2 Three-layer prototype

The design parameters for the three-layer prototype are given in Figure 5.5. The three-layer design provides a theoretical efficiency increase of 11% over the two-layer design. Referring to Figure 5.5, notice that the thickness of all layers is decreased over the corresponding layer thickness for the two-layer design.

The statistical evaluations of diffraction efficiency with respect to grating parameters are given in Figure 5.6. There is a similar trend to the sensitivity of the two-layer design to grating parameters in that the diffraction efficiency is most sensitive to grating layer thickness. In this case, the tolerance to that parameter for a 5% efficiency reduction is ~30nm, which is slightly less than the previous case. Tolerance to the offset and ridge width is comparable to that of the two-layer case at ~0.1μm. An analysis of homogeneous parameters is shown in Figure 5.7. A variation of 50nm for the homogeneous layer thickness would produce a 5% efficiency reduction while the cover layer thickness has a somewhat greater tolerance at ~90nm.

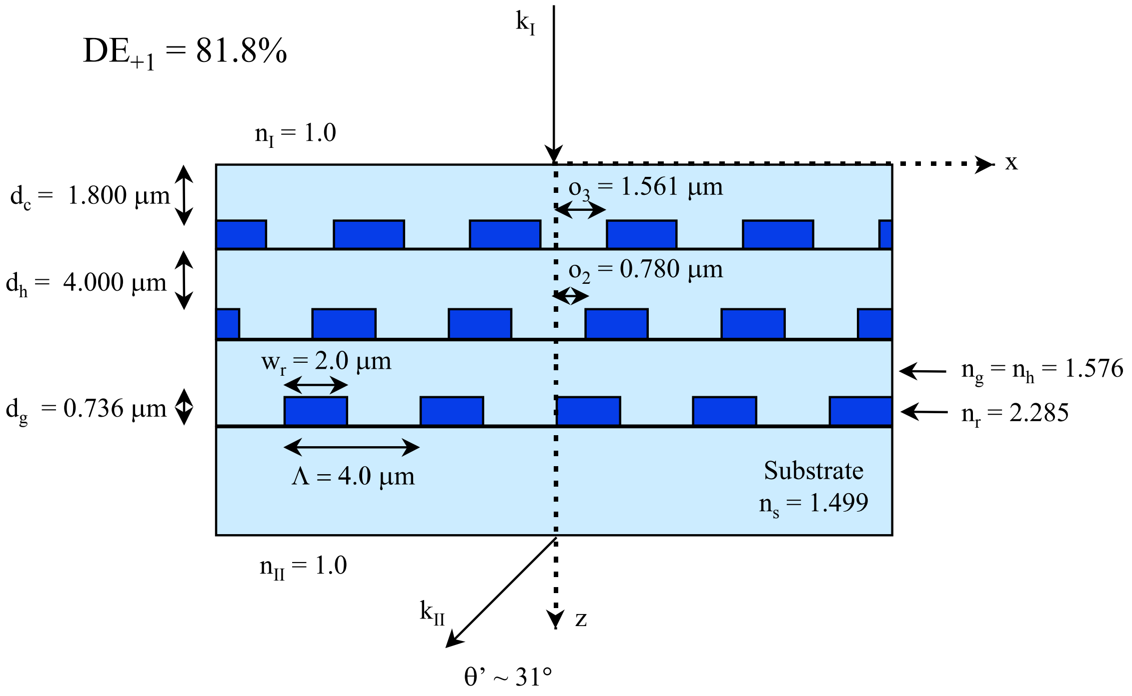

Figure 5.5 Design parameters for a three-layer prototype using measured refractive index values.

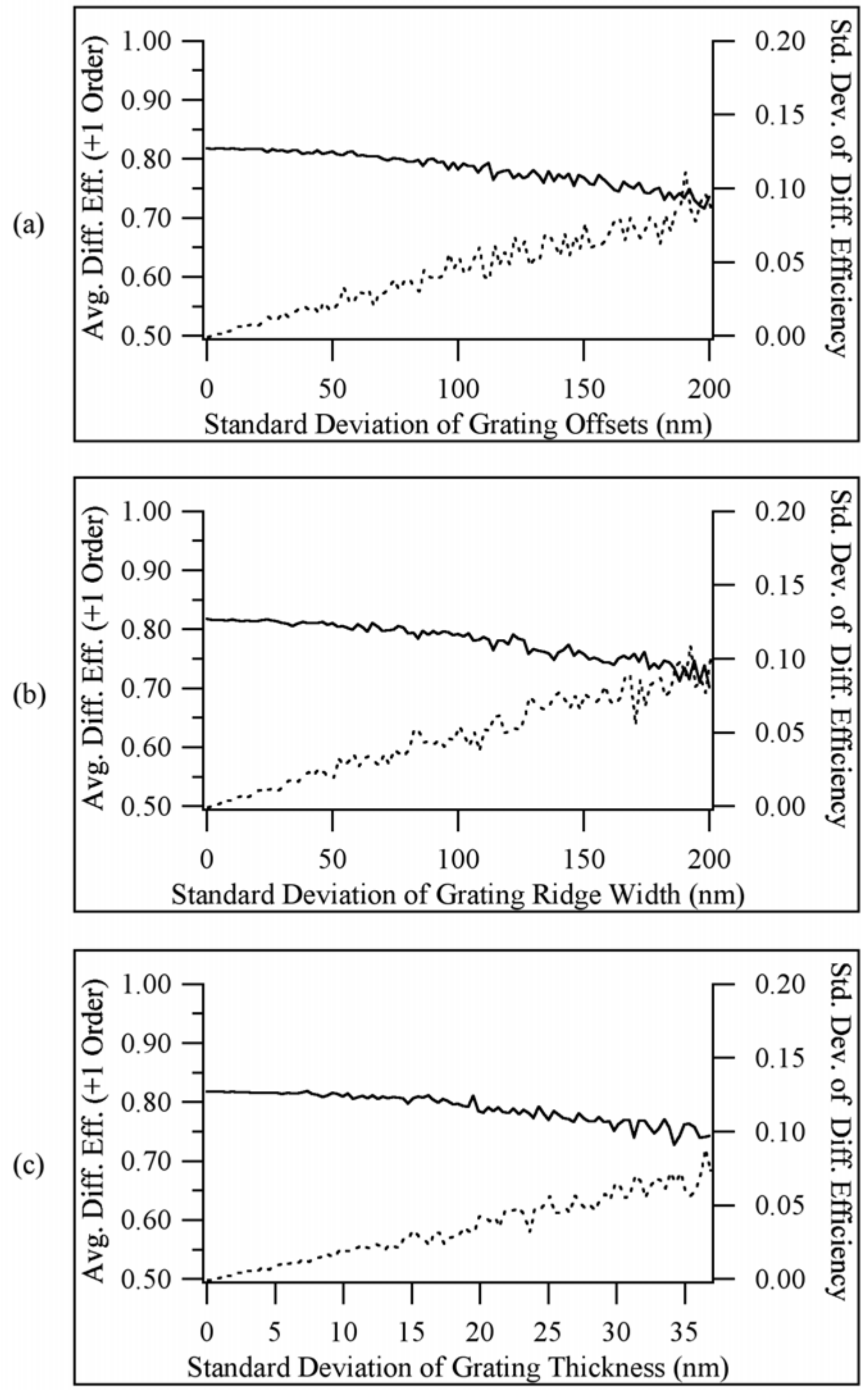

Figure 5.6 Effect of statistical variation of (a) grating offset, (b) ridge width, and (c) grating thickness on the diffraction efficiency of the three-layer prototype scanner element; $\lambda_0 = 2.05\mu m$, $\theta = 0°$, $n_I = 1.0$, $n_{II} = 1.0$, $n_r = 2.285$, $n_g = 1.576$, $d_g = 0.736\mu m$, $d_h = 4.0\mu m$, $d_c = 1.8\mu m$.

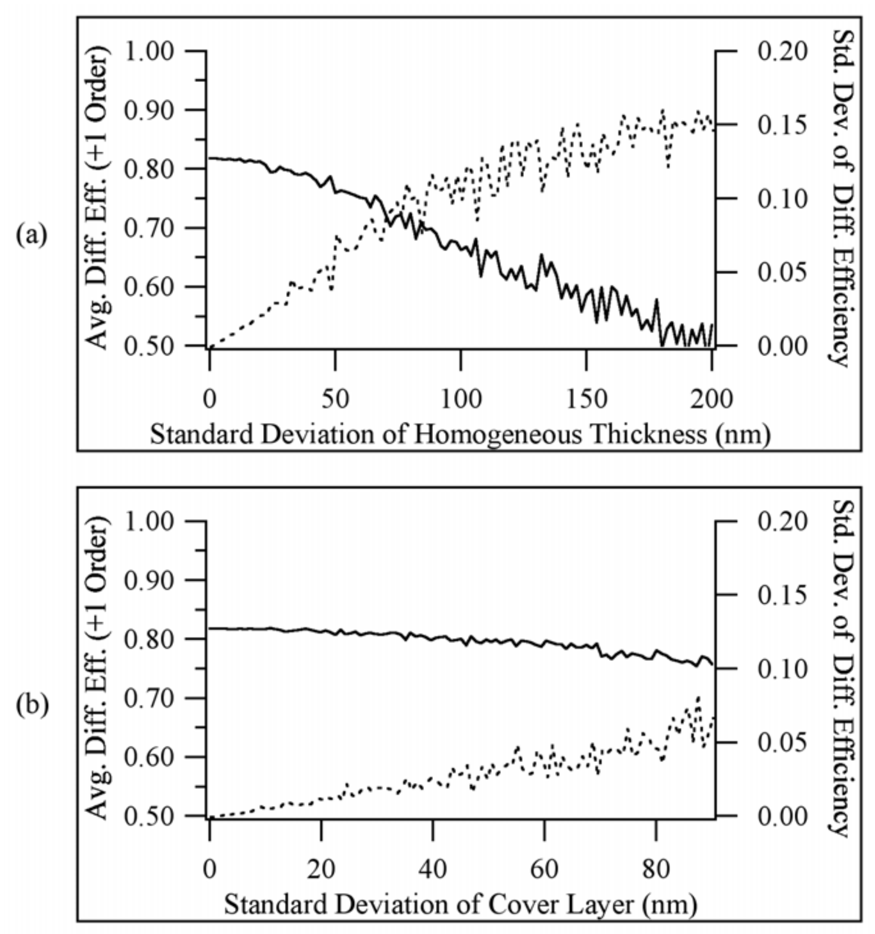

Figure 5.7 Effect of statistical variation of (a) homogeneous layer thickness and (b) cover layer thickness on the diffraction efficiency of the three-layer prototype scanner element; $\lambda_0 = 2.05\mu m$, $\theta = 0°$, $n_I = 1.0$, $n_{II} = 1.0$, $n_r = 2.285$, $n_g = 1.576$, $d_g = 0.736\mu m$, $d_h = 4.0\mu m$, $d_c = 1.8\mu m$.

Chapter 6

ALIGNMENT TECHNIQUE FOR GRATING OFFSETS

Analysis was presented in Chapter 5 to establish the tolerance permitted in the thickness of each layer and on the grating offsets while maintaining efficiency requirements. This analysis showed that the tolerance on the grating layers and homogeneous layers could be achieved using standard microfabrication techniques. The tolerance on the offsets, however, was more stringent than could be obtained with typical visual alignment. A high-precision alignment technique that was developed to meet this requirement will be discussed in this chapter.

6.1 Discussion

It has been suggested that the diffraction pattern produced by the superposition of identical gratings could be used for precise alignment [45], [46], [47]. This concept makes use of the fact that the resulting diffraction pattern is periodic as a function of relative displacement between the two gratings [48], [49], [50]. The work referenced above in this area of *double diffraction* has been concentrated in either obtaining maximum contrast in the diffraction pattern or in using it to enforce perfect alignment between two objects. However, double diffraction may readily be applied to the problem of interest here, namely achieving a specific alignment offset between gratings.

The diffraction pattern needed to align the grating layers in an SVDOE can be generated by using the phase grating on the substrate and the amplitude grating on the mask within the clear aperture of the grating region. A typical microfabrication alignment process uses a set of fixed alignment marks that should be “perfectly aligned” when placement is correct. For an SVDOE that implies that a separate set of alignment marks is required for each offset distance, i.e., for each design. The benefit of the approach described here is that a single photolithographic mask can be used for any SVDOE design with a specific deflection angle, e.g., any number of grating layers can be fabricated by changing the applied alignment offset.

The specific form of the pattern from double diffraction is a function of the separation distance between the gratings. It typically consists of major peaks and minor peaks as illustrated in Figure 6.1. The magnitude of the peaks varies as the separation distance between the gratings is varied; relative position of major compared with minor peaks can even interchange. This is illustrated in Figure 6.2, which is generated by the same two gratings as Figure 6.1, but with a separation distance equal to 50μm rather than 25μm. Therefore, knowledge of this distance is critical for determining and applying appropriate alignment parameters.

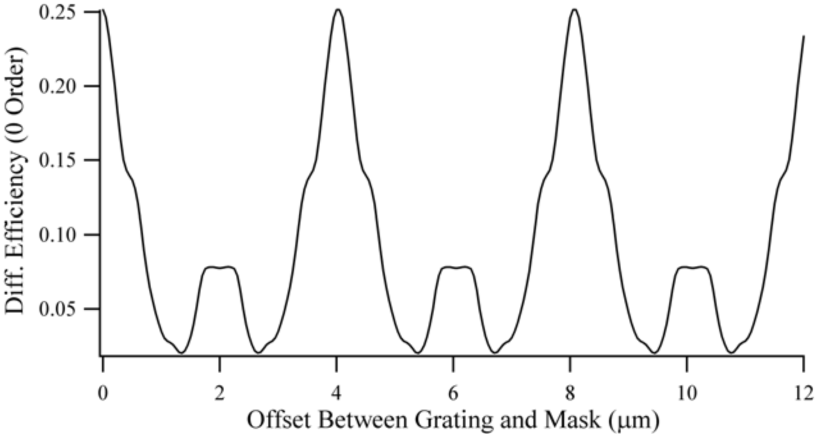

Figure 6.1 Example of double diffraction pattern in the 0^{th} order by phase grating/amplitude grating with 4μm period. Separation is 25μm, both the phase and amplitude gratings are 4μm period.

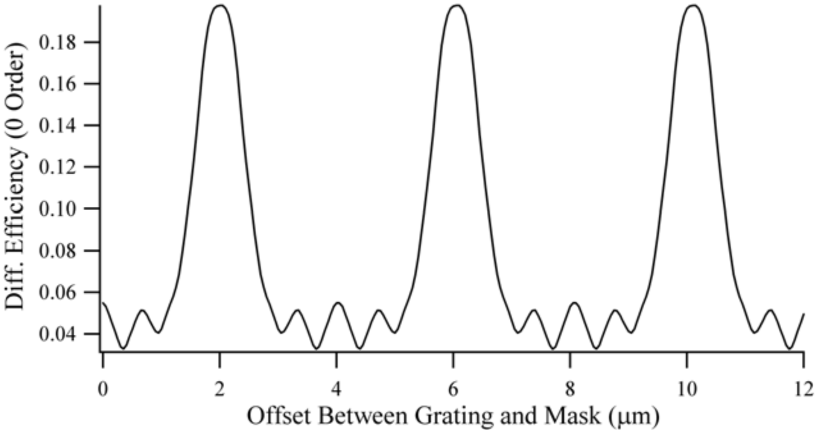

Figure 6.2 Example of double diffraction pattern in the 0th order by phase grating/amplitude grating with 4μm period. Separation is 50μm, both the phase and amplitude gratings are 4μm period.

The key point that allows use of this double diffraction pattern for alignment is that it is periodic with relative position, or offset, of the gratings. In the case under discussion here, the period is always identical to that of the gratings. This characteristic permits formulation of an alignment scheme whereby that period is used to precisely position the gratings with respect to each other. That scheme can be outlined as follows:

1. Simulate the expected double diffraction signal, using RCWA, as a function of grating displacement. It should be parameterized by the separation distance between the substrate and mask. The simulation should include all layers on the substrate and mask.
2. Measure the actual double diffraction signal during translation of the substrate with respect to the mask at several separation distances.
3. Compare the measured signals to the simulated signals to establish accurate separation distance calibrated to the mask aligner translation stage scale.

4. Select a specific separation distance where the alignment will be conducted. This is based primarily on the criteria that there must be free movement between the substrate and the mask, which is determined by the measured signals. However, the position of an intensity peak relative to the desired offset should also be considered. The latter is derived from the simulated signals.
5. Extract one period from the measured signal selected in Step 4 since the period of the double diffraction signal is identical to the grating period. Scale the extracted signal period to the offset range derived from the simulated signal at the corresponding separation distance.
6. To achieve a specific relative offset, correlate the desired offset to its intensity value from the simulated signal reference curve. Then align the substrate to the mask until that intensity value is detected and is stable.

6.2 Implementation

The alignment technique discussed above may be implemented by modifying the contact mask aligner as illustrated in Figure 6.3. There are four primary modifications: 1) accommodating and directing a light source to generate the diffraction pattern, 2) mounting a detector to record the pattern, 3) installing a high-precision actuator for control of relative position, and 4) establishing a computer interface to monitor and control the process.

Typical light sources used for alignment are broadband, white light sources intended for use with video microscopes. However, this application requires a monochromatic source in order to generate an appropriate diffraction pattern. In addition, the source power should be stable over the alignment time, a period of minutes to hours, since any fluctuations would lead to changes in magnitude of the detected pattern (signal) which could be interpreted as a lateral shift of the substrate and mask. A diode laser would meet the monochromatic requirement; power

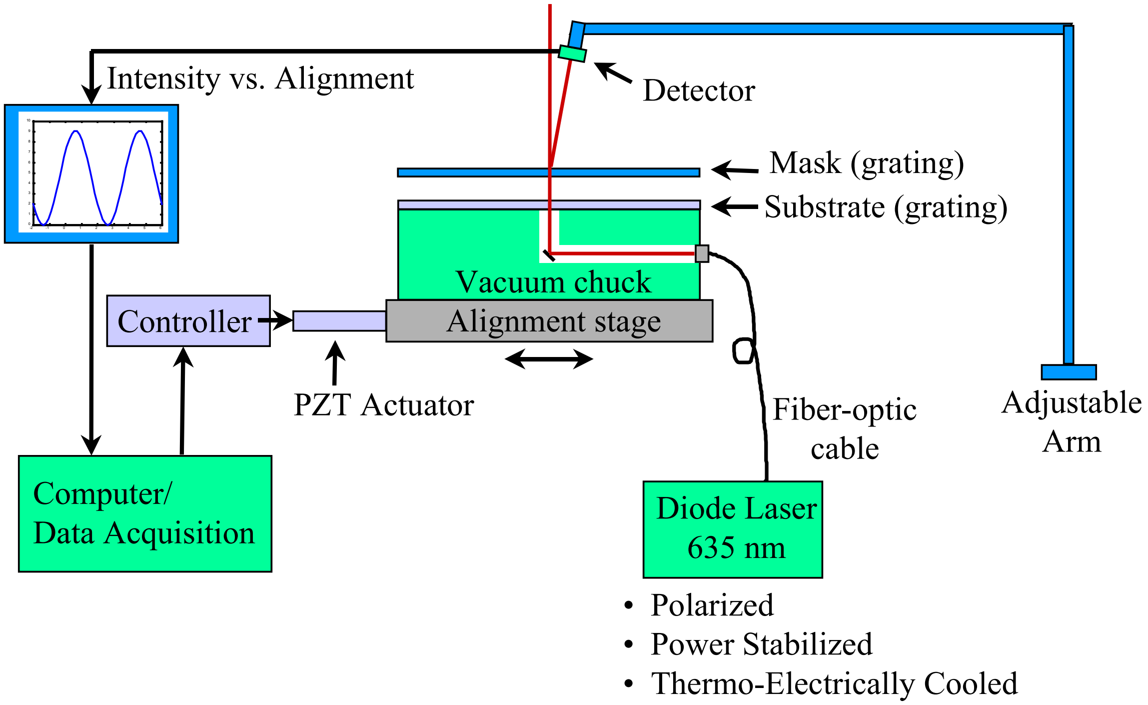

Figure 6.3 Block diagram of the implementation of the high-precision alignment technique.

stabilization and temperature control are needed to meet the remaining requirements since the diode laser output tends to drift with time and temperature changes. Delivery of the diode laser output to the alignment apparatus would be most easily facilitated by use of an optical fiber so that any heat generated by the diode or its stabilization systems is localized in separate packaging and not transferred to mask aligner components. Transfer of this heat could cause differential expansion of either the components or the substrate, adversely affecting alignment between constituent layers. A wavelength of 635nm is preferred for the diode since its proximity to the ubiquitous 632nm Helium Neon laser line implies that detector/filter components are readily available as is material property data. This wavelength is also benign to the photoresist on the substrate and can be transmitted through the components without adversely affecting the integrity of the layers. A laser meeting all these requirements was obtained (Melles Griot 56-IMS-009) with a beam diameter of 2.2 mm. All controls are internal to a compact laser package which is driven by a lab-quality, stabilized 5V power supply. The only source of instability is backreflection into the laser system.

The laser beam is delivered to the alignment system via a collimating lens package on the end of the fiber optic pigtail. A fixture on the substrate chuck clamps it securely. The fixture leads to a channel machined within the chuck to allow the laser beam to propagate to the center line of the chuck and then be turned by an adjustable mirror so that it propagates upward through the substrate and mask as shown in Figure 6.3. The adjustment capability on the mirror allows the beam to be directed through the system at an angle slightly away from normal to reduce backreflections that are known to cause laser instability [51], [52]. A shutter within the channel permits the laser beam to be blocked prior to the turning mirror. The surface of the substrate chuck contains a 0.25 inch diameter window placed approximately 1.0 inch away from the center of the chuck to allow laser propagation. The placement of the window is such that it is at the edge of the clear aperture of the gratings being fabricated as shown in Figure 6.4.

The detector for the diffraction pattern should be placed above the mask in a mount such that its position is repeatable but that it is easily removed from the area to allow exposure of photoresist. Such a mounting arm was designed and fabricated for the specified detector and application by Ms. Holly Cagle and Dr. David Lehner of NASA/MSFC. It consists of a vertical rod attached to the base plate of the mask aligner and a horizontal rod fastened to the vertical rod by an adjustable clamp. The detector position, at the end of the horizontal rod, can be translated along both the vertical and horizontal directions and it can be rotated about axes in those directions as well so that the active detector area can be centered over the diffracted beam. Discrimination between the zero and first diffracted orders is achieved by two distinct angular positions of the detector face, implemented through a kinematic-type mount. The arm permits rotation in the horizontal plane of greater than 120° so that the detector can be removed from the mask area for visual alignment or exposure, but can be returned to the same position for

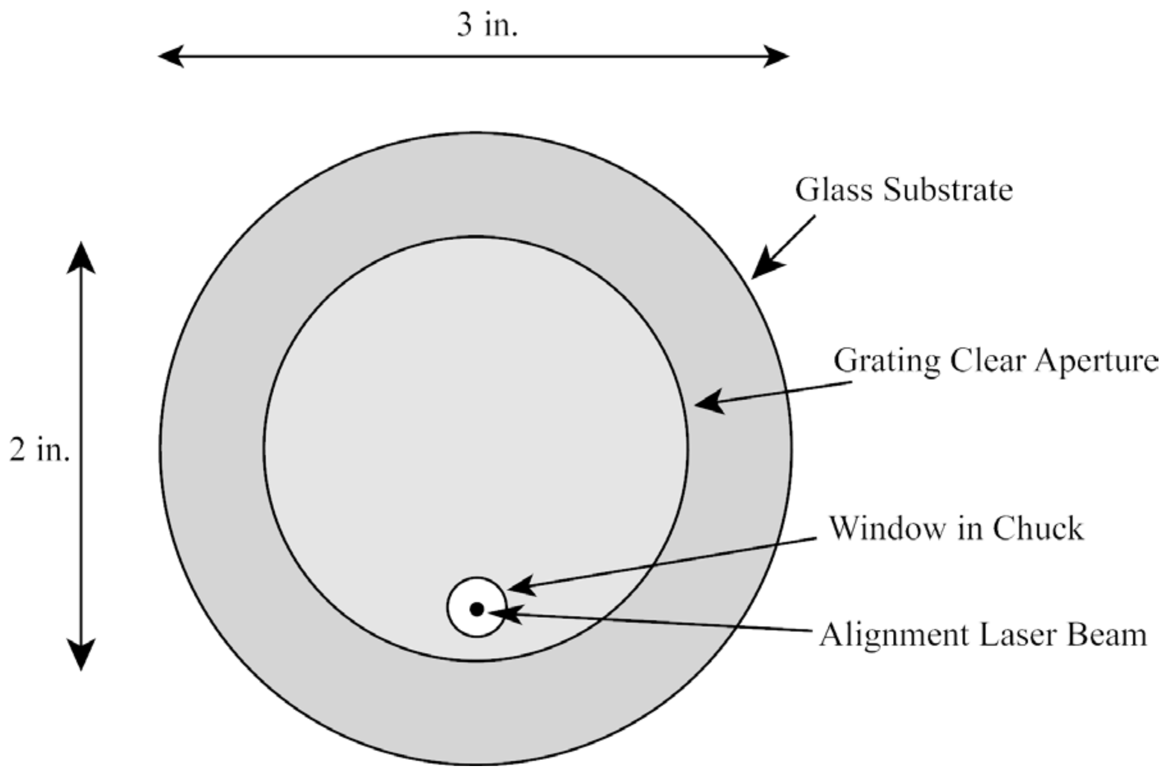

Figure 6.4 Top view of substrate chuck showing window to allow alignment laser beam to propagate through substrate to mask.

subsequent alignment processes. The detector (Thor Labs PDA55) is an amplified, switchable-gain, silicon device. A laser line interference filter centered at 635nm (Melles Griot 03 FIL 050) is placed in front of the detector.

Aligning gratings on the substrate and mask to within a small fraction of a micron with respect to each other requires an actuator with resolution smaller than the alignment tolerance. The manual actuators originally installed in the mask aligner have resolution of approximately one-half micron and, therefore, the actuator which controls the grating alignment dimension had to be replaced. A piezo-electric (PZT) driven actuator (Polytec PI P-854.0) was installed which provides 30μm of fine travel in 1nm increments while still providing 18mm travel in manual operation. Since PZT materials are known to behave non-linearly and to exhibit hysteresis, the motion used during alignment is approximately 15µm about the center of its 30µm range.

Computer control of the alignment process is necessary to maintain the required alignment tolerances. A PC-based system with a 16-bit analog-to-digital converter was installed to both control the PZT actuator and record the detector output. Control software was written that commands the PZT actuator to increment its position, wait a specified time period to allow settling of the translation stage, and then read the detector output.

Chapter 7

FABRICATION PROCESSES

This chapter provides a detailed discussion of the fabrication processes employed for SVDOE's. There are three basic steps: 1) Grating layer deposition and patterning, 2) Homogeneous layer deposition, and 3) Alignment to impart an offset between adjacent grating layers. The first step is achieved by typical microfabrication techniques while the homogeneous layer step uses an approach that is quickly becoming standard in fabrication of microdevices and Micro-Electrical-Mechanical Systems (MEMS). Alignment theory and implementation was been discussed in Chapter 6; a step-by-step process for applying it is presented here.

7.1 Grating material deposition and process parameters

A grating consists of a layer of TiO_2 which has been deposited on a substrate and then patterned with standard lithographic techniques. To transfer the pattern into the TiO_2 layer it is necessary to use an intermediate etch mask. Details of this process are discussed in this section and it is shown schematically in Figure 7.1.

The grating layer material, TiO_2, is deposited and processed by typical microfabrication techniques. The film is deposited by RF sputtering since that approach yields a very high-density, and consequently, a high refractive index film [53]. The sputtering is conducted at 5mTorr and 200W, which results in a deposition rate of ~5.0nm per minute. The thickness of a film deposited with these parameters has been measured and found to be radially symmetric and also to decrease monotonically by approximately 5% from the center to the edge of a 3-inch glass substrate.

The first step in patterning the TiO_2 film is to apply and pattern photoresist. The photoresist is applied over the TiO_2 film with a thickness of 0.5μm by spin-coating Microposit® S1805® photoresist at 4000rpm for 60 seconds. To prevent damage to the photoresist during contact printing, a softbake step follows at 115°C for 60 seconds on a hotplate. A mask aligner is then used to place the substrate with the TiO_2 film and the photoresist in contact with a photolithographic mask containing the desired grating pattern. Experiments with exposure and development time indicated that exposing for 2.9 seconds (with an ultra-violet light source operating at 365nm) and developing for 45 seconds produced a 50% fill factor, with rectangular bars remaining. The areas of the photoresist that are exposed to radiation become soluble in the developing solution and are removed by immersing the substrate in Microposit® 352 Developer. Any photoresist residue remaining on the TiO_2 in the exposed areas is removed via Reactive Ion Etching (RIE) with Oxygen at 40sccm and 100W for 15 seconds, which is called a descum etch. At this point, the photoresist forms a rectangular grating over the TiO_2 film.

The next step is to create a suitable etching mask for the TiO_2. The photoresist itself is frequently used in microfabrication as an etching mask. However, in this case the photoresist pattern would be destroyed by the combination of etching gases and etching time necessary to transfer the grating pattern into the TiO_2 layer. An alternative to using the photoresist as an etching mask in this instance is to use it to create a metallic mask capable of withstanding the pattern transfer process. This method is implemented by coating the substrate, the TiO_2 layer and the patterned photoresist with a 0.25μm Chromium layer. The Chromium is deposited by thermal evaporation since that method produces an anisotropic film, meaning that the top of the photoresist bars and the exposed TiO_2 are coated with Chromium, but not the vertical sidewalls of the photoresist grating. At this point, the surface of the substrate contains the photoresist grating pattern overcoated with Chromium and the negative of the grating pattern, in Chromium, deposited directly on the TiO_2. The photoresist is then removed, along with the Chromium layer covering it by a liftoff process, which consists of immersing the substrate in a photoresist remover, Microposit® 1165 Remover, in an ultrasonic bath for 5 minutes. The Chromium layer deposited directly over the TiO_2 is not affected when the photoresist is removed and remains on the surface in a grating pattern to perform as an etching mask.

The final step in the grating process is to transfer the pattern into the TiO_2 film. The exposed sections of the TiO_2 film are etched by RIE in a mixture of 20sccm CHF_3 and 20sccm SF_6 at a pressure of 15mTorr and a power of 175W. The etching rate is 252 Angstroms per minute. The Chromium remaining over the unetched segments of TiO_2 is stripped by immersing in a Chromium etching solution to yield a binary grating layer of TiO_2 on the glass substrate.

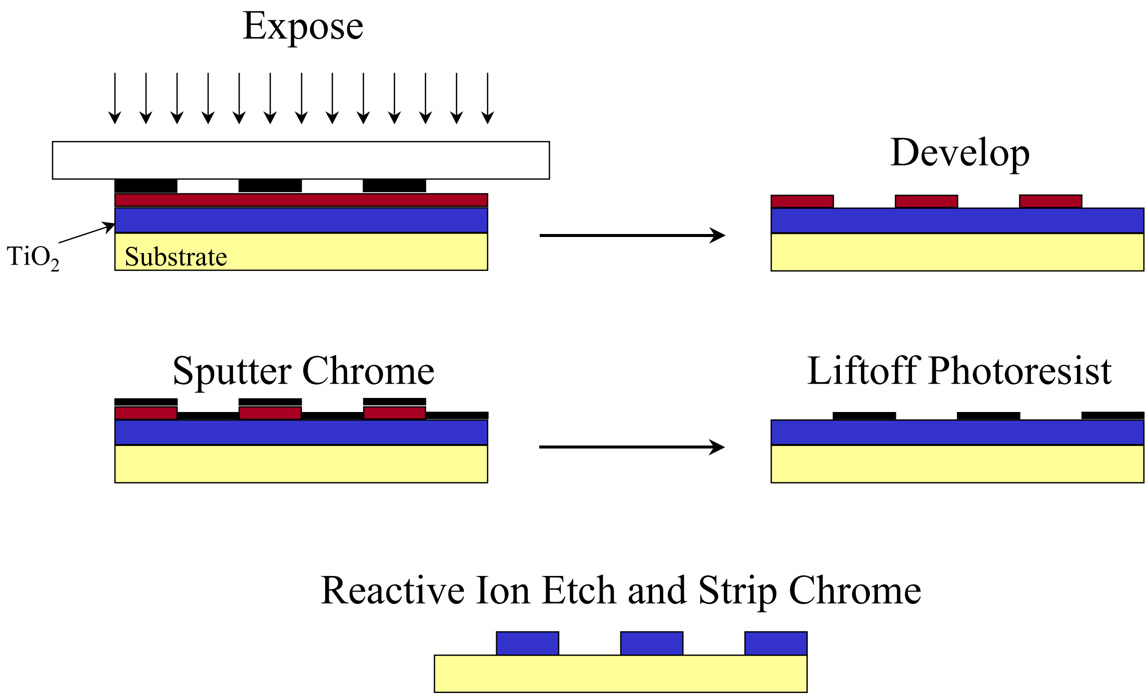

Figure 7.1 Illustration of the fabrication process for patterning a grating layer.

7.2 Homogeneous layer deposition and process parameters

The homogeneous layers in the designs for this application must completely fill in the grooves of the binary grating layer and form a layer of specific thickness above the grating. Also, the final surface of the homogeneous layer must be planar to facilitate deposition and fabrication of subsequent grating layers. To achieve this planar surface without chemical mechanical polishing, a photopolymer material is applied over the grating and is then heat-cured to form a durable layer. The photopolymer chosen for this application is Nano™ XP SU-8, which is a robust polymer capable of withstanding subsequent wet chemical processes such as development and liftoff as described in the previous section.

The SU-8 photopolymer is deposited over the grating by spin-coating and is cured through a number of bake steps on a hotplate. Its solvent is evaporated during these baking steps, not during spinning as is typical of most photoresist, making it susceptible to film stress induced during the curing process. Any film stress could alter the optical properties of the film or affect planarization, implying that control of the curing steps is critical to film quality. The curing steps begin with a softbake at 50°C for 30 seconds before the temperature is slowly ramped to 90°C, where it remains for one minute. The sample is then allowed to cool slowly by floating on a layer of nitrogen gas on top of the hot plate for one minute. Since SU-8 is a negative photoresist, a flood exposure to ultra-violet light is required to cross-link the polymer and make it impervious to subsequent chemical processes. The exposure time is dependent on film thickness; for the thicknesses used here, a 22 second exposure is sufficient. A second softbake step begins once again at 50°C for a time of 30 seconds before the temperature is, again, slowly ramped to 90°C. This time it bakes for two minutes at 90°C before floating on nitrogen gas on the hot plate for one minute. The SU-8 is then developed in P-type thinner for one minute before a final, hardbake step. The hardbake begins at 90°C, where it remains for 30 seconds then the temperature is slowly ramped to 200°C where it remains at two minutes. The thickness of an SU-8 film is affected by initial dispense volume and spin speed. Figure 7.2 illustrates SU-8 filling in the grooves of a grating and planarizing to prepare for the next grating layer.

While SU-8 is very appealing for its robust character, obtaining high quality films is difficult and tedious. In addition to the complicated deposition process described above, the film thickness can vary with humidity and temperature conditions in the clean room. Also, small defects, such as bubbles, can appear in an SU-8 film that is applied over a grating as a result of air becoming trapped in the grating grooves. Care must be exercised to control as many variables during processing and to avoid as many of these defects as possible in order to maintain SVDOE performance.

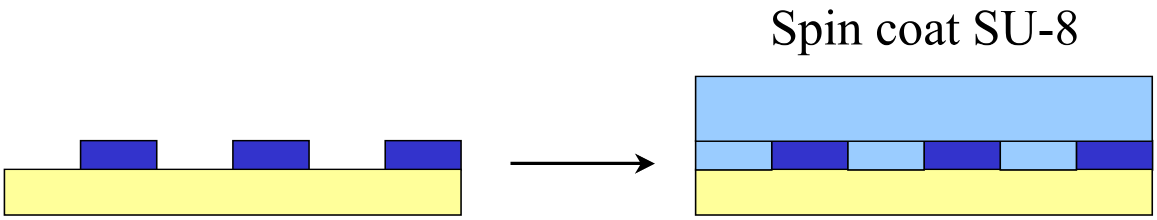

Figure 7.2 Illustration of deposition and planarization of a homogeneous layer.

7.3 Additional processes for subsequent grating layers

Subsequent grating layers are those layers that are deposited over the homogeneous layers. They are patterned using the same basic photolithographic technique discussed Section 7.1. However, two issues arise during the grating patterning process for these layers which must be accommodated. The first issue is overexposure of the photoresist due to backreflections from underlying grating layers during exposure. The second issue is damage to the homogeneous layer during RIE of the TiO_2 grating. Methods for mitigating these two effects are presented here.

Obtaining repeatable photoresist patterns relies on applying a consistent radiation dose to the photosensitive layer. Reflected radiation from the surface of a substrate or, in the case of SVDOE's, backscattered radiation from existing gratings, can alter the dose by causing overexposure and result in unreliable photoresist patterns. This problem can be mitigated by depositing an anti-reflective coating (ARC) immediately prior to the photoresist which absorbs the UV (365nm) exposure radiation before it reaches a surface to cause reflections or backscatter. The ARC used here, Brewer® XLX-20 ARC, is applied by spin-coating at 4000rpm for two minutes and then baking on a hotplate at 152°C, first for 45 seconds while floating on a layer of nitrogen gas then for 50 seconds in contact with the hotplate. Following exposure and development of the photoresist, the ARC is plasma etched by RIE to reveal TiO_2 in the grooves of the photoresist grating. The ARC etching chemistry consists of 8sccm of Helium and 8sccm of Oxygen at 10 mTorr pressure and 175 W power; the etching time is three minutes. The remaining procedures for the grating layer are identical to those for the first layer, i.e., deposit Chromium and perform a liftoff process, which removes the ARC as well, and then RIE for the TiO_2 grating layer.

The second difficulty arises during etching of the grating pattern into the TiO_2. The small nonuniformity in the film thickness from the center to the edge of the grating region implies a variation in the time required to completely remove the TiO_2 across the region. Also, slight variations in parameters during either the deposition or etching can affect the film thickness and/or etching time. In the case where etching is continued beyond the time required to remove the TiO_2 in an area of the substrate, the underlying SU-8 is exposed to the etching plasma. This is undesirable because the etching rate of SU-8 in the CHF_3/SF_6 chemistry is 513 Angstroms per minute compared to the 252 Angstroms per minute etching rate for TiO_2, implying that the

SU-8 can be etched very deeply in a relatively short period of time. This problem can be mitigated by depositing a layer of silicon dioxide (SiO_2) between the SU-8 and the TiO_2. Silicon dioxide is compatible with this situation because its etching rate in CHF_3/SF_6 is 241 Angstroms per minute, which is approximately equal to that for TiO_2, yet its refractive index is 1.526, which is very close to that of 1.576 for SU-8. Thus, SiO_2 serves the purpose of slowing the etch into the homogeneous layer while having minimal impact on performance of the SVDOE. The thickness of the SiO_2 layer is calculated based on the nonuniformity of the TiO_2 layer. The time difference required to completely etch through the thickest part of the TiO_2 compared to the thinnest part of that layer yields a maximum time period that the SiO_2 will be exposed to the etch, which can be combined with the SiO_2 etch rate to arrive at a thickness required to prevent damage to the SU-8. Any SiO_2 etching is compensated by being filled in when the next layer of SU-8 is deposited. Since the total homogeneous layer thickness is critical to SVDOE performance, the SU-8 thickness is reduced by an amount equal to the SiO_2 thickness. Achieving optimum SVDOE performance would require modifying its design to accommodate the SiO_2 layer and its associated refractive index.

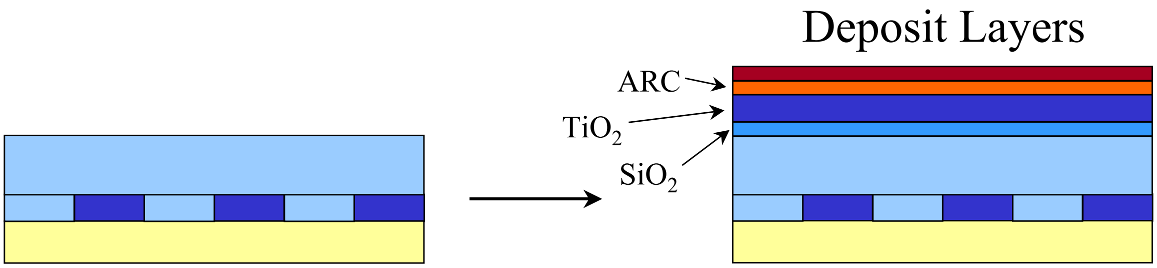

Figure 7.3 Illustration of additional material layers required for patterning second and subsequent grating layers.

7.4 Offset alignment

Applying a known offset between successive grating layers is the most challenging fabrication step associated with SVDOE's. In Chapter 6, an alignment approach which takes advantage of the double diffraction between gratings present on the substrate and the grating on the mask was discussed. To make use of this scheme it is necessary to simulate the double diffraction signal expected as the gratings are translated with respect to each other and then to successfully compare that simulation with the signal measured during equivalent translation in the alignment configuration. A reference frame for alignment and offset is established by this comparison. The final offset between the gratings is achieved by choosing a specific point within the reference frame, corresponding to a desired offset value, and positioning the mask and substrate such that the measured signal matches the expected value and is stable.

To simulate the expected double diffraction signal, the structure parameters of the layers in the system are used as input parameters to RCWA. The system in this case includes the substrate with any grating and homogeneous layers, ARC, photoresist, an air gap, and the mask, which consists of a Chromium grating on a quartz substrate. Each instance of the RCWA simulation produces the expected signal as a function of the relative offset, or translation, between the gratings on the mask and those on the substrate. The simulation is repeated with the air gap, or separation distance, between the substrate and mask as a variable parameter. The separation increment is set at 12.5µm to correspond to the calibrated, vertical motion in the mask aligner. This yields a family of curves where the placement of peaks and valleys within the offset scan is dependent on the separation distance.

Once the simulated curves are established they can be compared with signals measured during translation scans on the mask aligner. First, the mask and substrate are aligned manually as closely as possible using video microscopes to view alignment marks exterior to the grating region. Following manual alignment, the video microscopes are then retracted and the signal detector is moved into position above the window in the vacuum chuck. The double diffraction signal is measured while the substrate is translated approximately 15µm, which is greater than three grating periods, using the computer-controlled PZT actuator.

The initial scan is conducted at a separation distance assumed to be zero, meaning the mask and substrate are in soft contact. Then the separation distance is increased by 12.5µm increments as subsequent scans are conducted. Since there is some uncertainty as to the absolute separation distance when using the mask aligner, the simulated signals and the measured signals are compared to confirm this distance. In this comparison, the gross features and distinctive peak position shifts with increasing separation distance are used to determine and/or verify the distance. A series of scans conducted at four to eight different separation distances has proven sufficient to calibrate separation distance with enumeration on the mask aligner translation stage.

After separation distance has been calibrated, a specific distance is chosen to use for the alignment process. A general rule for making this determination is to select the smallest separation distance which allows free movement between the substrate and the mask. Scans taken at a very small separation distance, e.g., 0-25µm, exhibit friction between the mask and substrate which is evident by a measured signal that is either constant or varying much more slowly than expected during the first 4-5µm of the scan. Once the static friction is overcome by the force on the PZT the signal varies as expected for the remainder of the scan. A scan that is taken with friction between the components poses the possibility of alignment error being introduced during the scan, particularly rotation error. A scan at a very large separation distance, e.g., >100µm, poses a risk of alignment error being introduced during vertical translation to bring the mask and substrate into contact for exposure. Typical separation distances that are free from friction while being acceptably small are 37.5µm and 50µm.

Once a specific separation distance has been selected, several scans are conducted at that distance to ensure that the signal is stable. A successful offset alignment relies on the ability to reproduce the magnitude of the signal for a given relative offset between the mask and the substrate. Thus, any instabilities in the signal will result in an alignment error. The only source of signal instability that has been identified in the system is laser power fluctuation resulting from backreflections into the cavity. This fluctuation can be observed by monitoring the double diffraction signal while the mask and substrate are stationary. It can be minimized by adjusting the turning mirror within the substrate chuck so that backreflections are rejected and cannot reach the laser cavity. Eliminating the backreflections permits several (i.e., 3-4) consistent offset scans to be recorded. An example of a simulated scan is shown in Figure 7.4 and the corresponding consistent signal scans are shown in Figure 7.5.

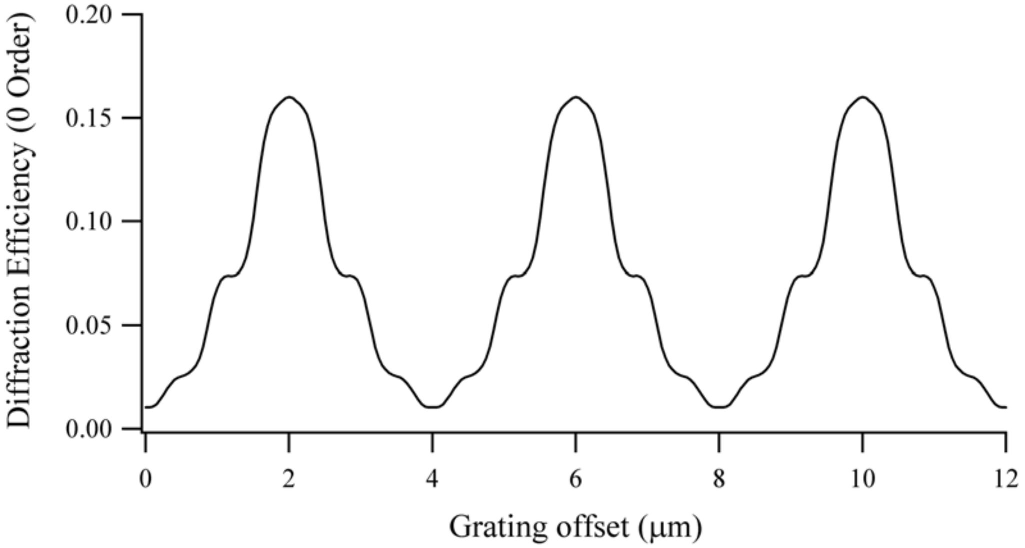

Figure 7.4 Example of a simulated signal curve.

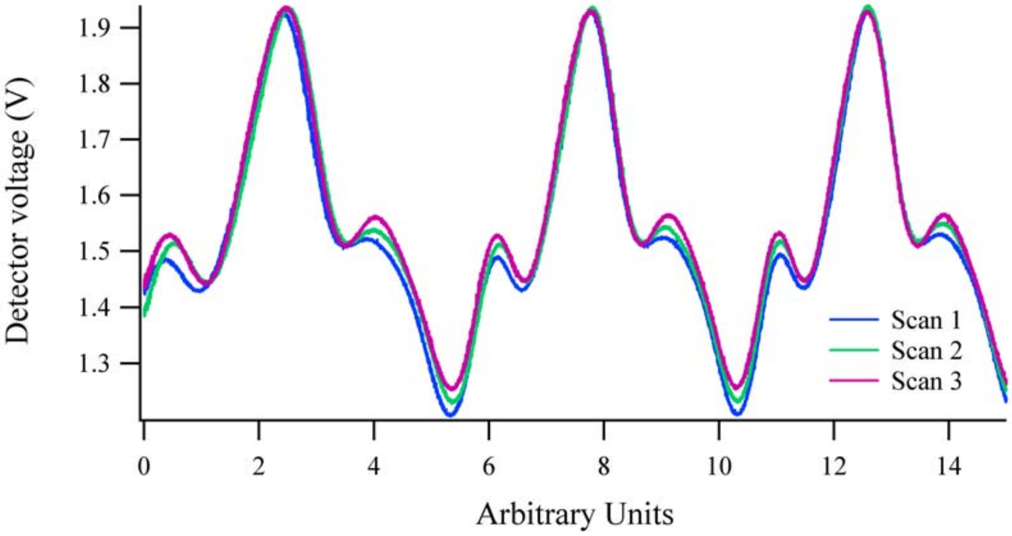

Figure 7.5 Example of measured signal curves which are self-consistent and also correspond to the same separation distance as the simulated curve in the previous figure.

One representative signal scan is chosen from the set of stable alignment scans discussed above to determine the offset alignment parameters. The corresponding voltage ramp that was applied to the PZT is also selected. The offset alignment process is shown in Figure 7.6 and Figure 7.7. The selected signal scan is smoothed using a boxcar (sliding window) algorithm to reduce noise present on the signal. After smoothing, one period of the signal and the corresponding segment of the voltage ramp are extracted as in Figure 7.7. Recall that one period of the signal coincides with one period of the relative offset between the mask and substrate. It is prudent to select a period from the end of the alignment scan rather than the beginning to avoid any instability associated with initiating a scan such as friction. The ordinate values of the extracted segments of the signal and the voltage ramp are scaled to one period of relative offset, using the simulated separation distance as a reference. For example, in Figure 7.7, the signal period chosen runs from one signal peak to the next. The corresponding simulated signal (Figure 7.4) indicates that the peaks occur at an offset value of 2μm and at 4μm intervals thereafter, so

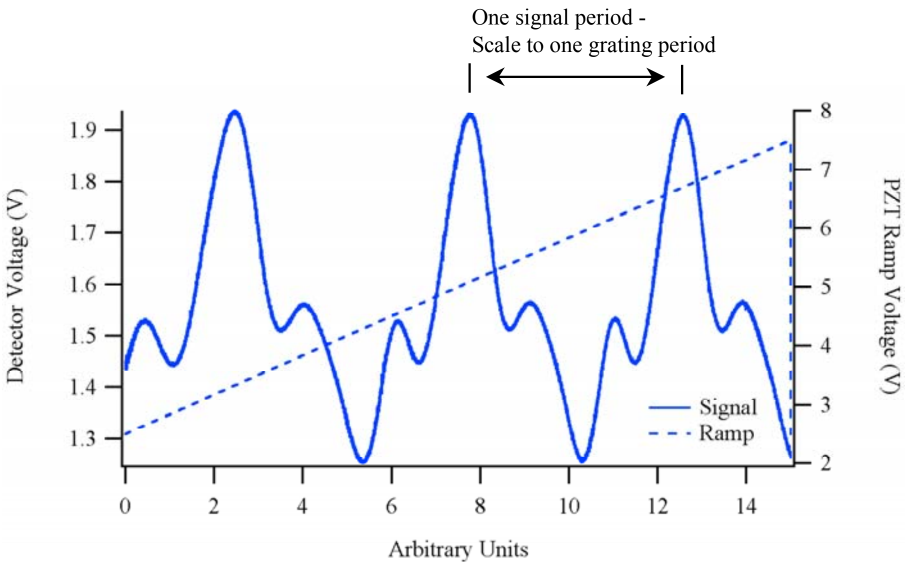

Figure 7.6 Signal and ramp from an alignment scan. One period of the simulated signal is extracted from this curve to scale to one period of grating offset.

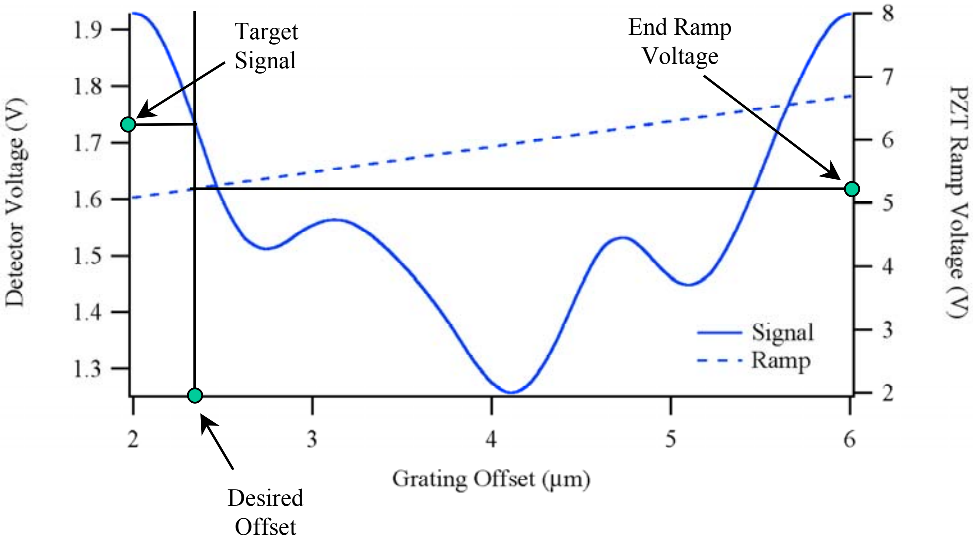

Figure 7.7 Illustration of scaling one period of the measured alignment curve, and its corresponding ramp voltage segment, to the period of grating offset derived from simulation. Final alignment parameters are determined from this scaled curve.

the ordinate values of the selected period are scaled from 2μm to 6μm. Once the signal period and its associated voltage ramp are selected and scaled, the signal and voltage values corresponding to the desired alignment offset can be determined. For example, in Figure 7.7, the desired offset value is shown as 2.5μm. The signal and voltage values, shown by the arrows, illustrate the signal that should be detected when that offset is achieved and the ending voltage ramp value that should be used to create the offset.

The alignment parameters derived from the representative scan above, i.e., target signal and ending voltage, are then applied to create the alignment offset. First, a new voltage ramp is created which begins at the same initial value as that used in the alignment scans, but terminates at the ending value derived above. This new alignment voltage ramp is applied to the PZT while the double diffraction signal is monitored, as before. When the terminating voltage is reached, the PZT motion ceases and the signal stabilizes as shown in Figure 7.8. The detected signal is evaluated against two criteria. First, the beginning segment of the scan must match the set of alignment scans taken previously. Second, the final, stabilized signal value must agree with the target signal within a specified tolerance. The allowed tolerance is generally defined by the design parameters and performance criteria. For the work described here the tolerance was maintained at ±0.1μm from the desired offset value. If the stabilized signal lies outside the tolerance, slight adjustments are made to the alignment ramp terminating voltage and the process is repeated until the desired tolerance is achieved. Once the stabilized signal lies within the tolerance, the substrate is brought into contact with the mask to prepare for exposure.

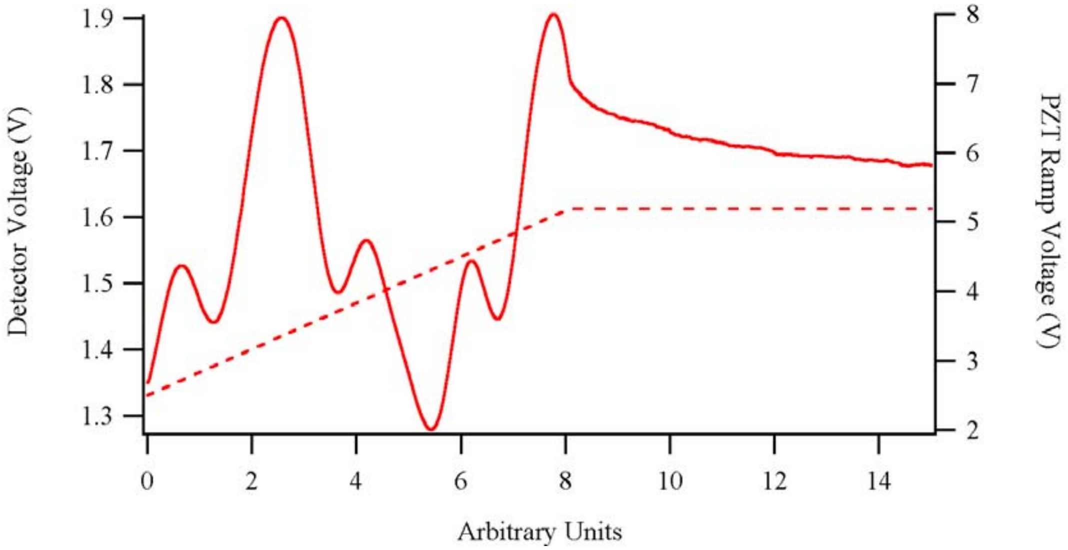

Figure 7.8 Example signal and PZT ramp voltage measured during a scan for final alignment.

Prior to exposure the alignment marks on the mask and substrate are examined with the video microscopes to look for obvious rotation. If rotation is observed, the marks are realigned and the offset alignment process is repeated. For the case of no rotation, the photoresist is exposed and the TiO_2 layer processing is completed as shown in Figure 7.1. Visual examination of the clear aperture of the grating region prior to exposure would provide improved assessment of the alignment, but there is insufficient magnification on the microscopes to resolve 2μm features.

Figure 7.9 illustrates exposure and processing of a second grating layer that has been aligned. Note that between the align and expose step and the process and etch step, all the processes discussed for the first grating layer and illustrated in Figure 7.1 must be carried out.

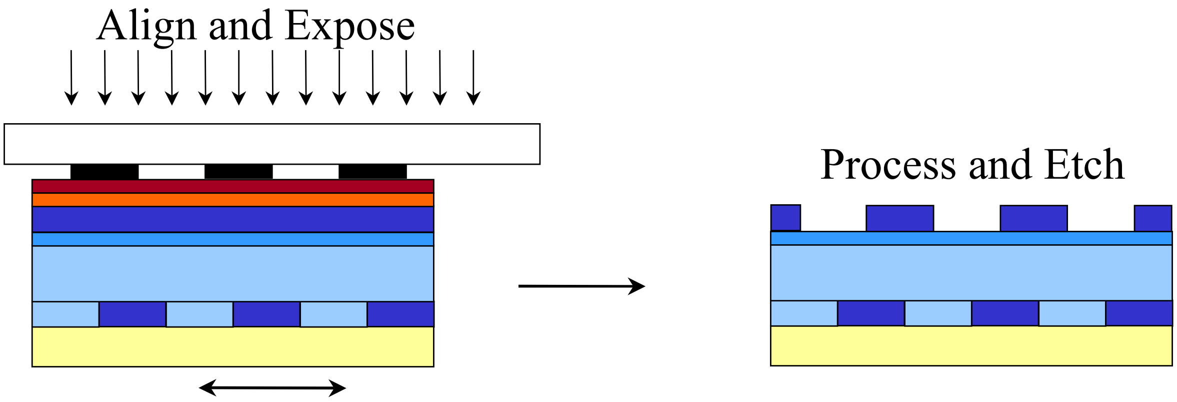

Figure 7.9 Schematic of aligning and exposing a second, or subsequent, grating layer.

Chapter 8

EVALUATION PROCESSES

Once an SVDOE has been fabricated, it must be evaluated to determine whether its performance and structural parameters meet specifications. Structural parameter evaluations include ridge width, layer thicknesses, and grating offset. Performance evaluations discussed here are diffraction efficiency as a function of input beam incidence angle on the optic, which is called angular sensitivity, for both TE and TM polarization orientations. These are conducted for multiple points within the clear aperture of the grating region.

8.1 Structural parameters

The capability to simulate a fabricated SVDOE in order to predict its actual performance for comparison with measured performance relies on knowledge of the structural parameters of the final device. The parameters of interest are layer thickness, ridge width in a grating layer, and relative offset between grating layers. These parameters are measured directly from micrographs of the SVDOE taken with a Scanning Electron Microscope (SEM).

Following optical testing, several small areas of the SVDOE are cleaved from the clear aperture of the grating region and examined in an SEM. The micrographs from these examinations can be stored electronically in a Tagged-Image File Format (TIFF) file which can be processed later. The TIFF file is pixelated with an intensity value in each pixel which can be correlated to a specific material. Surface features such as roughness or shadowing can also affect the intensity value. An example micrograph is shown in Figure 8.1. In this micrograph each of the layers is visible, beginning with the glass substrate at the very bottom. Proceeding upward there is a TiO_2 grating layer, followed by an SU-8 homogeneous layer which has filled in the grooves of the grating. The SiO_2 layer is visible between the SU-8 and the second TiO_2 grating. Finally, there is a cover layer of SU-8 to protect the uppermost grating layer.

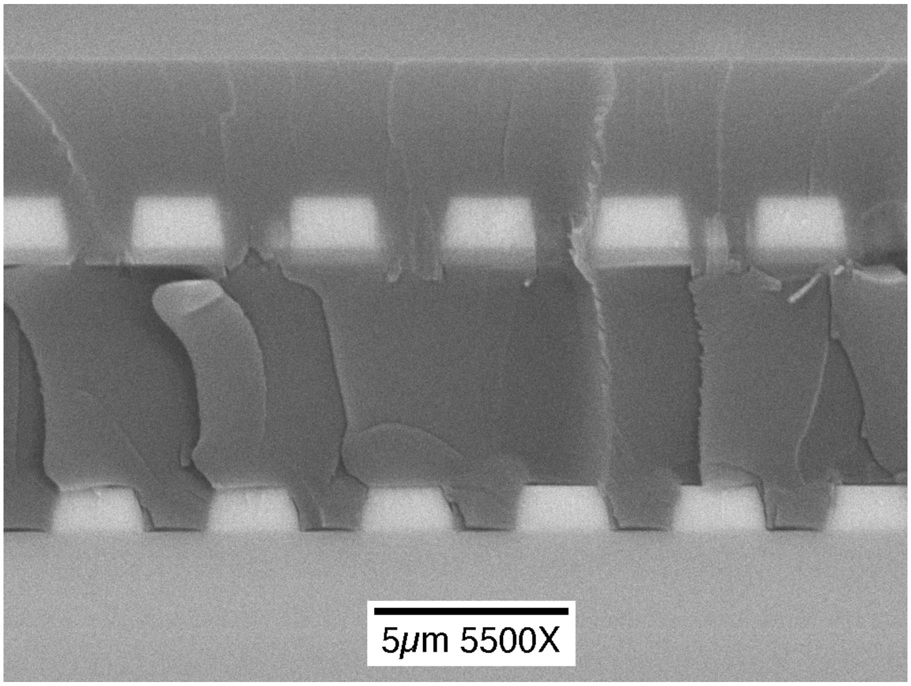

Figure 8.1 Example micrograph of an SVDOE which has been stored as a TIFF file.

The micrograph can be examined with the aid of image visualization software to determine boundaries between materials which, in turn, leads to calculation of structural parameters. Material boundaries are identified as row and column locations of specific pixels within the image where a material transition occurs. A pixel representing a transition between two adjacent materials is chosen by examining the intensity values in the region of the transition and applying a threshold criterion to identify a single pixel where the transition occurs. For a micrograph of a typical SVDOE, such as the one shown in Figure 8.1, material boundary pixels are specified at the corners of each grating ridge, at the bottom of the SiO_2 etch barrier layer, and at the top of the cover layer. The row and column locations of these boundary pixels are used to calculate average values for the grating period, grating layer thickness, grating ridge width, homogeneous layer thickness, and single values for etch barrier thickness and cover layer thickness. At this point, all values are expressed in terms of a number of pixels. The measurements are converted from pixels to microns by referencing the calculated number of pixels in a grating period to the known grating period, in microns, established on the photolithographic mask. The pixel to micron conversion is verified by applying the calculated conversion to the number of pixels in the scale bar on the image and comparing that to the measurement provided, in microns, on the scale bar.

Identifying the location of the corners of the grating ridges provides two measurements in addition to layer thickness and ridge width. First, the data allow the relative offset between grating layers to be calculated. Two variations of this measurement are given, one is referenced to the center of a ridge and the other is references to the center of a groove. Also, any slant present in the grating sidewalls as result of etching chemistry interactions [56], [54] can be calculated and accommodated in performance simulation.

8.2 Alignment assessment

Relative offset between grating layers provides the capability to set the preferred incidence angle of the SVDOE to any arbitrary value. It is also the most challenging aspect of the fabrication to implement. Thus, it deserves a great deal of attention in the assessment of an SVDOE.

The relative offset can be calculated in one of two ways. The first method was discussed in the previous section and relies on identifying the material boundary points of the grating profile in an image. The second method, which will be discussed in this section, is based on comparison of the phase of Fast Fourier Transforms (FFT) performed on each of the grating layers. This method has the benefit of providing increased efficiency of processing over the previous method.

8.2.1 Offset calculation

Calculation of grating layer offsets using the phase of an FFT relies, once again, on the TIFF file stored during examination with the SEM. Arrays of intensity values representing grating profiles can be extracted from this file and manipulated to provide the relative offset between grating layers. The first step in this process is to choose one grating layer, typically the grating residing on the substrate surface, as a reference position. A subsection of the image file containing an integral number of periods of the reference grating layer is then identified. From that subsection, a cross section of each grating layer is selected in the form of an array of intensity values.

The cross section arrays provide a two-dimensional "signal" representing the relative position of each grating layer. An FFT is performed on each of these signals, specifically to extract the phase. The phase shift between each layer is then converted to a physical offset between layers, which can be compared to the desired offset values.

One benefit of this approach over the method discussed in the previous section on determining structural parameters is that it can be implemented relatively quickly. For example, this method requires only a few minutes (<10) of operator intervention whereas the other method of choosing material boundaries requires approximately 45 minutes of intervention for a typical micrograph, such as the one seen in Figure 8.1, where five grating periods are imaged. This implies that a greater number of micrographs can be processed using this method which, in turn, implies improved assessment of the relative offset across the clear aperture of the grating region. Another benefit of the FFT approach of calculating relative offset is that it can be applied to micrographs where a large number of grating periods (e.g., 20) are imaged. Calculating the offset over an increased number of periods improves the accuracy of the result by averaging over fabrication imperfections, including both etching variations and registration errors between the grating layers.

8.2.2 Offset mapping throughout the grating region

Calculating the offset between grating layers at one point within the clear aperture of the grating region does not provide an accurate picture of the alignment between layers across the entire region. Registration errors between grating layers, rotation in particular, could cause variation in offset values across the region and a resulting variation in angular sensitivity. To obtain a more complete assessment of offset throughout the grating region, offset values are calculated at multiple, distributed positions. The offset values are then correlated, or “mapped,” to their position within the grating region and examined to discern a pattern across the region.

The offsets are calculated using the FFT method discussed in the previous section. The minimum number of positions probed in this manner have been three, with a larger number such as nine or ten preferred in order to obtain a more thorough mapping. Offsets are typically calculated at each position using two different micrograph views, one with approximately five grating periods imaged and one with approximately twenty grating periods imaged. Any differences between the offsets calculated from the two micrographs can be attributed to either rotation between grating layers within the area being observed or localized fabrication errors.

8.3 Angular sensitivity performance

The primary performance measure used for this work is a comparison between the measured and predicted angular sensitivity, defined as the diffraction efficiency as a function of the incidence angle of an input beam. Favorable comparison serves as verification of the RCWA simulation developed under this project. A second comparison, between measured performance and design performance, is possible only if structural parameters of the fabricated SVDOE are within acceptable tolerance of the design parameters. This section will discuss the equipment and procedures used to measure performance of a fabricated device as well as the approach to predicting its performance with RCWA.

8.3.1 Angular sensitivity measurement

The first step following fabrication of an SVDOE is to determine its angular sensitivity by measuring the diffraction efficiency of the element as a function of incidence. Figure 8.2 and Figure 8.3 are schematic drawings of the top and the side views, respectively, of the experimental apparatus used to make this measurement. Diffraction efficiency is defined here as the ratio of the measured intensity incident on the SVDOE to the intensity of the incident beam.

For this measurement, an SVDOE is placed on a multi-axis translation/rotation stage on an optical bench. The translation (x, y, z) allows probing of specific points in the grating region while the rotation (θ, ϕ) ensures the SVDOE is normal to the incident beam for initial alignment and to establish a reference for incidence angle. The SVDOE is then illuminated by a laser source, which is a diode-pumped solid-state Tm,Ho:YLF laser tuned to operate at 2.05μm. The peak power of the laser is approximately 17mW in TEM_{00} mode. A narrowband filter (not shown) immediately follows the laser to remove the colinear pump beam (780nm wavelength) from the optical train. Collimating optics significantly reduce the divergence present in the raw beam and produce a beam which is approximately 4mm in diameter. The resulting beam was found to have approximately 0.4mrad of convergence. A periscope, seen in Figure 8.3, raises the beam to the height required to sample the SVDOE grating region when it is placed on positioning stages. A polarizing cube ensures linear polarization (TM mode) immediately prior to the SVDOE under test. A half-wave plate can be placed in the system to rotate the polarization by 90° (TE mode). To examine the element as a function of incidence angle, a motorized rotation

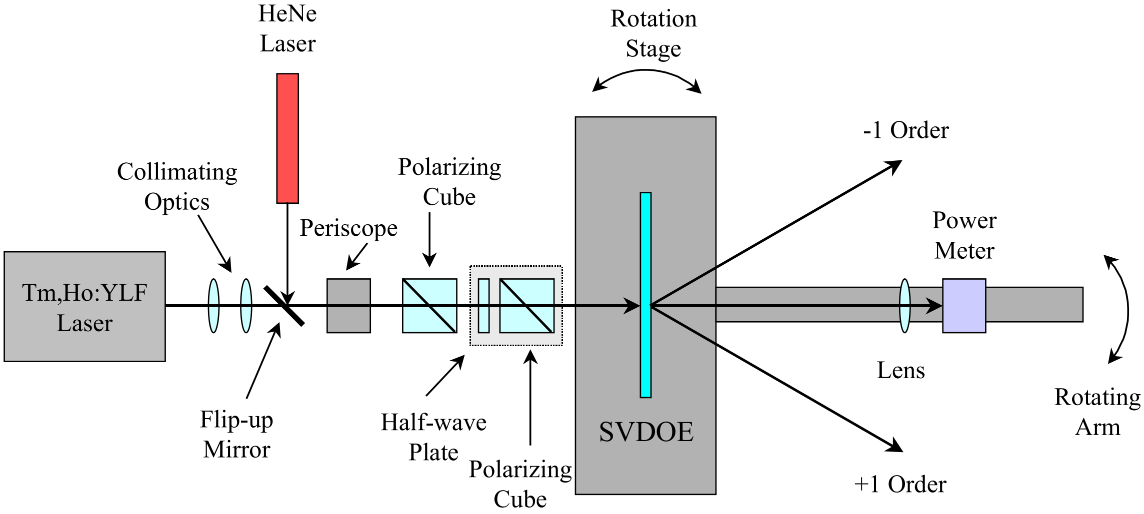

Figure 8.2 Top view of apparatus used to measure angular sensitivity of SVDOE.

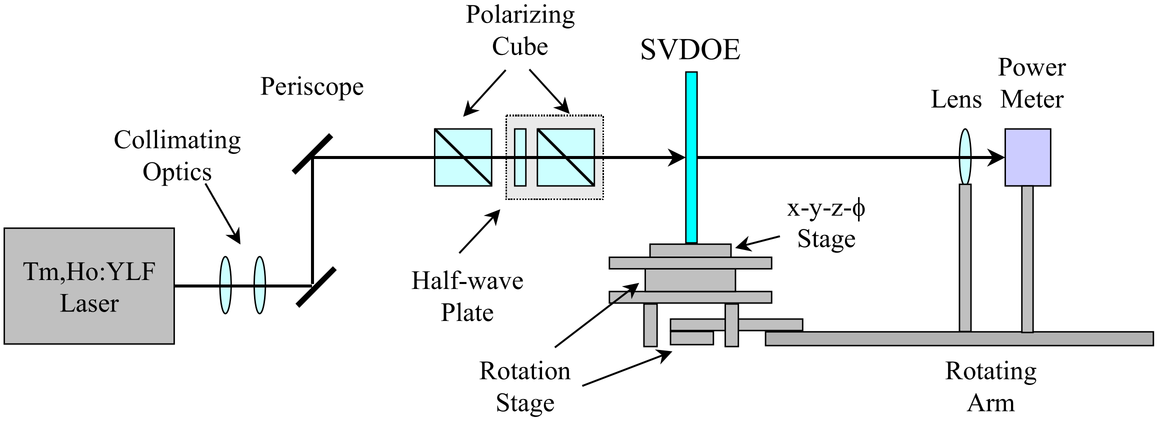

Figure 8.3 Side view of apparatus used to measure angular sensitivity of SVDOE.

stage below the SVDOE can be commanded to rotate the element to an angle, θ, with an accuracy of 0.01 degree. A rotating arm, consisting of a manual rotation stage directly below the motorized rotation stage with an attached optical rail, allows a detector to be placed in the diffracted beam. Diffracted power in any of the +1, 0, and –1 orders can be measured by rotating the detector, or power meter (Molectron PM3Q), to the proper diffraction angle. A lens ensures that all diffracted light in a single order is incident on the power meter. Figure 8.4 shows a diffracted beam from the SVDOE at the power meter; it is visualized using thermal response of liquid crystal paper.

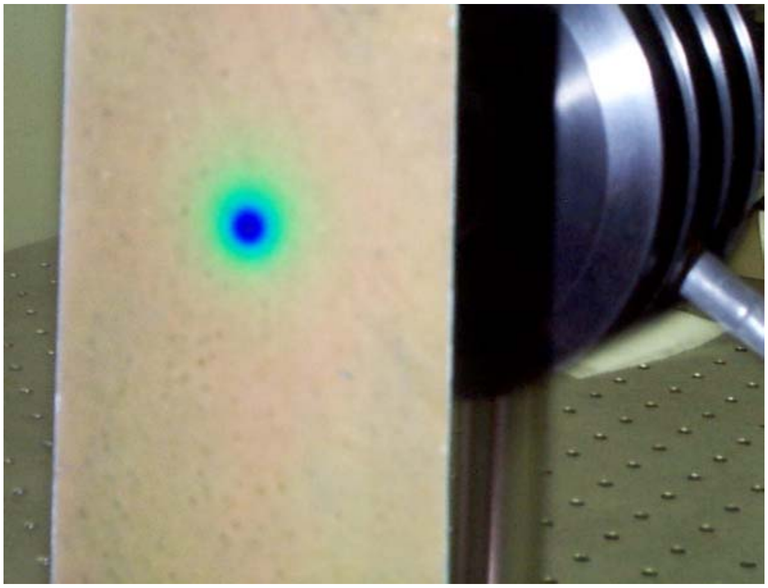

Figure 8.4 Representation of a beam diffracted from an SVDOE as a thermal response on liquid crystal paper.

When testing SVDOE's with this apparatus, the three primary diffracted orders are measured over a range of incidence angles from -15° to +15° in 0.5° increments. This range was chosen due to positioning constraints placed on the detector by the apparatus. The x-y-z translation of the element is then used to position different areas of the clear aperture of the grating region within the measurement beam to explore the performance across the region. In general, diffraction efficiency data is collected for three spots within the clear aperture of the grating region; one close to the center, another corresponding to the alignment laser beam position, and at least one more spot close to an edge of the grating region. Each spot where diffraction efficiency is measured is then marked on the surface of the substrate to ensure that the area is examined in the Scanning Electron Microscope (SEM). Parameters of the SVDOE structure, such as layer thickness and grating profile, corresponding to the measurement areas are determined from the SEM micrographs as discussed earlier in this chapter.

8.3.2 Angular sensitivity simulation

The measured angular sensitivity must be compared to predicted angular sensitivity in order to verify the RCWA simulation developed for the design and simulation of SVDOE's. The performance is predicted by using the basic structural parameters of the SVDOE, found using methods discussed earlier in this chapter, as input to the RCWA simulation. The angular sensitivity is then calculated and compared with the measured function.

The comparison can be made with arbitrary fidelity by increasing the complexity of the RCWA input. For example, each physical grating layer can be represented in the simulation by an arbitrary number of computational layers. This permits modification of the parameters of each computational layer (i.e., ridge width) to replicate the shape of a physical grating layer. Thus, a first-order comparison can be made by using one layer to represent a rectangular profile and then, if a particular etch chemistry results in a trapezoidal grating profile rather than a rectangular profile, the actual shape can be modeled.

Chapter 9

FABRICATION OF DEMONSTRATION ELEMENTS

This chapter discusses the realization of the prototype designs presented in Chapter 5. Topics covered include deposition and lithographic parameters for the individual layers and alignment procedures for two different cases. While the general alignment procedure is applicable for all SVDOE's, the alignment curves of diffraction efficiency as a function of offset between the substrate grating(s) and the mask are dependent on the specific layer structure.

The substrates used for these demonstration elements are wafers manufactured from soda lime glass with a three-inch diameter and a 1.1 millimeter thickness. Soda lime glass was used during development of fabrication processes since it is inexpensive. Fabrication of an element that must meet wavefront quality requirements would be executed using polished fused silica. The clear aperture of the grating region is contained in the central two-inch diameter of the wafer while the surrounding area contains alignment marks and 100μm grating regions. An example of a fabricated SVDOE is shown in Figure 9.1. The clear aperture of the grating region can be distinguished in the central two inches of the glass wafer.

9.1 Layer parameters

Chapter 7 provided a detailed discussion of deposition processes, lithographic parameters, and etching chemistry for the constituent layers of an SVDOE. This chapter provides the additional information necessary to convert those processes to a specific design. For example,

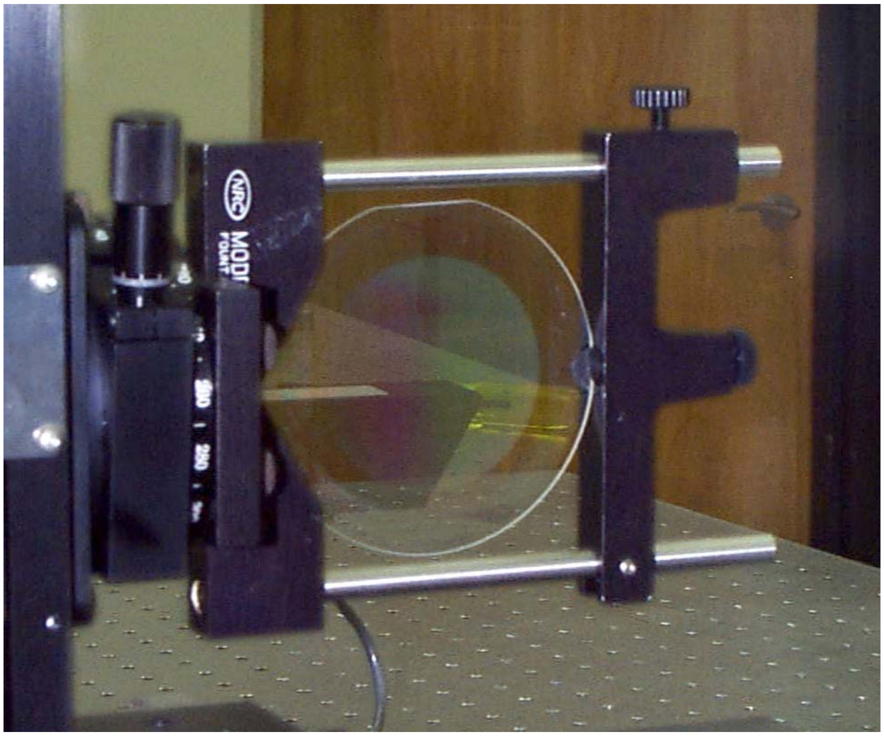

Figure 9.1 Photograph of fabricated SVDOE.

prototype SVDOE designs each require that layers in the device be fabricated to a precise thickness. The thickness of a TiO_2 grating layer is determined by deposition and etching times whereas thickness of an SU-8 layer is determined by spin speed, dispense volume, and polymer solid content. Those details will be provided in this chapter.

9.1.1 Two-layer prototype

The two-layer prototype design with structural parameters optimized for the measured values of the material optical properties was discussed in a previous chapter and is shown in Figure 5.3. The parameters that were used to fabricate each layer of an element based on this design are specified in Table 9.1. The layers are specified in this table according to the order of fabrication. For example, the first row of the table, which is labeled as the first grating layer, is directly on the substrate and is followed by the homogeneous layer and the etch barrier. The second layer is fabricated over the etch barrier layer and, finally, the cover layer is deposited to protect the second grating layer. Note that the etching time of each grating layer is affected by factors other than the deposition time. This is most likely due to either the materials directly below the grating layer, which can affect the etching chemistry, or by the total thickness of the underlying layers. The desired thickness of the homogeneous and cover layers is attained by proper combination of SU-8 formulation, dispense volume, and spin time.

Table 9.1 Fabrication parameters for two-layer prototype

Layer	Parameters
1st Grating layer: TiO_2	Deposition Time: 217 minutes Etching time: 60 minutes
Homogeneous layer: SU-8	Dispense Volume: 5 ml of SU-8 5 Spin Speed: 2700 RPM Spin Time: 20 seconds
Etch Barrier: SiO_2	Deposition Time: 1760 seconds
2nd Grating layer: TiO_2	Deposition Time: 217 minutes Etching time: 53 minutes
Cover layer: SU-8	Dispense Volume: 7 ml of SU-8 2 Spin Speed: 1100 RPM Spin Time: 20 seconds

9.1.2 Three-layer prototype

The three-layer prototype design with structural parameters optimized for the measured values of the material optical properties was discussed in a previous chapter and is shown in Figure 5.5. The parameters that were used to fabricate each layer of an element based on this design are specified in Table 9.2. As in the previous section on the two-layer prototype, layers are specified in this table according to the order of fabrication. Thus, the layer labeled as the first grating layer resides directly on top of the substrate and the third grating layer is farthest away from the substrate with the second grating layer in between. The fabrication parameters are optimized, again, by careful modification of the etching time for grating layers and by controlling the SU-8 formulation, dispense volume, and spin time for the homogeneous layers.

Table 9.2 Parameters for three-layer prototype

Layer		**Parameters**	
1st Grating layer:	TiO_2	Deposition Time: Etching time:	145 minutes 45 minutes
Homogeneous layer:	SU-8	Dispense Volume: Spin Speed: Spin Time:	5 ml of SU-8 5 1120 RPM 20 seconds
Etch Barrier:	SiO_2	Deposition Time:	1300 seconds
2nd Grating layer:	TiO_2	Deposition Time: Etching time:	145 minutes 40 minutes
Homogeneous layer:	SU-8	Dispense Volume: Spin Speed: Spin Time:	7 ml of SU-8 2 1100 RPM 20 seconds
Etch Barrier:	SiO_2	Deposition Time:	1300 seconds
3rd Grating layer:	TiO_2	Deposition Time: Etching time:	145 minutes 40 minutes
Cover layer:	SU-8	Dispense Volume: Spin Speed: Spin Time:	7 ml of SU-8 2 1850 RPM 20 seconds

9.2 Alignment

Recall from Chapter 6 that successful alignment during fabrication is dependent on comparison of measured diffraction patterns to simulated diffraction patterns. The specific form of the patterns is dependent on all parameters of the system, for example, layer thicknesses, relative refractive index values, and separation distance. In this section examples of alignment curves for the prototype element designs defined in Chapter 5 are presented and compared with curves measured during device fabrication.

9.2.1 Two-layer prototype

Examples of simulated alignment curves for the two-layer prototype are shown in Figure 9.2. The curves represent diffraction efficiency as a function of displacement between a grating ridge on the substrate and a chrome bar on the mask. The specific form of each curve is dependent on the separation distance between the layers on the substrate and the mask. The separation distance increment of 12.5μm corresponds to the scaling increment on the translation stage controlling vertical substrate motion in the mask aligner. Note that as the separation distance between the substrate and the mask is increased, for example, from 25μm to 50μm, the pattern oscillates between having a peak at zero offset (also 4μm offset since that is the period of the structure), which is perfectly aligned, and having a peak at 2μm offset, which is perfectly misaligned. The relative magnitude and shape of the peaks is very similar, implying that it would be difficult to use the pattern alone to confidently determine separation distance. Thus, it is important to be able to determine separation distance in another manner. Use of the video microscopes on the mask aligner has proven successful in establishing this distance for some cases by providing a reference for zero separation distance. Comparison of a series of simulated curves with a similar series of measured curves then permits calibration of separation distance.

Alignment curves which were measured during fabrication of a two-layer demonstration element are shown in Figure 9.3. The separation distances do not necessarily match one-to-one between Figure 9.2 and Figure 9.3 since, as discussed previously, it is very difficult to determine the distance solely from the measured curves. It is possible to see the same trend for oscillation of peaks between 0μm and 2μm offset. The first two curves indicate static friction between the substrate and mask since the signal and, hence the offset, does not change as the ramp voltage is initially applied to the PZT. Eventually the force applied by the PZT overcomes the static friction between the two components and the offset begins to change.

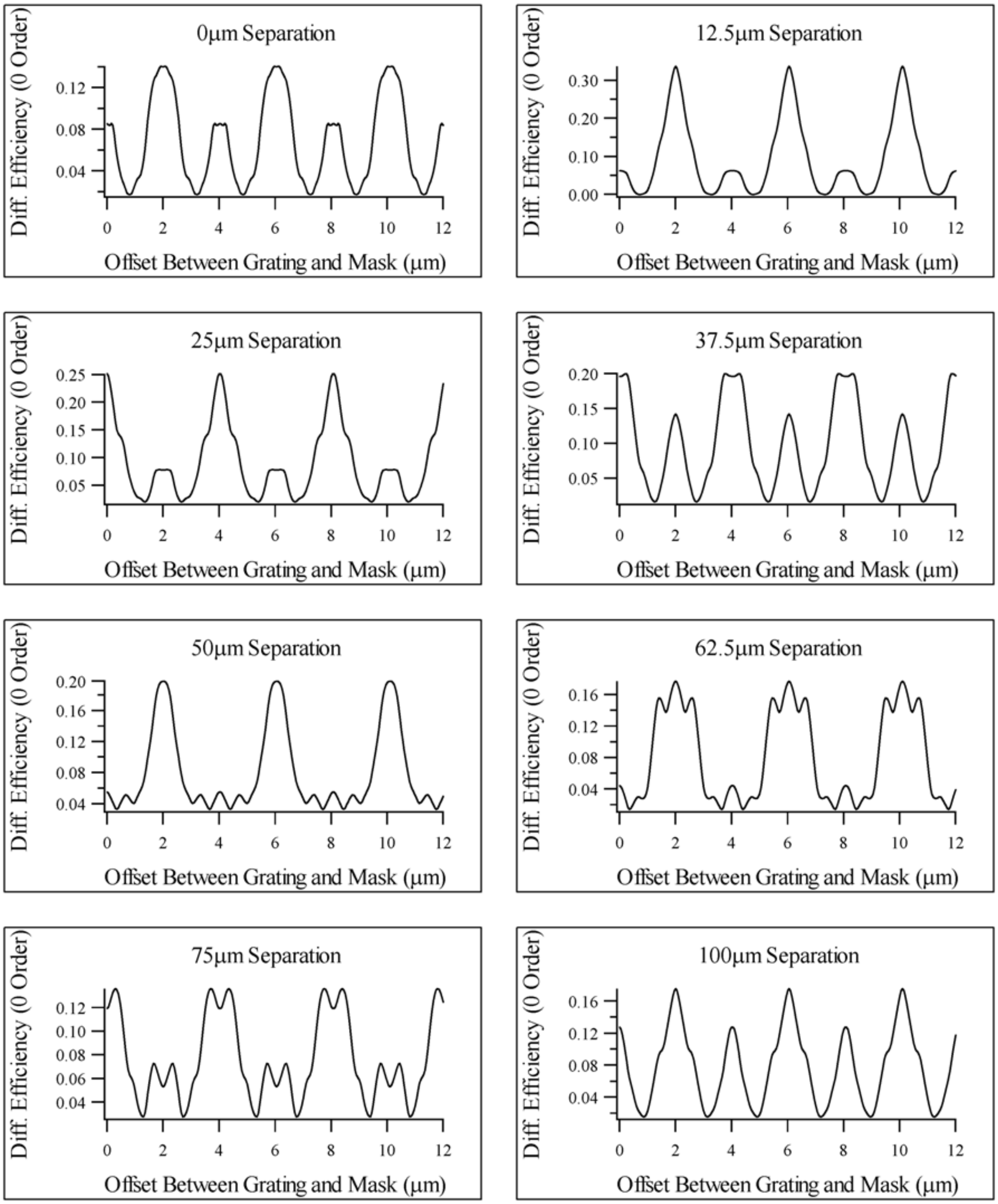

Figure 9.2 Series of simulated alignment curves, parameterized by separation distance, for two-layer prototype scanner element.

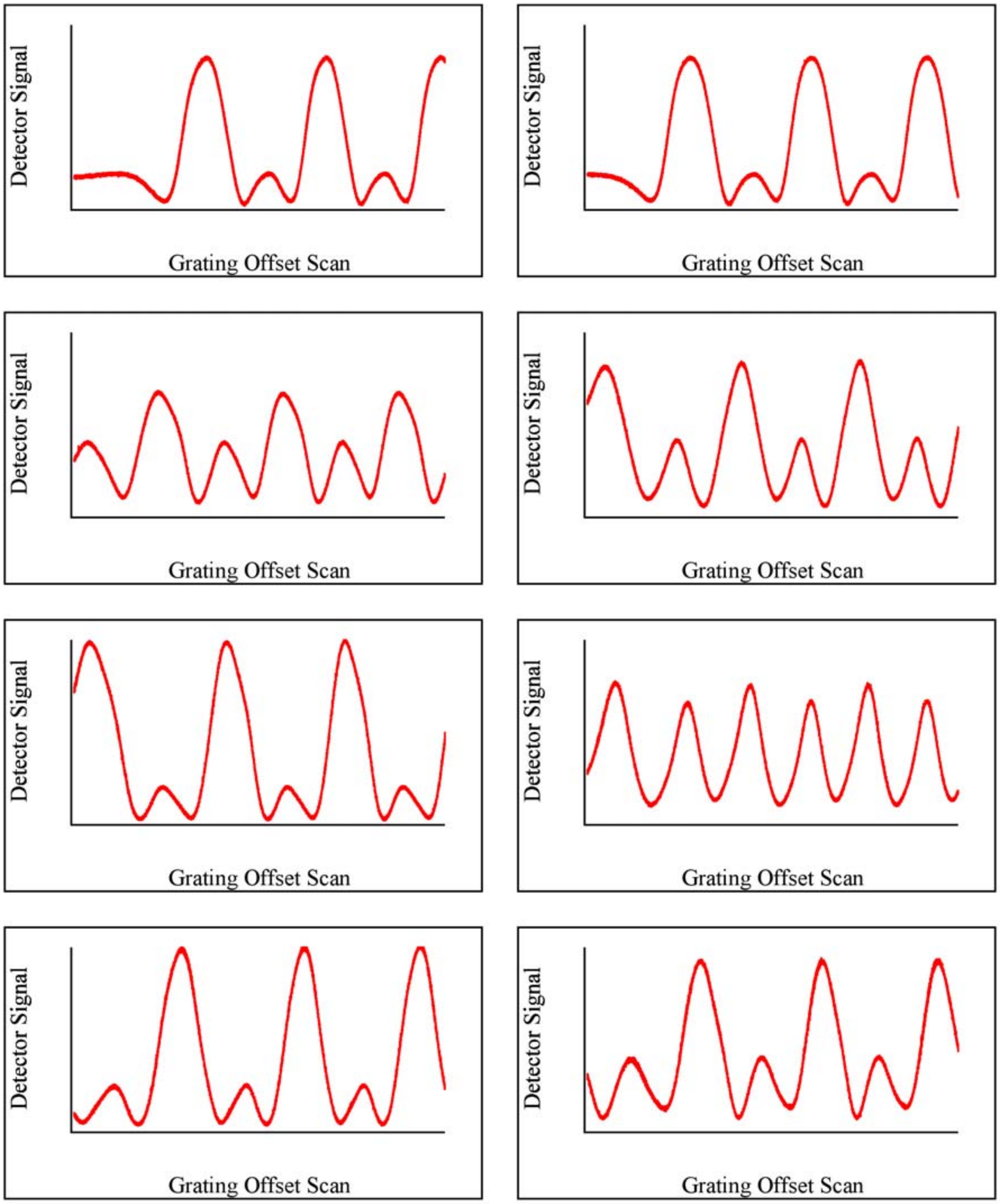

Figure 9.3 Series of measured alignment curves, parameterized by separation distance, for two-layer prototype scanner element.

9.2.2 Three-layer prototype

A three-layer SVDOE requires two alignment steps, each with its own characteristic set of alignment curves. The simulated curves for the second of the three layers are shown in Figure 9.4. Note that they are symmetric within a grating period, just as the curves for the two-layer prototype element. The simulated curves for this case contain features which are more distinctive with a change in separation distance than the corresponding curves for the two-layer prototype. For example, the simulated curve for a separation distance of 25μm has oscillations in the sidewalls of the primary signal peaks. The corresponding measured curves are shown in Figure 9.5. Recall that for the measured curves the increment in separation distance is 12.5μm, according to the scale on the translation stage, but the absolute separation distance must be inferred by comparison with the simulated curves. Visual comparison between the set of simulated curves and the set of measured curves for this case shows the same trend of features with a change in separation distance, particularly for 0 – 50μm, which encompasses the typical range of separation distance used during alignment.

The curve corresponding to 37.5μm separation distance was chosen for alignment based on the simulated curves since it exhibits a strong peak in a desirable position, 2μm, to achieve the required offset. The other consideration here is that a separation distance of 37.5μm is the minimum for a curve with a peak at 2μm. Since the substrate and mask must be brought into contact following alignment, it is desirable to keep the distance traveled after alignment minimum to avoid any possible misalignment during translation.

Simulated alignment curves for the third grating layer are shown in Figure 9.6. Note that the curves have become asymmetric, as might be expected when the underlying substrate has two grating layers placed at a relative offset. The offset between the substrate and the mask in the graph is referenced to the position of the second grating layer. The alignment curves show that the position of peak efficiency is no longer at 0μm or 2μm, but rather it is dependent on the SVDOE structure. Thus, an accurate alignment of the third grating layer requires knowledge of the underlying structure, implying all alignment steps must be as accurate as possible.

Once again, 37.5μm was targeted as the separation distance for alignment since the simulated curve shows a strong peak close to 2μm. The curves that were measured at separation distance increments during the alignment process are shown in Figure 9.7. As before, it is possible to make visual correlation between simulated and measured curves by tracking distinguishing features, allowing determination of separation distance.

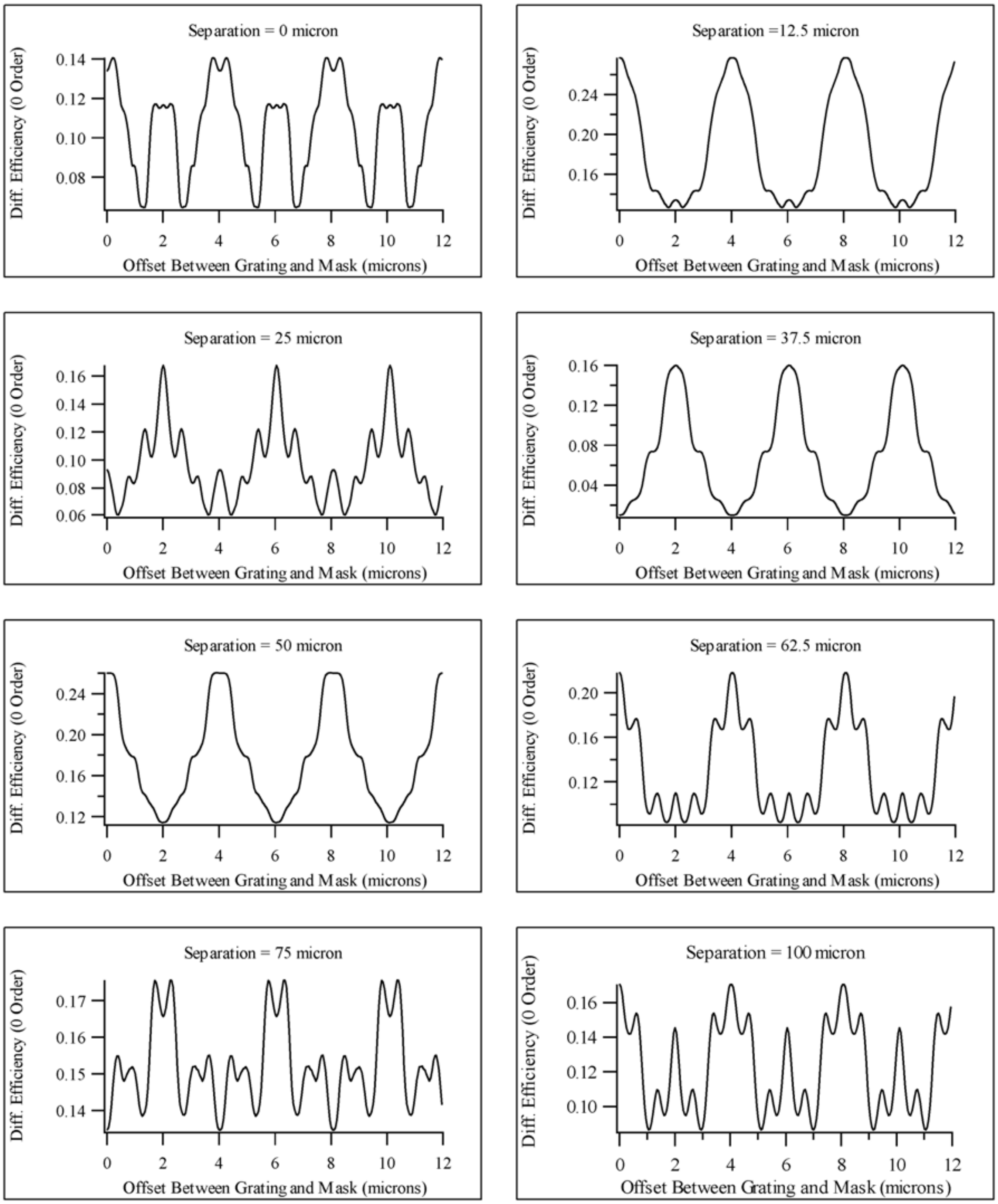

Figure 9.4 Series of simulated alignment curves for the second of three grating layers, parameterized by separation distance, for three-layer prototype scanner element.

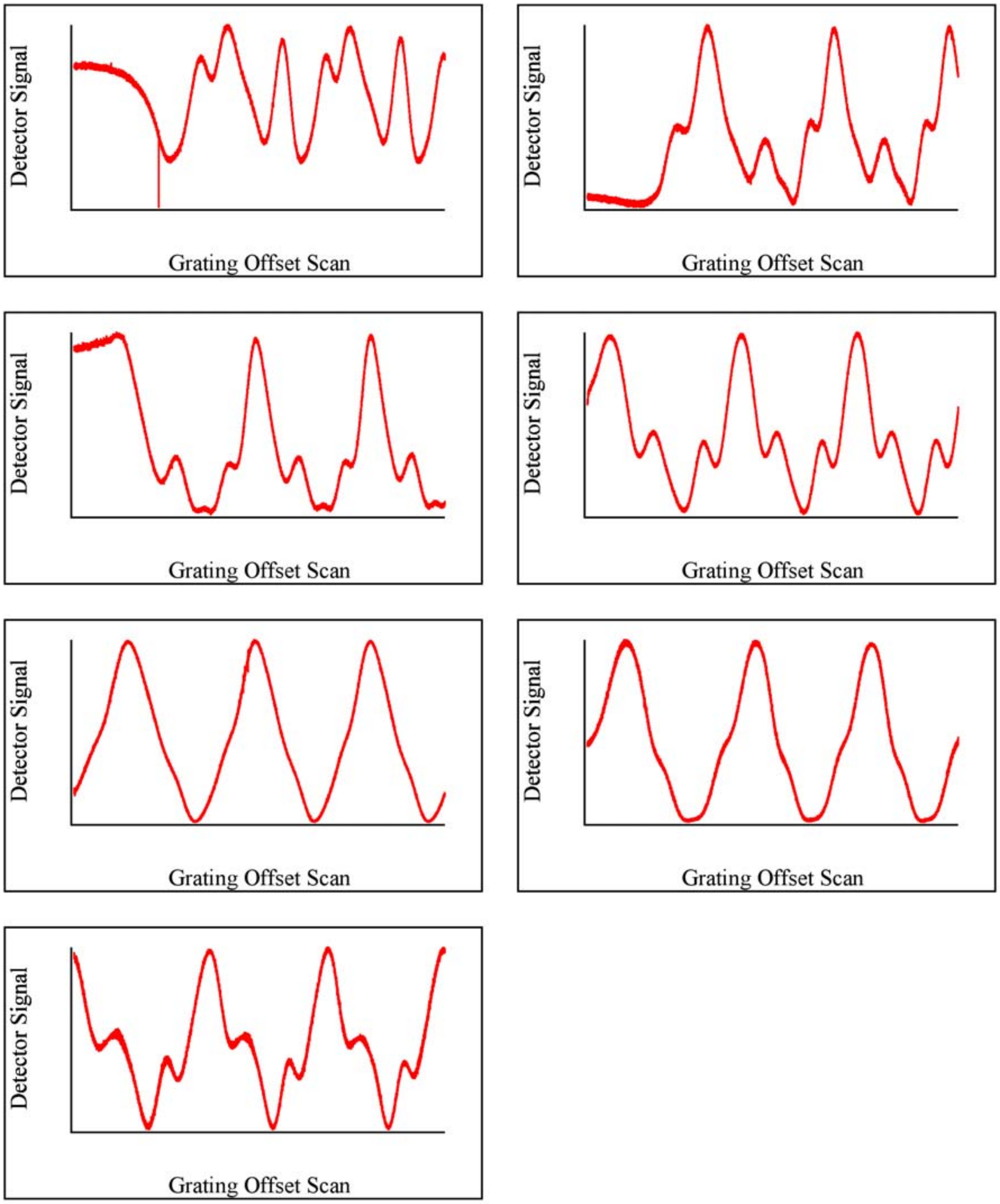

Figure 9.5 Series of measured alignment curves for the second of three grating layers parameterized by separation distance for three-layer prototype scanner element.

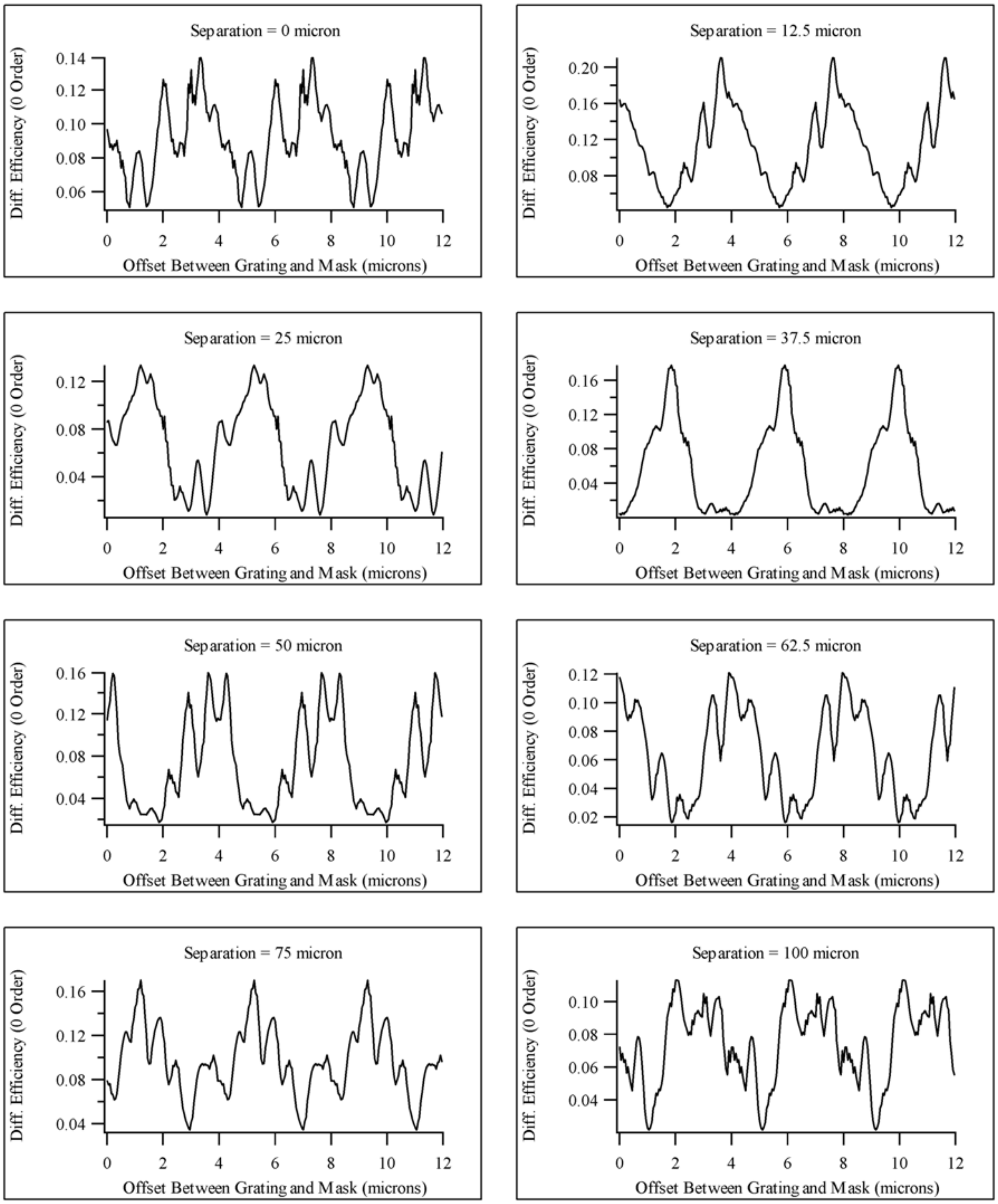

Separation = 0 micron

Separation = 12.5 micron

Separation = 25 micron

Separation = 37.5 micron

Separation = 50 micron

Separation = 62.5 micron

Separation = 75 micron

Separation = 100 micron

Figure 9.6 Series of simulated alignment curves for the third of three grating layers, parameterized by separation distance, for three-layer prototype scanner element.

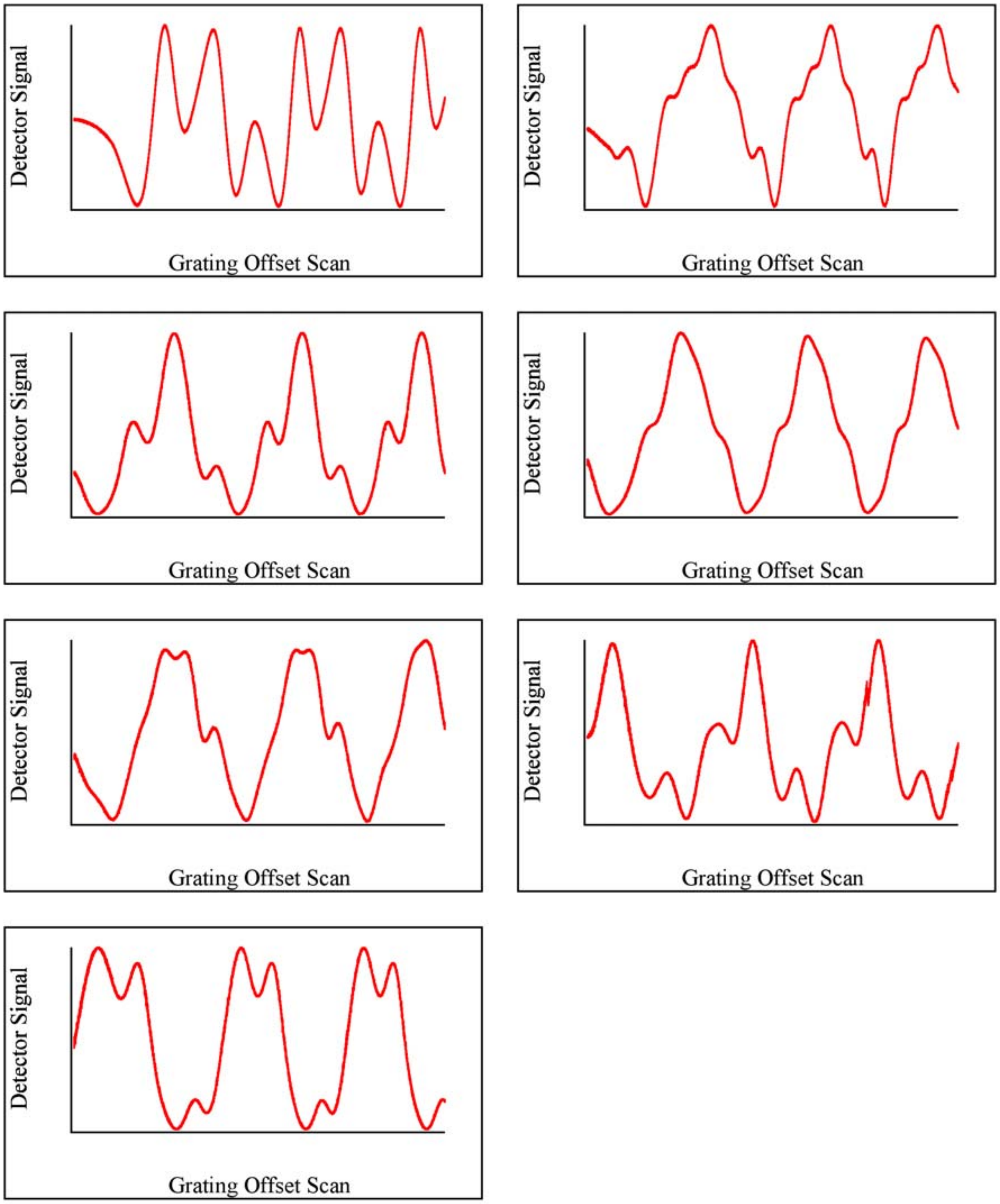

Figure 9.7 Series of measured alignment curves for the third of three grating layers, parameterized by separation distance, for three-layer prototype scanner element.

Chapter 10

EVALUATION OF DEMONSTRATION ELEMENTS

This chapter will present evaluations of SVDOE's that were fabricated according to the processes in the previous chapter. The evaluation processes were discussed in Chapter 8 and include determination of structural parameters, angular sensitivity, and alignment assessment. Two specific SVDOE samples will used throughout this chapter. The first is a representative two-layer sample. The other is the first fabricated three-layer sample.

10.1 Determination of structure parameters

Comparison of measured SVDOE performance with predicted performance requires a detailed description of the grating structure, within the measured area, as input to the RCWA model that was discussed in Chapter 3. These structure parameters are measured directly from micrographs taken with an SEM as discussed in Chapter 8. Several areas of the grating region are examined with the SEM, in addition to the areas where diffraction efficiency is measured, to provide an overall view of the fidelity of the fabrication processes and provide feedback for future process improvements.

This section will present micrographs of fabricated SVDOE's along with parameters measured from those micrographs. The TiO_2 grating layers and their offsets are apparent in these micrographs as is the SiO_2 layer. Vertical striations seen in homogeneous layers are the result of cleaving for examination in the SEM and are not indicative of structure within the layers.

10.1.1 Two-layer prototype

An example two-layer SVDOE, seen in Figure 10.1, was chosen as a representative sample from among those that were fabricated. Examining the micrograph in Figure 10.1, all the layers are readily apparent. Beginning from the bottom of the picture and proceeding upward, the first layer seen is the glass substrate. The next layer is a TiO_2 grating where the grooves have been filled in by the subsequent homogeneous layer of SU-8. The homogeneous layer, after filling in the grating grooves, forms a planar surface approximately 5.5μm above the top of the grating. A layer of SiO_2 is deposited over the homogeneous layer in a thickness of approximately 0.4μm. The upper, or second, grating layer is offset approximately 1.7μm to the right, which is 0.55μm greater than the desired amount of shift for this device. This is caused by additional motion introduced during translation to obtain contact for exposure. As a result, its peak diffraction efficiency will be not centered at normal incidence. The cover layer is apparent over the second grating layer, with air at the very top of the picture. Structural parameters measured from this micrograph are given in Table 10.1.

Careful examination of Figure 10.1 at the bottom of the grooves of the second grating layer reveals that the SiO_2 was etched in this region and, in fact, it appears to be completely removed. As discussed previously, its refractive index is very close to that of the SU-8, so this SiO_2 grating created in the homogeneous layer will only minimally affect the SVDOE performance once SU-8 fills the region. For optimum SVDOE performance design parameters should be modified to account for its effect.

Further examination of the structure shows that the sidewalls of the grating ridge have a small slant angle rather than being perfectly vertical. The slant angle is a consequence of the reactive ion etching process and is not uncommon for gratings fabricated in this manner [56]. Optimization of the reactive gas mixture, power, and pressure used in the etch process could potentially eliminate these effects [55].

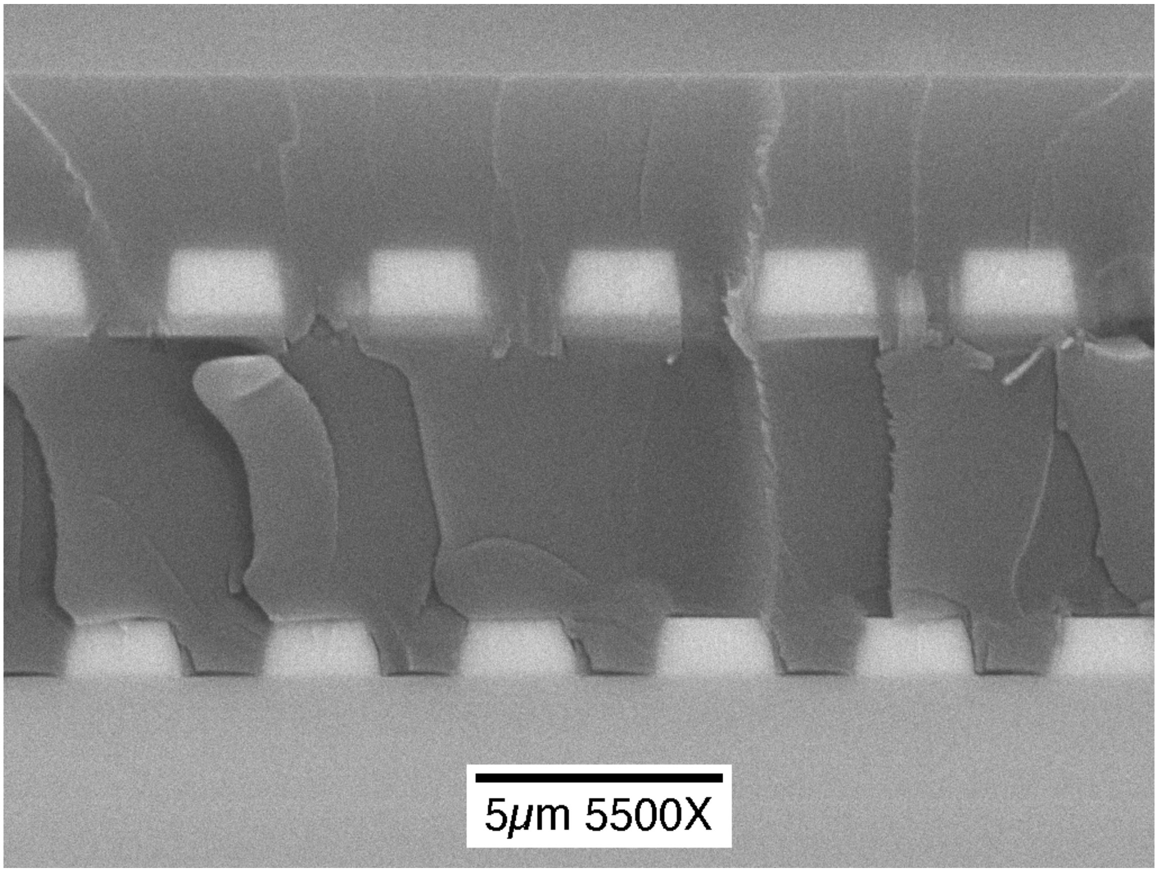

Figure 10.1 Micrograph of fabricated two-layer SVDOE.

Table 10.1 Structural parameters for fabricated two-layer SVDOE

Structural Parameter	**Measured Value (μm)**	**Design Value (μm)**
SU-8 cover layer	3.35	2.90
Second grating layer thickness	1.28	1.105
First grating layer thickness	1.19	1.105
Second grating layer ridge width	2.23	2.00
First grating layer ridge width	2.31	2.00
Thickness between second and first layer	6.02	5.90
Groove offset between second and first layers	2.31	1.154
Ridge offset between second and first layers	2.31	1.154

10.1.2 Three-layer prototype

The structure of the first fabricated three-layer prototype is shown in Figure 10.2. As with the two-layer sample, all grating layers are readily seen in this micrograph. The glass substrate is seen across the bottom of the micrograph with the first TiO_2 grating on top of it. This is followed by a homogeneous layer, which has filled in the grating grooves, and the SiO_2 etch barrier layer. The second TiO_2 grating, homogeneous layer, and etch barrier layer follows. Finally, the third TiO_2 grating layer and its cover layer of SU-8 can be seen. The structural parameters measured for this SVDOE are given in Table 10.2.

In the uppermost grating layer, the third layer, the grating ridges are significantly narrower than in the other two layers. This indicates an area in which the photoresist was overexposed as a result of poor contact between the substrate and the mask during the exposure. The difficulty with contact was visible during fabrication. Notice also in the third layer that the SiO_2 etch barrier is almost intact while in the second layer it is almost completely etched through. This is likely a consequence of the difference in thickness between the second and third grating layers as well as the difference in contact and subsequent exposure during the photolithographic step. The second and third grating layers were fabricated using the same process parameters.

The offset between the grating layers in this device are very close to absolute values which would create a diffraction efficiency peak in the -1 order when it is illuminated at normal incidence. This meets the basic requirement for the lidar scanner application, which is to have high diffraction efficiency into a single diffracted order for a normally incident beam. The lidar system then creates a conical scan pattern by rotating the scanning element about its optical axis.

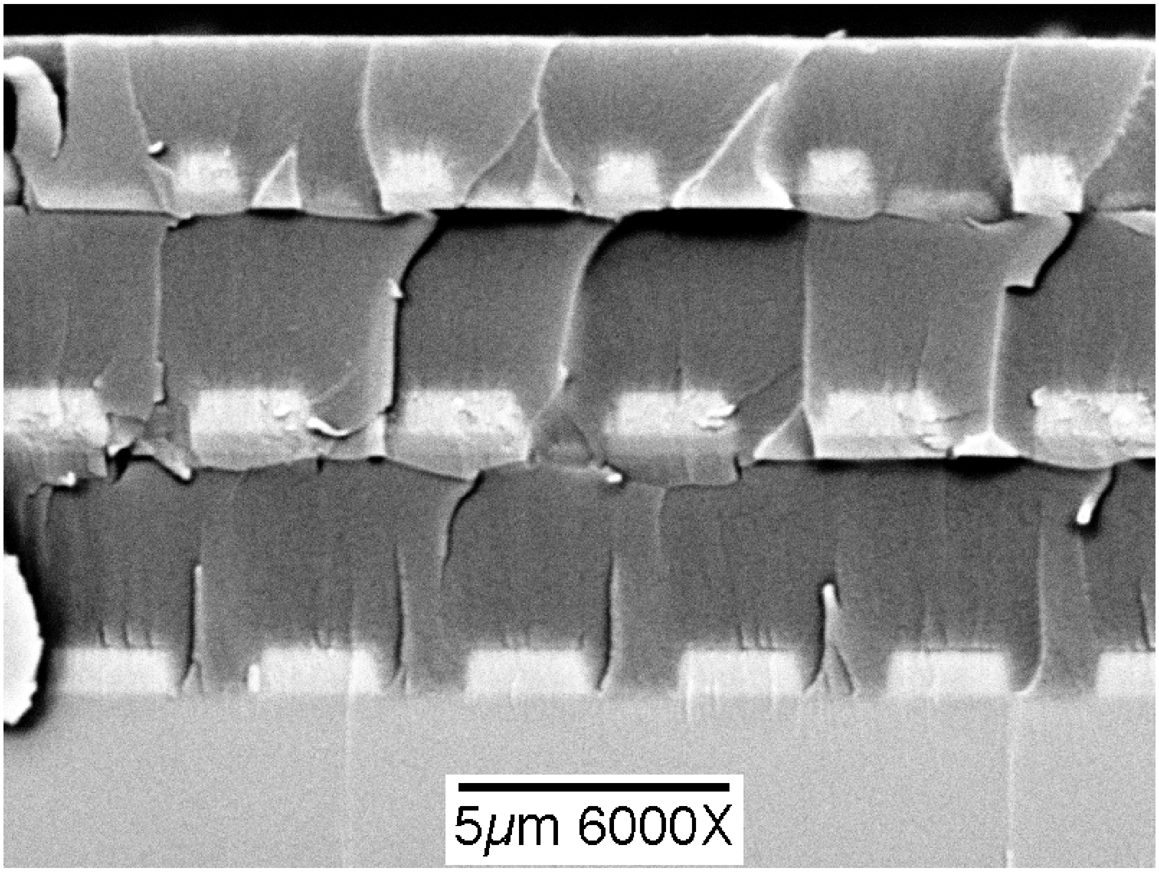

Figure 10.2 Micrograph of fabricated three-layer SVDOE.

Table 10.2 Structural parameters for fabricated three-layer SVDOE

Structural Parameter	Measured Value (μm)	Design Value (μm)
SU-8 cover layer	2.09	1.80
Third grating layer thickness	0.82	0.736
Second grating layer thickness	0.93	0.736
First grating layer thickness	0.91	0.736
Third grating layer ridge width	1.23	2.00
Second grating layer ridge width	2.31	2.00
First grating layer ridge width	2.33	2.00
Thickness between third and second layer	3.68	4.00
Thickness between second and first layer	4.06	4.00
Groove offset between third and first layers	-2.14	1.561
Ridge offset between third and first layers	-2.13	1.561
Groove offset between second and first layers	-1.27	0.780
Ridge offset between second and first layers	-1.29	0.780

10.2 Comparison of measured performance with simulation

The structural parameters measured in the previous section may be input to the RCWA simulation to predict angular sensitivity of the SVDOE. The predicted performance may then be compared with measured angular sensitivity to verify results from RCWA. This section will make such a comparison for the two- and three-layer SVDOE's examined in the previous section.

10.2.1 Two-layer prototype

Comparisons of predicted and measured angular sensitivity for the two-layer sample are seen in Figure 10.3, which is for TE polarization, and in Figure 10.4, which is for TM polarization. These comparisons correspond to the segment of the SVDOE seen in the SEM micrograph of Figure 10.1. The simulated performance assumes perfectly collimated light and vertical sidewalls on the grating ridges.

Visual examination of Figure 10.3 and Figure 10.4 shows excellent agreement between the simulated and measured curves. It is apparent from the graphs of the +1 order angular sensitivity for both polarizations that the peak diffraction efficiency does not occur at normal incidence as was desired. This angular shift is a result of the difference in the actual offset between the grating layers and the designed offset value. The peak value of the diffraction efficiency compared to the design value can be extrapolated from the difference in the measured structural parameters and the design parameters as well.

The rapid fluctuations present in the simulated curves of Figure 10.3 and Figure 10.4 are a valid representation of the SVDOE behavior rather than a computational artifact. In the discussion of SVDOE diffraction properties in Chapter 3 there is an illustration of the sensitivity of diffraction efficiency as a function of both grating strength (Figure 3.6 and Figure 3.7) and homogeneous layer thickness (Figure 3.11). For both cases the diffraction efficiency began to exhibit fluctuations that became more severe as the refractive index difference between grating ridges and grooves was increased from 0.1 to 0.5. For the two-layer SVDOE examined here, the actual refractive index difference is ~0.71 indicating that the fluctuations in the simulated curves are to be expected.

The fluctuations are not seen in the measured curves because the samples are taken at 0.5° increments rather than the 0.1° increments used in the simulation, thus de-emphasizing the fluctuations. The 0.5° increment on the measured data is a practical consideration based on equipment capabilities. The simulation is conducted at a 0.1° increment in order to obtain as much information as possible concerning SVDOE performance. The additional information is useful when comparing with measured data since the rotation stage which sets the incidence angle could cause a slight (<±0.1°) error in its position. For purposes of illustration, simulations corresponding to those in Figure 10.3 for TE polarization were performed at 0.5° increments. The comparison with measured data is shown in Figure 10.5.

The fluctuations are also minimized in the measured data because it is taken with a laser beam which has an inherent divergence angle rather than the collimated beam assumed for Figure 10.3 and Figure 10.4. The divergence angle in the beam implies that the measured data is averaged over the angular region, which effectively averages over the Fresnel reflections as well. Removing the assumption of collimated light by including the beam divergence measured in the laboratory results in the diffraction efficiency curves for TE polarization seen in Figure 10.6 and for TM polarization seen in Figure 10.7. The beam divergence was taken into account by averaging the calculated diffraction efficiency over seventeen equally spaced (0.025mrad) angles, representing the measured divergence of 0.4mrad centered about the specified incidence angle. Many of the fluctuations seen in previous diffraction efficiency curves are reduced here. This indicates, as has been discussed previously, that the diffraction efficiency is highly sensitive to Fresnel reflections between grating layers and that averaging over the beam divergence with different angles and, hence, reflections smoothes the system response.

Consider now the effect of removing the assumption of vertical sidewalls from the simulated diffraction efficiency. For example, apply slanted sidewalls to the grating using structural parameters that are, again, measured from the SEM micrographs. The angular sensitivity for TE polarization for this case is shown in Figure 10.8 and the corresponding comparison for TM polarization is shown in Figure 10.9. The gross response of the SVDOE to this change is minimal; the small peaks around -10° and -5° incidence angle are somewhat altered. This small effect due to slanted sidewalls is supported by previously published work [56], particularly for gratings that are designed for maximum diffraction efficiency. These curves assume collimated light. The effect of divergence can be included as before and the results are shown in Figure 10.10 for TE polarization and in Figure 10.11 for TM polarization.

The agreement between the measured and simulated data shown here was quantified by correlating the two data sets and normalizing the autocorrelation of the simulated data. The results for the two-layer prototype are shown in Table 10.3 for TE polarization and in Table 10.4 for TM polarization. This shows excellent agreement for this sample. It also confirms that including the slanted sidewalls has minimal effect, but that including the divergence does have some effect on the final result.

Table 10.3 Correlations for fabricated two-layer SVDOE for TE polarization

TE Polarization	**+1 Order**	**0 Order**	**-1 Order**
Rectangular sidewalls Collimated light	0.885002	0.849664	0.876534
Rectangular sidewalls Divergence	0.958812	0.895798	0.924256
Slanted sidewalls Collimated light	0.795348	0.852316	0.854458
Slanted sidewalls Divergence	0.89692	0.994356	0.928946

Table 10.4 Correlations for fabricated two-layer SVDOE for TM polarization

TM Polarization	**+1 Order**	**0 Order**	**-1 Order**
Rectangular sidewalls Collimated light	0.749611	0.978889	0.98865
Rectangular sidewalls Divergence	0.799954	1.03547	1.09774
Slanted sidewalls Collimated light	0.694805	0.91332	0.948291
Slanted sidewalls Divergence	0.796594	1.03034	1.09891

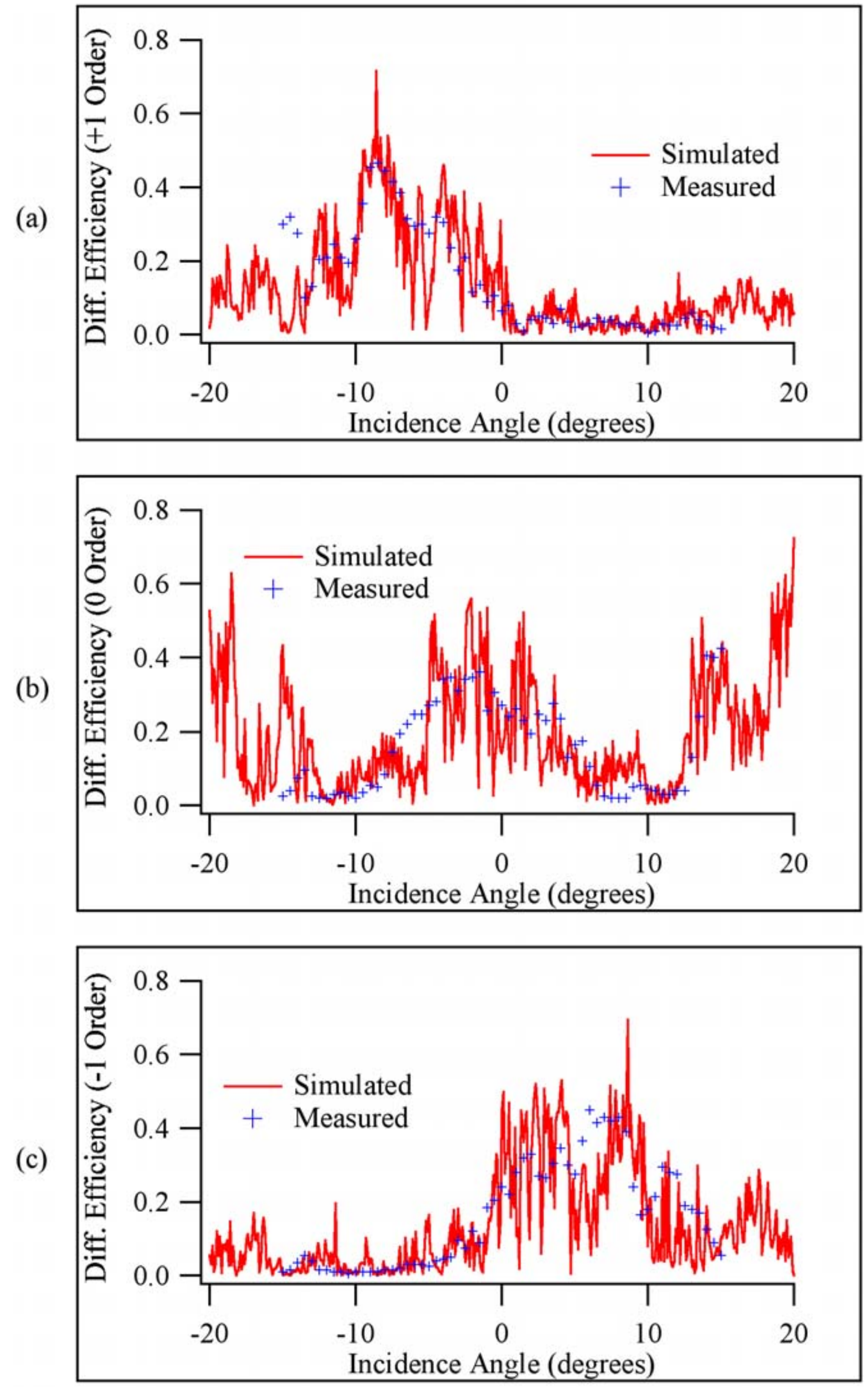

Figure 10.3 Comparison of measured and simulated angular sensitivity for (a) +1-order, (b) 0-order, and (c) –1-order for TE polarization for fabricated two-layer SVDOE. Assumes rectangular gratings and collimated readout beam.

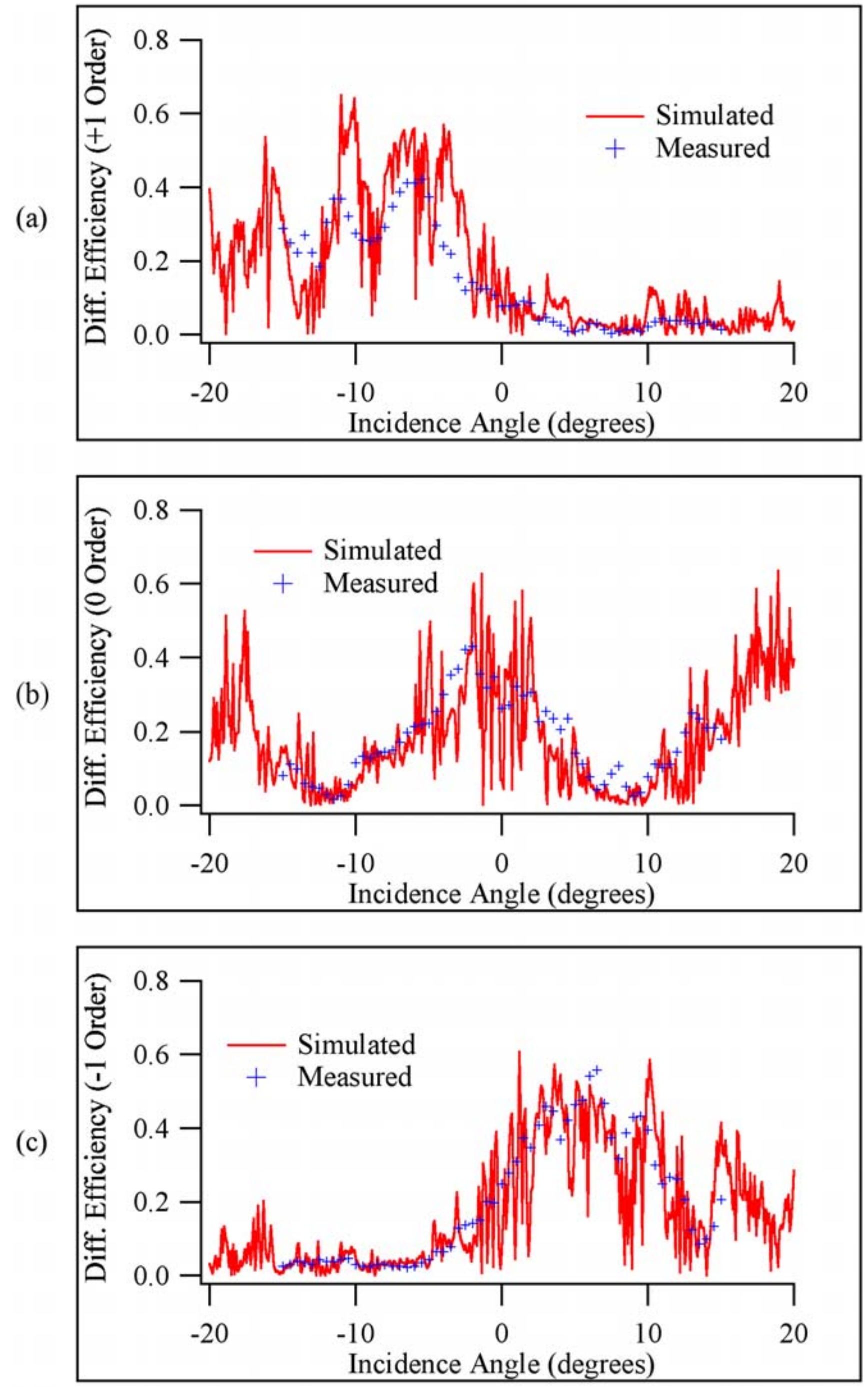

Figure 10.4 Comparison of measured and simulated angular sensitivity for (a) +1-order, (b) 0-order, and (c) –1-order for TM polarization for fabricated two-layer SVDOE. Assumes rectangular gratings and collimated readout beam.

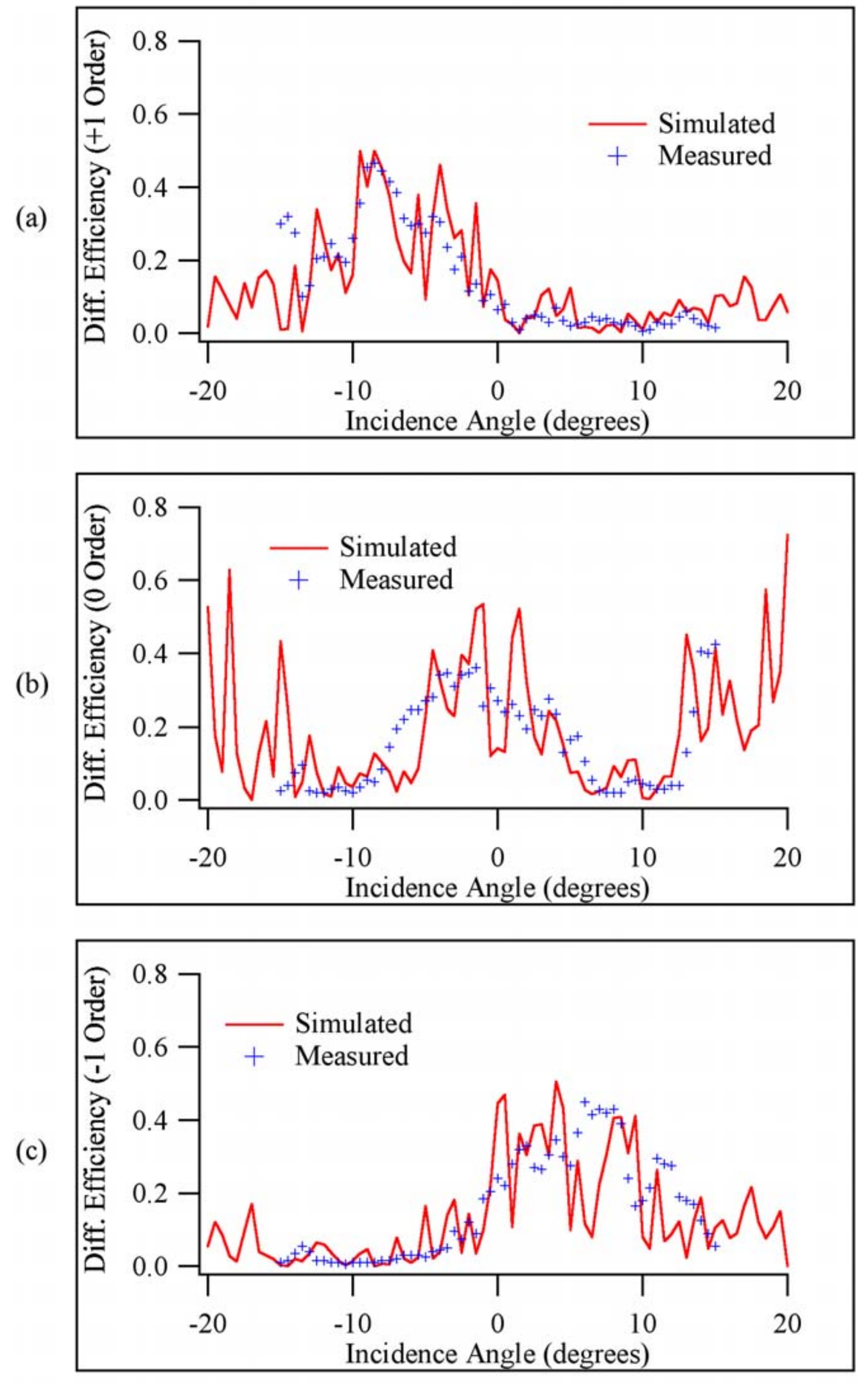

Figure 10.5 Comparison of measured and simulated angular sensitivity for (a) +1-order, (b) 0-order, and (c) –1-order for TE polarization for fabricated two-layer SVDOE. Assumes rectangular gratings and collimated readout beam. Simulated curves shown at 0.5º increments.

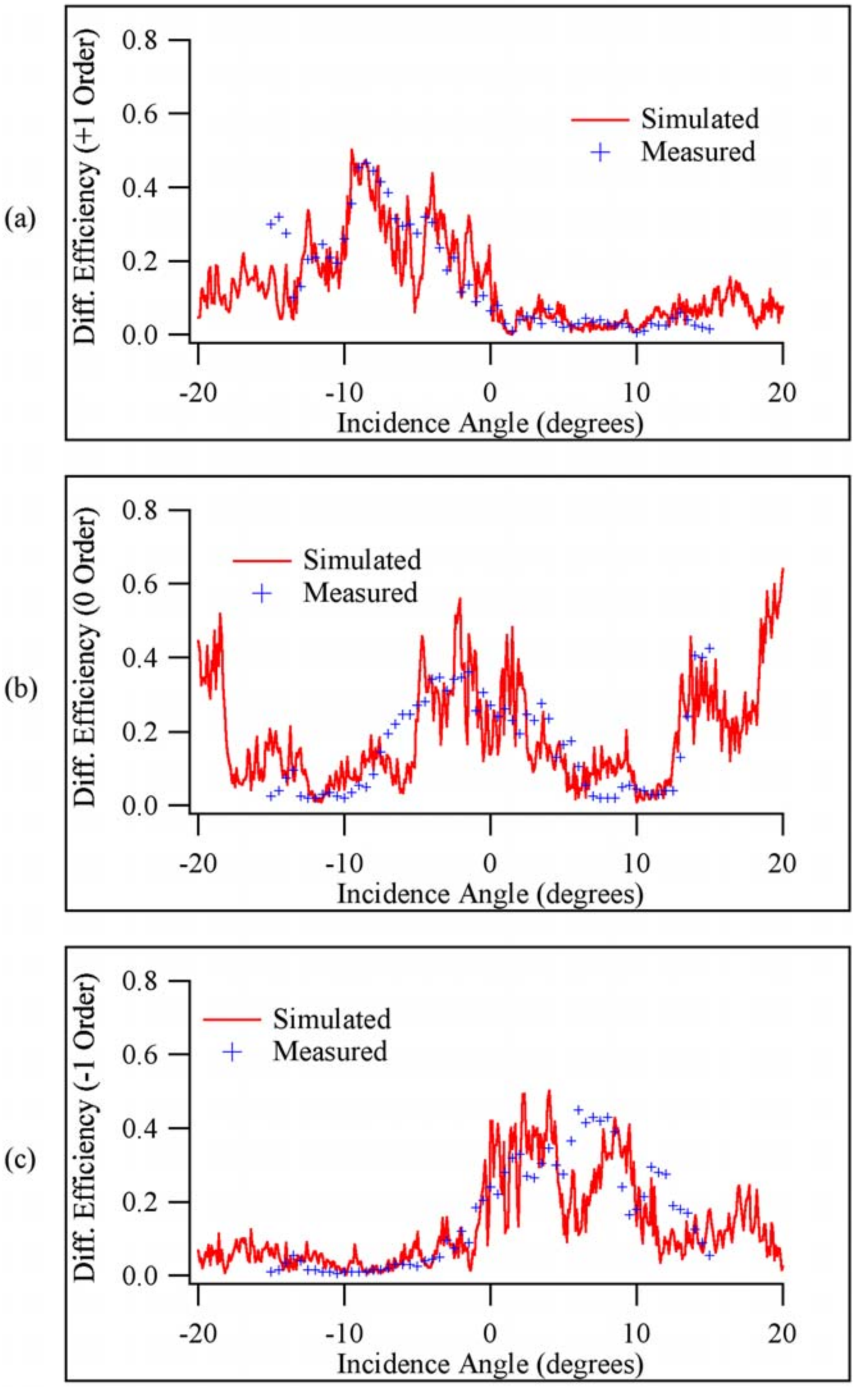

Figure 10.6 Comparison of measured and simulated angular sensitivity for (a) +1-order, (b) 0-order, and (c) –1-order for TE polarization for fabricated two-layer SVDOE. Assumes rectangular gratings; readout beam includes measured divergence.

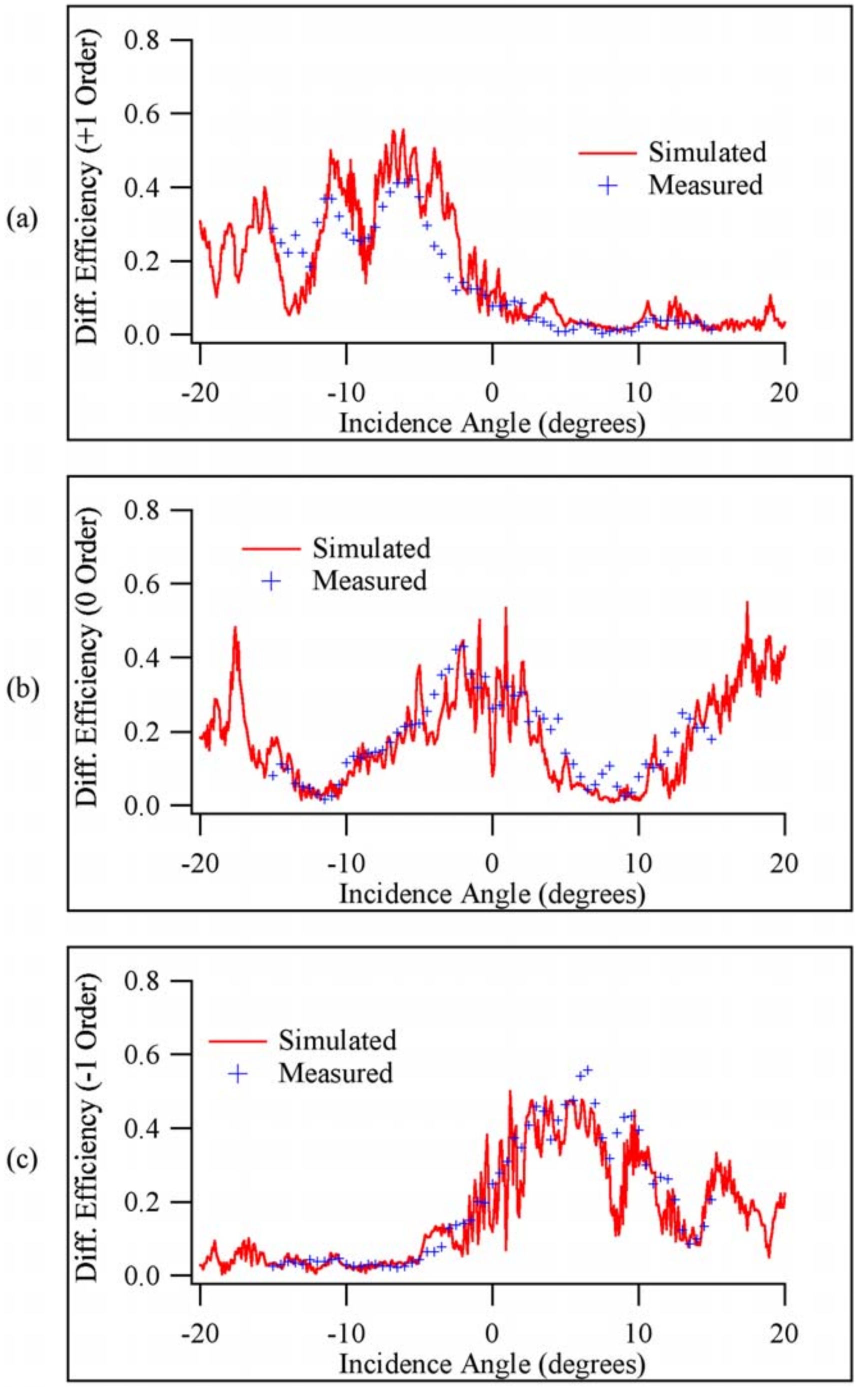

Figure 10.7 Comparison of measured and simulated angular sensitivity for (a) +1-order, (b) 0-order, and (c) –1-order for TM polarization for fabricated two-layer SVDOE. Assumes rectangular gratings; readout beam includes measured divergence.

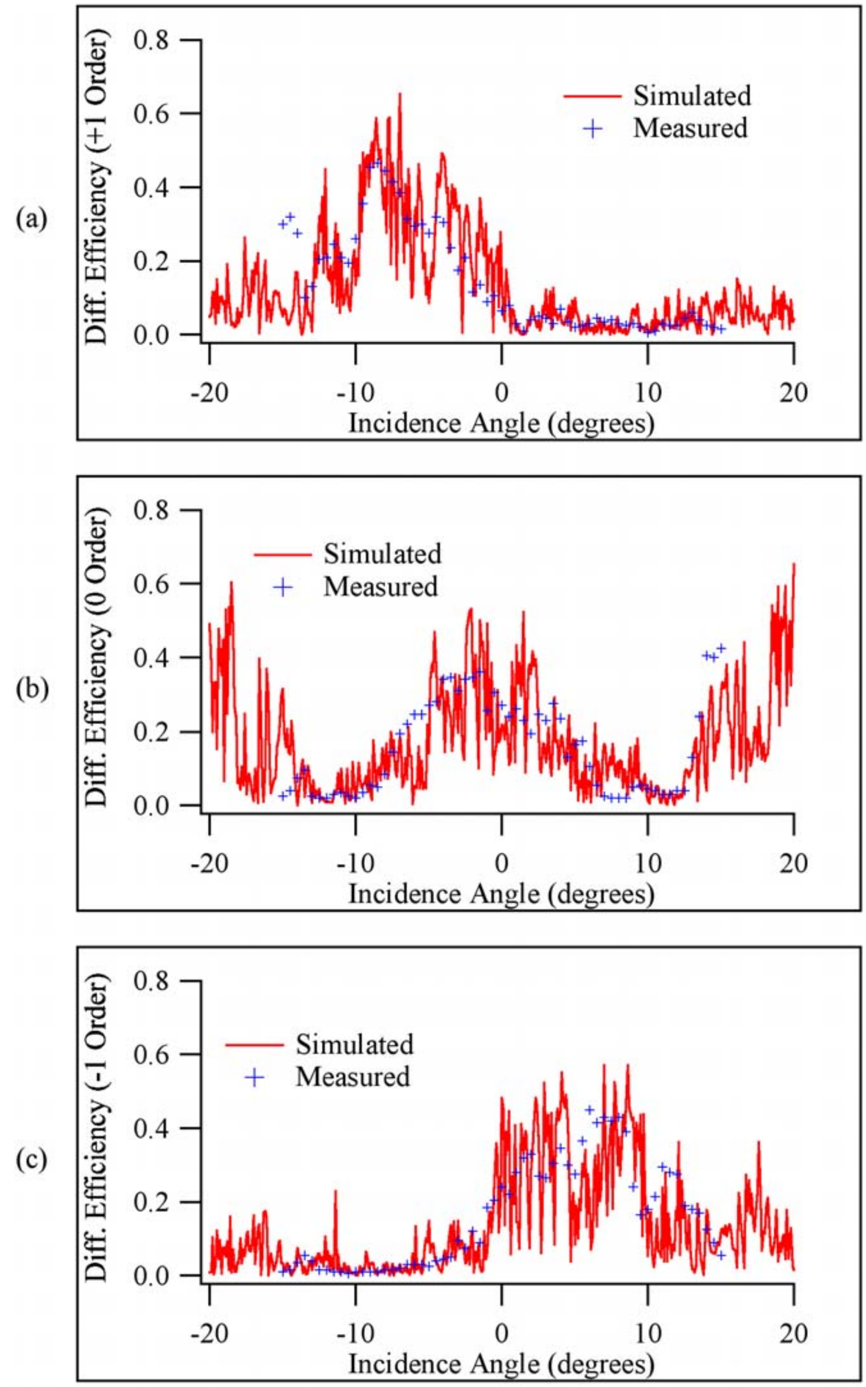

Figure 10.8 Comparison of measured and simulated angular sensitivity for (a) +1-order, (b) 0-order, and (c) –1-order for TE polarization for fabricated two-layer SVDOE. Assumes gratings with slanted sidewalls and collimated readout beam.

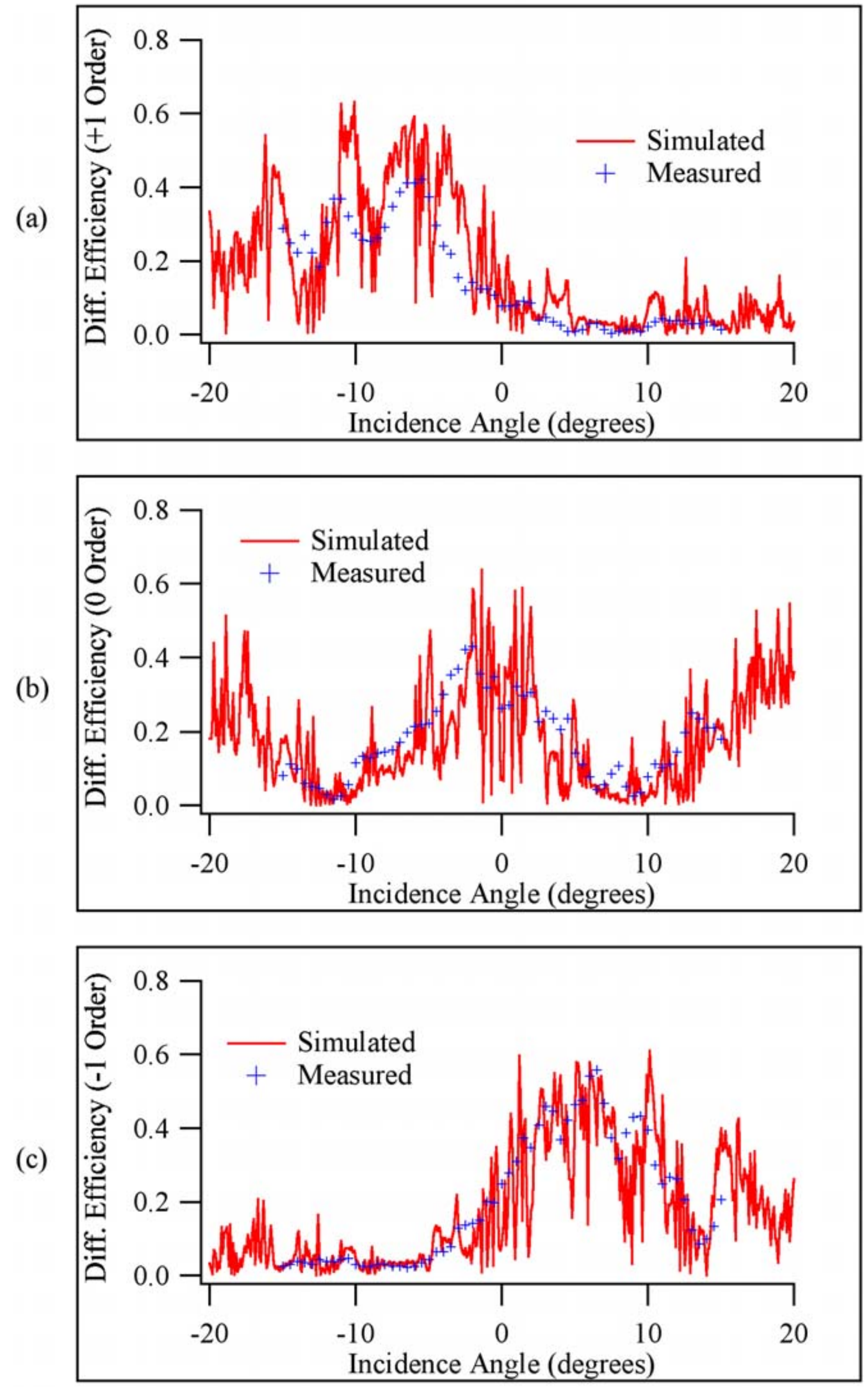

Figure 10.9 Comparison of measured and simulated angular sensitivity for (a) +1-order, (b) 0-order, and (c) –1-order for TM polarization for fabricated two-layer SVDOE. Assumes gratings with slanted sidewalls and collimated readout beam.

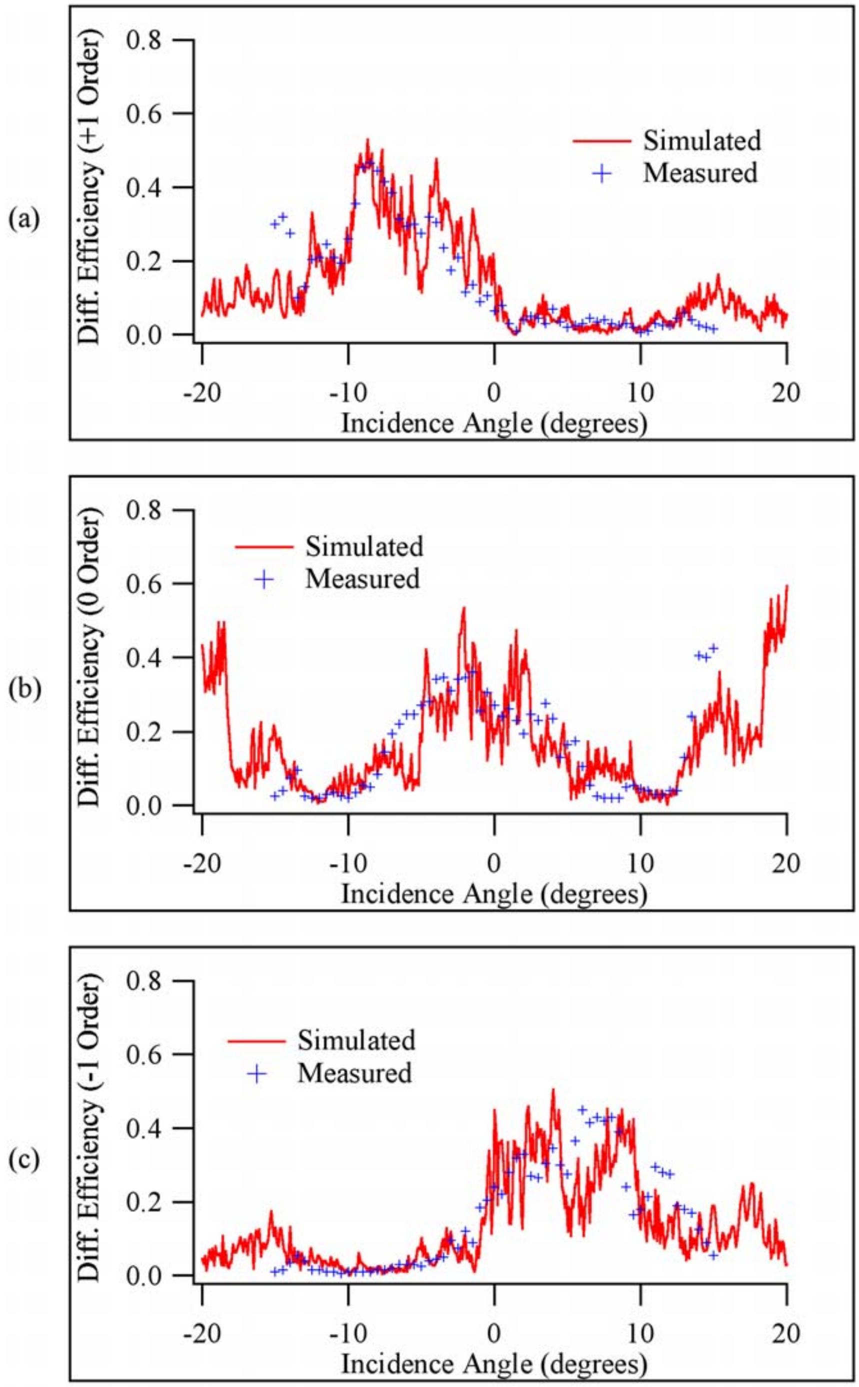

Figure 10.10 Comparison of measured and simulated angular sensitivity for (a) +1-order, (b) 0-order, and (c) –1-order for TE polarization for fabricated two-layer SVDOE. Assumes gratings with slanted sidewalls; readout beam includes measured divergence.

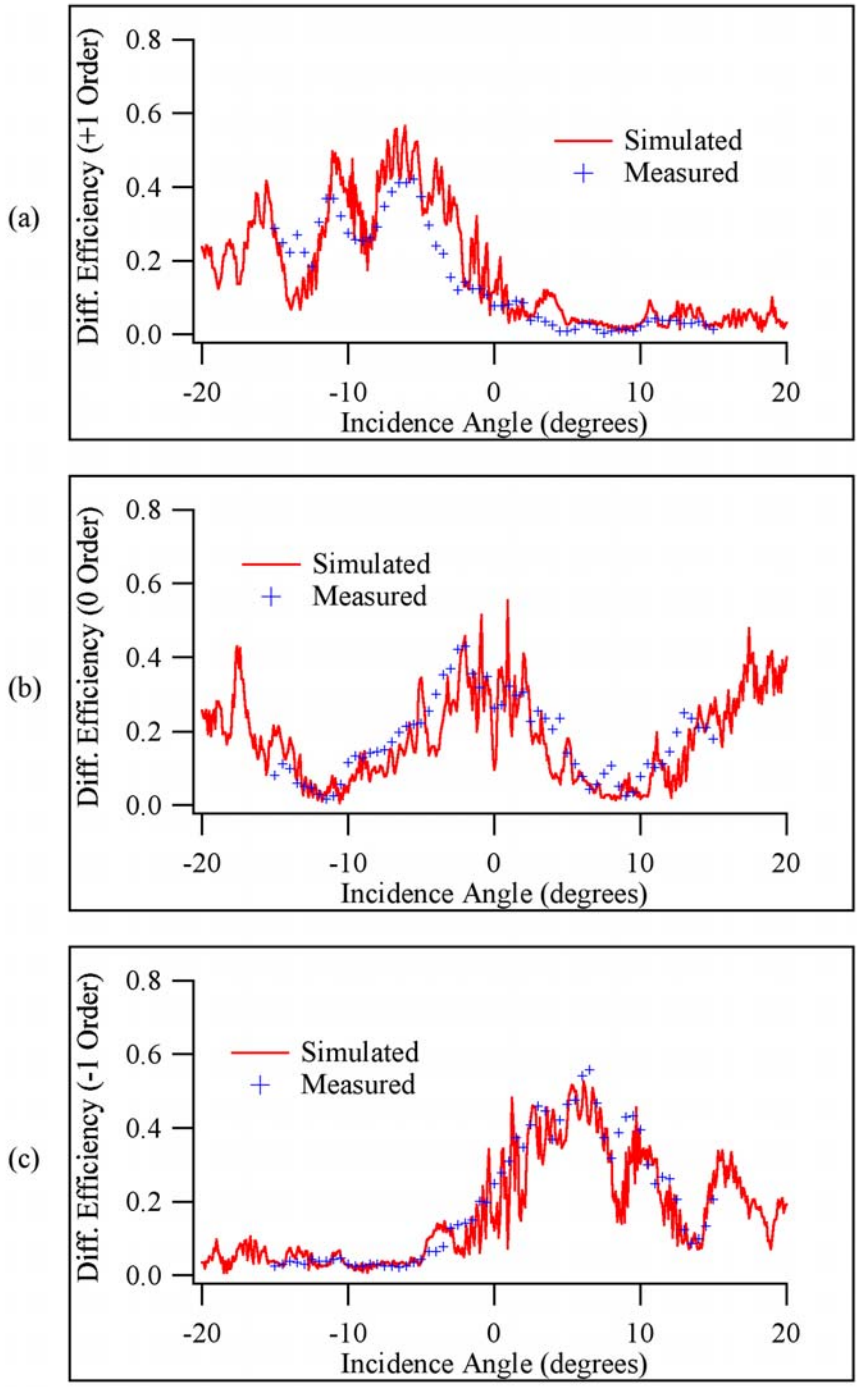

Figure 10.11 Comparison of measured and simulated angular sensitivity for (a) +1-order, (b) 0-order, and (c) –1-order for TM polarization for fabricated two-layer SVDOE. Assumes gratings with slanted sidewalls; readout beam includes measured divergence.

10.2.2 Three-layer prototype

Comparisons of simulated and measured angular sensitivity for the three-layer prototype seen in Figure 10.2 and described in Table 10.2, will be presented in this section. Figure 10.12 shows angular sensitivity for TE polarization while Figure 10.13 shows the same comparison for TM polarization. As before, these initial graphs assume a collimated input beam and vertical sidewalls for all gratings. Studies of removing these assumptions, similar to those done for the two-layer prototype, were also performed. When only the assumption of collimated light is removed, the results are shown in Figure 10.14 for TE polarization and in Figure 10.15 for TM polarization. Figure 10.16 and Figure 10.17 illustrate the effect of applying the grating sidewall shape measured from the micrographs for TE and TM polarization, respectively. As before, there is very little change in the angular sensitivity. The measured beam divergence was applied in Figure 10.18 and Figure 10.19 and, again, smoothing of the fluctuations is observed as a result of averaging over Fresnel reflections.

Visual examination of the graphs in Figure 10.12 and Figure 10.13 shows agreement between the simulated and measured curves, although not as close as for the two-layer prototype. The correlation data sets seen in Table 10.5 and Table 10.6 also reflect this. It is encouraging to note that the best agreement is observed around normal incidence for the −1 order, which is where peak diffraction efficiency is predicted based on the structural parameters. Angular position of peak diffraction efficiency is primarily due to the relative grating offsets.

Table 10.5 Correlation for fabricated three-layer SVDOE for TE polarization

TE Polarization	+1 Order	0 Order	-1 Order
Rectangular sidewalls Collimated light	0.654149	0.714142	0.798275
Rectangular sidewalls Divergence	0.657782	0.824431	0.825933
Slanted sidewalls Collimated light	0.617767	0.700951	0.816818
Slanted sidewalls Divergence	0.683683	0.748448	0.836524

Table 10.6 Correlation for fabricated three-layer SVDOE for TM polarization

TM Polarization	+1 Order	0 Order	-1 Order
Rectangular sidewalls Collimated light	0.538091	0.738675	0.851647
Rectangular sidewalls Divergence	0.551004	0.806055	0.916673
Slanted sidewalls Collimated light	0.487531	0.750539	0.850509
Slanted sidewalls Divergence	0.5552	0.794309	0.883005

While the stated goal for these SVDOE designs was to direct peak efficiency to normal incidence in the +1 order, the actual requirement for the lidar scanning element is to deflect a normally incident beam by 30° with high efficiency, regardless of order. Thus, this particular element would be acceptable in the final application.

A noticeable feature of the comparisons in Figure 10.12 and Figure 10.13 is the angular shift between measured and simulated data. Similar behavior has been observed for several of the fabricated two-layer samples. Possible causes for this shift include relative rotation between the grating layers, errors in structural parameter measurements resulting from micrograph calibration issues, and systematic measurement bias. The latter, experiment bias, was eliminated by verifying optical alignment of the measurement apparatus and re-evaluating procedures. Issues of SEM calibration were addressed by comparing measurements from two micrographs, each of the same structure, but at orthogonal orientations. These micrographs indicate a 5% difference in measurements taken in the horizontal direction compared to those taken in the vertical direction. A 5% error in the most critical parameter measurement influencing angular shift, relative grating offset, would cause only a ~0.5° shift in Figure 10.12 and Figure 10.13.

The remaining deviations in the angular sensitivity comparisons are most likely a result of relative rotation between the grating layers. The current implementation of the alignment scheme relies on probing the SVDOE at a single point near the edge of the grating region while the substrate grating(s) are translated with respect to the mask grating to achieve offset. Any deviation from pure translation due to mechanical causes of any rotation imparted during initial, visual alignment could manifest as rotation in the fabricated device. The alignment process also requires that the mask and substrate be separated during translation then returned to contact for exposure. This creates additional opportunities for rotation to be introduced.

To consider the effect of rotation on SVDOE performance, a scenario where there is one grating period of rotation across the clear aperture of the grating region will be considered. This corresponds to 4μm of change in the relative grating offset over a 5cm diameter. The beam of the 2μm laser, which is 4mm in diameter, could then encounter as much as 0.30μm of relative offset change across the area being tested. The design values for offset in the three-layer prototype examined here are 0.780μm and 1.561μm for the second and third layers, respectively. A change of 0.3μm in pure translation from these values would result in at least a 3° shift in angular sensitivity. However, the issue here is rotation, not pure translation, which is much more difficult to assess. It would certainly result in a shift of the angular sensitivity, but its particular manifestation would depend on the exact structural parameters. Simulation of this effect is beyond the scope of the work described here.

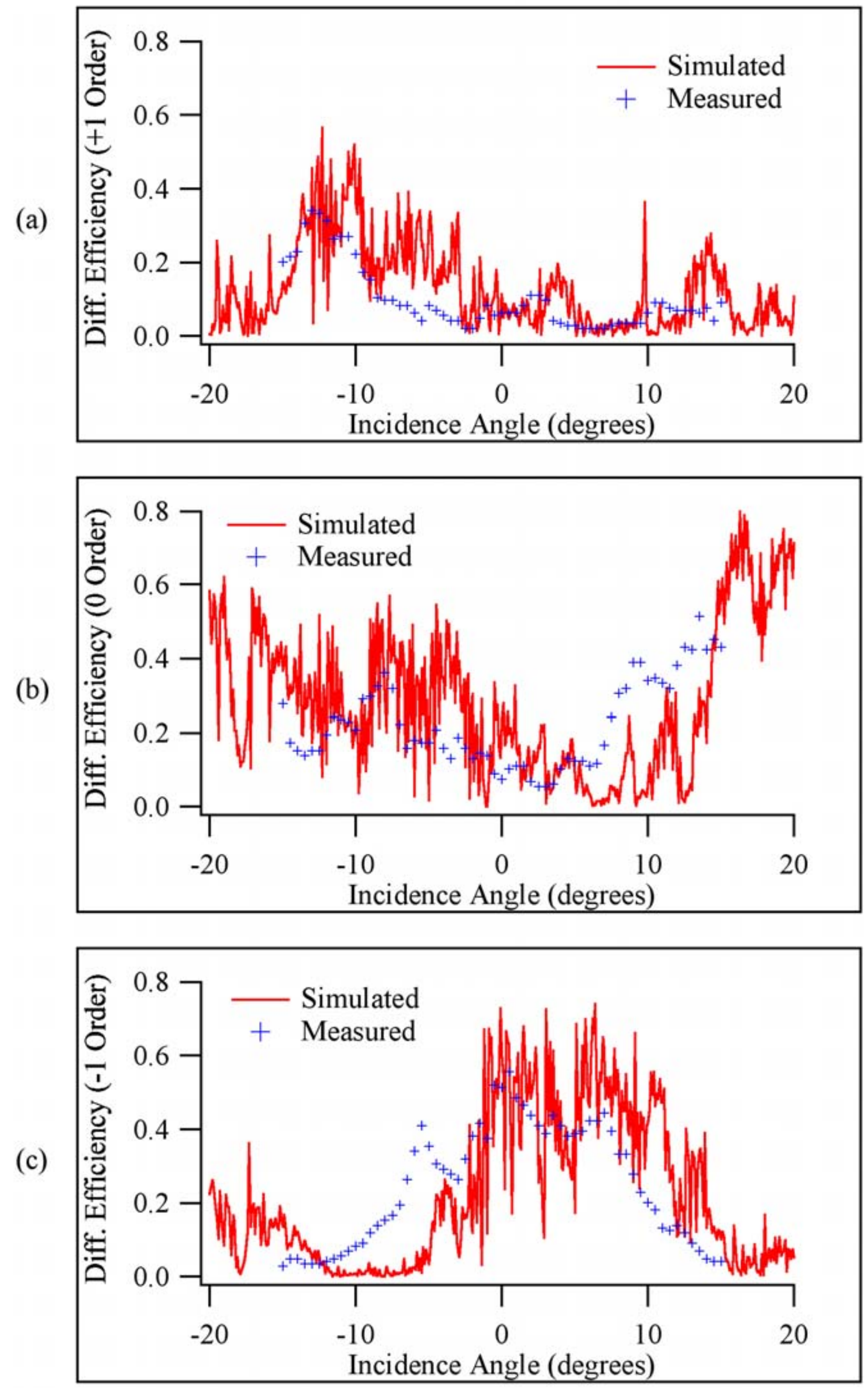

Figure 10.12 Comparison of measured and simulated angular sensitivity for (a) +1-order, (b) 0-order, and (c) –1-order for TE polarization for fabricated three-layer SVDOE. Assumes rectangular gratings and a collimated readout beam.

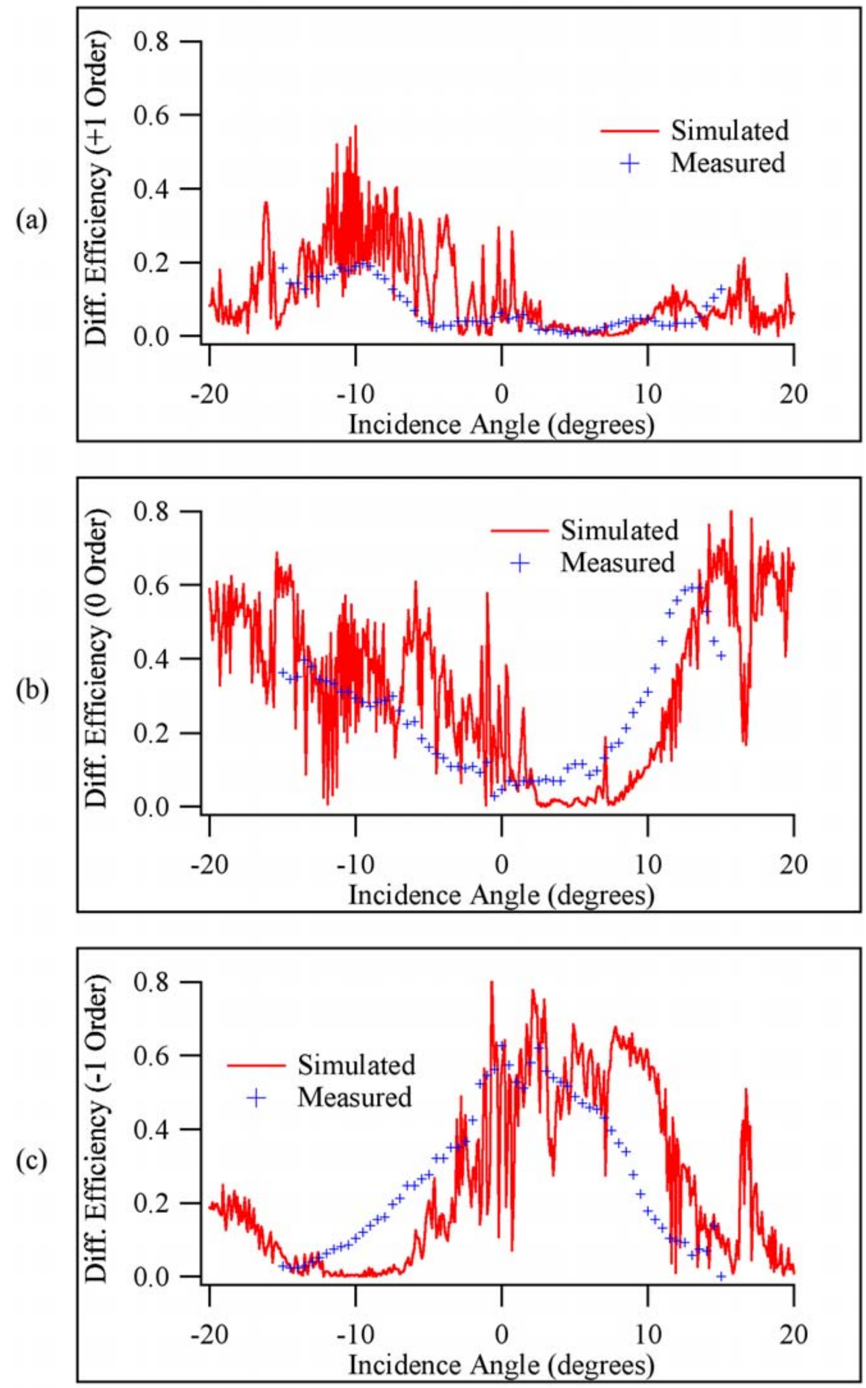

Figure 10.13 Comparison of measured and simulated angular sensitivity for (a) +1-order, (b) 0-order, and (c) –1-order for TM polarization for fabricated three-layer SVDOE. Assumes rectangular gratings and a collimated readout beam.

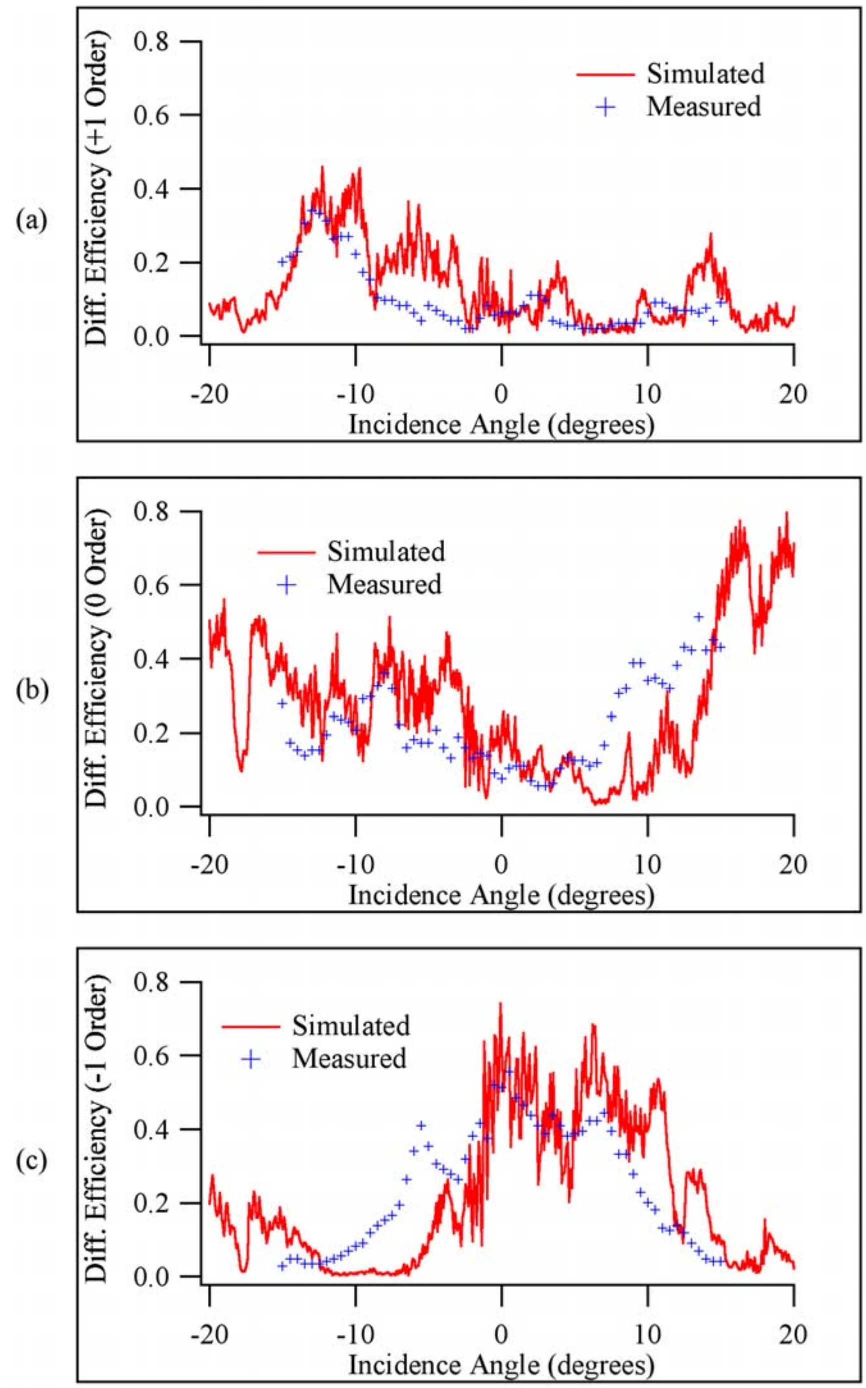

Figure 10.14 Comparison of measured and simulated angular sensitivity for (a) +1-order, (b) 0-order, and (c) –1-order for TE polarization for fabricated three-layer SVDOE. Assumes rectangular gratings; readout beam includes measured divergence.

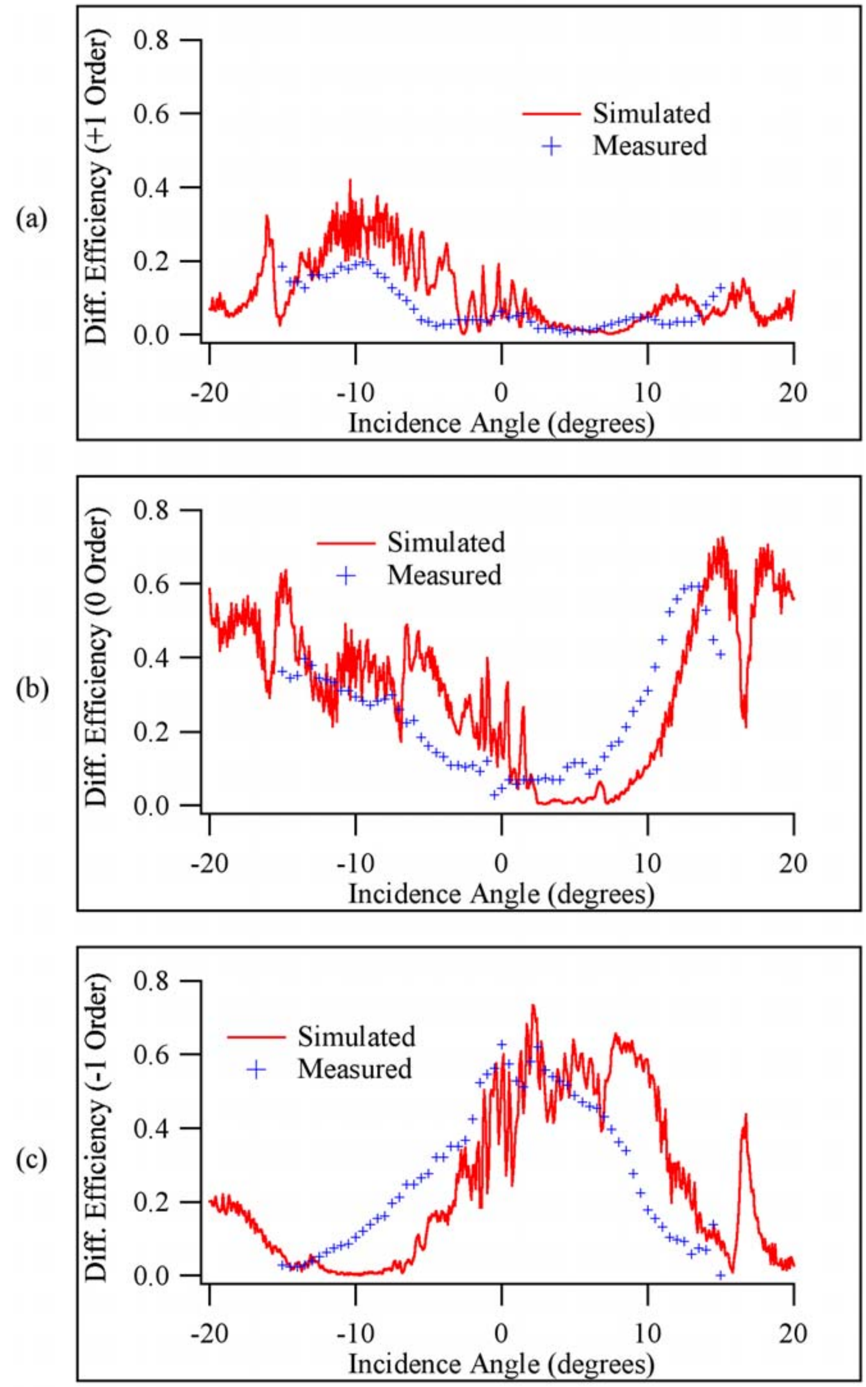

Figure 10.15 Comparison of measured and simulated angular sensitivity for (a) +1-order, (b) 0-order, and (c) –1-order for TM polarization for fabricated three-layer SVDOE. Assumes rectangular gratings; readout beam includes measured divergence.

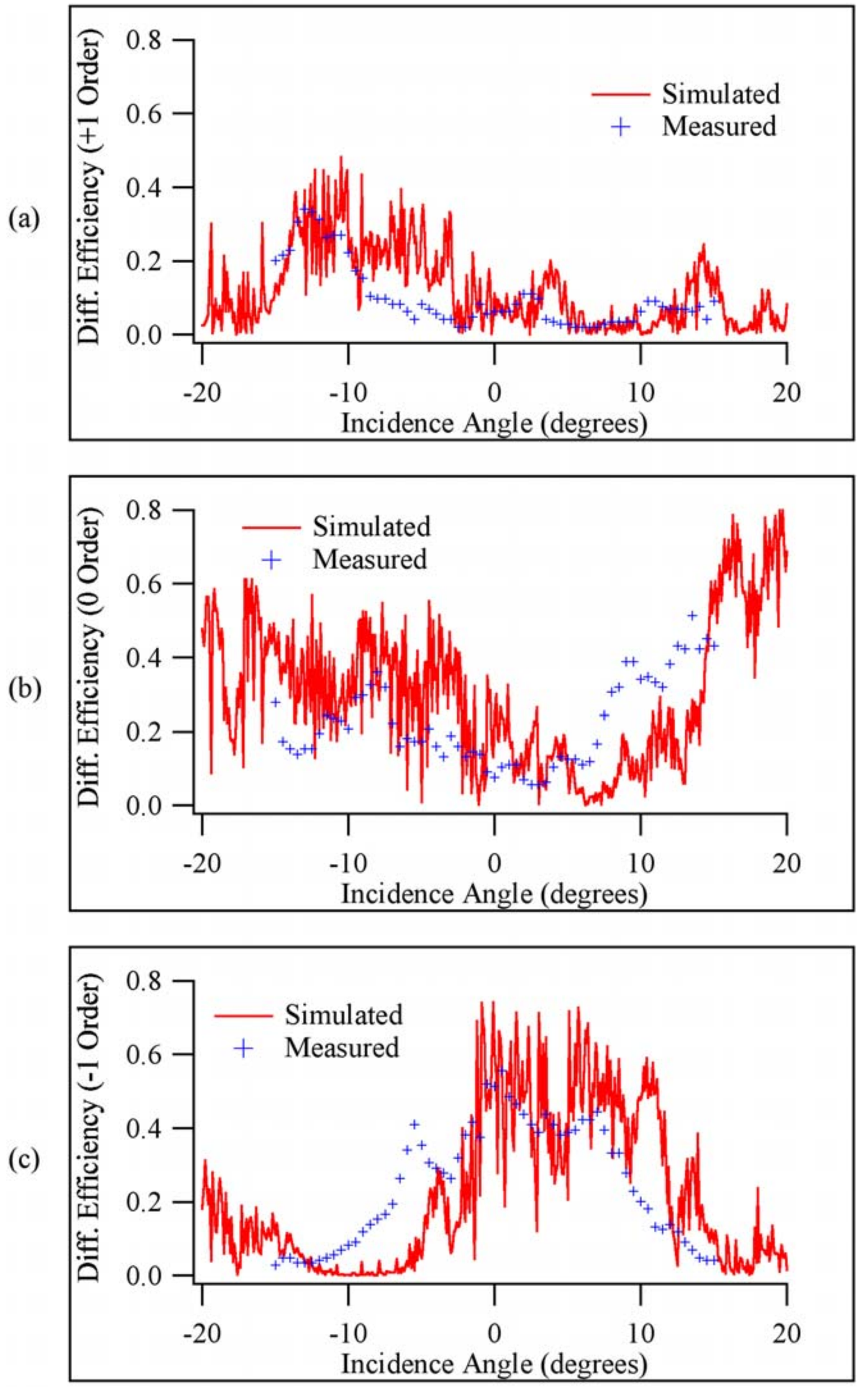

Figure 10.16 Comparison of measured and simulated angular sensitivity for (a) +1-order, (b) 0-order, and (c) –1-order for TE polarization for fabricated three-layer SVDOE. Assumes slanted sidewalls and collimated readout beam.

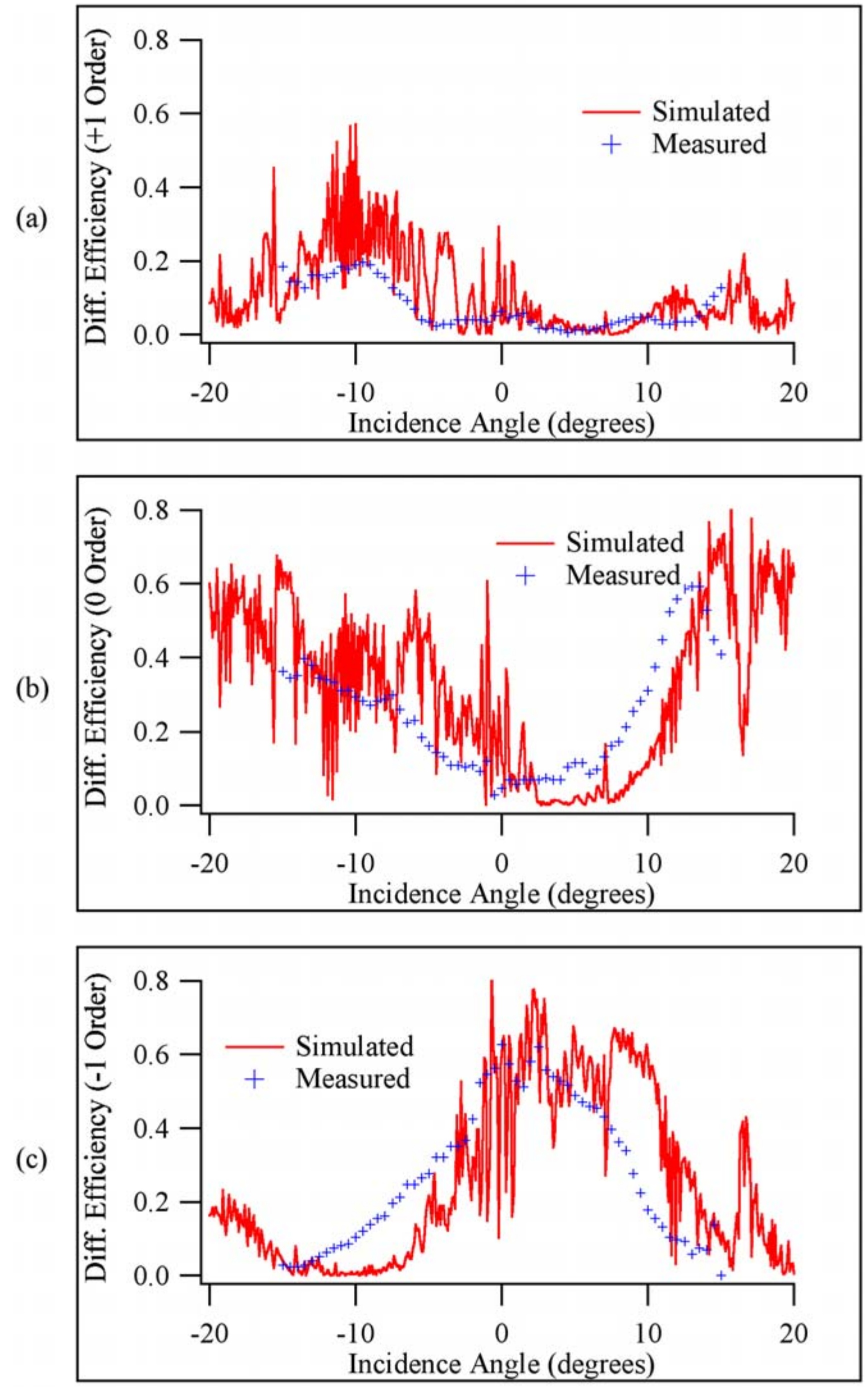

Figure 10.17 Comparison of measured and simulated angular sensitivity for (a) +1-order, (b) 0-order, and (c) –1-order for TM polarization for fabricated three-layer SVDOE. Assumes slanted sidewalls and collimated readout beam.

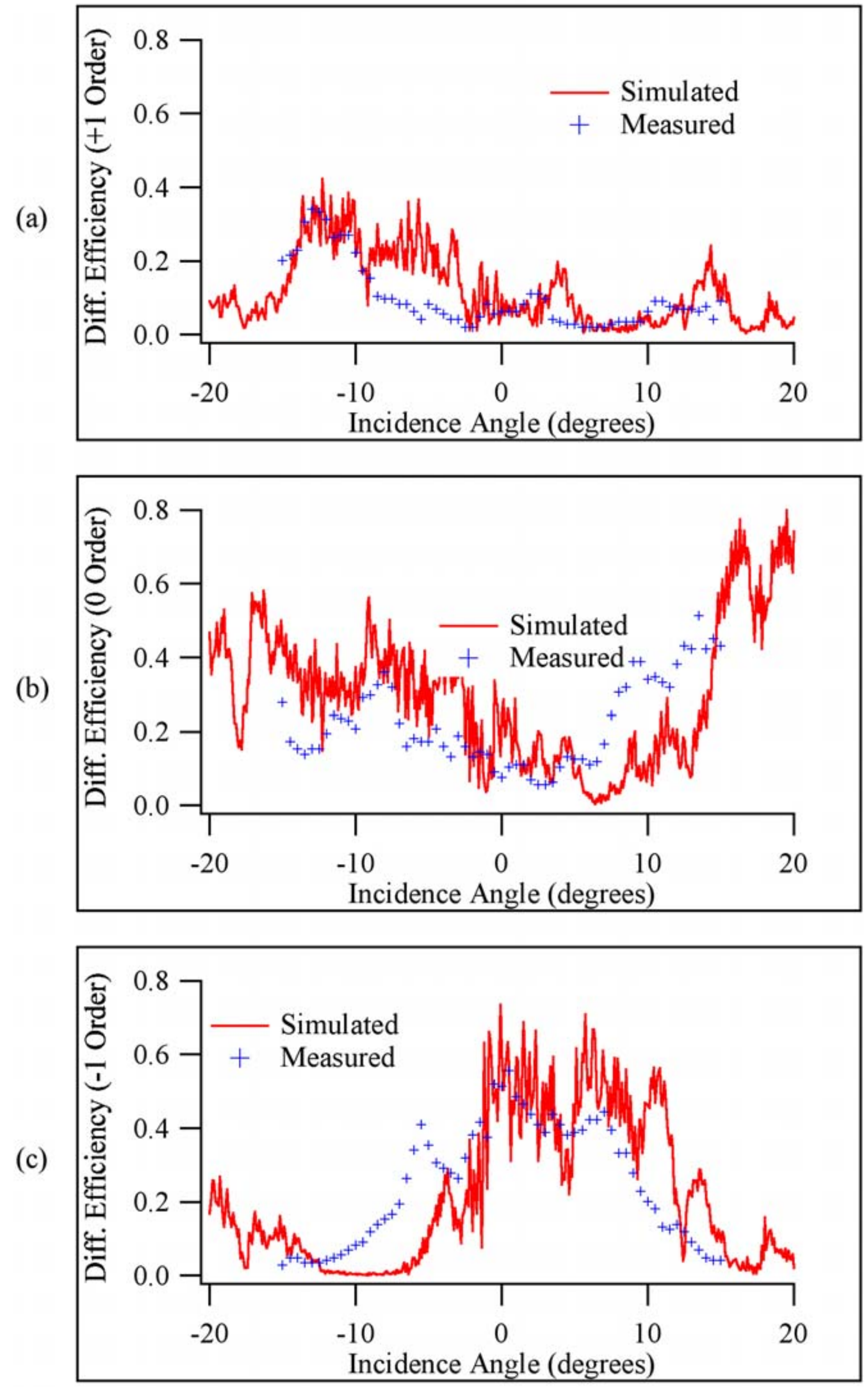

Figure 10.18 Comparison of measured and simulated angular sensitivity for (a) +1-order, (b) 0-order, and (c) –1-order for TE polarization for fabricated three-layer SVDOE. Assumes slanted sidewalls; readout beam includes measured divergence.

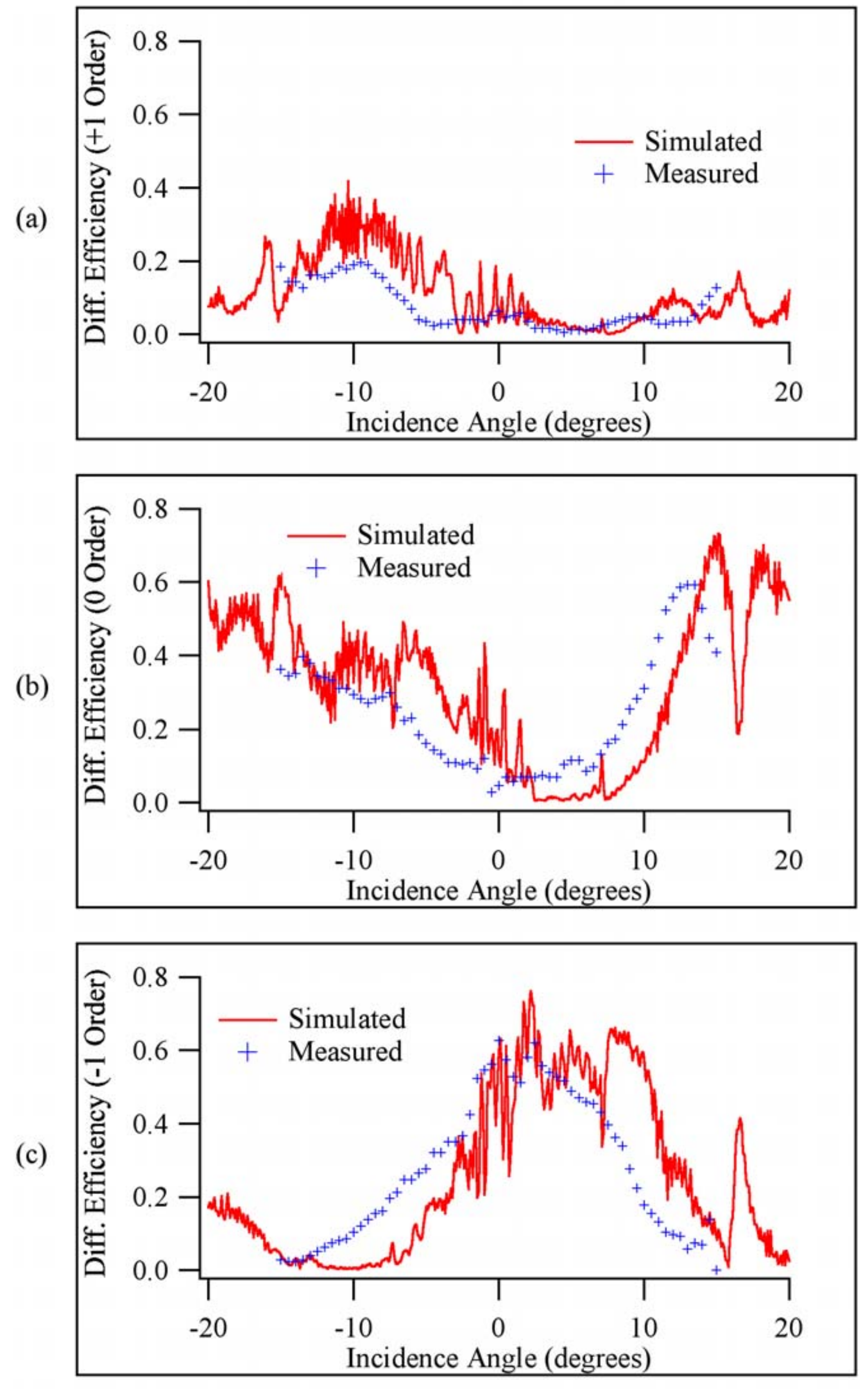

Figure 10.19 Comparison of measured and simulated angular sensitivity for (a) +1-order, (b) 0-order, and (c) –1-order for TM polarization for fabricated three-layer SVDOE. Assumes slanted sidewalls; readout beam includes measured divergence.

10.3 Alignments

The remaining evaluation to be made on a fabricated SVDOE is alignment assessment. The two aspects of this evaluation are comparison with design values and comparison across the grating region, e.g., rotation. This is done by examining several spots in the grating region. The offset values are calculated as described in Section 8.2.

10.3.1 Two-layer prototype

The same two-layer sample that has been discussed in previous sections will be used again here to illustrate alignment. For this particular sample there are alignment measurements at three points in the grating region; one slightly below the center, a second in the same horizontal plane at approximately the midpoint between the center and the edge, and a third in the vertical plane of the first spot but at the edge of the region. This last spot is within the area that is used in the alignment process.

The location of the measurement points and their corresponding grating offset values are shown in Figure 10.20. The two measurements in the horizontal direction agree within 0.02µm while the third measurement is different by approximately 0.30µm. This indicates that, while there is some amount of rotation present in the sample, it is not as severe as the example discussed previously. The fact that the magnitude of the measured rotation is small is consistent with the excellent agreement between simulated and measured angular sensitivity presented in the previous section.

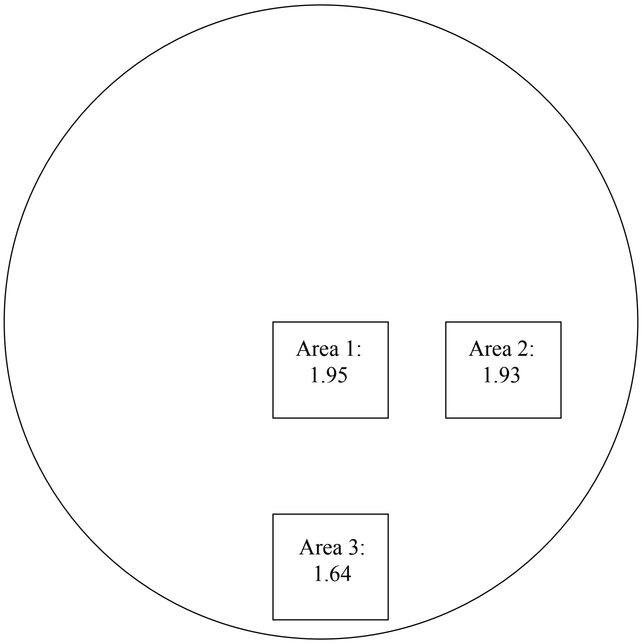

Figure 10.20 Diagram illustrating measured alignment offsets for fabricated two-layer SVDOE which are mapped into their position on the wafer.

10.3.2 Three-layer prototype

Measurement locations and corresponding grating offsets for the three-layer sample are shown in Figure 10.21. The bottom number in this figure is the offset between the first and second grating layers and the top number is the offset between the first and third grating layers. Examination of these values provides some insight into the differences between simulated and measured angular sensitivity for this sample. In particular, consideration of the offset values for the three points across the top of the region (Areas 1, 2, 3) shows that they are not consistent along that horizontal plane. Similarly, the offset values for the three vertical regions (Areas 2, 4, 5) are not consistent. Moreover, the degree of rotation is different for the second and the third grating layers. Applying specific values to these offset differences shows that the maximum difference for the second layer is 1.04μm, or 30% greater than the design value, and for the third layer is 2.08µm, or 25% greater than the design value. The fact that there is significant rotation present in this sample and that it is not consistent among the layers may account for much of the difference observed in the angular sensitivity comparisons for this sample.

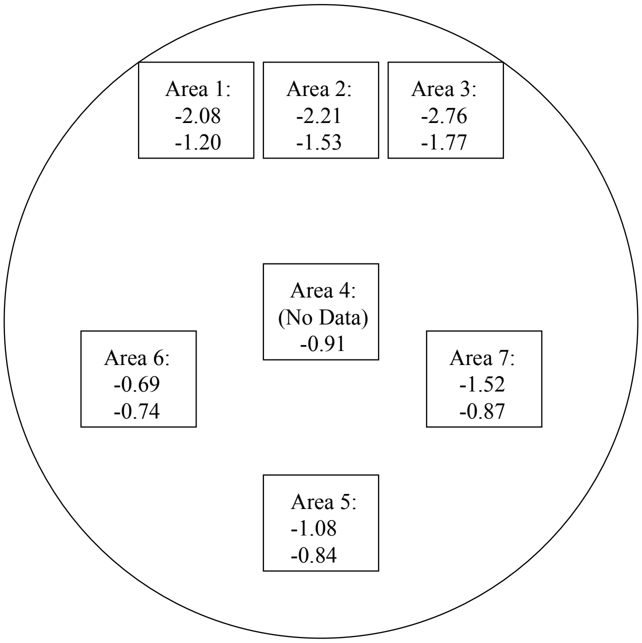

Figure 10.21 Diagram illustrating measured alignment offsets for fabricated three-layer SVDOE which are mapped into their position on the wafer. Bottom number is offset between first and second grating layers and top number is offset between first and third grating layers.

Chapter 11

DISCUSSIONS AND CONCLUSIONS

The previous chapters in this dissertation have provided detailed discussion of the theory, fabrication, and evaluation of SVDOE's. In this chapter those topics will be reviewed and summarized and the significance of the work within the fields of diffraction gratings and diffractive optics will be discussed. Issues identified throughout the course of this work will also be presented. Finally, recommendations for extension of the work and conclusions about the feasibility of SVDOE's as practical elements will be given.

11.1 Summary of accomplishments

Stratified volume diffractive optical elements have been proposed as a new class of high efficiency gratings for applications with requirements that are not suited to traditional volume holographic or diffractive optic techniques. The limitations of holographic gratings are typically related to materials issues such as refractive index difference at a given wavelength or degradation resulting from environmental exposure. Conversely, limitations of diffractive optic gratings are typically fabrication issues such as achieving the required minimum feature size, e.g., deep submicron, or aligning submicron features accurately. In SVDOE's the strengths of each method are exploited by using diffractive optic fabrication techniques to produce a structure which mimics the fringes in a volume holographic grating. The diffractive optic fabrication permits use of a wide range of materials while the fringe replication implies rectangular, binary gratings with 50% fill factor.

The interleaved grating layer and homogeneous layer structure of SVDOE's imparts unique diffraction properties to the elements. Physically, the stratifications separate the actions of modulation and diffraction of the incoming wavefront through the use of the binary gratings and the homogeneous layers, respectively. The separation of the two functions causes the diffractive properties of SVDOE's to be a sensitive function of individual layer thickness. This is manifested as periodic diffraction efficiency with changing layer thickness and fluctuations of the efficiency due to Fresnel reflections.

A rigorous electromagnetic simulation has been developed to model the behavior of this new type of diffractive optical element. The simulation uses RCWA with extensions included to accommodate homogeneous and grating layers of arbitrary number and order. Rigorous methods are required here since the constituent feature sizes are on the order of the wavelength of interest. While the simulation was developed for application to SVDOE's, it retained a general functionality for two-dimensional periodic structures and has been used to either design or verify several other diffractive elements [57], [58], [59], [60].

A systematic design process has been developed to obtain an optimal set of structural parameters for an SVDOE to meet the requirements of specific applications. Proceeding from the operational requirements of the application and a selection of materials for the device, the maximum modulation thickness is calculated using expressions derived from volume holographic theory. That thickness can be combined with the operational requirements as input to the RCWA simulation. A parametric set of designs is then established for the SVDOE. Design sets include structural parameters, performance predictions, and statistics of performance as a function of structural parameters to be used for establishing fabrication tolerances. Performance requirements are then applied to determine which design(s) from among the set should proceed to fabrication.

For this project, the design process has been applied to the development of a grating to be used as a lidar scanning element. The parametric designs indicated that an SVDOE with three grating layers could provide a peak diffraction efficiency sufficient to warrant consideration of an SVDOE scanning element as a replacement to the existing wedge scanner. To achieve full performance requirements an SVDOE with five or six grating layers would be needed. A three-layer SVDOE design was chosen as the fabrication goal for this work based on its potential performance. At the same time, a three-layer element demonstrates the fabrication techniques of interleaving grating and homogeneous layers and aligning the grating layers to construct an SVDOE. Addition of more grating layers is a straightforward extension of these techniques.

The multi-layer structure of SVDOE's required development of unique fabrication processes. In particular, a planarizing homogeneous layer embedded within an element is not common in diffractive optics. Typical techniques for over-coating a grating result in a conformal film, which would require chemical mechanical polishing to achieve a planar surface. Identification of the photopolymer SU-8, which would not only planarize by spin-coating and heat curing but would also withstand subsequent chemical processing, was a critical step. However, arriving at processing steps for SU-8 that minimized both film stress and defects and provided consistent film thickness required substantial effort.

The parametric designs for the lidar scanning element indicated that alignment between grating layers would be the most challenging fabrication step. Typical tolerances on visual alignment with a mask aligner are in the range of one micron. The SVDOE designs considered here required relative alignments between grating layers of less than one micron with tolerances of approximately 0.1 micron. In order to achieve these tolerances, a high precision alignment concept based on the concept of double diffraction was developed. It was implemented by transmitting a laser beam through both the substrate and mask and detecting the diffracted intensity as they are translated with respect to each other. Comparing the diffracted intensity pattern detected during alignment to a simulated pattern from RCWA permits alignment to the necessary tolerances.

Initial fabrication efforts for SVDOE's concentrated on elements with two grating layers. In this phase, fabrication processes for all layers within the structure were developed. This included deposition and patterning of grating layers, deposition of homogeneous layers, incorporating an etch barrier to protect the homogeneous layers, and grating alignment. A few difficulties in consistency of the alignment became apparent at this time. These can be attributed to tooling in the alignment apparatus and the mask aligner.

Fabrication continued for SVDOE's with the addition of a third grating layer. Once again, alignment proved to be somewhat problematic. Nonetheless, a three-layer SVDOE was successfully produced.

Evaluations of the two- and three-layer SVDOE's proved very satisfactory. Angular sensitivity measured from the fabricated elements agreed very well with RCWA simulations conducted using structural parameters measured from SEM micrographs. The micrographs revealed grating structures which clearly approached the design values. Measurements of grating offsets confirmed some issues with alignment. These issues of alignment are most likely responsible for any differences between measured and simulated angular sensitivity.

11.2 Significance of the work

The work described here has significance to both diffraction gratings and diffractive optics. At the highest level, SVDOE's represent a new type of grating that addresses a class of applications which might not be suitable for traditional grating types. Options for material selection and tuning the preferred incidence angle while maintaining high efficiency provide great flexibility in meeting design requirements. Also, the SVDOE designs studied here are relatively insensitive to input polarization, which is in contrast with traditional grating designs. While many high efficiency gratings are used simultaneously as polarizing elements, there are applications where high efficiency is desired in all polarizations [61], [62].

The benefits of SVDOE's to diffractive optics are primarily in fabrication. Immediately apparent are the unique use of homogeneous layers and the development of a high-precision alignment technique. Both approaches could be applied to numerous other devices and applications. Less obvious contributions are the fact that relatively coarse features have been combined to create a high-efficiency device and that the fabrication is scalable to large grating areas. These two aspects are intimately related and provided much of the impetus for developing SVDOE's.

Traditional high efficiency surface relief gratings typically require either submicron features or micron-scale features with a high aspect ratio. Fabrication of submicron features can be limited by size and alignment issues for lithographic processes or by practical grating area for direct-write methods (~1cm). Features with high aspect ratio, e.g., ratio of depth to width, can be difficult to fabricate with the straight sidewall profile desired. In SVDOE's the features are micron-scale and the aspect ratio is approximately one, both of which are very favorable to scaling to large areas through lithographic processes. In this work the fabricated grating area was 5cm in diameter compared to the 1cm diameter which is commonly used.

11.3 Remaining issues

The remaining issues in this study of SVDOE's reside in obtaining grating offset alignments that are both repeatable within the required tolerance ad consistent across the grating region. The repeatability is an issue of translational bias and consistency is an issue of rotation. These issues can be addressed through improved tooling on the mask aligner in tandem with improved implementation of the high-precision alignment scheme. Errors in registration between grating layers within an SVDOE has been identified as the most likely cause of discrepancies between their measured and simulated performance.

11.3.1 Mask aligner tooling improvements

Recall in the grating layer alignment scheme that there is translation in two directions and that the tolerance on alignment is too small to be detected visually. Coarse alignment is conducted using alignment marks on the mask and substrate which are viewed through video microscopes. The substrate is then translated vertically (negative z-direction) to obtain a separation distance with the mask to enable free movement between them. The alignment process is very sensitive to this distance. The substrate is translated horizontally (x-direction) to achieve offset alignment. Finally, the substrate is translated vertically again (positive z-direction) to obtain contact between the mask and substrate for exposure. Instability during any of these translations will potentially degrade alignment.

There are two approaches for addressing the alignment error, namely improving the original tooling on the mask aligner and improving implementation of the high-precision alignment scheme. For the mask aligner tooling the areas requiring attention are the vertical and horizontal translation. A submicron mechanical instability in either motion would be sufficient to introduce significant error into the alignment. A systematic bias could be accommodated, but efforts to identify such a bias via a series of SVDOE's with increasing offset alignments have not been successful. Conversations with the mask aligner designer/manufacturer have identified possible sources of mechanical error and efforts are on-going to detect these problems and correct them if necessary.

Another item associated with mask aligner tooling which warrants discussion is calibration of vertical translation. The signal detected during alignment is the only source of registering the two gratings, but it is very sensitive to the separation distance. While the translation stage is scaled, it is unclear whether the absolute motion is adequately calibrated to the scale. The separation distance is verified during alignment by comparing a series of signal traces at increasing distances with simulations and verifying the features of the signals. A calibration scheme would prove beneficial as a backup to determining the distance empirically from signal traces.

11.3.2 Alignment scheme improvements

The implementation of the alignment scheme could be modified to mitigate registration errors between the gratings as well. The current scheme relies on data collected from a single point at the very edge of the grating region to perform alignment over the entire region. Introducing additional data collection points within the current scheme and requiring correlation between them has potential to reduce registration errors, particularly rotation. An alignment scheme employing alternative alignment marks could also be considered. The microelectronics industry has thoroughly addressed the issue of alignment to very tight tolerances as the size of electronics has continued to diminish. Several schemes have been both proposed and implemented to achieve alignment tolerances as small as fractions of a nanometer [63], [64], [65], [66], [67], [68], [69], [70], [71], [72], [73]. One of these schemes could possibly be implemented, as was done for double diffraction, to improve the alignment tolerance and remove rotation from SVDOE's.

11.4 Recommendations for future research

There are a few aspects of SVDOE's which would benefit from further study. The fabrication issue of grating alignment, as discussed in the previous section, should be resolved in order to bring SVDOE's to the point of being a viable tool. This would seem to be primarily a matter of engineering implementation. Also, it would be instructive to verify the diffraction properties, e.g., periodic behavior with homogeneous layer thickness, through fabrication and testing of a series of SVDOE's with varying structural parameters. Similarly, lidar performance considerations such as wavefront quality and retardance can be evaluated and addressed as necessary through design and fabrication. These issues will be discussed more thoroughly in the next section since the lidar application has been used through this work as an illustrative example.

11.4.1 Discussion of lidar performance issues

Additional performance criteria should be considered for an element that will be used as a lidar scanner. These criteria, which were discussed in Chapter 2, include retardance, wavefront quality, and a polarization continuum between TE and TM for the input beam. The importance of these criteria arises primarily as a result of the heterodyne detection system employed in coherent lidar and its requirement for matching between polarization state and wavefront shape for optimum signal detection. The fact that the return signal from an atmospheric target is inherently weak exacerbates the need to collect as much of the return as possible by meeting the heterodyne detection requirements.

Both retardance and arbitrary linear polarization states can be measured with the addition of polarization optics in the apparatus shown in Figure 8.2. However, referring to Figure 4.4, it is expected that the performance would remain virtually unchanged as a function of input polarization states between TE and TM. Measurement of wavefront quality would require additional equipment. A first order measurement could be made using an interferometer operating at a standard wavelength, e.g., 633nm, and performing a typical wavelength scaling calculation. A more accurate assessment could be made by devising a measurement scheme which used a two micron laser as the illuminating source. All of these measurements were deferred to future studies of the suitability of SVDOE's as components of lidar systems.

11.5 Concluding remarks

Through this work SVDOE's have been conceptualized, simulated, fabricated, and tested. They have been shown to be an alternative grating technology capable of high diffraction efficiency using a combination of diffractive optics and volume holography. While there are a small number of fabrication issues to be resolved, SVDOE’s nonetheless present a viable grating tool for certain applications.

APPENDIX A

RIGOROUS COUPLED-WAVE ANALYSIS ALGORITHM ENCOMPASSING MULTI-LAYER STRUCTURES FOR PLANAR DIFFRACTION

The implementation of a stable and efficient rigorous coupled-wave analysis (RCWA) algorithm for planar diffraction by a periodic structure which includes both grating and homogeneous layers is presented in this appendix. Full details are given for the case of TE polarization to illustrate the incorporation of homogeneous layers into the algorithm such that both the number of layers of each type and their ordering may be arbitrary. The case of TM polarization will be considered briefly to identify points in the algorithm which differ from the implementation for TE polarization.

The RCWA obtains the exact solution of Maxwell's equations for electromagnetic diffraction by grating structures. It arrives at the solution without simplifying assumptions and without iterative techniques. The accuracy of the solution depends solely on the number of terms in the field space-harmonic expansion, with conservation of energy always being satisfied [28]. The basic formulation of the algorithm is to express the electromagnetic fields in the regions bounding the grating structure (the incident and transmitted regions) as solutions to Maxwell's equations and to express the fields within the grating region as space-harmonic expansions which are also solutions to Maxwell's equations. The tangential field components are then matched at each layer boundary within the structure to ensure continuity.

The algorithm presented here closely follows the formulation presented by Moharam, et al. [28], [29] wherein the tangential fields are expressed as a Fourier expansion in terms of space harmonics and then electromagnetic boundary conditions are applied at each layer in the structure. The expressions for the boundary conditions are written in matrix form and transmittance matrix methods are applied to reduce the system of equations to a single matrix equation encompassing all layers. Finally, enhanced transmittance matrix methods are applied to ensure that the matrix equation can be solved without numerical instabilities.

In the formulation discussed here, a linearly polarized beam is obliquely incident on a grating structure. The coordinate system definition for general three-dimensional diffraction from a single grating layer is shown in Figure A.1 A right-handed system is defined with the x-direction perpendicular to the grating grooves, the y-direction parallel to the grooves, and the z-direction normal to the grating plane. A linearly polarized electromagnetic wave with wave-vector, k, is incident on the grating at an arbitrary angle of incidence, θ, and at an azimuthal angle, ϕ. The plane of incidence is formed by the wave-vector and the z-axis. For the case of planar diffraction considered in this appendix, $\phi = 0$ and the incident polarization may be decomposed into a TE- ($\psi = 90°$) and a TM-polarization ($\psi = 0°$) problem, which may be solved independently. For this case, all the forward- and backward-diffracted orders lie in the plane of incidence, or the x-z plane. The grating is bounded in the incident region, or Region I, by a medium with refractive index n_I and in the exiting, or transmitted, region (Region II) by a medium with refractive index n_{II}.

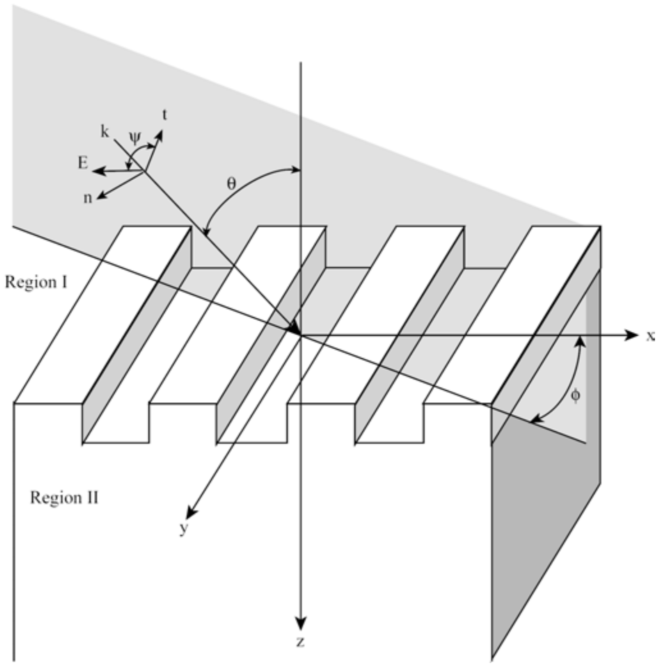

Figure A.1 Coordinate system definition for three-dimensional diffraction.

The geometry of the configuration considered here for a multi-layer structure, in this case an SVDOE, and planar diffraction is shown in Figure A.2. The thickness of each layer is denoted by d_ℓ where ℓ is the layer number within the structure, ranging from 1 to L.

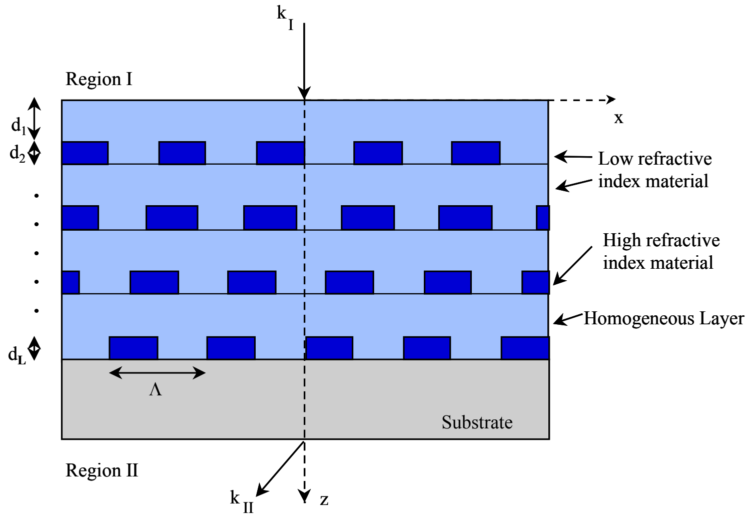

Figure A.2 Schematic illustration of the stratified volume diffractive optic element (SVDOE) structure. Binary grating layers are interleaved with homogeneous layers to achieve high efficiency. The gratings are shifted relative to one another, much like standard fringes in a volume grating, as a means to control the preferred incidence angle.

The algorithm for TE polarization begins by expressing the incident, normalized electric-field in Region I

$$E_{inc,y} = \exp\left[-jk_0 n_I \left(x\sin\theta + z\cos\theta\right)\right], \tag{A.1}$$

where $k_0 = 2\pi/\lambda_0$ and λ_0 is the wavelength of light in free space. The normalized solutions for the electric field in the input region (Region I, $0 < z$) and in the transmitted region (Region II) are given by

$$E_{I,y} = E_{inc,y} + \sum_{i=-\infty}^{\infty} R_i \exp\left[-j\left(k_{xi}x - k_{I,zi}z\right)\right], \tag{A.2}$$

$$E_{II,y} = \sum_{i=-\infty}^{\infty} T_i \exp\left\{-j\left[k_{xi}x + k_{II,zi}\left(z - D_L\right)\right]\right\}, \tag{A.3}$$

where

$$k_{xi} = k_0\left[n_I \sin\theta - i\left(\frac{\lambda_0}{\Lambda}\right)\right] \tag{A.4}$$

$$k_{M,zi} = \begin{cases} k_0\left[n_M{}^2 - \left(\dfrac{k_{xi}}{k_0}\right)^2\right]^{1/2} & k_0 n_M > k_{xi} \\ -jk_0\left[\left(\dfrac{k_{xi}}{k_0}\right)^2 - n_M{}^2\right]^{1/2} & k_{xi} > k_0 n_M \end{cases} \qquad M = I, II$$

and D_L is the total thickness of the grating region which is defined as

$$D_L = \sum_{p=1}^{L} d_p, \tag{A.5}$$

where d_p is the thickness of a given layer within the structure and L is the number of layers in the structure. Also, R_i is the normalized electric-field amplitude of the i^{th} backward-diffracted (reflected) wave in Region I and T_i is the normalized electric-field amplitude of the forward-diffracted (transmitted) wave in Region II. The magnetic-field in Region I and II can be obtained from Maxwell's equation

$$H = \left(\frac{j}{\omega\mu}\right)\nabla \times E, \tag{A.6}$$

where μ is the permeability of the region and ω is the angular optical frequency.

In the modulated region, the electric and magnetic fields may be expressed as the Fourier expansion in terms of the space-harmonic fields

$$E_{\ell,gy} = \sum_{i=-\infty}^{\infty} S_{\ell,yi}(z)\exp(-jk_{xi}x), \tag{A.7}$$

$$H_{\ell,gx} = -j\left(\frac{\varepsilon_0}{\mu_0}\right)^{\frac{1}{2}} \sum_{i=-\infty}^{\infty} U_{\ell,xi}(z)\exp(-jk_{xi}x), \tag{A.8}$$

where the subscript ℓ identifies a specific layer in the structure and $S_{\ell,i}(z)$ and $U_{\ell,i}(z)$ are normalized amplitudes of the ith space-harmonic fields such that $E_{\ell,g}$ and $H_{\ell,g}$ satisfy Maxwell's equations in the grating region. These are given as

$$\nabla \times \vec{H}_{\ell,g} = j\omega\varepsilon_0\varepsilon_\ell(x)\vec{E}_{\ell,g}, \tag{A.9}$$

$$\nabla \times \vec{E}_{\ell,g} = -j\omega\mu_0\vec{H}_{\ell,g}, \tag{A.10}$$

where ε_0 is the permittivity of free space, μ_0 is the permeability of free space, and the function $\varepsilon_\ell(x)$ represents the Fourier series expansion of the relativity permittivity in a layer within the grating region ($0 < z < d$) and is given in Equation (A.11)

$$\varepsilon_\ell(x) = \sum_{h=-\infty}^{\infty} \varepsilon_{\ell,h}\exp(j\frac{2\pi h}{\Lambda}x). \tag{A.11}$$

In the preceding equation, $\varepsilon_{\ell,h}$ is the h-th Fourier component of the relative permittivity in the grating region, which is complex for lossy or nonsymmetric dielectric gratings, and Λ is the grating period. Expanding the cross products given that only $E_{\ell,gy}$ will be used for the case of TE polarization yields

$$\frac{\partial E_{\ell,gy}}{\partial z} = j\omega\mu_0 H_{\ell,gx}, \tag{A.12}$$

$$\frac{\partial H_{\ell,gx}}{\partial z} = j\omega\varepsilon_0\varepsilon(x)E_{\ell,gy} + \frac{\partial H_{\ell,gz}}{\partial x}. \tag{A.13}$$

Substituting from the space-harmonic expansions into the expressions for Maxwell's equation in the grating region and eliminating $H_{\ell,gz}$ yields the coupled-wave equations

$$\frac{\partial S_{\ell,yi}(z)}{\partial z} = k_0 U_{\ell,xi}(z), \tag{A.14}$$

$$\frac{\partial U_{\ell,xi}(z)}{\partial z} = \left(\frac{k_{\ell,xi}{}^2}{k_0}\right) S_{\ell,yi}(z) - k_0 \sum_{p=1}^{N} \varepsilon_{(i-p)} S_{\ell,yp}(z). \tag{A.15}$$

There are now two single-order, coupled differential equations for the tangential components of the electric and magnetic fields. They may be written as a matrix equation

$$\begin{bmatrix} \dfrac{\partial S_{\ell,y}(z)}{\partial z'} \\ \dfrac{U_{\ell,x}(z)}{\partial z'} \end{bmatrix} = \begin{bmatrix} 0 & I \\ A_\ell & 0 \end{bmatrix} \begin{bmatrix} S_{\ell,y}(z) \\ U_{\ell,x}(z) \end{bmatrix}. \tag{A.16}$$

Equation (A.16) may be reduced by taking the second derivative with respect to z' and substituting for the first-order partial derivatives from the coupled-wave equations to obtain a second-order equation

$$\begin{bmatrix} \dfrac{\partial^2 S_{\ell,y}}{\partial (z')^2} \end{bmatrix} = \left[A_\ell\right]\left[S_{\ell,y}\right], \tag{A.17}$$

where $z' = k_0 z$, and A_ℓ is defined as

$$A_\ell = K_x{}^2 - E_\ell, \tag{A.18}$$

where E_ℓ is the matrix of permittivity harmonic components with its $(i,p)^{th}$ element equal to $\varepsilon_{(i-p)}$, K_x is a diagonal matrix with elements k_{xi}/k_0, and I is the identity matrix. Note that A_ℓ, E_ℓ, and K_x are (n x n) matrices, where n is the number of space harmonics retained in the field expansion, with the i^{th} row of the matrix corresponding to the i^{th} space harmonic. Equation (A.16) is a (2n x 2n) matrix which is reduced in (A.17) to an (n x n) matrix.

The set of coupled wave equations is solved by calculating the eigenvalues and eigenvectors associated with the matrix A_ℓ. The space harmonics of the tangential electric and magnetic fields in the grating layers are then given by Equations (A.19) and (A.20)

$$S_{\ell,yi}(z)=\sum_{m=1}^{n} w_{\ell,i,m}\left\{c_{\ell,m}{}^{+}\exp\left(-k_0 q_{\ell,m}(z-D_{\ell-1})\right)+c_{\ell,m}{}^{-}\exp\left[k_0 q_{\ell,m}\left(z-D_{\ell}\right)\right]\right\}, \qquad (A.19)$$

$$U_{\ell,xi}(z)=\sum_{m=1}^{n} v_{\ell,i,m}\left\{-c_{\ell,m}{}^{+}\exp\left(-k_0 q_{\ell,m}\left(z-D_{\ell-1}\right)\right)+c_{\ell,m}{}^{-}\exp\left[k_0 q_{\ell,m}\left(z-D_{\ell}\right)\right]\right\}, \qquad (A.20)$$

where $w_{\ell,i,m}$ and $q_{\ell,m}$ are the elements of the eigenvector matrix W and the positive square root of the eigenvalues of the matrix A, respectively. The quantity $v_{\ell,i,m}=q_{\ell,m}w_{\ell,i,m}$ is the i,m element of the matrix $V_\ell = W_\ell Q'_\ell$, where Q'_ℓ is a diagonal matrix elements $q_{\ell,m}$. The quantities $c_{\ell,m}{}^{+}$ and $c_{\ell,m}{}^{-}$ are the unknown coefficients to be determined from the boundary conditions. Also, D_ℓ is the total depth of the structure to the bottom of the ℓ^{th} layer and is defined in Equation (A.21)

$$D_\ell=\sum_{p=1}^{\ell} d_p\,. \qquad (A.21)$$

Note that the exponential terms involving the positive square root of the eigenvalues are normalized to prevent possible numerical overflow.

The expressions for the fields in the grating region thus far have limited to those for grating layers, i.e., those layers with permittivity modulation. However, to generalize the algorithm to include homogeneous layers, it is necessary to develop expressions for the fields in those layers as well. These expressions are direct solutions of the wave equation. They are interpreted as the space harmonics of the tangential electric and magnetic fields in the homogeneous layers and are given in Equations (A.22) and (A.23)

$$S_{\ell,yi}(z)=P_{\ell,i}\exp\left[-k_0\gamma_{\ell,i}\left(z-D_{\ell-1}\right)\right]+Q_{\ell,i}\exp\left[k_0\gamma_{\ell,i}\left(z-D_{\ell}\right)\right], \qquad (A.22)$$

$$U_{\ell,xi}(z)=-\gamma_{\ell,i}P_{\ell,i}\exp\left[-k_0\gamma_{\ell,i}\left(z-D_{\ell-1}\right)\right]+\gamma_{\ell,i}Q_{\ell,i}\exp\left[k_0\gamma_{\ell,i}\left(z-D_{\ell}\right)\right], \qquad (A.23)$$

where

$$\gamma_{\ell,i} = j\left[n_{\ell,h}{}^2 - \left(\frac{k_{xi}}{k_0}\right)^2 \right]^{1/2} . \tag{A.24}$$

The quantities P_ℓ and Q_ℓ are diagonal matrices with elements that are the electric field amplitudes in the homogeneous layer in the $+z$ direction and the $-z$ direction, respectively. They are the unknown coefficients that are to be calculated from the boundary conditions, similar to $c_{\ell,m}{}^+$ and $c_{\ell,m}{}^-$ for the case of a modulated layer. As discussed previously, P_ℓ and Q_ℓ are (n x n) matrices, where n is the number of space harmonics retained in the field expansion, with the i^{th} row of the matrix corresponding to the i^{th} space harmonic. The quantity $n_{\ell,h}$ is the refractive index of the homogeneous layer. Again, in the space-harmonic expressions the exponential terms involving the positive square roots of the eigenvalues are normalized to prevent numerical overflow by ensuring that the arguments of the exponential are always negative.

This discussion of the RCWA algorithm has progressed to providing expressions for the tangential electric- and magnetic-field components in the regions external to the grating and for the tangential space-harmonics of the electric and magnetic fields inside the grating region for both modulated and homogeneous layers. In order to calculate the amplitudes of the diffracted fields in Regions I and II, i.e., R_i and T_i, the tangential field components are matched at each of the layer boundaries in the multi-layer structure. This process will be illustrated by applying it to a structure such as the one seen in Figure A.2 In this case the first layer encountered beyond Region I is a homogeneous layer, with alternating grating and homogeneous layers following.

At the input boundary (i.e., z=0) the expressions for matching the tangential field components are given by

$$\delta_{i0} + R_i = \sum_{m=1}^{n} w_{1,i,m}\left[c_{1,m}{}^+ + c_{1,m}{}^- \exp(-k_0 q_{1,m} d_1) \right], \tag{A.25}$$

$$j\left[n_I \cos\theta\delta_{i0} - \left(\frac{k_{I,zi}}{k_0}\right) R_i \right] = \sum_{m=1}^{n} v_{1,i,m}\left[c_{1,m}{}^+ + c_{1,m}{}^- \exp(-k_0 q_{1,m} d_1) \right], \tag{A.26}$$

which may be written in matrix form

$$\begin{bmatrix} \delta_{i,0} \\ jn_I \cos\theta \delta_{i,0} \end{bmatrix} + \begin{bmatrix} I \\ -jY_I \end{bmatrix} R = \begin{bmatrix} I & G_1 \\ \Gamma_1 & -\Gamma_1 G_1 \end{bmatrix} \begin{bmatrix} P_1 \\ Q_1 \end{bmatrix}, \tag{A.27}$$

where Y_I is the diagonal matrix with elements $k_{I,zi}/k_0$, Γ_1 is the diagonal matrix with elements γ_1, and G_1 is the diagonal matrix with elements $\exp(-k_0\gamma_1 d_1)$. The last three matrix definitions may be generalized to any homogeneous layer by using the appropriate subscript, ℓ.

Proceeding to the next layer boundary (i.e., $z = d_1 = D_1$), again, match the tangential field components. For this case the match occurs at the interface between a homogeneous layer and a modulated, or grating layer. The space harmonic expressions at this interface are found by substituting the appropriate distance in the z-direction, $z = D_1$, and also substituting $D_{\ell-1} = 0$ to yield

$$\begin{bmatrix} G_1 & I \\ \Gamma_1 G_1 & -\Gamma_1 \end{bmatrix} \begin{bmatrix} P_1 \\ Q_1 \end{bmatrix} = \begin{bmatrix} W_2 & W_2 X_2 \\ V_2 & -V_2 X_2 \end{bmatrix} \begin{bmatrix} C_2^{+} \\ C_2^{-} \end{bmatrix}, \tag{A.28}$$

where X_2 is the diagonal matrix with elements $\exp(-k_0 q_{2,1,m} d_2)$ and d_2 is the thickness of the layer. Also, C_2^{+} and C_2^{-} are diagonal matrices with elements $c_{2,m}^{+}$ and $c_{2,m}^{-}$, respectively.

Proceeding to the next layer boundary (i.e., $z = D_2$), again, match the tangential field components. For this case the match occurs at the interface where the beam exits a grating layer and enters a homogeneous layer. The space harmonic expressions at this interface are found by substituting the appropriate distance in the z-direction, $z = D_2$, and also substituting $D_{\ell-1} = D_1$ to yield

$$\begin{bmatrix} W_2 X_2 & W_2 \\ V_2 X_2 & -V_2 \end{bmatrix} \begin{bmatrix} C_2^{+} \\ C_2^{-} \end{bmatrix} = \begin{bmatrix} I & G_3 \\ \Gamma_3 & -\Gamma_3 G_3 \end{bmatrix} \begin{bmatrix} P_3 \\ Q_3 \end{bmatrix}. \tag{A.29}$$

Continuing to the final boundary, the interface occurs when the beam exits a grating layer and enters Region II, i.e., it is transmitted into the exiting media. The expressions for matching the tangential field components are given in matrix form by

$$\begin{bmatrix} W_L X_L & W_L \\ V_L X_L & -V_L \end{bmatrix} \begin{bmatrix} C_L^{+} \\ C_L^{-} \end{bmatrix} = \begin{bmatrix} I \\ jY_{II} \end{bmatrix} T , \tag{A.30}$$

where Y_{II} is the diagonal matrix with elements $k_{II,zi} / k_0$.

Examination of the right-hand-side of Equation (A.27) shows that the matrix representation for the tangential field components when entering a homogeneous layer is given by

$$\begin{bmatrix} I & G_\ell \\ \Gamma_\ell & -\Gamma_\ell G_\ell \end{bmatrix} \begin{bmatrix} P_\ell \\ Q_\ell \end{bmatrix}. \tag{A.31}$$

Similarly, the left-hand-side of Equation (A.28) shows that the matrix representation for the tangential field components when exiting a homogeneous layer is

$$\begin{bmatrix} G_\ell & I \\ \Gamma_\ell G_\ell & -\Gamma_\ell \end{bmatrix} \begin{bmatrix} P_\ell \\ Q_\ell \end{bmatrix}. \tag{A.32}$$

The corresponding matrices for fields entering and exiting grating layers are given in the right-hand-side of Equation (A.28) and the left-hand-side of Equation (A.29), respectively They are given again in (A.33)

$$\begin{bmatrix} W_\ell & W_\ell X_\ell \\ V_\ell & -V_\ell X_\ell \end{bmatrix} \begin{bmatrix} C_\ell^{+} \\ C_\ell^{-} \end{bmatrix} \quad \text{and} \quad \begin{bmatrix} W_\ell X_\ell & W_\ell \\ V_\ell X_\ell & -V_\ell \end{bmatrix} \begin{bmatrix} C_\ell^{+} \\ C_\ell^{-} \end{bmatrix}. \tag{A.33}$$

Considering Equation (A.31) and the first matrix product in Equation (A.33), the matrices have a common format (i.e., dimensions, row and column position of exponential terms) which can be expressed as

$$\begin{bmatrix} A_{\ell,1} & A_{\ell,1} XX_\ell \\ A_{\ell,2} & -A_{\ell,2} XX_\ell \end{bmatrix} \begin{bmatrix} D_{\ell,1} \\ D_{\ell,2} \end{bmatrix}. \tag{A.34}$$

Similarly, Equation (A.32) and the second matrix product in Equation (A.33) also have a common format, which is given by

$$\begin{bmatrix} A_{\ell,1}XX_{\ell} & A_{\ell,1} \\ A_{\ell,2}XX_{\ell} & -A_{\ell,2} \end{bmatrix} \begin{bmatrix} D_{\ell,1} \\ D_{\ell,2} \end{bmatrix}. \tag{A.35}$$

The capability to express the space-harmonic matrices of grating layers and homogeneous layers in a common format permits implementation of a computational algorithm which is independent of the number of layers in a grating structure, the type of layers, and the ordering of the constituent layers. Such an algorithm is very flexible when applied to the analysis of periodic structures. The remaining restrictions on such an algorithm are that all grating layers have identical period and that each grating layer consist of only two materials. The latter restriction can be addressed in the Fourier series expansion of the permittivity of a grating layer.

After obtaining equations for the matching tangential field components at each layer boundary, a system of equations exists that can be solved for R_i and T_i by standard techniques. This can be accomplished without any numerical instability for any number of grating layers, any layer thickness, or any number of refractive indices. The possibility for numerical inaccuracy, such as overflow, has been preempted by normalization of the exponential terms in the space harmonic expansions. The difficulty with such a solution is that, for a large number of layers, the system of equations also becomes large and can be computationally inefficient. A transmittance matrix approach can be applied to reduce the size of a system of simultaneous equations. However, the approach itself can introduce additional numerical instability. This problem can be eliminated by applying enhanced transmittance techniques to the reduced system of equations to obtain a final solution. Both the transmittance matrix approach and the enhanced transmittance matrix techniques will be applied to solve the system of equations here.

The transmittance matrix approach is used to eliminate the intermediate coefficients in the system of equations and solve directly for the field amplitudes R_i and T_i. Begin the process with the matrix equation for the matched tangential field components at the last boundary in the system $(\ell = L)$ as shown in

$$\begin{bmatrix} A_{L,1}XX_L & A_{L,1} \\ A_{L,2}XX_L & -A_{L,2} \end{bmatrix} \begin{bmatrix} D_{L,1} \\ D_{L,2} \end{bmatrix} = \begin{bmatrix} I \\ jY_{II} \end{bmatrix} T \,. \tag{A.36}$$

Invert the space harmonic matrix from Equation (A.36) to arrive at an expression in terms of the coefficients

$$\begin{bmatrix} D_{L,1} \\ D_{L,2} \end{bmatrix} = \begin{bmatrix} A_{L,1}XX_L & A_{L,1} \\ A_{L,2}XX_L & -A_{L,2} \end{bmatrix}^{-1} \begin{bmatrix} I \\ jY_{II} \end{bmatrix} T \,. \tag{A.37}$$

Substitute from Equation (A.37) into the equation at the previous boundary $(\ell = L-1)$ to obtain the matrix equation

$$\begin{bmatrix} A_{L-1,1}XX_{L-1} & A_{L-1,1} \\ A_{L-1,2}XX_{L-1} & -A_{L-1,2} \end{bmatrix} \begin{bmatrix} D_{L-1,1} \\ D_{L-1,2} \end{bmatrix} = \tag{A.38}$$

$$\begin{bmatrix} A_{L,1} & A_{L,1}XX_L \\ A_{L,2} & -A_{L,2}XX_L \end{bmatrix} \begin{bmatrix} A_{L,1}XX_L & A_{L,1} \\ A_{L,2}XX_L & -A_{L,2} \end{bmatrix}^{-1} \begin{bmatrix} I \\ jY_{II} \end{bmatrix} T \,.$$

This process is repeated for the remaining layer boundaries to arrive at a representation for the entire system of equations that may be written as

$$\begin{bmatrix} \delta_{i,0} \\ jn_I \cos\theta\delta_{i,0} \end{bmatrix} + \begin{bmatrix} I \\ -jY_I \end{bmatrix} R = \prod_{\ell=1}^{L} \begin{bmatrix} A_{\ell,1} & A_{\ell,1}XX_\ell \\ A_{\ell,2} & -A_{\ell,2}XX_\ell \end{bmatrix} \begin{bmatrix} A_{\ell,1}XX_\ell & A_{\ell,1} \\ A_{\ell,2}XX_\ell & -A_{\ell,2} \end{bmatrix}^{-1} \begin{bmatrix} I \\ jY_{II} \end{bmatrix} T \,. \tag{A.39}$$

Equation (A.39) includes one matrix inversion for each layer. The matrix to be inverted may become ill-conditioned, e.g., the exponential terms may approach zero, for the case of lossy media or an evanescent wave. Inversion of an ill-conditioned matrix may produce elements with large values that cannot be represented within the numerical accuracy of a computer. Thus, the introduction of transmittance techniques has the potential to introduce errors into the solution or cause the system not to converge properly. This problem can be addressed by enhanced transmittance matrix techniques. Begin by examining the final three matrices in Equation (A.39). These are given in Equation (A.40)

$$\begin{bmatrix} A_{L,1}XX_L & A_{L,1} \\ A_{L,2}XX_L & -A_{L,2} \end{bmatrix}^{-1} \begin{bmatrix} f_{L+1} \\ g_{L+1} \end{bmatrix} T \,, \tag{A.40}$$

where $f_{L+1} = I$ and $g_{L+1} = jY_{II}$. The space-harmonic matrix to be inverted may be factored to separate the exponential terms

$$\begin{bmatrix} XX_L & 0 \\ 0 & I \end{bmatrix}^{-1} \begin{bmatrix} A_{L,1} & A_{L,1} \\ A_{L,2} & -A_{L,2} \end{bmatrix}^{-1} \begin{bmatrix} f_{L+1} \\ g_{L+1} \end{bmatrix} T. \tag{A.41}$$

Of the two matrices to be inverted in Equation (A.41), the one on the right may be inverted without numerical instability. The overall product may be simplified by multiplying the two matrices in the middle in Equation (A.41) as

$$\begin{bmatrix} a_L \\ b_L \end{bmatrix} = \begin{bmatrix} A_{L,1} & A_{L,1} \\ A_{L,2} & -A_{L,2} \end{bmatrix}^{-1} \begin{bmatrix} f_{L+1} \\ g_{L+1} \end{bmatrix}. \tag{A.42}$$

Equation (A.41) may then be written as

$$\begin{bmatrix} XX_L & 0 \\ 0 & I \end{bmatrix}^{-1} \begin{bmatrix} a_L \\ b_L \end{bmatrix} T. \tag{A.43}$$

The matrix remaining to be inverted in Equation (A.43) can be ill-conditioned and can produce numerical instability as discussed previously. This problem can be avoided by making the substitution

$$T = a_L{}^{-1} XX_L T_L, \tag{A.44}$$

then Equation (A.43) be written in a final form as

$$\begin{bmatrix} I \\ b_L a_L{}^{-1} XX_L \end{bmatrix} T_L. \tag{A.45}$$

This process has simplified the last three matrices of Equation (A.39). However, there is one matrix remaining in the product for each layer of the structure that must also be considered. That matrix is shown below multiplied by Equation (A.45)

$$\begin{bmatrix} A_{L,1} & A_{L,1} XX_L \\ A_{L,2} & -A_{L,2} XX_L \end{bmatrix} \begin{bmatrix} I \\ b_L a_L{}^{-1} XX_L \end{bmatrix} T_L. \tag{A.46}$$

The matrix on the left in the preceding equation may be factored to separate the exponential components, as was done in Equation (A.41). This is illustrated factorization is given by

$$\begin{bmatrix} A_{L,1} & A_{L,1} \\ A_{L,2} & -A_{L,2} \end{bmatrix} \begin{bmatrix} I & 0 \\ 0 & XX_L \end{bmatrix} \begin{bmatrix} I \\ b_L a_L{}^{-1} XX_L \end{bmatrix} T_L \,. \tag{A.47}$$

The product of the two middle matrices is performed to yield the expression

$$\begin{bmatrix} A_{L,1} & A_{L,1} \\ A_{L,2} & -A_{L,2} \end{bmatrix} \begin{bmatrix} I \\ XX_L b_L a_L{}^{-1} XX_L \end{bmatrix} T_L \,, \tag{A.48}$$

and then the two matrices on the left are multiplied to yield a final matrix product for the layer under consideration,

$$\begin{bmatrix} A_{L,1}\left(I + XX_L b_L a_L{}^{-1} XX_L\right) \\ A_{L,2}\left(I - XX_L b_L a_L{}^{-1} XX_L\right) \end{bmatrix} T_L \,, \tag{A.49}$$

or, in a simplified form

$$\begin{bmatrix} f_L' \\ g_L' \end{bmatrix} T_L \,. \tag{A.50}$$

The above procedure is repeated for all layers such that Equation (A.39) is reduced to a final equation for the system, which may be expressed as

$$\begin{bmatrix} \delta_{i,0} \\ jn_I \cos\theta \delta_{i,0} \end{bmatrix} + \begin{bmatrix} I \\ -jY_I \end{bmatrix} R = \begin{bmatrix} A_{1,1}\left(I + XX_1 b_1 a_1{}^{-1} XX_1\right) \\ A_{1,2}\left(I - XX_1 b_1 a_1{}^{-1} XX_1\right) \end{bmatrix} T_1 \,, \tag{A.51}$$

where $T = a_L{}^{-1} XX_L a_{L-1}{}^{-1} XX_{L-1} \ldots a_2{}^{-1} XX_2 a_1{}^{-1} XX_1 T_1$. Equation (A.51) may then be reduced to a form which is easily solved for R_i and T_i without numerical instability. Intermediate steps in this rearrangement are given in the following two equations

$$\begin{bmatrix} I \\ -jY_I \end{bmatrix} R - \begin{bmatrix} A_{1,1}\left(I + XX_1 b_1 a_1{}^{-1} XX_1\right) \\ A_{1,2}\left(I - XX_1 b_1 a_1{}^{-1} XX_1\right) \end{bmatrix} T_1 = - \begin{bmatrix} \delta_{i,0} \\ jn_I \cos\theta \delta_{i,0} \end{bmatrix} , \tag{A.52}$$

$$\begin{bmatrix} -I & A_{1,1}\left(I + XX_1 b_1 a_1^{-1} XX_1\right) \\ jY_I & A_{1,2}\left(I - XX_1 b_1 a_1^{-1} XX_1\right) \end{bmatrix} \begin{bmatrix} R \\ T_1 \end{bmatrix} = \begin{bmatrix} \delta_{i,0} \\ jn_I \cos\theta \delta_{i,0} \end{bmatrix}, \tag{A.53}$$

and the final representation is given by

$$\begin{bmatrix} R \\ T_1 \end{bmatrix} = \begin{bmatrix} -I & A_{1,1}\left(I + XX_1 b_1 a_1^{-1} XX_1\right) \\ jY_I & A_{1,2}\left(I - XX_1 b_1 a_1^{-1} XX_1\right) \end{bmatrix}^{-1} \begin{bmatrix} \delta_{i,0} \\ jn_I \cos\theta \delta_{i,0} \end{bmatrix}. \tag{A.54}$$

The diffraction efficiencies are defined as

$$DE_{ri} = R_i R_i^* \operatorname{Re}\left(\frac{k_{I,zi}}{k_0 n_I \cos\theta} \right), \tag{A.55}$$

$$DE_{ti} = T_i T_i^* \operatorname{Re}\left(\frac{k_{II,zi}}{k_0 n_I \cos\theta} \right), \tag{A.56}$$

where DE_{ri} is the diffraction efficiency in the i-th reflected order and DE_{ti} is the corresponding value in the i-th transmitted order. This completes the discussion of planar diffraction for TE polarization.

Now, consider the case of TM polarization. The discussion presented here serves primarily to clarify differences between the formulation for the two polarization modes. For TM polarization, the incident normalized field is written in terms of the magnetic-field vector in Region I,

$$H_{inc,y} = \exp\left[-jk_0 n_I \left(\cos\theta\, x + \cos\theta\, z\right)\right]. \tag{A.57}$$

The normalized solutions for the magnetic field in the input region (Region I, 0 < z) and in the transmitted region (Region II, z > d) are similar to those given for the electric field for TE polarization in Equation (A.2) and (A.3) and will not be repeated here.

The electric-field in Regions I and II can be obtained from the Maxwell equation

$$E = \left(\frac{-j}{\omega \varepsilon_0 n^2} \right) \nabla \times H. \tag{A.58}$$

Proceeding as in TE case, in the modulated region the electric and magnetic vector fields may be expressed as the Fourier expansion in terms of the space-harmonic fields. These are substituted into Maxwell's equation valid for the modulated region and the component $E_{\ell,gz}$ is eliminated. This leads to a set of coupled-wave equations which may be written in matrix form as

$$\begin{bmatrix} \dfrac{\partial U_{\ell,y}}{\partial z'} \\ \dfrac{\partial S_{\ell,x}}{\partial z'} \end{bmatrix} = \begin{bmatrix} 0 & E_\ell \\ B_\ell & 0 \end{bmatrix} \begin{bmatrix} U_{\ell,y} \\ S_{\ell,x} \end{bmatrix}. \tag{A.59}$$

This may be reduced from a (2n x 2n) system of equations to an (n x n) system as discussed earlier by taking the second derivative with respect to z' and substituting from the first-order equations to obtain the second-order differential equation, expressed in matrix form as

$$\left[\frac{\partial^2 U_{\ell,y}}{\partial (z')^2} \right] = \left[E_\ell B_\ell \right] \left[U_{\ell,y} \right], \tag{A.60}$$

where

$$B_\ell = K_x E_\ell^{-1} K_x - I. \tag{A.61}$$

At this point a slight deviation from the formulation presented by Moharam, et al. [28] is made to incorporate the changes recommended by Li [38] to improve the speed of the convergence to an accurate solution. Recall that the accuracy of RCWA is a function of the number of space harmonics retained in the calculation. Also, that the number of space harmonics retained controls the dimensions of all the preceding matrix equations. Then, improving the speed of convergence corresponds to obtaining an accurate solution with fewer space harmonics, which implies solving matrix equations with smaller dimensions, thereby decreasing computational time required to obtain the solution. Li also demonstrated the ability to apply his formulation to obtain an accurate solution to problems which otherwise may not converge at all.

The changes recommended by Li entail preserving continuity of the coupled-wave equations through proper formulation of the discontinuities in the permittivity function. For the case of TM polarization considered here, this means modifying Equation (A.60) so that it is written as

$$\left[\frac{\partial^2 U_{\ell,y}}{\partial(z')^2}\right]=\left[\left(\frac{1}{E_\ell}\right)^{-1} B_\ell\right]\left[U_{\ell,y}\right]. \tag{A.62}$$

The solution as outlined by Moharam, et al. remains valid from this point forward. The coupled-wave equations given by Equation (A.62) are solved by calculating the eigenvalues and the eigenvectors associated with the (n x n) matrix. These eigenvectors and eigenvalues provide the space-harmonic expansion for the magnetic field which can then be used with Maxwell's equation to provide the space-harmonic expansion for the electric field. The tangential components of the electric and magnetic field are matched at each boundary within the structure and an expression for the entire system is derived, similar to Equation (A.39). This expression is reduced as shown for the case of TE polarization to a system of equations that can be solved without numerical instability.

Finally, the diffraction efficiencies for the case of TM polarization are given by

$$DE_{ri}=R_i R_i^* \operatorname{Re}\left(\frac{k_{I,zi}}{k_0 n_I \cos\theta}\right), \tag{A.63}$$

$$DE_{ti}=T_i T_i^* \frac{\operatorname{Re}\left(\dfrac{k_{II,zi}}{n_{II}^2}\right)}{\left(\dfrac{k_0\cos\theta}{n_I}\right)}. \tag{A.64}$$

APPENDIX B

RIGOROUS COUPLED-WAVE ANALYSIS ALGORITHM ENCOMPASSING MULTI-LAYER STRUCTURES FOR CONICAL DIFFRACTION

The implementation of a stable and efficient rigorous coupled-wave analysis (RCWA) algorithm for conical diffraction by a periodic structure which includes both grating and homogeneous layers is presented in this appendix.

The RCWA obtains the exact solution of Maxwell's equations for electromagnetic diffraction by grating structures. It arrives at the solution without simplifying assumptions and without iterative techniques. The accuracy of the solution depends solely on the number of terms in the field space-harmonic expansion, with conservation of energy always being satisfied [28]. The basic formulation of the algorithm is to express the electromagnetic fields in the regions bounding the grating structure (the incident and transmitted regions) as solutions to Maxwell's equations and to express the fields within the grating region as space-harmonic expansions which are also solutions to Maxwell's equations. The tangential field components are then matched at each layer boundary within the structure to ensure continuity.

The algorithm presented here closely follows the formulation presented by Moharam, et al. [28], [29] wherein the tangential fields are expressed as a Fourier expansion in terms of space harmonics and then electromagnetic boundary conditions are applied at each layer in the structure. The expressions for the boundary conditions are written in matrix form and transmittance matrix methods are applied to reduce the system of equations to a single matrix equation encompassing all layers. Finally, enhanced transmittance matrix methods are applied to ensure that the matrix equation can be solved without numerical instabilities.

In the formulation discussed here, a linearly polarized beam is obliquely incident on a grating structure. The coordinate system definition for general three-dimensional diffraction from a single grating layer is shown in Figure B.1. A right-handed system is defined with the x-direction perpendicular to the grating grooves, the y-direction parallel to the grooves, and the z-direction normal to the grating plane. A linearly polarized electromagnetic wave with wave-vector, k, is incident on the grating at an arbitrary angle of incidence, θ, and at an azimuthal angle, ϕ. The plane of incidence is formed by the wave-vector and the z-axis. For the general case of three-dimensional diffraction ($\phi \neq 0$), or conical diffraction, the diffracted wave-vectors lie on the surface of a cone and the perpendicular and parallel components of the fields are coupled and must be solved simultaneously. The grating is bounded in the incident region, or Region I, by a medium with refractive index n_I and in the exiting, or transmitted, region (Region II) by a medium with refractive index n_{II}.

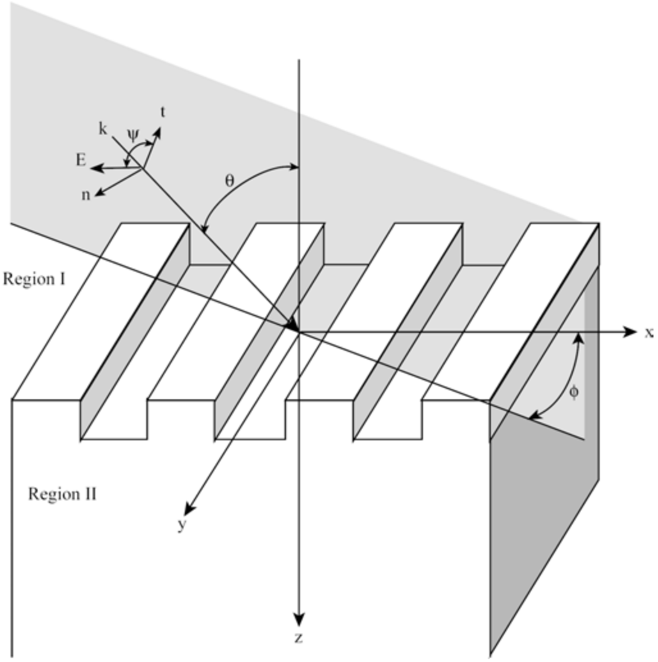

Figure B.1 Coordinate system definition for three-dimensional diffraction.

The geometry of the configuration considered here for a multi-layer structure, in this case an SVDOE, is shown in Figure B.2. The figure illustrates planar diffraction ($\phi = 0$) and normal incidence ($\theta = 0$) for clarity in defining the layer structure, even though this appendix is concerned with conical diffraction. The thickness of each layer is denoted by d_ℓ where ℓ is the layer number within the structure, ranging from 1 to L.

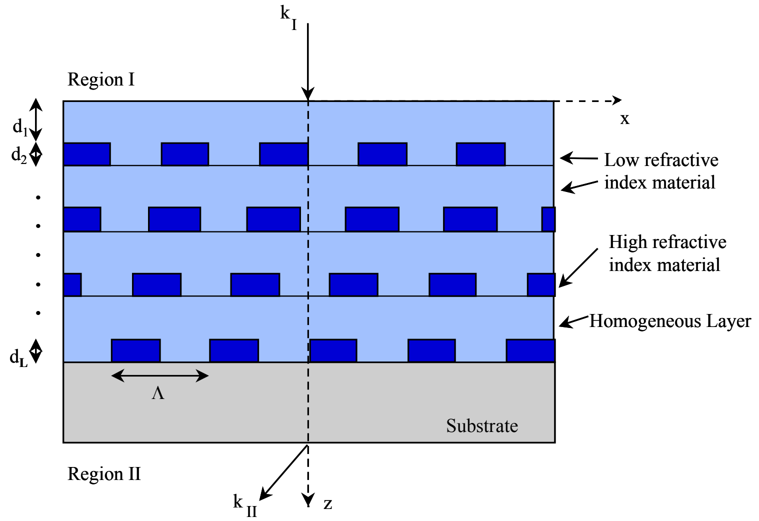

Figure B.2 Schematic illustration of the stratified volume diffractive optic element (SVDOE) structure. Binary grating layers are interleaved with homogeneous layers to achieve high efficiency. The gratings are shifted relative to one another, much like standard fringes in a volume grating, as a means to control the preferred incidence angle.

The algorithm for conical diffraction begins by expressing the incident, normalized electric-field vector in Region I

$$\vec{E}_{inc} = \hat{u}\exp[-jk_0 n_I(x\sin\theta\cos\phi + y\sin\theta\sin\phi + z\cos\theta)], \tag{B.1}$$

where $k_0 = 2\pi/\lambda_0$ and λ_0 is the wavelength of light in free space and $\hat{u}$ is the unit vector

$$\hat{u} = (\cos\psi\cos\theta\cos\phi - \sin\psi\sin\phi)\hat{x} + (\cos\psi\cos\theta\cos\phi - \sin\psi\cos\phi)\hat{y} - \cos\psi\sin\phi\hat{z}. \tag{B.2}$$

In Equation (B.2) ψ is the angle between the electric-field vector and the plane of incidence. For $\psi = 0°$ the polarization is TM mode and for $\psi = 90°$ polarization is TE mode, meaning that the magnetic and the electric fields, respectively, are perpendicular to the plane of incidence.

The normalized solutions for the electric field vector in the input region (Region I, 0 < z) and in the transmitted region (Region II) are given by

$$\vec{E}_I = \vec{E}_{inc} + \sum_{i=-\infty}^{\infty} \vec{R}_i \exp[-j(k_{xi}x + k_y y - k_{I,zi}z)]\,, \tag{B.3}$$

$$\vec{E}_{II} = \sum_{i=-\infty}^{\infty} \vec{T}_i \exp\{-j[k_{xi}x + k_y y + k_{II,zi}(z - D_L)]\}\,, \tag{B.4}$$

where

$$k_{xi} = k_0[n_I \sin\theta \cos\phi - i(\lambda_0 / \Lambda)], \tag{B.5}$$

$$k_y = k_0 n_I \sin\theta \sin\phi,$$

$$k_{M,zi} = \begin{cases} \left[\left(k_0 n_M\right)^2 - k_{xi}{}^2 - k_y{}^2\right]^{1/2} & k_0 n_M > \left(k_{xi}{}^2 + k_y{}^2\right)^{1/2} \\ -j\left[k_{xi}{}^2 + k_y{}^2 - \left(k_0 n_M\right)^2\right]^{1/2} & \left(k_{xi}{}^2 + k_y{}^2\right)^{1/2} > k_0 n_M\,, \\ & M = I, II \end{cases}$$

and D_L is the total thickness of the grating region, which is defined as

$$D_L = \sum_{p=1}^{L} d_p\,, \tag{B.6}$$

where d_p is the thickness of a given layer within the structure. Also, $\vec{R}_i$ is the normalized vector electric-field amplitude of the i^{th} backward-diffracted (reflected) wave in Region I and $\vec{T}_i$ is the normalized electric-field vector amplitude of the forward-diffracted (transmitted) wave in Region II. The magnetic-field vectors in Region I and II can be obtained from Maxwell's equation

$$\nabla \times \vec{H} = j\omega\varepsilon_0 n^2 \vec{E}\,. \tag{B.7}$$

The corresponding Maxwell equation for the electric-field vectors is given by

$$\nabla \times \vec{E} = -j\omega\mu_0 \vec{H}\,, \tag{B.8}$$

where μ is the permeability of the region and ω is the angular optical frequency. Note that the output plane of diffraction, in the case of conical diffraction, for the i^{th} propagating diffraction order has an inclination angle given by

$$\varphi_i = \tan^{-1}(k_y / k_{xi}). \tag{B.9}$$

In the modulated region, the electric and magnetic vector fields may be expressed as the Fourier expansion in terms of the space-harmonic fields

$$\vec{E}_{\ell,g} = \sum_{i=-\infty}^{\infty} \left[S_{\ell,xi}(z)\hat{x} + S_{\ell,yi}(z)\hat{y} + S_{\ell,zi}(z)\hat{z} \right] \exp\left[-j(k_{xi}x + k_y y)\right], \tag{B.10}$$

$$\vec{H}_{\ell,g} = -j\left(\frac{\varepsilon_0}{\mu_0}\right)^{1/2} \sum_{i=-\infty}^{\infty} \left[U_{\ell,xi}(z)\hat{x} + U_{\ell,yi}(z)\hat{y} + U_{\ell,zi}(z)\hat{z} \right] \exp\left[-j(k_{xi}x + k_y y)\right], \tag{B.11}$$

where the subscript ℓ identifies a specific layer in the structure and $S_{\ell,i}(z)$ and $U_{\ell,i}(z)$ are normalized vector amplitudes of the ith space-harmonic fields such that $\vec{E}_{\ell,g}$ and $\vec{H}_{\ell,g}$ satisfy Maxwell's equations in the grating region. Maxwell's equations may be expressed as

$$\nabla \times \vec{H}_{\ell,g} = j\omega\varepsilon_0\varepsilon_\ell(x)\vec{E}_{\ell,g}, \tag{B.12}$$

$$\nabla \times \vec{E}_{\ell,g} = -j\omega\mu_0\vec{H}_{\ell,g}, \tag{B.13}$$

where ε_0 is the permittivity of free space, μ_0 is the permeability of free space, and the function $\varepsilon_\ell(x)$ represents the Fourier series expansion of the relativity permittivity in a layer within the grating region ($0 < z < d_\ell$), which is given by

$$\varepsilon_\ell(x) = \sum_{h=-\infty}^{\infty} \varepsilon_{\ell,h} \exp\left(j\frac{2\pi h}{\Lambda}x\right). \tag{B.14}$$

In the preceding equation, $\varepsilon_{\ell,h}$ is the h-th Fourier component of the relative permittivity in the grating region, which is complex for lossy or nonsymmetric dielectric gratings, and Λ is the grating period.

Solving Maxwell's equations in the grating region is accomplished by substituting the space-harmonic expression for the electric field in that region, Equation (B.10), into Maxwell's curl equation for the electric field, Equation (B.13), to obtain the vector component equation

$$\begin{aligned}-j\omega\mu_0\vec{H}_{\ell,g} &= \hat{i}\left(-jk_y S_{\ell,zi}(z)-\frac{\partial}{\partial z}S_{\ell,yi}(z)\right)-\hat{j}\left(-jk_{xi}S_{\ell,zi}(z)-\frac{\partial}{\partial z}S_{\ell,xi}(z)\right)\\ &+\hat{k}\left(-jk_{xi}S_{\ell,yi}(z)+jk_y S_{\ell,xi}(z)\right)\end{aligned}. \qquad \text{(B.15)}$$

Substituting from the space-harmonic expression for the magnetic field in the grating region, Equation (B.11), into the vector component equation for the magnetic field, (B.15), and separating the vector components into independent equations yields the first-order coupled equations

$$-\omega\sqrt{\mu_0\varepsilon_0}\,U_{\ell,xi}(z) = -jk_y S_{\ell,zi}(z)-\frac{\partial}{\partial z}S_{\ell,yi}(z)\,, \qquad \text{(B.16)}$$

$$-\omega\sqrt{\mu_0\varepsilon_0}\,U_{\ell,yi}(z) = jk_{xi}S_{\ell,zi}(z)+\frac{\partial}{\partial z}S_{\ell,xi}(z)\,, \qquad \text{(B.17)}$$

$$-\omega\sqrt{\mu_0\varepsilon_0}\,U_{\ell,zi}(z) = -jk_{xi}S_{\ell,yi}(z)+jk_y S_{\ell,xi}(z)\,. \qquad \text{(B.18)}$$

Similarly, substituting the space-harmonic expression for the magnetic field in the grating region, Equation (B.11), into Maxwell's curl equation for the magnetic field, (B.12), yields the vector component equation for the electric field

$$-j\omega\varepsilon_0\varepsilon_\ell(x)\vec{E}_{\ell,g} = \begin{bmatrix} \hat{i}\left(-jk_y U_{\ell,zi}(z)-\frac{\partial}{\partial z}U_{\ell,yi}(z)\right) \\ -\hat{j}\left(-jk_{xi}U_{\ell,zi}(z)-\frac{\partial}{\partial z}U_{\ell,xi}(z)\right) \\ +\hat{k}\left(-jk_{xi}U_{\ell,yi}(z)+jk_y U_{\ell,xi}(z)\right)\end{bmatrix}\left(-j\sqrt{\frac{\varepsilon_0}{\mu_0}}\right). \qquad \text{(B.19)}$$

Substituting from the space-harmonic expression for the electric field in the grating region, Equation (B.10), into the vector component equation for the electric field, (B.19), and separating the vector components into independent equations yields a second set of coupled, first-order equations given by

$$j\omega\varepsilon_0\varepsilon_\ell(x)S_{\ell,xi}(z) = \left(-jk_y U_{\ell,zi}(z)-\frac{\partial}{\partial z}U_{\ell,yi}(z)\right)\left(-j\sqrt{\frac{\varepsilon_0}{\mu_0}}\right), \qquad \text{(B.20)}$$

$$j\omega\varepsilon_0\varepsilon_\ell(x)S_{\ell,yi}(z) = \left(jk_{xi}U_{\ell,zi}(z) + \frac{\partial}{\partial z}U_{\ell,xi}(z)\right)\left(-j\sqrt{\frac{\varepsilon_0}{\mu_0}}\right), \tag{B.21}$$

$$j\omega\varepsilon_0\varepsilon_\ell(x)S_{\ell,zi}(z) = \left(-jk_{xi}U_{\ell,yi}(z) + jk_y U_{\ell,xi}(z)\right)\left(-j\sqrt{\frac{\varepsilon_0}{\mu_0}}\right). \tag{B.22}$$

The next step is to eliminate the normal components of the electric and magnetic fields, those corresponding to $E_{\ell,gz}$ and $H_{\ell,gz}$, from the two sets of first-order coupled equations. Substituting from Equation (B.22) into both Equations (B.16) and (B.17) yields the expressions for the derivatives of $S_{\ell,yi}(z)$ and $S_{\ell,xi}(z)$ given in Equations (B.23) and (B.24)

$$\frac{\partial}{\partial z}\frac{S_{\ell,yi}(z)}{k_0} = \frac{k_y}{k_0}\varepsilon_\ell(x)^{-1}\frac{k_{xi}}{k_0}U_{\ell,yi}(z) + \left(1 - \frac{k_y}{k_0}\varepsilon_\ell(x)^{-1}\frac{k_y}{k_0}\right)U_{\ell,xi}(z), \tag{B.23}$$

$$\frac{\partial}{\partial z}\frac{S_{\ell,xi}(z)}{k_0} = \left(\frac{k_{xi}}{k_0}\varepsilon_\ell(x)^{-1}\frac{k_{xi}}{k_0} - 1\right)U_{\ell,yi}(z) - \frac{k_{xi}}{k_0}\varepsilon_\ell(x)^{-1}\frac{k_y}{k_0}U_{\ell,xi}(z). \tag{B.24}$$

Using a similar approach to obtain expressions for the derivatives of $U_{\ell,yi}(z)$ and $U_{\ell,xi}(z)$, substitute from Equation (B.18) into Equations (B.20) and (B.21). This yields the expressions

$$\frac{\partial}{\partial z}\frac{U_{\ell,yi}(z)}{k_0} = \frac{k_y}{k_0}\frac{k_{xi}}{k_0}S_{\ell,yi}(z) + \left(\varepsilon_\ell(x) - \frac{k_y^{\,2}}{k_0^{\,2}}\right)S_{\ell,xi}(z), \tag{B.25}$$

$$\frac{\partial}{\partial z}\frac{U_{\ell,xi}(z)}{k_0} = \left(\frac{k_{xi}^{\,2}}{k_0^{\,2}} - \varepsilon_\ell(x)\right)S_{\ell,yi}(z) - \frac{k_{xi}}{k_0}\frac{k_y}{k_0}S_{\ell,xi}(z). \tag{B.26}$$

There are now four single-order, coupled differential equations for the tangential components of the electric and magnetic fields. They may be written as a matrix equation

$$\begin{bmatrix} \dfrac{\partial S_{\ell,y}(z)}{\partial(z')} \\ \dfrac{\partial S_{\ell,x}(z)}{\partial(z')} \\ \dfrac{\partial U_{\ell,y}(z)}{\partial(z')} \\ \dfrac{\partial U_{\ell,x}(z)}{\partial(z')} \end{bmatrix} = \begin{bmatrix} 0 & 0 & K_y E_\ell^{-1} K_x & I - K_y E_\ell^{-1} K_y \\ 0 & 0 & K_x E_\ell^{-1} K_x - I & -K_x E_\ell^{-1} K_y \\ K_x K_y & E_\ell - K_y^2 & 0 & 0 \\ K_x^2 - E_\ell & -K_x K_y & 0 & 0 \end{bmatrix} \begin{bmatrix} S_{\ell,y}(z) \\ S_{\ell,x}(z) \\ U_{\ell,y}(z) \\ U_{\ell,x}(z) \end{bmatrix}, \tag{B.27}$$

where $z' = k_0 z$, E_ℓ is the matrix of permittivity harmonic components with its $(i,p)^{th}$ element equal to $\varepsilon_{\ell,(i-p)}$, K_x is a diagonal matrix with elements k_{xi}/k_0, and K_y is a diagonal matrix with elements k_y/k_0. Note that E_ℓ, K_x, and K_y are (n x n) matrices, where n is the number of space harmonics retained in the field expansion, with the i^{th} row of the matrix corresponding to the i^{th} space harmonic. Equation (B.27), then, is a (4n x 4n) matrix.

Equation (B.27) may be reduced from a (4n x 4n) matrix to a (2n x 2n) matrix as a means to reduce the computational time required to solve the system of equations. The reduction is initiated by taking the second derivative of the constituent equations, Equations (B.23)–(B.26), with respect to z'. This yields the equations

$$\frac{\partial^2 S_{\ell,yi}(z)}{\partial(z')^2} = K_y E_\ell^{-1} K_x \frac{\partial U_{\ell,yi}(z)}{\partial z'} + \left(I - K_y E_\ell^{-1} K_y\right) \frac{\partial U_{\ell,xi}(z)}{\partial z'}, \tag{B.28}$$

$$\frac{\partial^2 S_{\ell,xi}(z)}{\partial(z')^2} = \left(K_x E_\ell^{-1} K_x - I\right) \frac{\partial U_{\ell,yi}(z)}{\partial z'} + K_x E_\ell^{-1} K_y \frac{\partial U_{\ell,xi}(z)}{\partial z'}, \tag{B.29}$$

$$\frac{\partial^2 U_{\ell,yi}(z)}{\partial(z')^2} = K_y K_x \frac{\partial S_{\ell,yi}(z)}{\partial z'} + \left(E_\ell - K_y^2\right) \frac{\partial S_{\ell,xi}(z)}{\partial z'}, \tag{B.30}$$

$$\frac{\partial^2 U_{\ell,yi}(z)}{\partial(z')^2} = \left(K_x^2 - E_\ell\right) \frac{\partial S_{\ell,yi}(z)}{\partial z'} + K_x K_y \frac{\partial S_{\ell,xi}(z)}{\partial z'}. \tag{B.31}$$

The first-order partial derivatives in Equations (B.28)–(B.31) are replaced by substituting from the set of coupled, single-order differential Equations (B.23)–(B.26). This results in either of the (2n x 2n) matrix equations

$$\begin{bmatrix} \dfrac{\partial^2 S_{\ell,y}(z)}{\partial (z')^2} \\ \dfrac{\partial^2 S_{\ell,x}(z)}{\partial (z')^2} \end{bmatrix} = \begin{bmatrix} K_x{}^2 + J_\ell E_\ell & K_y \left[E_\ell{}^{-1} K_x E_\ell - K_x \right] \\ K_x \left[E_\ell{}^{-1} K_y E_\ell - K_y \right] & K_y{}^2 + B_\ell E_\ell \end{bmatrix} \begin{bmatrix} S_{\ell,y}(z) \\ S_{\ell,x}(z) \end{bmatrix} \tag{B.32}$$

$$\begin{bmatrix} \dfrac{\partial^2 U_{\ell,y}(z)}{\partial (z')^2} \\ \dfrac{\partial^2 U_{\ell,x}(z)}{\partial (z')^2} \end{bmatrix} = \begin{bmatrix} K_y{}^2 + E_\ell B_\ell & \left[K_x - E_\ell K_x E_\ell{}^{-1} \right] K_y \\ \left[K_y - E_\ell K_y E_\ell{}^{-1} \right] K_x & K_x{}^2 + E_\ell D_\ell \end{bmatrix} \begin{bmatrix} U_{\ell,y}(z) \\ U_{\ell,x}(z) \end{bmatrix}, \tag{B.33}$$

where B_ℓ and D_ℓ are defined as

$$B_\ell = K_x E_\ell{}^{-1} K_x - I, \tag{B.34}$$

$$J_\ell = K_y E_\ell{}^{-1} K_y - I, \tag{B.35}$$

where I is the identity matrix.

For the special case when the diagonal matrix K_y is a unity matrix multiplied by a constant, as in the case for conical mount for a one-dimensional grating, further simplification is possible and Equations (B.32) and (B.33) reduce to the following two (n x n) matrix equations

$$\left[\dfrac{\partial^2 S_{\ell,x}(z)}{\partial (z')^2} \right] = \left[k_y{}^2 I + B_\ell E_\ell \right] \left[S_{\ell,x}(z) \right], \tag{B.36}$$

$$\left[\dfrac{\partial^2 U_{\ell,x}(z)}{\partial (z')^2} \right] = \left[k_y{}^2 I + A_\ell \right] \left[U_{\ell,x}(z) \right]. \tag{B.37}$$

The submatrix A_ℓ has dimensions (n x n) and is defined as

$$A_{\ell} = K_x^{\ 2} - E_{\ell}\,. \tag{B.38}$$

At this point a slight deviation from the formulation presented by Moharam, et al. [28] is made to incorporate the changes recommended by Li [38] to improve the speed of the convergence to an accurate solution. Recall that the accuracy of RCWA is a function of the number of space harmonics retained in the calculation. Also, that the number of space harmonics retained controls the dimensions of all the preceding matrix equations. Then, improving the speed of convergence corresponds to obtaining an accurate solution with fewer space harmonics, which implies solving matrix equations with smaller dimensions, thereby decreasing computational time required to obtain the solution.

The changes recommended by Li entail preserving continuity of the coupled-wave equations through proper formulation of the discontinuities in the permittivity function. For the case of conical diffraction considered here, this means modifying Equation (B.36) as shown in Equation (B.39):

$$\left[\frac{\partial^2 S_{\ell,x}(z)}{\partial (z')^2}\right] = \left[k_y^{\ 2} I + B_{\ell}\left(\frac{1}{E_{\ell}}\right)^{-1}\right]\left[S_{\ell,x}(z)\right]. \tag{B.39}$$

The solution as outlined by Moharam, et al. remains valid from this point forward. The set of coupled-wave equations given by Equations (B.39) and (B.37) are solved by calculating the eigenvalues and the eigenvectors associated with two (n x n) matrices. The reduction of the coupled wave equations from a (4n x 4n) system to a (n x n) system of equations reduces the eigenvalues' and the eigenvectors' computational time by a factor of 32. For the two-dimensional grating diffraction problem, the (2n x 2n) system of equations given in Equations (B.32) and (B.33) may be used to determine the eigenvalues and the eigenvectors for an improvement in the numerical efficiency of a factor of 4 over the original formulation.

The second-order coupled-wave equations in the grating region can now be solved. The solutions are the space harmonics of the tangential electric and magnetic fields in the grating layers and are given in Equations (B.40)-(B.43) below. Equation (B.40) is found directly from Equation (B.37) and Equation (B.41) is found directly from Equation (B.39). Equation (B.42) is obtained by substituting Equations (B.40) and (B.41) into Equation (B.25). Similarly, Equation (B.43) is obtained by substituting Equations (B.40) and (B.41) into Equation (B.24). The space harmonics are given by

$$U_{\ell,xi}(z)=\sum_{m=1}^{n} w_{\ell,1,i,m}\begin{Bmatrix} -c_{\ell,1,m}{}^{+}\exp\left[-k_0 q_{\ell,1,m}\left(z-D_{\ell-1}\right)\right] \\ +c_{\ell,1,m}{}^{-}\exp\left[k_0 q_{\ell,1,m}\left(z-D_{\ell}\right)\right] \end{Bmatrix}, \tag{B.40}$$

$$S_{\ell,xi}(z)=\sum_{m=1}^{n} w_{\ell,2,i,m}\begin{Bmatrix} c_{\ell,2,m}{}^{+}\exp\left[-k_0 q_{\ell,2,m}\left(z-D_{\ell-1}\right)\right] \\ +c_{\ell,2,m}{}^{-}\exp\left[k_0 q_{\ell,2,m}\left(z-D_{\ell}\right)\right] \end{Bmatrix}, \tag{B.41}$$

$$\begin{aligned} S_{\ell,yi}(z)=&\sum_{m=1}^{n} v_{\ell,11,i,m}\begin{Bmatrix} c_{\ell,1,m}{}^{+}\exp\left[-k_0 q_{\ell,2,m}\left(z-D_{\ell-1}\right)\right] \\ +c_{\ell,1,m}{}^{-}\exp\left[k_0 q_{\ell,1,m}\left(z-D_{\ell}\right)\right] \end{Bmatrix}+ \\ &\sum_{m=1}^{n} v_{\ell,12,i,m}\begin{Bmatrix} c_{\ell,2,m}{}^{+}\exp\left[-k_0 q_{\ell,2,m}\left(z-D_{\ell-1}\right)\right] \\ +c_{\ell,2,m}{}^{-}\exp\left[k_0 q_{\ell,2,m}\left(z-D_{\ell}\right)\right] \end{Bmatrix}, \end{aligned} \tag{B.42}$$

$$\begin{aligned} U_{\ell,yi}(z)=&\sum_{m=1}^{n} v_{\ell,21,i,m}\begin{Bmatrix} c_{\ell,1,m}{}^{+}\exp\left[-k_0 q_{\ell,2,m}\left(z-D_{\ell-1}\right)\right] \\ +c_{\ell,1,m}{}^{-}\exp\left[k_0 q_{\ell,1,m}\left(z-D_{\ell}\right)\right] \end{Bmatrix}+ \\ &\sum_{m=1}^{n} v_{\ell,22,i,m}\begin{Bmatrix} c_{\ell,2,m}{}^{+}\exp\left[-k_0 q_{\ell,2,m}\left(z-D_{\ell-1}\right)\right] \\ +c_{\ell,2,m}{}^{-}\exp\left[k_0 q_{\ell,2,m}\left(z-D_{\ell}\right)\right] \end{Bmatrix}, \end{aligned} \tag{B.43}$$

where $w_{\ell,1,i,m}$ and $q_{\ell,1,m}$ are the elements of the eigenvector matrix $W_{\ell,1}$ and the positive square root of the eigenvalues of the matrix $\left[k_y{}^2 I + A\right]$, respectively. The quantities $w_{\ell,2,i,m}$ and $q_{\ell,2,m}$ are the elements of the eigenvector matrix W_2 and the positive square root of the eigenvalues of the matrix $\left[k_y{}^2 I + B_\ell\left(\frac{1}{E_\ell}\right)^{-1}\right]$, respectively. The quantities $v_{\ell,11,i,m}$, $v_{\ell,12,i,m}$, $v_{\ell,21,i,m}$, and $v_{\ell,22,i,m}$ are the elements of the matrices $V_{\ell,11}$, $V_{\ell,12}$, $V_{\ell,21}$, and $V_{\ell,22}$ and are given by

$$V_{\ell,11} = A_\ell{}^{-1} W_{\ell,1} Q_{\ell 1}, \tag{B.44}$$

$$V_{\ell,12} = \left(k_y / k_0\right) A_\ell^{-1} K_x W_{\ell,2}, \tag{B.45}$$

$$V_{\ell,21} = \left(k_y / k_0\right) B_\ell^{-1} K_x E_\ell^{-1} W_{\ell,1}, \tag{B.46}$$

$$V_{\ell,22} = B_\ell^{-1} W_{\ell,2} Q_{\ell,2}, \tag{B.47}$$

where $Q_{\ell,1}$ and $Q_{\ell,2}$ are diagonal matrices with elements $q_{\ell,1,m}$ and $q_{\ell,2,m}$, respectively. The quantities $c_{\ell,1,m}^{+}$, $c_{\ell,1,m}^{-}$, $c_{\ell,2,m}^{+}$, and $c_{\ell,2,m}^{-}$ are the unknown coefficients, i.e., the ones to be determined from the boundary conditions. Also, D_ℓ is the total depth of the structure to the bottom of the ℓ^{th} layer and is defined as

$$D_\ell = \sum_{p=1}^{\ell} d_p . \tag{B.48}$$

Note that in the space-harmonic expressions, Equations (B.40)–(B.43), the exponential terms involving the positive square roots of the eigenvalues are normalized to prevent numerical overflow by ensuring that the arguments of the exponential are always negative.

The expressions for the fields in the grating region thus far have limited to those for grating layers, i.e., those layers with permittivity modulation. However, to generalize the algorithm to include homogeneous layers, it is necessary to develop expressions for the fields in those layers as well. These expressions are direct solutions of the wave equation. They are interpreted as the space harmonics of the tangential electric and magnetic fields in the homogeneous layers and can be written as

$$U_{\ell,xi}(z) = -\gamma_{\ell,i} PE_{\ell,i} \exp\left[-k_0\gamma_{\ell,i}\left(z - D_{\ell-1}\right)\right] + \gamma_{\ell,i} QE_{\ell,i} \exp\left[k_0\gamma_{\ell,i}\left(z - D_\ell\right)\right], \tag{B.49}$$

$$S_{\ell,xi}(z) = \frac{-\gamma_{\ell,i}}{n_\ell^2} PM_{\ell,i} \exp\left[-k_0\gamma_{\ell,i}\left(z - D_{\ell-1}\right)\right] + \frac{\gamma_{\ell,i}}{n_\ell^2} QM_{\ell,1} \exp\left[k_0\gamma_{\ell,i}\left(z - D_\ell\right)\right], \tag{B.50}$$

$$S_{\ell,yi}(z) = PE_{\ell,i} \exp\left[-k_0\gamma_{\ell,i}\left(z - D_{\ell-1}\right)\right] + QE_{\ell,i} \exp\left[k_0\gamma_{\ell.i}\left(z - D_\ell\right)\right], \tag{B.51}$$

$$U_{\ell,yi}(z) = PM_{\ell,i} \exp\left[-k_0\gamma_{\ell,i}\left(z - D_{\ell-1}\right)\right] + QM_{\ell,i} \exp\left[k_0\gamma_{\ell,i}\left(z - D_\ell\right)\right], \tag{B.52}$$

where

$$\gamma_{\ell,i} = j\left[n_\ell^{\,2} - \left(\frac{k_{xi}}{k_0}\right)^2 - \left(\frac{k_y}{k_0}\right)^2\right]^{1/2} . \qquad \text{(B.53)}$$

The quantities PE_ℓ and QE_ℓ are diagonal matrices with elements that are the electric field amplitudes in the homogeneous layer in the $+z$ direction and the $-z$ direction, respectively. Similarly, the quantities PM_ℓ and QM_ℓ are the magnetic field amplitudes in the homogeneous layer in the $+z$ direction and the $-z$ direction, respectively. They are the unknown coefficients that are to be calculated from the boundary conditions, similar to $c_{\ell,1,m}^{\;+}$, $c_{\ell,1,m}^{\;-}$, $c_{\ell,2,m}^{\;+}$, and $c_{\ell,2,m}^{\;-}$ for the case of a modulated layer. As discussed previously, PE_ℓ, QE_ℓ, PM_ℓ, and QM_ℓ are (n x n) matrices, where n is the number of space harmonics retained in the field expansion, with the i^{th} row of the matrix corresponding to the i^{th} space harmonic. The quantity $n_{\ell,h}$ is the refractive index of the homogeneous layer. Again, in the space-harmonic expressions, Equations (B.49)–(B.52), the exponential terms involving the positive square roots of the eigenvalues are normalized to prevent numerical overflow by ensuring that the arguments of the exponential are always negative.

This discussion of the RCWA algorithm has progressed to providing expressions for the tangential electric- and magnetic-field components in the regions external to the grating and for the tangential space-harmonics of the electric and magnetic fields inside the grating region for both modulated and homogeneous layers. In order to calculate the amplitudes of the diffracted fields in Regions I and II, i.e., R_i and T_i, the tangential field components (rotated into the diffraction plane) are matched at each of the layer boundaries in the multi-layer structure. This process will be illustrated by applying it to a structure such as the one seen in Figure B.2. In this case the first layer encountered beyond Region I is a homogeneous layer, with alternating grating and homogeneous layers following.

At the input boundary (i.e., z=0) the expressions for matching the tangential field components are

$$\sin\psi\delta_{i0} + R_{s,i} = \cos\varphi_i S_{1,yi}(0) - \sin\varphi_i S_{1,xi}(0), \tag{B.54}$$

$$j\left[\sin\psi\, n_I \cos\theta - \left(\frac{k_{I,zi}}{k_0}\right) R_{s,i}\right] = -\left[\cos\varphi_i\, U_{1,xi}(0) + \sin\varphi_i\, U_{1,yi}(0)\right], \tag{B.55}$$

$$\cos\psi\cos\theta - j\left[\frac{k_{I,zi}}{\left(k_0 n_I^{\,2}\right)}\right] R_{p,i} = \cos\varphi_i\, S_{1,xi}(0) + \sin\varphi_i\, S_{1,yi}(0), \tag{B.56}$$

$$-jn_I\cos\psi + R_{p,i} = -\left[\cos\varphi_i U_{1,yi}(0) - \sin\varphi_i U_{1,xi}(0)\right], \tag{B.57}$$

where $R_{s,i}$ and $R_{p,i}$ are the components of the amplitude of the electric- and the magnetic-field vectors, respectively, normal to the diffraction plane given by Equation (B.9). They may be considered the TE and the TM components of the reflected diffracted field and are defined as

$$R_{s,i} = \cos\varphi_i R_{yi} - \sin\varphi_i R_{xi}, \tag{B.58}$$

$$R_{p,i} = \left(\frac{-j}{k_0}\right)\left[\cos\varphi_i\left(k_{I,zi}R_{xi} - k_{xi}R_{zi}\right) - \sin\varphi_i\left(k_y R_{zi} + k_{I,zi}R_{yi}\right)\right].$$

Equations (B.54) through (B.57) are expressed in terms of the space harmonic expansions in a given layer. The specific form of the space harmonics is dependent on whether the layer is modulated or homogeneous. For the structure under consideration here the layer is homogeneous, so Equations (B. 54)-(B. 57) may be written in matrix form as

$$\begin{bmatrix} \sin\psi\delta_{i0} \\ j\sin\psi n_I\cos\theta\delta_{i0} \\ -j\cos\psi n_I\delta_{i0} \\ \cos\psi\cos\theta\delta_{i0} \end{bmatrix} + \begin{bmatrix} I & 0 \\ -jY_I & 0 \\ 0 & I \\ 0 & -jZ_I \end{bmatrix} \begin{bmatrix} R_s \\ R_p \end{bmatrix} = \tag{B.59}$$

$$\begin{bmatrix} F_c & F_s\Omega_1 & F_cG_1 & -F_s\Omega_1G_1 \\ F_c\Gamma_1 & -F_s & -F_c\Gamma_1G_1 & -F_sG_1 \\ -F_s\Gamma_1 & -F_c & F_s\Gamma_1G_1 & -F_cG_1 \\ F_s & -F_c\Omega_1 & F_sG_1 & F_c\Omega_1G_1 \end{bmatrix} \begin{bmatrix} PE_1 \\ PM_1 \\ QE_1 \\ QM_1 \end{bmatrix},$$

where Y_I is the diagonal matrix with elements $k_{I,zi}/k_0$ and Z_I is the diagonal matrix with elements $k_{I,zi}/\left(k_0 n_I^2\right)$. The matrices F_c and F_s are diagonal with elements $\cos\varphi_i$ and $\sin\varphi_i$, respectively. Also, Γ_1 is the diagonal matrix with elements γ_1, Ω_1 is the diagonal matrix with elements $\frac{\gamma_1}{n_1^2}$, and G_1 is the diagonal matrix with elements $\exp\left(-k_0\gamma_1 d_1\right)$.

Proceeding to the next layer boundary (i.e., $z = d_1 = D_1$), again, match the tangential field components. For this case the match occurs at the interface where the beam exits a homogeneous layer and enters a modulated, or grating layer. The space harmonic expressions at this interface are found by substituting the appropriate distance in the z-direction, $z = D_1$, and also substituting $D_{\ell-1} = 0$ to yield the matrix equation

$$\begin{bmatrix} F_cG_1 & F_s\Omega_1G_1 & F_c & -F_s\Omega_1 \\ F_c\Gamma_1G_1 & -F_sG_1 & -F_c\Gamma_1 & -F_s \\ -F_s\Gamma_1G_1 & -F_cG_1 & F_s\Gamma_1 & -F_c \\ F_sG_1 & -F_c\Omega_1G_1 & F_s & F_c\Omega_1 \end{bmatrix}\begin{bmatrix} PE_1 \\ PM_1 \\ QE_1 \\ QM_1 \end{bmatrix} = \begin{bmatrix} V_{2,ss} & V_{2,sp} & V_{2,ss}X_{2,1} & V_{2,sp}X_{2,2} \\ W_{2,ss} & W_{2,sp} & -W_{2,ss}X_{2,1} & -W_{2,sp}X_{2,2} \\ W_{2,ps} & W_{2,pp} & -W_{2,ps}X_{2,1} & -W_{2,pp}X_{2,2} \\ V_{2,ps} & V_{2,pp} & V_{2,ps}X_{2,1} & V_{2,pp}X_{2,2} \end{bmatrix}\begin{bmatrix} C_{2,1}^{+} \\ C_{2,2}^{+} \\ C_{2,1}^{-} \\ C_{2,2}^{-} \end{bmatrix}, \tag{B.60}$$

where

$$V_{\ell,ss} = F_c V_{\ell,11}, \tag{B.61}$$

$$W_{\ell,ss} = F_c W_{\ell,1} + F_s V_{\ell,21}, \tag{B.62}$$

$$V_{\ell,sp} = F_c V_{\ell,12} - F_s W_{\ell,2}, \tag{B.63}$$

$$W_{\ell,sp} = F_s V_{\ell,22}, \tag{B.64}$$

$$W_{\ell,pp} = F_c V_{\ell,22}, \tag{B.65}$$

$$V_{\ell,pp} = F_c W_{\ell,2} + F_s V_{\ell,12}, \tag{B.66}$$

$$W_{\ell,ps} = F_c V_{\ell,21} - F_s W_{\ell,1}, \tag{B.67}$$

$$V_{\ell,ps} = F_s V_{\ell,11}, \tag{B.68}$$

$X_{\ell,1}$ is the diagonal matrix with elements $\exp\left(-k_0 q_{\ell,1,m} d_\ell\right)$, $X_{\ell,2}$ is the diagonal matrix with elements $\exp\left(-k_0 q_{\ell,2,m} d_\ell\right)$, and d_ℓ is thickness of the layer. Also, $C_{\ell,1}{}^{+}$, $C_{\ell,2}{}^{+}$, $C_{\ell,1}{}^{-}$, and $C_{\ell,2}{}^{-}$ are diagonal matrices with elements $c_{\ell,1,m}{}^{+}$, $c_{\ell,2,m}{}^{+}$, $c_{\ell,1,m}{}^{-}$, and $c_{\ell,2,m}{}^{-}$, respectively.

Proceeding to the next layer boundary (i.e., $z = D_2$), again, match the tangential field components. For this case the match occurs at the interface where the beam exits a grating layer and enters a homogeneous layer. The space harmonic expressions at this interface are found by substituting the appropriate distance in the z-direction, $z = D_2$ and also substituting $D_{\ell-1} = D_1$ to yield the matrix equation

$$\begin{bmatrix} V_{2,ss}X_{2,1} & V_{2,sp}X_{2,2} & V_{2,ss} & V_{2,sp} \\ W_{2,ss}X_{2,1} & W_{2,sp}X_{2,2} & -W_{2,ss} & -W_{2,sp} \\ W_{2,ps}X_{2,1} & W_{2,pp}X_{2,2} & -W_{2,ps} & -W_{2,pp} \\ V_{2,ps}X_{2,1} & V_{2,pp}X_{2,2} & V_{2,ps} & V_{2,pp} \end{bmatrix} \begin{bmatrix} C_{2,1}{}^{+} \\ C_{2,2}{}^{+} \\ C_{2,1}{}^{-} \\ C_{2,2}{}^{-} \end{bmatrix} = \begin{bmatrix} F_c & F_s\Omega_3 & F_cG_3 & -F_s\Omega_3G_3 \\ F_c\Gamma_3 & -F_s & -F_c\Gamma_3G_3 & -F_sG_3 \\ -F_s\Gamma_3 & -F_c & F_s\Gamma_3G_3 & -F_cG_3 \\ F_s & -F_c\Omega_3 & F_sG_3 & F_c\Omega_3G_3 \end{bmatrix} \begin{bmatrix} PE_3 \\ PM_3 \\ QE_3 \\ QM_3 \end{bmatrix} . \tag{B.69}$$

Continuing to the final boundary, the interface occurs where the beam exits a grating layer and enters Region II, i.e., it is transmitted into the exiting media. The expressions for matching the tangential field components are given by

$$\cos\varphi_i S_{yi}(d) - \sin\varphi_i S_{xi}(d) = T_{s,i}, \tag{B.70}$$

$$-\left[\cos\varphi_i U_{xi}(d) + \sin\varphi_i U_{yi}(d)\right] = j\left(\frac{k_{II,zi}}{k_0}\right) T_{s,i}, \tag{B.71}$$

$$-\left[\cos\varphi_i U_{yi}(d) + \sin\varphi_i U_{xi}(d)\right] = T_{p,i}, \tag{B.72}$$

$$\cos\varphi_i S_{xi}(d) + \sin\varphi_i S_{yi}(d) = j\left(\frac{k_{II,zi}}{k_0 {n_I}^2}\right) T_{p,i}, \tag{B.73}$$

where $T_{s,i}$ and $T_{p,i}$ are the components of the amplitude of the electric- and the magnetic-field vectors normal to the diffraction plane given by Equation (B.9). They may be considered the TE and the TM components of the transmitted diffracted field and are defined as

$$T_{s,i} = \cos\phi_i T_{yi} - \sin\phi_i T_{xi}, \tag{B.74}$$

$$T_{p,i} = \left(\frac{-j}{k_0}\right)\left[\cos\phi_i\left(k_{II,zi}T_{xi} - k_{xi}T_{zi}\right) - \sin\phi_i\left(k_y T_{zi} - k_{II,zi}T_{yi}\right)\right]. \tag{B.75}$$

Equations (B.70)–(B.73) can be written as a matrix equation with a formulation given by

$$\begin{bmatrix} V_{L,ss}X_{L,1} & V_{L,sp}X_{L,2} & V_{L,ss} & V_{L,sp} \\ W_{L,ss}X_{L,1} & W_{L,sp}X_{L,2} & -W_{L,ss} & -W_{L,sp} \\ W_{L,ps}X_{L,1} & W_{L,pp}X_{L,2} & -W_{L,ps} & -W_{L,pp} \\ V_{L,ps}X_{L,1} & V_{L,pp}X_{L,2} & V_{L,ps} & V_{L,pp} \end{bmatrix} \begin{bmatrix} {C_{L,1}}^+ \\ {C_{L,2}}^+ \\ {C_{L,1}}^- \\ {C_{L,2}}^- \end{bmatrix} = \begin{bmatrix} I & 0 \\ jY_{II} & 0 \\ 0 & I \\ 0 & jZ_{II} \end{bmatrix} \begin{bmatrix} T_s \\ T_p \end{bmatrix}, \tag{B.76}$$

where Y_{II} is the diagonal matrix with elements $k_{II,zi}/k_0$ and Z_{II} is the diagonal matrix with elements $k_{II,zi}/\left(k_0 {n_{II}}^2\right)$.

Examination of the right-hand-side of Equation (B.59) shows that the matrix representation for the tangential field components when entering a homogeneous layer is given by

$$\begin{bmatrix} F_c & F_s\Omega_\ell & F_c G_\ell & -F_s\Omega_\ell G_\ell \\ F_c\Gamma_\ell & -F_s & -F_c\Gamma_\ell G_\ell & -F_s G_\ell \\ -F_s\Gamma_\ell & -F_c & F_s\Gamma_\ell G_\ell & -F_c G_\ell \\ F_s & -F_c\Omega_\ell & F_s G_\ell & F_c\Omega_\ell G_\ell \end{bmatrix} \begin{bmatrix} PE_\ell \\ PM_\ell \\ QE_\ell \\ QM_\ell \end{bmatrix}. \tag{B.77}$$

Similarly, the left-hand-side of Equation (B.60) shows that the matrix representation for the tangential field components when exiting a homogeneous layer is as given by

$$\begin{bmatrix} \mathrm{F_c G_\ell} & \mathrm{F_s \Omega_\ell G_\ell} & \mathrm{F_c} & -\mathrm{F_s \Omega_\ell} \\ \mathrm{F_c \Gamma_\ell G_\ell} & -\mathrm{F_s G_\ell} & -\mathrm{F_c \Gamma_\ell} & -\mathrm{F_s} \\ -\mathrm{F_s \Gamma_\ell G_\ell} & -\mathrm{F_c G_\ell} & \mathrm{F_s \Gamma_\ell} & -\mathrm{F_c} \\ \mathrm{F_s G_\ell} & -\mathrm{F_c \Omega_\ell G_\ell} & \mathrm{F_s} & \mathrm{F_c \Omega_\ell} \end{bmatrix} \begin{bmatrix} \mathrm{PE}_\ell \\ \mathrm{PM}_\ell \\ \mathrm{QE}_\ell \\ \mathrm{QM}_\ell \end{bmatrix}. \tag{B.78}$$

The corresponding matrices for fields entering and exiting grating layers are given in the right-hand-side of Equation (B.60) and the left-hand-side of Equation (B.69), respectively For convenience, they are presented here again as

$$\begin{bmatrix} \mathrm{V}_{\ell,\mathrm{ss}} & \mathrm{V}_{\ell,\mathrm{sp}} & \mathrm{V}_{\ell,\mathrm{ss}}\mathrm{X}_{\ell,1} & \mathrm{V}_{\ell,\mathrm{sp}}\mathrm{X}_{\ell,2} \\ \mathrm{W}_{\ell,\mathrm{ss}} & \mathrm{W}_{\ell,\mathrm{sp}} & -\mathrm{W}_{\ell,\mathrm{ss}}\mathrm{X}_{\ell,1} & -\mathrm{W}_{\ell,\mathrm{sp}}\mathrm{X}_{\ell,2} \\ \mathrm{W}_{\ell,\mathrm{ps}} & \mathrm{W}_{\ell,\mathrm{pp}} & -\mathrm{W}_{\ell,\mathrm{ps}}\mathrm{X}_{\ell,1} & -\mathrm{W}_{\ell,\mathrm{pp}}\mathrm{X}_{\ell,2} \\ \mathrm{V}_{\ell,\mathrm{ps}} & \mathrm{V}_{\ell,\mathrm{pp}} & \mathrm{V}_{\ell,\mathrm{ps}}\mathrm{X}_{\ell,1} & \mathrm{V}_{\ell,\mathrm{pp}}\mathrm{X}_{\ell,2} \end{bmatrix} \begin{bmatrix} \mathrm{C}_{\ell,1}{}^{+} \\ \mathrm{C}_{\ell,2}{}^{+} \\ \mathrm{C}_{\ell,1}{}^{-} \\ \mathrm{C}_{\ell,2}{}^{-} \end{bmatrix} \text{ and} \tag{B.79}$$

$$\begin{bmatrix} \mathrm{V}_{\ell,\mathrm{ss}}\mathrm{X}_{\ell,1} & \mathrm{V}_{\ell,\mathrm{sp}}\mathrm{X}_{\ell,2} & \mathrm{V}_{\ell,\mathrm{ss}} & \mathrm{V}_{\ell,\mathrm{sp}} \\ \mathrm{W}_{\ell,\mathrm{ss}}\mathrm{X}_{\ell,1} & \mathrm{W}_{\ell,\mathrm{sp}}\mathrm{X}_{\ell,2} & -\mathrm{W}_{\ell,\mathrm{ss}} & -\mathrm{W}_{\ell,\mathrm{sp}} \\ \mathrm{W}_{\ell,\mathrm{ps}}\mathrm{X}_{\ell,1} & \mathrm{W}_{\ell,\mathrm{pp}}\mathrm{X}_{\ell,2} & -\mathrm{W}_{\ell,\mathrm{ps}} & -\mathrm{W}_{\ell,\mathrm{pp}} \\ \mathrm{V}_{\ell,\mathrm{ps}}\mathrm{X}_{\ell,1} & \mathrm{V}_{\ell,\mathrm{pp}}\mathrm{X}_{\ell,2} & \mathrm{V}_{\ell,\mathrm{ps}} & \mathrm{V}_{\ell,\mathrm{pp}} \end{bmatrix} \begin{bmatrix} \mathrm{C}_{\ell,1}{}^{+} \\ \mathrm{C}_{\ell,2}{}^{+} \\ \mathrm{C}_{\ell,1}{}^{-} \\ \mathrm{C}_{\ell,2}{}^{-} \end{bmatrix}.$$

Considering Equation (B.77) and the first matrix product in Equation (B.79), the matrices have a common format (i.e., dimensions, row and column position of exponential terms) which can be expressed as

$$\begin{bmatrix} \mathrm{A}_{\ell,11} & \mathrm{A}_{\ell,12} & \mathrm{A}_{\ell,11}\mathrm{XX}_{\ell,1} & \mathrm{A}_{\ell,12}\mathrm{XX}_{\ell,2} \\ \mathrm{A}_{\ell,21} & \mathrm{A}_{\ell,22} & \mathrm{A}_{\ell,21}\mathrm{XX}_{\ell,1} & \mathrm{A}_{\ell,22}\mathrm{XX}_{\ell,2} \\ \mathrm{A}_{\ell,31} & \mathrm{A}_{\ell,32} & \mathrm{A}_{\ell,31}\mathrm{XX}_{\ell,1} & \mathrm{A}_{\ell,32}\mathrm{XX}_{\ell,2} \\ \mathrm{A}_{\ell,41} & \mathrm{A}_{\ell,42} & \mathrm{A}_{\ell,41}\mathrm{XX}_{\ell,1} & \mathrm{A}_{\ell,42}\mathrm{XX}_{\ell,2} \end{bmatrix} \begin{bmatrix} \mathrm{D}_{\ell,1} \\ \mathrm{D}_{\ell,2} \\ \mathrm{D}_{\ell,3} \\ \mathrm{D}_{\ell,4} \end{bmatrix}. \tag{B.80}$$

Similarly, Equation (B.78) and the second matrix product in Equation (B. 79) also have a common format, which is given as

$$\begin{bmatrix} \mathrm{A}_{\ell,11}\mathrm{XX}_{\ell,1} & \mathrm{A}_{\ell,12}\mathrm{XX}_{\ell,2} & \mathrm{A}_{\ell,11} & \mathrm{A}_{\ell,12} \\ \mathrm{A}_{\ell,21}\mathrm{XX}_{\ell,1} & \mathrm{A}_{\ell,22}\mathrm{XX}_{\ell,2} & \mathrm{A}_{\ell,21} & \mathrm{A}_{\ell,22} \\ \mathrm{A}_{\ell,31}\mathrm{XX}_{\ell,1} & \mathrm{A}_{\ell,32}\mathrm{XX}_{\ell,2} & \mathrm{A}_{\ell,31} & \mathrm{A}_{\ell,32} \\ \mathrm{A}_{\ell,41}\mathrm{XX}_{\ell,1} & \mathrm{A}_{\ell,42}\mathrm{XX}_{\ell,2} & \mathrm{A}_{\ell,41} & \mathrm{A}_{\ell,42} \end{bmatrix} \begin{bmatrix} \mathrm{D}_{\ell,1} \\ \mathrm{D}_{\ell,2} \\ \mathrm{D}_{\ell,3} \\ \mathrm{D}_{\ell,4} \end{bmatrix}. \tag{B.81}$$

The capability to express the space-harmonic matrices of grating layers and homogeneous layers in a common format permits implementation of a computational algorithm which is independent of the number of layers in a grating structure, the type of layers, and the ordering of the constituent layers. Such an algorithm is very flexible when applied to the analysis of periodic structures. The remaining restrictions on such an algorithm are that all grating layers have identical period and that each grating layer consist of only two materials. The latter restriction can be addressed in the Fourier series expansion of the permittivity of a grating layer.

After obtaining equations for the matching tangential field components at each layer boundary, a system of equations exists that can be solved for R_{i} and T_{i} by standard techniques. This can be accomplished without any numerical instability for any number of grating layers, any layer thickness, or any number of refractive indices. The possibility for numerical inaccuracy, such as overflow, has been preempted by normalization of the exponential terms in the space harmonic expansions. The difficulty with such a solution is that, for a large number of layers, the system of equations also becomes large and can be computationally inefficient. A transmittance matrix approach can be applied to reduce the size of a system of simultaneous equations. However, the approach itself can introduce additional numerical instability. This problem can be eliminated by applying enhanced transmittance techniques to the reduced system of equations to obtain a final solution. Both the transmittance matrix approach and the enhanced transmittance matrix techniques will be applied to solve the system of equations here.

The transmittance matrix approach is used to eliminate the intermediate coefficients in the system of equations and solve directly for the field amplitudes R_{i} and T_{i}. Begin the process with the matrix equation for the matched tangential field components at the last boundary in the system $(\ell = \mathrm{L})$ as shown in

$$\begin{bmatrix} A_{L,11}XX_{L,1} & A_{L,12}XX_{L,2} & A_{L,11} & A_{L,12} \\ A_{L,21}XX_{L,1} & A_{L,22}XX_{L,2} & A_{L,21} & A_{L,22} \\ A_{L,31}XX_{L,1} & A_{L,32}XX_{L,2} & A_{L,31} & A_{L,32} \\ A_{L,41}XX_{L,1} & A_{L,42}XX_{L,2} & A_{L,41} & A_{L,42} \end{bmatrix} \begin{bmatrix} D_{L,1} \\ D_{L,2} \\ D_{L,3} \\ D_{L,4} \end{bmatrix} = \begin{bmatrix} I & 0 \\ jY_{II} & 0 \\ 0 & I \\ 0 & Z_{II} \end{bmatrix} \begin{bmatrix} T_s \\ T_p \end{bmatrix}. \tag{B.82}$$

Invert the space harmonic matrix from above to arrive at an expression in terms of the coefficients as given by

$$\begin{bmatrix} D_{L,1} \\ D_{L,2} \\ D_{L,3} \\ D_{L,4} \end{bmatrix} = \begin{bmatrix} A_{L,11}XX_{L,1} & A_{L,12}XX_{L,2} & A_{L,11} & A_{L,12} \\ A_{L,21}XX_{L,1} & A_{L,22}XX_{L,2} & A_{L,21} & A_{L,22} \\ A_{L,31}XX_{L,1} & A_{L,32}XX_{L,2} & A_{L,31} & A_{L,32} \\ A_{L,41}XX_{L,1} & A_{L,42}XX_{L,2} & A_{L,41} & A_{L,42} \end{bmatrix}^{-1} \begin{bmatrix} I & 0 \\ jY_{II} & 0 \\ 0 & I \\ 0 & Z_{II} \end{bmatrix} \begin{bmatrix} T_s \\ T_p \end{bmatrix}. \tag{B.83}$$

Substitute from Equation (B.83) into the equation at the previous boundary $(\ell = L-1)$ to obtain the following matrix equation

$$\begin{bmatrix} A_{L-1,11}XX_{L-1,1} & A_{L-1,12}XX_{L-1,2} & A_{L-1,11} & A_{L-1,12} \\ A_{L-1,21}XX_{L-1,1} & A_{L-1,22}XX_{L-1,2} & A_{L-1,21} & A_{L-1,22} \\ A_{L-1,31}XX_{L-1,1} & A_{L-1,32}XX_{L-1,2} & A_{L-1,31} & A_{L-1,32} \\ A_{L-1,41}XX_{L-1,1} & A_{L-1,42}XX_{L-1,2} & A_{L-1,41} & A_{L-1,42} \end{bmatrix} \begin{bmatrix} D_{L-1,1} \\ D_{L-1,2} \\ D_{L-1,3} \\ D_{L-1,4} \end{bmatrix} =$$

$$\begin{bmatrix} A_{L,11} & A_{L,12} & A_{L,11}XX_{L,1} & A_{L,12}XX_{L,2} \\ A_{L,21} & A_{L,22} & A_{L,21}XX_{L,1} & A_{L,22}XX_{L,2} \\ A_{L,31} & A_{L,32} & A_{L,31}XX_{L,1} & A_{L,32}XX_{L,2} \\ A_{L,41} & A_{L,42} & A_{L,41}XX_{L,1} & A_{L,42}XX_{L,2} \end{bmatrix} \quad . \tag{B.84}$$

$$\begin{bmatrix} A_{L,11}XX_{L,1} & A_{L,12}XX_{L,2} & A_{L,11} & A_{L,12} \\ A_{L,21}XX_{L,1} & A_{L,22}XX_{L,2} & A_{L,21} & A_{L,22} \\ A_{L,31}XX_{L,1} & A_{L,32}XX_{L,2} & A_{L,31} & A_{L,32} \\ A_{L,41}XX_{L,1} & A_{L,42}XX_{L,2} & A_{L,41} & A_{L,42} \end{bmatrix}^{-1} \begin{bmatrix} I & 0 \\ jY_{II} & 0 \\ 0 & I \\ 0 & Z_{II} \end{bmatrix} \begin{bmatrix} T_s \\ T_p \end{bmatrix}$$

This process is repeated for the remaining layer boundaries to arrive at a representation for the entire system of equations that may be written as

$$\begin{bmatrix} \sin\psi\delta_{i0} \\ j\sin\psi n_I \cos\theta\delta_{i0} \\ -j\cos\psi n_I\delta_{i0} \\ \cos\psi\cos\theta\delta_{i0} \end{bmatrix} + \begin{bmatrix} I & 0 \\ -jY_I & 0 \\ 0 & I \\ 0 & -jZ_I \end{bmatrix} \begin{bmatrix} R_s \\ R_p \end{bmatrix} \tag{B.85}$$

$$=\prod_{\ell=1}^{L}\begin{bmatrix} A_{\ell,11} & A_{\ell,12} & A_{\ell,11}XX_{\ell,1} & A_{\ell,12}XX_{\ell,2} \\ A_{\ell,21} & A_{\ell,22} & A_{\ell,21}XX_{\ell,1} & A_{\ell,22}XX_{\ell,2} \\ A_{\ell,31} & A_{\ell,32} & A_{\ell,31}XX_{\ell,1} & A_{\ell,32}XX_{\ell,2} \\ A_{\ell,41} & A_{\ell,42} & A_{\ell,41}XX_{\ell,1} & A_{\ell,42}XX_{\ell,2} \end{bmatrix}$$

$$\times\begin{bmatrix} A_{\ell,11}XX_{\ell,1} & A_{\ell,12}XX_{\ell,2} & A_{\ell,11} & A_{\ell,12} \\ A_{\ell,21}XX_{\ell,1} & A_{\ell,22}XX_{\ell,2} & A_{\ell,21} & A_{\ell,22} \\ A_{\ell,31}XX_{\ell,1} & A_{\ell,32}XX_{\ell,2} & A_{\ell,31} & A_{\ell,32} \\ A_{\ell,41}XX_{\ell,1} & A_{\ell,42}XX_{\ell,2} & A_{\ell,41} & A_{\ell,42} \end{bmatrix}^{-1}\begin{bmatrix} I & 0 \\ jY_{II} & 0 \\ 0 & I \\ 0 & jZ_{II} \end{bmatrix}\begin{bmatrix} T_s \\ T_p \end{bmatrix}.$$

The previous equation includes one matrix inversion for each layer. The matrix to be inverted may become ill-conditioned, e.g., the exponential terms may approach zero, for the case of lossy media or an evanescent wave. Inversion of an ill-conditioned matrix may produce elements with large values that cannot be represented within the numerical accuracy of a computer. Thus, the introduction of transmittance techniques has the potential to introduce errors into the solution or cause the system not to converge properly. This problem can be addressed by enhanced transmittance matrix techniques. Begin by examining the final three matrices in Equation (B.85), which are given by

$$\begin{bmatrix} A_{L,11}XX_{L,1} & A_{L,12}XX_{L,2} & A_{L,11} & A_{L,12} \\ A_{L,21}XX_{L,1} & A_{L,22}XX_{L,2} & A_{L,21} & A_{L,22} \\ A_{L,31}XX_{L,1} & A_{L,32}XX_{L,2} & A_{L,31} & A_{L,32} \\ A_{L,41}XX_{L,1} & A_{L,42}XX_{L,2} & A_{L,41} & A_{L,42} \end{bmatrix}^{-1}\begin{bmatrix} I & 0 \\ jY_{II} & 0 \\ 0 & I \\ 0 & jZ_{II} \end{bmatrix}\begin{bmatrix} T_s \\ T_p \end{bmatrix}. \tag{B.86}$$

The space-harmonic matrix to be inverted may be factored to separate the exponential terms as

$$\begin{bmatrix} XX_{L,1} & 0 & 0 & 0 \\ 0 & XX_{L,2} & 0 & 0 \\ 0 & 0 & I & 0 \\ 0 & 0 & 0 & I \end{bmatrix}^{-1}\begin{bmatrix} A_{L,11} & A_{L,12} & A_{L,11} & A_{L,12} \\ A_{L,21} & A_{L,22} & A_{L,21} & A_{L,22} \\ A_{L,31} & A_{L,32} & A_{L,31} & A_{L,32} \\ A_{L,41} & A_{L,42} & A_{L,41} & A_{L,42} \end{bmatrix}^{-1}\begin{bmatrix} I & 0 \\ jY_{II} & 0 \\ 0 & I \\ 0 & jZ_{II} \end{bmatrix}\begin{bmatrix} T_s \\ T_p \end{bmatrix}. \tag{B.87}$$

Of the two matrices to be inverted in Equation (B.87), the one on the right may be inverted without numerical instability. The overall product may be simplified by multiplying the two matrices in the middle in Equation (B. 87) as illustrated by

$$\begin{bmatrix} a_{11} & a_{12} \\ a_{21} & a_{22} \\ a_{31} & a_{32} \\ a_{41} & a_{42} \end{bmatrix} = \begin{bmatrix} A_{L,11} & A_{L,12} & A_{L,11} & A_{L,12} \\ A_{L,21} & A_{L,22} & A_{L,21} & A_{L,22} \\ A_{L,31} & A_{L,32} & A_{L,31} & A_{L,32} \\ A_{L,41} & A_{L,42} & A_{L,41} & A_{L,42} \end{bmatrix}^{-1} \begin{bmatrix} I & 0 \\ jY_{II} & 0 \\ 0 & I \\ 0 & jZ_{II} \end{bmatrix}. \tag{B.88}$$

Equation (B.87) may then be written as

$$\begin{bmatrix} XX_{L,1} & 0 & 0 & 0 \\ 0 & XX_{L,2} & 0 & 0 \\ 0 & 0 & I & 0 \\ 0 & 0 & 0 & I \end{bmatrix}^{-1} \begin{bmatrix} a_{11} & a_{12} \\ a_{21} & a_{22} \\ a_{31} & a_{32} \\ a_{41} & a_{42} \end{bmatrix} \begin{bmatrix} T_s \\ T_p \end{bmatrix}. \tag{B.89}$$

This equation may be simplified further by making the following substitutions

$$XX_L = \begin{bmatrix} XX_{L,1} & 0 \\ 0 & XX_{L,2} \end{bmatrix}, \tag{B.90}$$

$$II = \begin{bmatrix} I & 0 \\ 0 & I \end{bmatrix}, \tag{B.91}$$

$$a_L = \begin{bmatrix} a_{11} & a_{12} \\ a_{21} & a_{22} \end{bmatrix}, \tag{B.92}$$

$$b_L = \begin{bmatrix} a_{31} & a_{32} \\ a_{41} & a_{42} \end{bmatrix}, \tag{B.93}$$

$$T = \begin{bmatrix} T_s \\ T_p \end{bmatrix}, \tag{B.94}$$

which implies that the simplified equation may then be written as

$$\begin{bmatrix} XX_L & 0 \\ 0 & II \end{bmatrix}^{-1} \begin{bmatrix} a_L \\ b_L \end{bmatrix} T. \tag{B.95}$$

The one matrix remaining to be inverted can be ill-conditioned and can produce numerical instability as discussed previously. This problem can be avoided by making the substitution

$$T = a_L{}^{-1} XX_L T_L, \tag{B.96}$$

which permits Equation (B.95) to be written as

$$\begin{bmatrix} \mathrm{II} \\ \mathrm{b_L a_L}^{-1}\mathrm{XX_L} \end{bmatrix} \mathrm{T_L} \,. \tag{B.97}$$

This process has simplified the last three matrices of Equation (B.85). However, there is one matrix remaining in the product for each layer of the structure that must also be considered. This is written as

$$\begin{bmatrix} \mathrm{A_{L,11}} & \mathrm{A_{L,12}} & \mathrm{A_{L,11}XX_{L,1}} & \mathrm{A_{L,12}XX_{L,2}} \\ \mathrm{A_{L,21}} & \mathrm{A_{L,22}} & \mathrm{A_{L,21}XX_{L,1}} & \mathrm{A_{L,22}XX_{L,2}} \\ \mathrm{A_{L,31}} & \mathrm{A_{L,32}} & \mathrm{A_{L,31}XX_{L,1}} & \mathrm{A_{L,32}XX_{L,2}} \\ \mathrm{A_{L,41}} & \mathrm{A_{L,42}} & \mathrm{A_{L,41}XX_{L,1}} & \mathrm{A_{L,42}XX_{L,2}} \end{bmatrix} \begin{bmatrix} \mathrm{II} \\ \mathrm{b_L a_L}^{-1}\mathrm{XX_L} \end{bmatrix} \mathrm{T_L} \,. \tag{B.98}$$

The matrix on the left may be factored to separate the exponential components, as was done in Equation (B.87). For this case, the factors become

$$\begin{bmatrix} \mathrm{A_{L,11}} & \mathrm{A_{L,12}} & \mathrm{A_{L,11}} & \mathrm{A_{L,12}} \\ \mathrm{A_{L,21}} & \mathrm{A_{L,22}} & \mathrm{A_{L,21}} & \mathrm{A_{L,22}} \\ \mathrm{A_{L,31}} & \mathrm{A_{L,32}} & \mathrm{A_{L,31}} & \mathrm{A_{L,32}} \\ \mathrm{A_{L,41}} & \mathrm{A_{L,42}} & \mathrm{A_{L,41}} & \mathrm{A_{L,42}} \end{bmatrix} \begin{bmatrix} \mathrm{I} & 0 & 0 & 0 \\ 0 & \mathrm{I} & 0 & 0 \\ 0 & 0 & \mathrm{XX_{L,1}} & 0 \\ 0 & 0 & 0 & \mathrm{XX_{L,2}} \end{bmatrix} \begin{bmatrix} \mathrm{II} \\ \mathrm{b_L a_L}^{-1}\mathrm{XX_L} \end{bmatrix} \mathrm{T_L} \,. \tag{B.99}$$

The substitutions from Equations (B.90) and (B.91) can be made to simplify the previous expression such that it becomes

$$\begin{bmatrix} \mathrm{A_{L,11}} & \mathrm{A_{L,12}} & \mathrm{A_{L,11}} & \mathrm{A_{L,12}} \\ \mathrm{A_{L,21}} & \mathrm{A_{L,22}} & \mathrm{A_{L,21}} & \mathrm{A_{L,22}} \\ \mathrm{A_{L,31}} & \mathrm{A_{L,32}} & \mathrm{A_{L,31}} & \mathrm{A_{L,32}} \\ \mathrm{A_{L,41}} & \mathrm{A_{L,42}} & \mathrm{A_{L,41}} & \mathrm{A_{L,42}} \end{bmatrix} \begin{bmatrix} \mathrm{II} & 0 \\ 0 & \mathrm{XX_L} \end{bmatrix} \begin{bmatrix} \mathrm{II} \\ \mathrm{b_L a_L}^{-1}\mathrm{XX_L} \end{bmatrix} \mathrm{T_L} \,, \tag{B.100}$$

and the product of the two matrices in the middle is performed to yield

$$\begin{bmatrix} \mathrm{A_{L,11}} & \mathrm{A_{L,12}} & \mathrm{A_{L,11}} & \mathrm{A_{L,12}} \\ \mathrm{A_{L,21}} & \mathrm{A_{L,22}} & \mathrm{A_{L,21}} & \mathrm{A_{L,22}} \\ \mathrm{A_{L,31}} & \mathrm{A_{L,32}} & \mathrm{A_{L,31}} & \mathrm{A_{L,32}} \\ \mathrm{A_{L,41}} & \mathrm{A_{L,42}} & \mathrm{A_{L,41}} & \mathrm{A_{L,42}} \end{bmatrix} \begin{bmatrix} \mathrm{II} \\ \mathrm{XX_L b_L a_L}^{-1}\mathrm{XX_L} \end{bmatrix} \mathrm{T_L} \,. \tag{B.101}$$

Finally, the matrix product in the expression above may be represented by the substitution

$$\begin{bmatrix} A'_{L,11} & A'_{L,12} \\ A'_{L,21} & A'_{L,22} \\ A'_{L,31} & A'_{L,32} \\ A'_{L,41} & A'_{L,42} \end{bmatrix} = \begin{bmatrix} A_{L,11} & A_{L,12} & A_{L,11} & A_{L,12} \\ A_{L,21} & A_{L,22} & A_{L,21} & A_{L,22} \\ A_{L,31} & A_{L,32} & A_{L,31} & A_{L,32} \\ A_{L,41} & A_{L,42} & A_{L,41} & A_{L,42} \end{bmatrix} \begin{bmatrix} II \\ XX_L b_L a_L{}^{-1} XX_L \end{bmatrix}, \tag{B.102}$$

to yield a final matrix product for the layer under consideration,

$$\begin{bmatrix} A'_{L,11} & A'_{L,12} \\ A'_{L,21} & A'_{L,22} \\ A'_{L,31} & A'_{L,32} \\ A'_{L,41} & A'_{L,42} \end{bmatrix} \begin{bmatrix} T_{L,s} \\ T_{L,p} \end{bmatrix}. \tag{B.103}$$

The above procedure is repeated for all layers such that Equation (B.85) is reduced to a final equation for the system, which is represented as

$$\begin{bmatrix} \sin\psi\delta_{i0} \\ j\sin\psi n_I \cos\theta\delta_{i0} \\ -j\cos\psi n_I\delta_{i0} \\ \cos\psi\cos\theta\delta_{i0} \end{bmatrix} + \begin{bmatrix} I & 0 \\ -jY_I & 0 \\ 0 & I \\ 0 & -jZ_I \end{bmatrix} \begin{bmatrix} R_s \\ R_p \end{bmatrix} = \begin{bmatrix} A'_{11} & A'_{12} \\ A'_{21} & A'_{22} \\ A'_{31} & A'_{32} \\ A'_{41} & A'_{42} \end{bmatrix} \begin{bmatrix} T_{1,s} \\ T_{1,p} \end{bmatrix}, \tag{B.104}$$

where $T = a_L{}^{-1}XX_L a_{L-1}{}^{-1}XX_{L-1} \ldots a_2{}^{-1}XX_2 a_1{}^{-1}XX_1 T_1$.

Equation (B.104) may then be reduced to a form which is easily solved for R_i and T_i without numerical instability. An intermediate step in this rearrangement is

$$\begin{bmatrix} -I & 0 & A'_{11} & A'_{12} \\ jY_I & 0 & A'_{21} & A'_{22} \\ 0 & -I & A'_{31} & A'_{32} \\ 0 & jZ_I & A'_{41} & A'_{42} \end{bmatrix} \begin{bmatrix} R_s \\ R_p \\ T_{1,s} \\ T_{1,p} \end{bmatrix} = \begin{bmatrix} \sin\psi\delta_{i0} \\ j\sin\psi n_I \cos\theta\delta_{i0} \\ -j\cos\psi n_I\delta_{i0} \\ \cos\psi\cos\theta\delta_{i0} \end{bmatrix}, \tag{B.105}$$

and the final representation is given by

$$\begin{bmatrix} R_s \\ R_p \\ T_{1,s} \\ T_{1,p} \end{bmatrix} = \begin{bmatrix} -I & 0 & A'_{11} & A'_{12} \\ jY_I & 0 & A'_{21} & A'_{22} \\ 0 & -I & A'_{31} & A'_{32} \\ 0 & jZ_I & A'_{41} & A'_{42} \end{bmatrix}^{-1} \begin{bmatrix} \sin\psi\delta_{i0} \\ j\sin\psi n_I \cos\theta\delta_{i0} \\ -j\cos\psi n_I\delta_{i0} \\ \cos\psi\cos\theta\delta_{i0} \end{bmatrix}. \tag{B.106}$$

The diffraction efficiencies are defined by the expressions

$$DE_{ri} = \left|R_{s,i}\right|^2 \mathrm{Re}\left(\frac{k_{I,zi}}{k_0 n_I \cos\theta}\right) + \left|R_{p,i}\right|^2 \mathrm{Re}\left(\frac{\dfrac{k_{II,zi}}{n_I{}^2}}{k_0 n_I \cos\theta}\right), \tag{B.107}$$

$$DE_{ti} = \left|T_{s,i}\right|^2 \mathrm{Re}\left(\frac{k_{II,zi}}{k_0 n_I \cos\theta}\right) + \left|T_{p,i}\right|^2 \mathrm{Re}\left(\frac{\dfrac{k_{II,zi}}{n_{II}{}^2}}{k_0 n_I \cos\theta}\right). \tag{B.108}$$

APPENDIX C

RIGOROUS COUPLED WAVE ANALYSIS MODEL

This appendix contains a software listing of the Rigorous Coupled Wave Analysis (RCWA) model. The RCWA model is implemented in the commercial analysis package Matlab. The listing is formatted in a monospaced font in order to preserve its readability.

```
function rcwa_fields(field_flag)
%  Multi-Layer Grating (Filename rcwa_fields.m)
%
%  Calculates reflectance and transmission coefficients using
%  Rigorous Coupled Wave Analysis (RCWA) for conical or planar
% (TE, TM) diffraction from a multi-layer structure on a substrate.
%  Layers may be either homogeneous or binary gratings and may be
%  combined in any order.
%  Allows complex refractive index.
%
%***********************************************
%
%  Diana M. Chambers
%
%***********************************************
%  Assumptions:
%    1. Simple, binary grating
%    1a.  All gratings must have the same period
%    2. Coordinate system:
%          x=0 at rising edge of a grating ridge,
%                 runs perpendicular to grating
%          z=0 at top of grating, runs thru grating into substrate
%    3. The matrix A has real eigenvalues;
%          A must be Hermitian (or symmetric)
%
%------------------------------------------------------------------------------
%
%  Input file format
%
%  GUI Mode:
%  This software assumes interface through the GUI "rcwa.m"
%  Data input is handled in the GUI.
%
%  Batch Mode:
%  When Run! - RCWA Only is selected a popup window prompts the user for
%     a file name.  This file should contain the names of input parameter
%     files to be batched, each on a separate line.
%     The input parameter file format is as follows:
%
%     The file is ASCII format arranged by lines.  The first line is a
```

```
%     character string to define the column headings:  Parameter,
%     Min, Max, Increment, Algorithm (reference to index function).
%     These headings are ignored when reading the file.
%     The second line is blank.
%     The following 11 lines contain system parameters in the column format
%     given above.  The parameters listed are wavelength, theta, phi, psi,
%     grating period, number of positive orders, number of negative orders,
%     incident media index (real), exiting media index (real and imaginary) and
%     number of layers.
%
%     Layer parameters follow with each layer preceded by a blank line and a
%     line with a character string to specify either grating or homogeneous.
%     Parameters defined for a grating layer are thickness, grating offset,
%     ridge width, refractive index of ridge (real and imaginary) and
%     refractive index of the groove (real and imaginary).
%     Parameters for a homogeneous layer are thickness and refractive
%     index (real and imaginary).
%
%     Example input file:
%
%PARAMETER               MIN            MAX         INCREMENT       ALGORITHM
%
%lambda             2.060000e+000  2.060000e+000  0.000000e+000
%theta              0.000000e+000  0.000000e+000  0.000000e+000
%phi                0.000000e+000  0.000000e+000  0.000000e+000
%psi                9.000000e+001  9.000000e+001  0.000000e+000
%grating_period     4.000000e+000  4.000000e+000  0.000000e+000
%num_orders_pos     1.000000e+001  1.000000e+001  0.000000e+000
%num_orders_neg     1.000000e+001  1.000000e+001  0.000000e+000
%Re_index_I         1.500000e+000  1.500000e+000  0.000000e+000      Linear
%Re_index_II        1.500000e+000  1.500000e+000  0.000000e+000      Linear
%Im_index_II        0.000000e+000  0.000000e+000  0.000000e+000      Linear
%num_layers          2
%
%                             GRATING_LAYER
%thickness          1.000000e+000  1.000000e+000  0.000000e+000
%grating_offset     1.889000e+000  1.889000e+000  0.000000e+000
%ridge_width        2.000000e+000  2.000000e+000  0.000000e+000
%Re_index_ridge     2.000000e+000  2.000000e+000  0.000000e+000      Linear
%Im_index_ridge     0.000000e+000  0.000000e+000  0.000000e+000      Linear
```

```
%Re_index_groove    1.500000e+000  1.500000e+000  0.000000e+000      Linear
%Im_index_groove    0.000000e+000  0.000000e+000  0.000000e+000      Linear
%
%                           HOMOGENEOUS_LAYER
%thickness          4.400000e+000  4.400000e+000  0.000000e+000
%Re_uniform_index   1.500000e+000  1.500000e+000  0.000000e+000      Linear
%Im_uniform_index   0.000000e+000  0.000000e+000  0.000000e+000      Linear
%
%
%     Diffraction efficiencies will be calculated and stored in the output file
%     for each set of input parameters.
%     There is no inherent limit to the number of data sets or layers.
%
%     Variable descriptions are found below.
%
%------------------------------------------------------------------------------
%
%  Output file format
%
%  All variables are output using the '%g' format in a fprintf function.
%
%  Two output files are generated.  Both files will contain one output line for
%  each set of input parameters.
%
%  For output_mode = 1, the first file contains only information about the +1
%  order, preceded by basic parameters:
%  lambda_0, theta_0, grating_period, num_orders, DE1, DE_R(+1), and DE_T(+1)
%  where:  DE1 is total reflected and transmitted energy in the +1 order and
%          DE_R and DE_T are the individual components.
%
%  For output_mode = 2, the first file contains only 0 order DE_R & DE_T values
%
%  For output_mode = 3, the first file is the same as for output_mode = 2 with
%  the addition of the phase of the transmitted 0 order.
%
%  The second file contains all orders up to where +/- are symmetric.
%  The orders are interleaved according to the formst:
%  lambda_0, theta_0, grating_period, DE1, DE_R(0), DE_T(0), DE_R(+1), DE_T(+1),
%      DE_R(-1), DE_T(-1), DE_R(+2), DE_T(+2), DE_R(-2), DE_T(-2) . . .
%
```

```
%  Modifications to the output file format can be made in the fprintf
%  statements at the end of the file.
%
%  Output file names are chosen by the user in GUI mode.  For batch mode, the
%  file names are created by using the input parameter file name and replacing
%  the '.dat' extension by either '.1' or '.0' for one file, dependent on
%  output mode option, and '.all' for the second file.
%
%
%  Field matrix output file format:
%
%  One file is created for each pertinent field component.  The files are
%  formatted and tab delimited.  The first row begins with a tab, then contains
%  the z position of each column. The first column of subsequent rows contains
%  the x position of that row.  The remaining elements in each row contain the
%  field matrix values.
%
%------------------------------------------------------------------------------
%
%  Variable Definitions
%
%  lambda_0         Free space wavelength (microns)
%  theta            Incident angle, rotation about y-axis (degrees)
%                   (Range of theta uses theta_min, theta_max, theta_step)
%  phi_0            Incident angle, rotation about z-axis (degrees)
%  psi_0            Angle of electric field wrt plane of incidence, 0=TM, 90=TE
%  Re(index_I)      Real part of Refractive index in Region I, incident region
%  Im(index_I)      Imaginary part of Refractive index in Region I, incident
%                   region
%  Re(index_II)     Real part of Refractive index in Region II, substrate
%  Im(index_II)     Imaginary part of Refractive index in Region II, substrate
%  grating_period   Period of grating (microns)
%  num_layers       Number of layers, grating and homogeneous combined
%  num_orders_pos   Number of positive orders retained in calculation
%  num_orders_neg   Number of negative orders retained in calculation
%
%  layer_id           Distinguishes grating (=1) from uniform (=2) layer
%  thickness          Thickness of uniform or grating layer (microns)
%  Re(uniform_index)  Real part of Refractive index of uniform layer
%  Im(uniform_index)  Imaginary part of Refractive index of uniform layer
```

```
%  grating_offset     Offset from x=0 of rising edge of grating (microns)
%  ridge_width        Width of grating ridge (microns)
%  Re(index_ridge)    Real part of Refractive index of ridges of grating
%  Im(index_ridge)    Imaginary part of Refractive index of ridges of grating
%  Re(index_groove)   Real part of Refractive index of grooves of grating
%  Im(index_groove)   Imaginary part of Refractive index of grooves of grating
%
%  dif_pol          Diffraction/polarization 1=TE, 2=TM, 3=Conical
%  Emat_offset      Offset into permittivity matrix
%  E_val            Eigenvalues
%  E_vec            Eigenvectors
%  E_prod           Product of eigenvalues and eigenvectors
%
%  incident           Matrix representing incident E/H fields
%  convert_T          Accum. conversion factor to recover transmitted energies;
%                     result of enhanced transmittance matrix technique
%  fou_harmoncs       Fourier harmonics for relative permittivity
%  rec_fou_harmonics  Reciprocal fourier harmonics
%  E                  Relative permittivity matrix
%  rec_E              Reciprocal relative permittivity matrix
%
%
%------------------------------------------------------------------------------
%------------------------------------------------------------------------------
%
%  Determine run mode, if ==1 -> GUI, if ==2 -> batch
%
%  Run Mode option
h_menu_runmode = findobj(0, 'Tag', 'RunMode');
runmodemenulist = get(h_menu_runmode,'UserData');
run_mode = runmodemenulist(length(runmodemenulist));

if (run_mode == 2)     % Batch mode

   %  Get name of file containing list of file names to batch
   [infile,pathname] = uigetfile ('*.*', 'Open Input File', 100, 100);

   [inf_list, message] = eval(['fopen ( ''' pathname infile ''', ''r'')']);
   if inf_list == -1
      error(message)
```

```
   end

   file_name = fscanf(inf_list, '%s\n',1);
   Read_input_file(pathname, file_name)

end    % Check for batch mode
another_case = 1;

while (another_case)

%
%  Get data from GUI
%
h_menu_sysparams = findobj(0, 'Tag', 'SysParams');
sys_param_list = get(h_menu_sysparams, 'UserData');
grating_period_min = sys_param_list(1);
grating_period_max = sys_param_list(2);
grating_period_incr = sys_param_list(3);
lambda_min = sys_param_list(4);
lambda_max = sys_param_list(5);
lambda_incr = sys_param_list(6);
num_orders_pos_min = sys_param_list(7);
num_orders_pos_max = sys_param_list(8);
num_orders_pos_incr = sys_param_list(9);
num_orders_neg_min = sys_param_list(10);
num_orders_neg_max = sys_param_list(11);
num_orders_neg_incr = sys_param_list(12);
dif_pol = sys_param_list(13);
theta_min = sys_param_list(14);
theta_max = sys_param_list(15);
theta_incr = sys_param_list(16);
phi_min = sys_param_list(17);
phi_max = sys_param_list(18);
phi_incr = sys_param_list(19);
psi_min = sys_param_list(20);
psi_max = sys_param_list(21);
psi_incr = sys_param_list(22);
Re_index_I_c0 = sys_param_list(23);
Re_index_I_c1 = sys_param_list(24);
Re_index_I_c2 = sys_param_list(25);
```

```
inc_algor = sys_param_list(26);
Re_index_II_c0 = sys_param_list(27);
Re_index_II_c1 = sys_param_list(28);
Re_index_II_c2 = sys_param_list(29);
exitre_algor = sys_param_list(30);
Im_index_II_c0 = sys_param_list(31);
Im_index_II_c1 = sys_param_list(32);
Im_index_II_c2 = sys_param_list(33);
exitim_algor = sys_param_list(34);

h_menu_displayer = findobj(0, 'Tag', 'DispLayers');
disp_layer_list = get(h_menu_displayer, 'UserData');
num_layers = disp_layer_list(1);
ostart = 2;
oend = 1+num_layers;
layer_id = disp_layer_list(ostart:oend);
ostart = ostart+num_layers;
oend = oend+num_layers;
thickness_min = disp_layer_list(ostart:oend);
ostart = ostart+num_layers;
oend = oend+num_layers;
thickness_max = disp_layer_list(ostart:oend);
ostart = ostart+num_layers;
oend = oend+num_layers;
thickness_incr = disp_layer_list(ostart:oend);
ostart = ostart+num_layers;
oend = oend+num_layers;
grating_off_min = disp_layer_list(ostart:oend);
ostart = ostart+num_layers;
oend = oend+num_layers;
grating_off_max = disp_layer_list(ostart:oend);
ostart = ostart+num_layers;
oend = oend+num_layers;
grating_off_incr = disp_layer_list(ostart:oend);
ostart = ostart+num_layers;
oend = oend+num_layers;
ridge_width_min = disp_layer_list(ostart:oend);
ostart = ostart+num_layers;
oend = oend+num_layers;
ridge_width_max = disp_layer_list(ostart:oend);
```

```
ostart = ostart+num_layers;
oend = oend+num_layers;
ridge_width_incr = disp_layer_list(ostart:oend);
ostart = ostart+num_layers;
oend = oend+num_layers;
Re_uniform_index_c0 = disp_layer_list(ostart:oend);
ostart = ostart+num_layers;
oend = oend+num_layers;
Re_uniform_index_c1 = disp_layer_list(ostart:oend);
ostart = ostart+num_layers;
oend = oend+num_layers;
Re_uniform_index_c2 = disp_layer_list(ostart:oend);
ostart = ostart+num_layers;
oend = oend+num_layers;
uindexre_algor = disp_layer_list(ostart:oend);
ostart = ostart+num_layers;
oend = oend+num_layers;
Im_uniform_index_c0 = disp_layer_list(ostart:oend);
ostart = ostart+num_layers;
oend = oend+num_layers;
Im_uniform_index_c1 = disp_layer_list(ostart:oend);
ostart = ostart+num_layers;
oend = oend+num_layers;
Im_uniform_index_c2 = disp_layer_list(ostart:oend);
ostart = ostart+num_layers;
oend = oend+num_layers;
uindexim_algor = disp_layer_list(ostart:oend);
ostart = ostart+num_layers;
oend = oend+num_layers;
Re_index_ridge_c0 = disp_layer_list(ostart:oend);
ostart = ostart+num_layers;
oend = oend+num_layers;
Re_index_ridge_c1 = disp_layer_list(ostart:oend);
ostart = ostart+num_layers;
oend = oend+num_layers;
Re_index_ridge_c2 = disp_layer_list(ostart:oend);
ostart = ostart+num_layers;
oend = oend+num_layers;
rdindexre_algor = disp_layer_list(ostart:oend);
ostart = ostart+num_layers;
```

```
oend = oend+num_layers;
Im_index_ridge_c0 = disp_layer_list(ostart:oend);
ostart = ostart+num_layers;
oend = oend+num_layers;
Im_index_ridge_c1 = disp_layer_list(ostart:oend);
ostart = ostart+num_layers;
oend = oend+num_layers;
Im_index_ridge_c2 = disp_layer_list(ostart:oend);
ostart = ostart+num_layers;
oend = oend+num_layers;
rdindexim_algor = disp_layer_list(ostart:oend);
ostart = ostart+num_layers;
oend = oend+num_layers;
Re_index_groove_c0 = disp_layer_list(ostart:oend);
ostart = ostart+num_layers;
oend = oend+num_layers;
Re_index_groove_c1 = disp_layer_list(ostart:oend);
ostart = ostart+num_layers;
oend = oend+num_layers;
Re_index_groove_c2 = disp_layer_list(ostart:oend);
ostart = ostart+num_layers;
oend = oend+num_layers;
grindexre_algor = disp_layer_list(ostart:oend);
ostart = ostart+num_layers;
oend = oend+num_layers;
Im_index_groove_c0 = disp_layer_list(ostart:oend);
ostart = ostart+num_layers;
oend = oend+num_layers;
Im_index_groove_c1 = disp_layer_list(ostart:oend);
ostart = ostart+num_layers;
oend = oend+num_layers;
Im_index_groove_c2 = disp_layer_list(ostart:oend);
ostart = ostart+num_layers;
oend = oend+num_layers;
grindexim_algor = disp_layer_list(ostart:oend);
ostart = ostart+num_layers;
oend = oend+num_layers;
disp_layer = disp_layer_list(ostart);
if (disp_layer < 1)
   disp_layer = 1;
```

```
end
if (disp_layer > num_layers)
   disp_layer = num_layers;
end

%  Output option
h_menu_output = findobj(0, 'Tag', 'OutputOption');
outputmenulist = get(h_menu_output,'UserData');
output_mode = outputmenulist(length(outputmenulist));


%
%  Set proper offsets into permittivity matrix
%
num_gratings = 0;
num_uniform = 0;
for nl=1:num_layers
   if layer_id(nl) == 1;
      num_gratings = num_gratings+1;
      Emat_offset(nl) = num_gratings;
   else
      num_uniform = num_uniform+1;
      Gmat_offset(nl) = num_uniform;
   end
end

if strcmp(lower(field_flag), 'calc_fields')
   h_menu_fieldspecs = findobj(0, 'Tag', 'FieldSpecs');
   field_spec_list = get(h_menu_fieldspecs, 'UserData');
   dist_before = field_spec_list(1);
   dist_after = field_spec_list(2);
   z_resolution = field_spec_list(3);
   dist_along = field_spec_list(4);
   x_resolution = field_spec_list(5);
   dist_parallel = field_spec_list(6);
   y_resolution = field_spec_list(7);
   z_max = field_spec_list(8);
   z_min = field_spec_list(9);
   x_max = field_spec_list(10);
   x_min = field_spec_list(11);
```

```
   y_max = field_spec_list(12);
   y_min = field_spec_list(13);
   z_out = field_spec_list(14:length(field_spec_list));
end

h_menu_layers = findobj(0, 'Tag', 'Layers');

%------------------------------------------------------------------------------
%
%  Get output file names from user (output_mode == 1), or
%  Set up automatic file names (output_mode == 0,1 and/or run_mode == 2)
%
if (run_mode == 1)     % GUI mode
   h_menu_load = findobj(0, 'Tag', 'LoadMenu');
   file_name = get(h_menu_load,'UserData');
   if (output_mode == 1)   % +1 order output
      DefaultFilename = MakeName(file_name,'.dat','.1');
      MessageTextOutFile = '+1 order file name';
   elseif (output_mode == 2)   % 0 order output (wiregrid)
      DefaultFilename = MakeName(file_name,'.dat','.0');
      MessageTextOutFile = '0 order file name (wiregrid)';
   elseif (output_mode == 3)   % 0 order output (waveplate)
      DefaultFilename = MakeName(file_name,'.dat','.0');
      MessageTextOutFile = '0 order file name (waveplate)';
   end
   [outfile, path_outf] = uiputfile( DefaultFilename, MessageTextOutFile);
   [outf, message] = eval(['fopen (''' path_outf outfile ''', ''w'')']);
   if outf == -1
      error(message)
   end

   DefaultFilename = MakeName(file_name,'.dat','.all');
   [outfile2, path_outf2] = uiputfile( DefaultFilename, ...
                                 'Name of file of all orders');
   [outf2, message] = eval(['fopen (''' path_outf2 outfile2 ''', ''w'')']);
   if outf2 == -1
      error(message)
   end
else                  % Batch mode
   if (output_mode == 1)   % +1 order output
```

```
      appendstring = '.1';
   elseif (output_mode == 2)   % 0 order output (wiregrid)
      appendstring = '.0';
   elseif (output_mode == 3)   % 0 order output (waveplate)
      appendstring = '.0';
   end
   file_out = MakeName(file_name,'.dat',appendstring)
   [outf, message] = eval(['fopen ( ''' pathname file_out ''', ''w'')']);
   if outf == -1
      error(message)
   end
   file_out2 =  MakeName(file_name,'.dat','.all')
   [outf2, message] = eval(['fopen ( ''' pathname file_out2 ''', ''w'')']);
   if outf2 == -1
      error(message)
   end
end

if strcmp(lower(field_flag), 'calc_fields')
   switch dif_pol
      case 1     % TE
         [Eyfield_out, path_outf] = ...
             uiputfile( 'Eyfield.out', 'Name of Ey field output file')
         [Eyfld_outf, message] = ...
             eval(['fopen (''' path_outf Eyfield_out ''', ''w'')']);
         if Eyfld_outf == -1
            error(message)
         end
         [Eyfield_0_out, path_outf] = ...
             uiputfile( 'Eyfield_0.out', 'Name of Ey field output file')
         [Eyfld_0_outf, message] = ...
             eval(['fopen (''' path_outf Eyfield_0_out ''', ''w'')']);
         if Eyfld_0_outf == -1
            error(message)
         end
         [Eyfield_1_out, path_outf] = ...
             uiputfile( 'Eyfield_1.out', 'Name of Ey field output file')
         [Eyfld_1_outf, message] = ...
             eval(['fopen (''' path_outf Eyfield_1_out ''', ''w'')']);
         if Eyfld_1_outf == -1
```

```
         error(message)
      end
      [Hxfield_out, path_outf] = ...
          uiputfile( 'Hxfield.out', 'Name of Hx field output file')
      [Hxfld_outf, message] = ...
          eval(['fopen (''' path_outf Hxfield_out ''', ''w'')']);
      if Hxfld_outf == -1
         error(message)
      end
   case 2     % TM
      [Hyfield_out, path_outf] = ...
          uiputfile( 'Hyfield.out', 'Name of Hy field output file')
      [Hyfld_outf, message] = ...
          eval(['fopen (''' path_outf Hyfield_out ''', ''w'')']);
      if Hyfld_outf == -1
         error(message)
      end
      [Exfield_out, path_outf] = ...
          uiputfile( 'Exfield.out', 'Name of Ex field output file')
      [Exfld_outf, message] = ...
          eval(['fopen (''' path_outf Exfield_out ''', ''w'')']);
      if Exfld_outf == -1
         error(message)
      end
   case 3     % Conical
      [Eyfield_out, path_outf] = ...
          uiputfile( 'Eyfield.out', 'Name of Ey field output file')
      [Eyfld_outf, message] = ...
          eval(['fopen (''' path_outf Eyfield_out ''', ''w'')']);
      if Eyfld_outf == -1
         error(message)
      end
      [Hxfield_out, path_outf] = ...
          uiputfile( 'Hxfield.out', 'Name of Hx field output file')
      [Hxfld_outf, message] = ...
          eval(['fopen (''' path_outf Hxfield_out ''', ''w'')']);
      if Hxfld_outf == -1
         error(message)
      end
      [Hyfield_out, path_outf] = ...
```

```
             uiputfile( 'Hyfield.out', 'Name of Hy field output file')
         [Hyfld_outf, message] = ...
             eval(['fopen (''' path_outf Hyfield_out ''', ''w'')']);
         if Hyfld_outf == -1
            error(message)
         end
         [Exfield_out, path_outf] = ...
             uiputfile( 'Exfield.out', 'Name of Ex field output file')
         [Exfld_outf, message] = ...
             eval(['fopen (''' path_outf Exfield_out ''', ''w'')']);
         if Exfld_outf == -1
            error(message)
         end
   end        % End switch on dif_pol
end           % End if calc_fields

%
%  Set up headers in output files
%
if (output_mode == 1)
   fprintf(outf,...
      'lambda\ttheta\tphi\tpsi\tgrating_period\tnum_orders\tnum_layers\t');
   for ii = 1:num_layers
      fprintf(outf,'thickness_%g\t',ii);
   end
   for ii = 1:num_layers
      fprintf(outf,'grating_offset_%g\t',ii);
   end
   for ii = 1:num_layers
      fprintf(outf,'ridge_width_%g\t',ii);
   end
   fprintf(outf,'DE1\tDE_R1\tDE_T1\tConsv_Energy\tOrder_of_Consv\n');
else   %if (output_mode == 2) | (output_mode ==3)
   fprintf(outf,'IGOR\nWAVES/D ');
   fprintf(outf,'%s, %s',MakeName(file_name,'.dat','_R'),...
                         MakeName(file_name,'.dat','_T') );
   if (output_mode == 2)
      fprintf(outf,'\n');
   else
      phasewavename = MakeName(file_name,'.dat','_Tp');
```

```
      endIgorstring = [ 'X Unwrap 2.0, ' phasewavename ];
      fprintf(outf,', %s\n',phasewavename );
   end
   fprintf(outf,'BEGIN\n');
end
fprintf(outf2,...
   'lambda\ttheta\tphi\tpsi\tgrating_period\tnum_orders\tnum_layers\t');
for ii = 1:num_layers
   fprintf(outf2,'thickness_%g\t',ii);
end
for ii = 1:num_layers
   fprintf(outf2,'grating_offset_%g\t',ii);
end
for ii = 1:num_layers
   fprintf(outf2,'ridge_width_%g\t',ii);
end
fprintf(outf2,'DE1\tDE_R0\tDE_T0\t');
for ix=1:min(num_orders_pos_max, num_orders_neg_max)
   fprintf(outf2,'DE_R%g\tDE_T%g\tDE_R_%g\tDE_T_%g\t',...
                 ix,ix,ix,ix);
end
fprintf(outf2,'Consv_Energy \tOrder_of_Consv\tphase_1\tphase0\tphase1\n');

%-------------------------------------------------------------------------------
%
%  Start a timer
%

tic

%-------------------------------------------------------------------------------
%
%  Set up number of cases
%  NOTE:  Should execute minimum number of cases spec'd by input
%
num_cases = inf;
if ( theta_incr ~= 0)
   temp = fix( ((theta_max - theta_min)/theta_incr) ) + 1;
   num_cases = min(temp, num_cases);
end
```

```
if ( phi_incr ~= 0)
   temp = fix( ((phi_max - phi_min)/phi_incr) ) + 1;
   num_cases = min(temp, num_cases);
end
if ( psi_incr ~= 0 )
   temp = fix( ((psi_max - psi_min)/psi_incr) ) + 1;
   num_cases = min(temp, num_cases);
end
if ( grating_period_incr ~= 0 )
   temp = fix( ((grating_period_max - ...
                 grating_period_min)/grating_period_incr) ) + 1;
   num_cases = min(temp, num_cases);
end
if ( lambda_incr ~= 0 )
   temp = fix( ((lambda_max - lambda_min)/lambda_incr) ) + 1;
   num_cases = min(temp, num_cases);
end
if ( num_orders_pos_incr ~= 0 )
   temp = fix( ((num_orders_pos_max - ...
                 num_orders_pos_min)/num_orders_pos_incr) ) + 1;
   num_cases = min(temp, num_cases);
end
if ( num_orders_neg_incr ~= 0 )
   temp = fix( ((num_orders_neg_max - ...
                 num_orders_neg_min)/num_orders_neg_incr) ) + 1;
   num_cases = min(temp, num_cases);
end
if ( inc_algor == 1 )  %linear
   if (Re_index_I_c2 ~= 0)
      temp = fix( ((Re_index_I_c1 - Re_index_I_c0)/Re_index_I_c2) ) + 1;
      num_cases = min(temp, num_cases);
   end
end
if ( exitre_algor == 1 )  %linear
   if (Re_index_II_c2 ~= 0)
      temp = fix( ((Re_index_II_c1 - Re_index_II_c0)/Re_index_II_c2) ) + 1;
      num_cases = min(temp, num_cases);
   end
end
if ( exitim_algor == 1 )  %linear
```

```
   if (Im_index_II_c2 ~= 0)
      temp = fix( ((Im_index_II_c1 - Im_index_II_c0)/RIm_index_II_c2) ) + 1;
      num_cases = min(temp, num_cases);
   end
end
for nl = 1:num_layers
   if ( thickness_incr(nl) ~= 0)
      temp = fix( ( (thickness_max(nl) - ...
                     thickness_min(nl))/thickness_incr(nl)) ) + 1;
      num_cases = min(temp, num_cases);
   end
   if ( grating_off_incr(nl) ~= 0)
      temp = fix( ((grating_off_max(nl) - ...
                    grating_off_min(nl))/grating_off_incr(nl)) ) + 1;
      num_cases = min(temp, num_cases);
   end
   if ( ridge_width_incr(nl) ~= 0 )
      temp = fix( ((ridge_width_max(nl) - ...
                    ridge_width_min(nl))/ridge_width_incr(nl)) +.001 ) + 1;
      num_cases = min(temp, num_cases);
   end
   if (layer_id(nl) == 1)   % grating
      if ( rdindexre_algor(nl) == 1 )   % linear
         if (Re_index_ridge_c2(nl) ~= 0)
            temp = fix( ((Re_index_ridge_c1(nl) - ...
                          Re_index_ridge_c0(nl))/Re_index_ridge_c2(nl)) ) + 1;
            num_cases = min(temp, num_cases);
         end
      end
      if ( rdindexim_algor(nl) == 1 )  % linear
         if (Im_index_ridge_c2(nl) ~= 0)
            temp = fix( ((Im_index_ridge_c1(nl) - ...
                          Im_index_ridge_c0(nl))/Im_index_ridge_c2(nl)) ) + 1;
            num_cases = min(temp, num_cases);
         end
      end
      if ( grindexre_algor(nl) == 1 )   % linear
         if (Re_index_groove_c2(nl) ~= 0)
            temp = fix( ((Re_index_groove_c1(nl) - ...
                          Re_index_groove_c0(nl))/Re_index_groove_c2(nl)) ) + 1;
```

```
            num_cases = min(temp, num_cases);
         end
      end
      if ( grindexim_algor(nl) == 1 )  % linear
         if (Im_index_groove_c2(nl) ~= 0)
            temp = fix( ((Im_index_groove_c1(nl) - ...
                          Im_index_groove_c0(nl))/Im_index_groove_c2(nl)) ) + 1;
            num_cases = min(temp, num_cases);
         end
      end
   elseif (layer_id(nl) == 2)  % uniform
      if ( uindexre_algor(nl) == 1 )   % linear
         if (Re_uniform_index_c2(nl) ~= 0)
            temp = fix( ((Re_uniform_index_c1(nl) - ...
                          Re_uniform_index_c0(nl))/ ...
                          Re_uniform_index_c2(nl)) ) + 1;
            num_cases = min(temp, num_cases);
         end
      end
      if ( uindexim_algor(nl) == 1 )  % linear
         if (Im_uniform_index_c2(nl) ~= 0)
            temp = fix( ((Im_uniform_index_c1(nl) - ...
                          Im_uniform_index_c0(nl))/ ...
                          Im_uniform_index_c2(nl)) ) + 1;
            num_cases = min(temp, num_cases);
         end
      end
   end      % Grating vs. Uniform layer
end         % Cycle through layers

if ( num_cases == inf)
   num_cases = 1;
end

%  Outer loop for multiple cases
%
for ncase=1:1:num_cases

%-----------------------------------------------------------------------------
%
```

```
%  Constants
%
theta_0 = (theta_min+theta_incr*(ncase-1))*pi/180;
phi_0 = (phi_min+phi_incr*(ncase-1))*pi/180;
psi_0 = (psi_min+psi_incr*(ncase-1))*pi/180;
grating_period = (grating_period_min + grating_period_incr*(ncase-1));
lambda_0 = (lambda_min + lambda_incr*(ncase-1));
num_orders_pos = (num_orders_pos_min + num_orders_pos_incr*(ncase-1));
num_orders_neg = (num_orders_neg_min + num_orders_neg_incr*(ncase-1));
if (inc_algor == 1)   % linear
   Re_index_I = (Re_index_I_c0 + Re_index_I_c2*(ncase-1));
elseif (inc_algor == 2)  % quadratic
   Re_index_I = Re_index_I_c0 + Re_index_I_c1*lambda_0 + ...
                Re_index_I_c2*lambda_0*lambda_0;
end
if (exitre_algor == 1)   % linear
   Re_index_II = (Re_index_II_c0 + Re_index_II_c2*(ncase-1));
elseif (exitre_algor == 2)  % quadratic
   Re_index_II = Re_index_II_c0 + Re_index_II_c1*lambda_0 + ...
                 Re_index_II_c2*lambda_0*lambda_0;
end
if (exitim_algor == 1)   % linear
   Im_index_II = (Im_index_II_c0 + Im_index_II_c2*(ncase-1));
elseif (exitre_algor == 2)  % quadratic
   Im_index_II = Im_index_II_c0 + Im_index_II_c1*lambda_0 + ...
                 Im_index_II_c2*lambda_0*lambda_0;
end
index_I = Re_index_I;
index_II = Re_index_II + i*Im_index_II;

n = -num_orders_neg:num_orders_pos;
num_orders = num_orders_neg + num_orders_pos + 1;
two_n = -num_orders:num_orders;
k0 = 2*pi/lambda_0;
mu_0 = (4*pi)*1e-7;
epsilon_0 = 8.85e-12;
Zee0 = sqrt(mu_0/epsilon_0);
I = eye(num_orders);
zero = zeros(num_orders);
```

```
for nl = 1:num_layers
   thickness(nl) = thickness_min(nl) + thickness_incr(nl)*(ncase-1);
   grating_offset(nl) = grating_off_min(nl) + grating_off_incr(nl)*(ncase-1);
   ridge_width(nl) = ridge_width_min(nl) + ridge_width_incr(nl)*(ncase-1);
   if (layer_id(nl) == 1)   % grating
      if (rdindexre_algor(nl) == 1)   % linear
         Re_index_ridge = (Re_index_ridge_c0(nl) + ...
                           Re_index_ridge_c2(nl)*(ncase-1));
      elseif (rdindexre_algor(nl) == 2)  % quadratic
         Re_index_ridge = Re_index_ridge_c0(nl) + ...
                          Re_index_ridge_c1(nl)*lambda_0 + ...
                          Re_index_ridge_c2(nl)*lambda_0*lambda_0;
      end
      if (rdindexim_algor(nl) == 1)   % linear
         Im_index_ridge = (Im_index_ridge_c0(nl) + ...
                           Im_index_ridge_c2(nl)*(ncase-1));
      elseif (rdindexim_algor(nl) == 2)  % quadratic
         Im_index_ridge = Im_index_ridge_c0(nl) + ...
                          Im_index_ridge_c1(nl)*lambda_0 + ...
                          Im_index_ridge_c2(nl)*lambda_0*lambda_0;
      end
      if (grindexre_algor(nl) == 1)   % linear
         Re_index_groove = (Re_index_groove_c0(nl) + ...
                            Re_index_groove_c2(nl)*(ncase-1));
      elseif (grindexre_algor(nl) == 2)  % quadratic
         Re_index_groove = Re_index_groove_c0(nl) + ...
                           Re_index_groove_c1(nl)*lambda_0 + ...
                           Re_index_groove_c2(nl)*lambda_0*lambda_0;
      end
      if (grindexim_algor(nl) == 1)   % linear
         Im_index_groove = (Im_index_groove_c0(nl) + ...
                            Im_index_groove_c2(nl)*(ncase-1));
      elseif (grindexim_algor(nl) == 2)  % quadratic
         Im_index_groove = Im_index_groove_c0(nl) + ...
                           Im_index_groove_c1(nl)*lambda_0 + ...
                           Im_index_groove_c2(nl)*lambda_0*lambda_0;
      end
      index_ridge(nl) = Re_index_ridge + i*Im_index_ridge;
      index_groove(nl) = Re_index_groove + i*Im_index_groove;
   elseif (layer_id(nl) == 2)   % uniform
```

```
      if (uindexre_algor(nl) == 1)   % linear
         Re_uniform_index = (Re_uniform_index_c0(nl) + ...
                             Re_uniform_index_c2(nl)*(ncase-1));
      elseif (uindexre_algor(nl) == 2)  % quadratic
         Re_uniform_index = Re_uniform_index_c0(nl) + ...
                            Re_uniform_index_c1(nl)*lambda_0 + ...
                            Re_uniform_index_c2(nl)*lambda_0*lambda_0;
      end
      if (uindexim_algor(nl) == 1)   % linear
         Im_uniform_index = (Im_uniform_index_c0(nl) + ...
                             Im_uniform_index_c2(nl)*(ncase-1));
      elseif (rdindexim_algor(nl) == 2)  % quadratic
         Im_uniform_index = Im_uniform_index_c0(nl) + ...
                            Im_uniform_index_c1(nl)*lambda_0 + ...
                            Im_uniform_index_c2(nl)*lambda_0*lambda_0;
      end
      uniform_index(nl) = Re_uniform_index + i*Im_uniform_index;
   end   % Grating vs. Uniform layer
end

if (ncase == 1 | num_orders_pos_incr ~= 0 | num_orders_neg_incr ~=0)
   fou_harmonics = zeros(1,2*num_orders);
   rec_fou_harmonics = zeros(1,2*num_orders+1);
   E = zeros(num_orders,num_orders,num_gratings);
   rec_E = zeros(num_orders,num_orders,num_gratings);
   W = zeros(num_orders,num_orders,num_gratings);
   Q2 = zeros(num_orders,num_orders,num_gratings);
   Q = zeros(num_orders,num_orders,num_gratings);
   V = zeros(num_orders,num_orders,num_gratings);
   Gamma_arg = zeros(1,num_orders);
   Gamma = zeros(num_orders,num_orders,num_uniform);
   E_vec = zeros(num_layers);
   E_val = zeros(num_layers);
   E_prod = zeros(num_layers);
   if (dif_pol == 3)      % Conical
      ai_X = zeros(2*num_orders,2*num_orders,num_layers);
      b_ai_X = zeros(2*num_orders,2*num_orders,num_layers);
      EbainvE = zeros(2*num_orders,2*num_orders,num_layers);
      convert_T = zeros(2*num_orders,2*num_orders,num_layers);
   else                   % TE or TM
```

```
      ai_X = zeros(num_orders,num_orders,num_layers);
      b_ai_X = zeros(num_orders,num_orders,num_layers);
      EbainvE = zeros(num_orders,num_orders,num_layers);
      convert_T = zeros(num_orders,num_orders,num_layers);
   end
end


%------------------------------------------------------------------------------
%
%  Variable initialization
%
num_integ_pts = 1000;              % provides sufficient accuracy
integ_spacing = grating_period/num_integ_pts;

%------------------------------------------------------------------------------
%
%  Arrays - allocate memory
%
phi_i = zeros(1,num_orders);
X = zeros(num_orders);
G = zeros(num_orders);
ainv = zeros(num_orders);
exp_func = zeros(num_orders);

%------------------------------------------------------------------------------
%  Calculate fourier harmonics by integration

   for nl=1:num_layers
      if ( layer_id(nl) == 1 )          % A grating layer

         if (grating_period_incr ~= 0 |...
             grating_off_incr(nl) ~= 0 | ridge_width_incr(nl) ~= 0 |...
             num_orders_pos_incr ~= 0 | num_orders_neg_incr ~=0 | ...
             Re_index_ridge_c2(nl) ~= 0 | Im_index_ridge_c2(nl) ~= 0 | ...
             Re_index_groove_c2(nl) ~= 0 | Im_index_groove_c2(nl) ~= 0 | ...
             ncase == 1)

         while ( grating_offset(nl) > grating_period)
            grating_offset(nl) = grating_offset(nl) - grating_period;
```

```
end


groove_width = grating_period - ridge_width(nl);
if (grating_offset(nl) > groove_width)
   y1_index = index_ridge(nl);
   x1 = 0:integ_spacing:(grating_offset(nl) - groove_width);
   y2_index = index_groove(nl);
   x2 = (grating_offset(nl) - ...
         groove_width):integ_spacing:grating_offset(nl);
   y3_index = index_ridge(nl);
   x3 = grating_offset(nl):integ_spacing:grating_period;
else
   y1_index = index_groove(nl);
   x1 = 0:integ_spacing:grating_offset(nl);
   y2_index = index_ridge(nl);
   x2 = grating_offset(nl):integ_spacing:(grating_offset(nl) + ...
                                             ridge_width(nl));
   y3_index = index_groove(nl);
   x3 = (grating_offset(nl) + ...
         ridge_width(nl)):integ_spacing:grating_period;
end

for ii = 1:2*num_orders
   y1 = (y1_index^2)*...
        exp(-j*(ii-(num_orders+1))*(2*pi/grating_period)*x1);
   y2 = (y2_index^2)*...
        exp(-j*(ii-(num_orders+1))*(2*pi/grating_period)*x2);
   y3 = (y3_index^2)*...
        exp(-j*(ii-(num_orders+1))*(2*pi/grating_period)*x3);
   if (length(x1) > 1)
      section1 = trapz(x1,y1);
   else
      section1 = 0;
   end
   if (length(x2) > 1)
      section2 = trapz(x2,y2);
   else
      section2 = 0;
   end
```

```
            if (length(x3) > 1)
               section3 = trapz(x3,y3);
            else
               section3 = 0;
            end
            fou_harmonics(ii) = ...
               (1/grating_period)*(section1 + section2 + section3);
         end

         for ii = 1:num_orders
         E(ii,:,Emat_offset(nl)) = ...
            fou_harmonics( ii - (1:num_orders) + (num_orders+1) );
         end

         if (dif_pol ~= 1)   % True for TM or Conical
%  Calculate reciprocal fourier harmonics by integration
%
            for ii = 1:2*num_orders
               y1 = (1/y1_index^2)*...
                    exp(-j*(ii-(num_orders+1))*(2*pi/grating_period)*x1);
               y2 = (1/y2_index^2)*...
                    exp(-j*(ii-(num_orders+1))*(2*pi/grating_period)*x2);
               y3 = (1/y3_index^2)*...
                    exp(-j*(ii-(num_orders+1))*(2*pi/grating_period)*x3);
               if (length(x1) > 1)
                  section1 = trapz(x1,y1);
               else
                  section1 = 0;
               end
               if (length(x2) > 1)
                  section2 = trapz(x2,y2);
               else
                  section2 = 0;
               end
               if (length(x3) > 1)
                  section3 = trapz(x3,y3);
               else
                  section3 = 0;
               end
               rec_fou_harmonics(ii) = ...
```

```
                  (1/grating_period)*(section1+section2+section3);
            end

            for ii = 1:num_orders
               rec_E(ii,:,Emat_offset(nl)) = ...
                  rec_fou_harmonics( ii - (1:num_orders) + (num_orders+1) );
            end
         end     % End loop for not TE (TM or Conical)
      end        % End loop for increment or first case
   end        % End loop for layer type
end           % End loop for num_layers


   kx = zeros (1, num_orders);
   ky = zeros (1, num_orders);
   kIz = zeros (1, num_orders);
   kIIz = zeros (1, num_orders);
   fou_harmonics = zeros(1,2*num_orders);
   exp_func = zeros(num_orders);
   if (dif_pol == 3)                      % Conical
      convert_T = [ I zero; zero I];
      incident = zeros(1,4*num_orders);
   else
      convert_T = I;     % TE/TM
      incident = zeros(1,2*num_orders);
   end

%------------------------------------------------------------------------------
%
%  System Calculations
%
%  Set up matrix Kx2 - diagonal matrix of wavenumber, including Floquet condition

   kx = k0*(index_I*sin(theta_0)*cos(phi_0) - n*(lambda_0/grating_period));
   kx2 = kx.^2;
   kx_k0 = kx/k0;
   kx_k0_2 = kx_k0.^2;
   Kx = diag(kx_k0);
   Kx2 = diag(kx_k0_2);
```

```
   ky = k0*index_I*sin(theta_0)*sin(phi_0);
   ky_k0 = ky/k0;
   ky2 = ky^2;
   ky_k0_2 = ky_k0^2;
   ky2I = ky2*I;

   index_I_2 = index_I^2;
   index_II_2 = index_II^2;

   if (ky == 0)
      phi_i = zeros(1,num_orders);
   else
      phi_i = atan(ky./kx);
   end
   Fc = diag(cos(phi_i));
   Fs = diag(sin(phi_i));

%  Set up matrices Y - diagonal with elements (k/k0)
%
     for ino = 1:num_orders
        if (sqrt(kx2(ino) + ky2) < k0*index_I )
           kIz(ino) = sqrt( (k0*index_I)^2 - kx2(ino) - ky2 );
        else
           kIz(ino) = -j*sqrt( (kx2(ino) + ky2) - (k0*index_I)^2 );
        end
     end
     for ino = 1:num_orders
        if (sqrt(kx2(ino) + ky2) < k0*index_II )
           kIIz(ino) = sqrt( (k0*index_II)^2 - kx2(ino) - ky2 );
        else
           kIIz(ino) = -j*sqrt( (kx2(ino) + ky2) - (k0*index_II)^2 );
        end
     end
%   kIz = conj(k0*sqrt(index_I_2 - kx_k0_2 - ky_k0_2));
%   kIIz = conj(k0*sqrt(index_II_2 - kx_k0_2 - ky_k0_2));

   kIz_k0 = kIz/k0;
   kIIz_k0 = kIIz/k0;

   YI = diag(kIz_k0);
```

```
   YII = diag(kIIz_k0);
   ZI = diag(kIz_k0/index_I_2);
   ZII = diag(kIIz_k0/index_II_2);

   if (dif_pol == 1)                 % TE
      incident(num_orders_neg+1) = 1;
      incident(num_orders + num_orders_neg + 1) = j*index_I*cos(theta_0);
      f_g = [ I; j*YII ];
   elseif (dif_pol == 2)             % TM
      incident(num_orders_neg+1) = 1;
      incident(num_orders + num_orders_neg + 1) = j*cos(theta_0)/index_I;
      f_g = [ I; j*ZII ];
   else                              % Conical
      incident(num_orders_neg+1) = sin(psi_0);
      incident(num_orders + num_orders_neg + 1) = ...
         j*index_I*sin(psi_0)*cos(theta_0);
      incident(2*num_orders + num_orders_neg + 1) = -j*index_I*cos(psi_0);
      incident(3*num_orders + num_orders_neg + 1) = cos(psi_0)*cos(theta_0);
      f_g = [ I zero; j*YII zero; zero I; zero j*ZII];
   end

%------------------------------------------------------------------------------
%------------------------------------------------------------------------------
%
%  Loop for layer calculations
%

   for nl = num_layers:-1:1

      if ( layer_id(nl) == 1 )       % A grating layer

%------------------------------------------------------------------------------
%
%  Grating Calculations
%  Calculate the matrices W, Q and V
%
%  W1 is eigenvector matrix of [ky^2*I + (Kx2-E)]
%  Q1 is diagonal matrix, positive square roots of eigenvalues of Kx2-E
%
```

```
if (dif_pol == 1)            % TE
   A = Kx2 - E(:,:,Emat_offset(nl));
   [W(:,:,nl),Q2] = eig(A);
   Q(:,:,nl) = sqrt(Q2);
   V(:,:,nl)=W(:,:,nl)*Q(:,:,nl);

   E_vec = W(:,:,nl);
   E_val = Q(:,:,nl);
   E_prod = V(:,:,nl);
   temp = [E_vec E_vec;E_prod -E_prod];
   exp_func = diag(exp(-k0*diag(E_val)*thickness(nl)));

elseif (dif_pol == 2)       % TM
   recEinv = inv(rec_E(:,:,Emat_offset(nl)));
   Einv = inv(E(:,:,Emat_offset(nl)));
   EB = recEinv*(Kx*Einv*Kx-I);
   [W(:,:,nl),Q2] = eig(EB);
   Q(:,:,nl) = sqrt(Q2);
   V(:,:,nl)=rec_E(:,:,Emat_offset(nl))*W(:,:,nl)*Q(:,:,nl);

   E_vec = W(:,:,nl);
   E_val = Q(:,:,nl);
   E_prod = V(:,:,nl);
   temp = [E_vec E_vec;E_prod -E_prod];
   exp_func = diag(exp(-k0*diag(E_val)*thickness(nl)));

else                        % Conical
   A = Kx2 - E(:,:,Emat_offset(nl));
   temp = ky2I + A;
   [W1(:,:,nl),Q12] = eig(temp);
   Q1(:,:,nl) = sqrt(Q12);

   Einv = inv(E(:,:,Emat_offset(nl)));
   recEinv = inv(rec_E(:,:,Emat_offset(nl)));
   B = (Kx*Einv*Kx-I);
   temp = ky2I + B*E(:,:,Emat_offset(nl));
   [W2(:,:,nl),Q22] = eig(temp);
   Q2(:,:,nl) = sqrt(Q22);

   Ainv = inv(A);
```

```
            Binv = inv(B);
            V11(:,:,nl) = Ainv*W1(:,:,nl)*Q1(:,:,nl);
            V12(:,:,nl) = (ky_k0)*Ainv*Kx*W2(:,:,nl);
            V21(:,:,nl) = (ky_k0)*Binv*Kx*Einv*W1(:,:,nl);
            V22(:,:,nl) = Binv*W2(:,:,nl)*Q2(:,:,nl);

            Vss(:,:,nl) = Fc*V11(:,:,nl);
            Wss(:,:,nl) = Fc*W1(:,:,nl) + Fs*V21(:,:,nl);
            Vsp(:,:,nl) = Fc*V12(:,:,nl) - Fs*W2(:,:,nl);
            Wsp(:,:,nl) = Fs*V22(:,:,nl);
            Wpp(:,:,nl) = Fc*V22(:,:,nl);
            Vpp(:,:,nl) = Fc*W2(:,:,nl) + Fs*V12(:,:,nl);
            Wps(:,:,nl) = Fc*V21(:,:,nl) - Fs*W1(:,:,nl);
            Vps(:,:,nl) = Fs*V11(:,:,nl);

            X1 = diag(exp(-k0*diag(Q1(:,:,nl))*thickness(nl)));
            X2 = diag(exp(-k0*diag(Q2(:,:,nl))*thickness(nl)));

            X = [X1 zero; zero X2];
            exp_func =X;

            temp = [Vss(:,:,nl) Vsp(:,:,nl) Vss(:,:,nl) Vsp(:,:,nl);...
                    Wss(:,:,nl) Wsp(:,:,nl) -Wss(:,:,nl) -Wsp(:,:,nl);...
                    Wps(:,:,nl) Wpp(:,:,nl) -Wps(:,:,nl) -Wpp(:,:,nl);...
                    Vps(:,:,nl) Vpp(:,:,nl) Vps(:,:,nl) Vpp(:,:,nl)];
         end         % Polarization dependence for a grating layer

      else    %  A uniform layer
%-------------------------------------------------------------------------------
 %
 %  Uniform Calculations

         if (dif_pol == 1)            % TE
            n_2 = uniform_index(nl)^2;
            for ino = 1:num_orders
               if (sqrt(kx_k0_2(ino) + ky_k0_2) < uniform_index(nl) )
                  Gamma_arg(ino) = sqrt( n_2 - kx_k0_2(ino) - ky_k0_2 );
               else
                  Gamma_arg(ino) = -j*sqrt( (kx_k0_2(ino) + ky_k0_2) - n_2 );
               end
```

```
    end
    Gamma(:,:,Gmat_offset(nl)) = diag(j*Gamma_arg);

    E_vec =I;
    E_val = Gamma(:,:,Gmat_offset(nl));
    E_prod = Gamma(:,:,Gmat_offset(nl));
    temp = [E_vec E_vec;E_prod -E_prod];
    exp_func = diag(exp(-k0*diag(E_val)*thickness(nl)));

elseif (dif_pol == 2)
    n_2 = uniform_index(nl)^2;
    for ino = 1:num_orders
       if (sqrt(kx_k0_2(ino) + ky_k0_2) < uniform_index(nl) )
          Gamma_arg(ino) = sqrt( n_2 - kx_k0_2(ino) - ky_k0_2 );
       else
          Gamma_arg(ino) = -j*sqrt( (kx_k0_2(ino) + ky_k0_2) - n_2 );
       end
    end
    Gamma(:,:,Gmat_offset(nl)) = diag(j*Gamma_arg);

    E_vec =I;                  % TM
    E_val = Gamma(:,:,Gmat_offset(nl));
    E_prod = Gamma(:,:,Gmat_offset(nl))/(uniform_index(nl)^2);
    temp = [E_vec E_vec;E_prod -E_prod];
    exp_func = diag(exp(-k0*diag(E_val)*thickness(nl)));

else                          % Conical
    n_2 = uniform_index(nl)^2;
    for ino = 1:num_orders
       if (sqrt(kx_k0_2(ino) + ky_k0_2) < uniform_index(nl) )
          Gamma_arg(ino) = sqrt( n_2 - kx_k0_2(ino) - ky_k0_2 );
       else
          Gamma_arg(ino) = -j*sqrt( (kx_k0_2(ino) + ky_k0_2) - n_2 );
       end
    end
    Gamma(:,:,Gmat_offset(nl)) = diag(j*Gamma_arg);

    G = diag(exp(-k0*diag(Gamma(:,:,Gmat_offset(nl)))*thickness(nl)));
    exp_func  = [G zero; zero G];
```

```
           Fsg(:,:,Gmat_offset(nl)) = Fs*Gamma(:,:,Gmat_offset(nl));
           Fsgn(:,:,Gmat_offset(nl)) = Fsg(:,:,Gmat_offset(nl))/n_2;
           Fcg(:,:,Gmat_offset(nl)) = Fc*Gamma(:,:,Gmat_offset(nl));
           Fcgn(:,:,Gmat_offset(nl)) = Fcg(:,:,Gmat_offset(nl))/n_2;

           temp = ...
              [Fc  Fsgn(:,:,Gmat_offset(nl)) Fc -Fsgn(:,:,Gmat_offset(nl));...
               Fcg(:,:,Gmat_offset(nl))  -Fs -Fcg(:,:,Gmat_offset(nl)) -Fs;...
              -Fsg(:,:,Gmat_offset(nl))  -Fc  Fsg(:,:,Gmat_offset(nl)) -Fc;...
               Fs -Fcgn(:,:,Gmat_offset(nl)) Fs  Fcgn(:,:,Gmat_offset(nl))];

        end     % Polarization dependence for uniform layer
     end        % Grating vs. Uniform layer

%  Solve the system of equations to get reflection and transmission
%  coefficients
%
%  Combine the reflectance and transmission equations through c+ and c-,
%  apply techniques from enhanced transmittance approach,
%  rearrange so the system can be solved using LU or QR methods.


     [tU,tS,tV] = svd(temp);
     t_inv = tV*inv(tS)*tU';
     a_b = t_inv*f_g;
     if (dif_pol == 3)              % Conical
        a = a_b( 1:2*num_orders , : );
        b = a_b( 2*num_orders+1:size(a_b) , : );
     else                           % TE/TM
        a = a_b( 1:num_orders , : );
        b = a_b( num_orders+1:size(a_b) , : );
     end

     [aU,aS,aV] = svd(a);
     ainv = aV*inv(aS)*aU';
     ai_X(:,:,nl) = ainv*exp_func;
     b_ai_X(:,:,nl) = b*ai_X(:,:,nl);
     EbainvE = exp_func*b_ai_X(:,:,nl);

     if (dif_pol == 3)              % Conical
```

```
         f_g = temp*[I zero; zero I; EbainvE];
      else                           % TE/TM
         f_g = [E_vec*(I + EbainvE) ; E_prod*(I - EbainvE)];
      end

 %  Accumulate conversion back to T so don't have to save values for each layer

      convert_T = convert_T*ai_X(:,:,nl);  % Loop runs backwards ->  +1

   end        %---End loop for layer calculations

%  Calculate Reflection/Transmission coefficients
%
   if (dif_pol == 1)            % TE
      transfer = [ -1*I E_vec*(I + EbainvE) ; j*YI E_prod*(I - EbainvE) ];
      R_T1 = transfer\incident.';

      R = R_T1( 1:num_orders );
      T1 = R_T1( num_orders+1:size(R_T1) );
      T = convert_T*T1;

%  Calculate Diffraction Efficiencies
%
      DE_R = real((R.*conj(R).*real(kIz_k0/(index_I*cos(theta_0)))')');
      DE_T = real((T.*conj(T).*real(kIIz_k0/(index_I*cos(theta_0)))')');

   elseif (dif_pol == 2)            % TM
      transfer = [ -1*I E_vec*(I + EbainvE) ; j*ZI E_prod*(I - EbainvE) ];
      R_T1 = transfer\incident.';

      R = R_T1( 1:num_orders );
      T1 = R_T1( num_orders+1:size(R_T1) );
      T = convert_T*T1;

%  Calculate Diffraction Efficiencies
%
      DE_R = (R.*conj(R).*real(kIz_k0/(index_I*cos(theta_0)))')';
      DE_T = (T.*conj(T).*(real(kIIz_k0/index_II_2))'/(cos(theta_0)/index_I))';

   else                            % Conical
```

```
      transfer = [ -I zero; j*YI zero; zero -I; zero j*ZI];
      transfer( : , 2*num_orders+1:4*num_orders) = f_g;
      R_TL = transfer\incident.';

      Rs = R_TL( 1:num_orders );
      Rp = R_TL( num_orders+1:2*num_orders );
      T1 = R_TL( 2*num_orders+1:size(R_TL) );

      T = convert_T*T1;
      Ts = T(1:num_orders);
      Tp = T(num_orders+1:size(T));

%  Calculate Diffraction Efficiencies
%
      if (theta_0 == 90.*pi/180.)
         DE_R = zeros(1,num_orders);
         DE_R(num_orders_neg+1) = 1;
         DE_R
         DE_T = zeros(1,num_orders)
         disp('This is a canned answer')
      else
         nIcos = index_I*cos(theta_0);
         DE_R = (Rs.*conj(Rs).*real(kIz_k0/nIcos)')' + ...
                (Rp.*conj(Rp).*real((kIz_k0/index_I_2)/nIcos)')';
         DE_T = (Ts.*conj(Ts).*real(kIIz_k0/nIcos)')' + ...
                (Tp.*conj(Tp).*real((kIIz_k0/index_II_2)/nIcos)')';
      end
   end             % Polarization dependence for R/T coefficients and DE

   DE1 = DE_R(num_orders_neg+2) + DE_T(num_orders_neg+2);
   Consv_Energy = sum(DE_R') + sum(DE_T');
   Order_of_Consv = Consv_Energy - 1

%------------------------------------------------------------------------------
%
%  Write output file
%

%  Write selected output to the first file
   if (output_mode == 1)   % +1 order output
```

```
      fprintf(outf,'%g\t', lambda_0, theta_0*180/pi, phi_0*180/pi, ...
                    psi_0*180/pi, grating_period, ...
                    num_orders, num_layers, thickness, grating_offset, ...
                    ridge_width, DE1, DE_R(num_orders_neg+2), ...
                    DE_T(num_orders_neg+2), Consv_Energy, Order_of_Consv);
   elseif (output_mode == 2)   % 0 order output (wiregrid)
      fprintf(outf,'%15e\t', DE_R(num_orders_neg+1),DE_T(num_orders_neg+1));
   elseif (output_mode == 3)   % 0 order output (waveplate)
      fprintf(outf,'%15e\t', DE_R(num_orders_neg+1),DE_T(num_orders_neg+1), ...
                             angle(T(num_orders_neg+1))/pi );
   end   %
   fprintf(outf,'\n');
%  Second file contains all orders up to where +/- are symmetric
   fprintf(outf2,'%g\t', lambda_0, theta_0*180/pi, phi_0*180/pi, ...
                    psi_0*180/pi, grating_period, ...
                    num_orders, num_layers, thickness, grating_offset, ...
                    ridge_width, DE1, DE_R(num_orders_neg+1), ...
                                      DE_T(num_orders_neg+1));
   for ix=1:min(num_orders_pos, num_orders_neg)
      fprintf(outf2,'%g\t%g\t%g\t%g\t', DE_R((num_orders_neg+1)+ix), ...
                                        DE_T((num_orders_neg+1)+ix),...
                                        DE_R((num_orders_neg+1)-ix), ...
                                        DE_T((num_orders_neg+1)-ix));
   end
   fprintf(outf2,'%g\t%g\t%g\t%g\t%g\n', Consv_Energy, Order_of_Consv,...
                                         angle(T(num_orders_neg))/pi,...
                                         angle(T(num_orders_neg+1))/pi,...
                                         angle(T(num_orders_neg+2))/pi);

end                     % End - Number of cases (incidence angles) to run

if (run_mode == 1)  % GUI mode
   another_case = 0;
else                % batch mode
   if (feof(inf_list))
      another_case = 0;
   else
      if (output_mode == 2)
         fprintf(outf,'END\n ');
      elseif (output_mode == 3)
```

```
         fprintf(outf,'END\n ');
%         fprintf(outf,'END\n%s\n ',endIgorstring);
      end
      fclose(outf);
      fclose(outf2);
      toc
      file_name = fscanf(inf_list, '%s\n',1);
      Read_input_file(pathname, file_name)

      if (output_mode == 1)   % +1 order output
         appendstring = '.1';
      elseif (output_mode == 2)   % 0 order output (wiregrid)
         appendstring = '.0';
      elseif (output_mode == 3)   % 0 order output (waveplate)
         appendstring = '.0';
      end
      file_out = MakeName(file_name,'.dat',appendstring);
      [outf, message] = eval(['fopen ( ''' pathname file_out ''', ''w'')']);
      if outf == -1
         error(message)
      end
      file_out2 =  MakeName(file_name,'.dat','.all');
      [outf2, message] = eval(['fopen ( ''' pathname file_out2 ''', ''w'')']);
      if outf2 == -1
         error(message)
      end
      another_case = 1;
   end            % feof on list file
end            % GUI vs. batch mode


end                     % End - Check on another_case

%------------------------------------------------------------------------------
%
%  Close files
%
if (output_mode == 2)
   fprintf(outf,'END\n ');
elseif (output_mode == 3)
```

```
   fprintf(outf,'END\n ');
%   fprintf(outf,'END\n%s\n ',endIgorstring);
end
fclose(outf);
fclose(outf2);
if (run_mode == 2)   %  Batch mode
   fclose(inf_list);
end

%------------------------------------------------------------------------------
%
%  Field Calculations
%

if strcmp(lower(field_flag), 'calc_fields')

%  Calculate constants
   z_min = -1*dist_before;
   x_min = 0;
   x_max = dist_along;
   y_min = 0;
   y_max = dist_parallel;

   cpsi = cos(psi_0);
   spsi = sin(psi_0);
   cphi = cos(phi_0);
   sphi = sin(phi_0);
   ctheta = cos(theta_0);
   stheta = sin(theta_0);

   ord_0 = num_orders_neg+1;
   ord_1 = num_orders_neg+2;

%  Calculate fields in incident region

   zI = z_min:z_resolution:0;
   x = x_min:x_resolution:x_max; % Generate x pts
   z_out = zI;   % Array for file output

   switch dif_pol
```

```
     case 1    % TE
%       Preallocate arrays for fields
        Ey_I_field = zeros(length(x),length(zI));
        Ey_0_I_field = zeros(length(x),length(zI));
        Ey_1_I_field = zeros(length(x),length(zI));
        Hx_I_field = zeros(length(x),length(zI));
        [xl,zl] = meshgrid(x,zI);
%       Calculate each field point
        for zl =1:1:length(zI)
           for xl = 1:1:length(x)
              Ey_I_field(xl,zl) = exp(-i*k0*index_I*(x(xl)*stheta + ...
                                    zI(zl)*ctheta)) ...
                                + R'*exp(-j*(kx*x(xl) - kIz*zI(zl)))';
              Ey_0_I_field(xl,zl) = exp(-i*k0*index_I*(x(xl)*stheta + ...
                                    zI(zl)*ctheta)) + ...
                                    R(ord_0)*exp(-j*(kx(ord_0)*x(xl) - ...
                                                    kIz(ord_0)*zI(zl)));
              Ey_1_I_field(xl,zl) = R(ord_1)*exp(-j*(kx(ord_1)*x(xl) - ...
                                                    kIz(ord_1)*zI(zl)));
              Hx_I_field(xl,zl) = (1/(k0*Zee0))*(k0*index_I*ctheta.*...
                                  exp(-i*k0*index_I*(x(xl)*stheta + ...
                                                     zI(zl)*ctheta)) ...
                                + (-1*kIz).*R'*exp(-i*(kx*x(xl) - ...
                                                       kIz*zI(zl)))');
           end  % x loop
        end    % z loop
%       Store in matrix for complete field description
        Ey_field = Ey_I_field(1:length(x), 1:length(zI));
        Ey_0_field = Ey_0_I_field(1:length(x), 1:length(zI));
        Ey_1_field = Ey_1_I_field(1:length(x), 1:length(zI));
        Hx_field = Hx_I_field(1:length(x), 1:length(zI));
     case 2    % TM
%       Preallocate arrays for fields
        Hy_I_field = zeros(length(x),length(zI));
        Ex_I_field = zeros(length(x),length(zI));
%       Calculate each field point
        for zl = 1:1:length(zI)
           for xl = 1:1:length(x)
              Hy_I_field(xl,zl) = exp(-i*k0*index_I*(x(xl)*stheta + ...
                                                    zI(zl)*ctheta)) ...
```

```
                                + R'*exp(-j*(kx*x(xl) - kIz*zI(zl)))';
              Ex_I_field(xl,zl) = (Zee0/k0/index_I_2)*...
                                  (-1*k0*index_I*ctheta.*...
                                   exp(-i*k0*index_I*(x(xl)*stheta + ...
                                                     zI(zl)*ctheta)) ...
                                +  kIz.*R'*exp(-i*(kx*x(xl) - ...
                                                   kIz*zI(zl)))');
            end  % x loop
        end    % z loop
%       Store in matrix for complete field description
        Hy_field = Hy_I_field(1:length(x), 1:length(zI));
        Ex_field = Ex_I_field(1:length(x), 1:length(zI));
     case 3    % Conical
%       Preallocate arrays for fields
        Ey_I_field = zeros(length(x),length(zI));
        Hx_I_field = zeros(length(x),length(zI));
        Hy_I_field = zeros(length(x),length(zI));
        Ex_I_field = zeros(length(x),length(zI));
%       Calculate each field point
        for zl = 1:1:length(zI)
           for xl = 1:1:length(x)
              y = 0;
              ux = cpsi*ctheta*cphi - spsi*sphi;
              uy = cpsi*ctheta*sphi + spsi*cphi;
              Rx = Rp.*ctheta*cphi + Rs.*sphi;
              Ry = Rp.*(ctheta*sphi) + Rs.*cphi;
              Ey_I_field(xl,zl) = ...
                 uy.*exp(-i*k0*index_I*(x(xl)*stheta*cphi + ...
                                        y*stheta*sphi + ...
                                        zI(zl)*ctheta)) + ...
                 Ry'*exp(-i*(kx*x(xl) + ky*y - kIz*zI(zl)))';
              Hx_I_field(xl,zl) = ...
                 (1/(k0*Zee0)).*(uy*k0*index_I*ctheta.*...
                                   exp(-i*k0*index_I*(x(xl)*stheta*cphi + ...
                                       y*stheta*sphi + zI(zl)*ctheta)) ...
                                + (-1*kIz.*Ry'*exp(-i*(kx*x(xl) + ky*y - ...
                                    kIz*zI(zl)))'));
              Hy_I_field(xl,zl) = ...
                 (-1/(k0*Zee0)).*(ux*k0*index_I*ctheta.*...
                                    exp(-i*k0*index_I*(x(xl)*stheta*cphi + ...
```

```
                                       y*stheta*sphi + zI(zl)*ctheta)) ...
                                 + kIz.*Rx'*exp(-i*(kx*x(xl) + ky*y - ...
                                   kIz*zI(zl)))');
               Ex_I_field(xl,zl) = ...
                  ux.*exp(-i*k0*index_I*(x(xl)*stheta*cphi + ...
                                        y*stheta*sphi + ...
                                        zI(zl)*ctheta)) + ...
                  Rx'*exp(-i*(kx*x(xl) + ky*y - kIz*zI(zl)))';
             end  % x loop
         end    % z loop
 %       Store in matrix for complete field description
         Ey_field = Ey_I_field(1:length(x), 1:length(zI));
         Hx_field = Hx_I_field(1:length(x), 1:length(zI));
         Hy_field = Hy_I_field(1:length(x), 1:length(zI));
         Ex_field = Ex_I_field(1:length(x), 1:length(zI));
   end    % Polarization switch for incident region

   D_lm1 = 0;
   Tconv = T1;
   for nl = 1:1:num_layers

      D_l = D_lm1 + thickness(nl);
      z = (D_lm1+z_resolution):z_resolution:D_l;   % Generate z pts
      zmDlm1 = z - D_lm1;
      zmDl = z - D_l;
      start = length(z_out)+1;
      z_out(start:(start+length(z)-1)) = z;        % Array for file output

%  Preallocate arrays for fields
      switch dif_pol
         case 1    % TE
            Ey_layer = zeros(length(x),length(z));
            Ey_0_layer = zeros(length(x),length(z));
            Ey_1_layer = zeros(length(x),length(z));
            Hx_layer = zeros(length(x),length(z));
         case 2    % TM
            Hy_layer = zeros(length(x),length(z));
            Ex_layer = zeros(length(x),length(z));
         case 3    % Conical
            Ey_layer = zeros(length(x),length(z));
```

```
           Hx_layer = zeros(length(x),length(z));
           Hy_layer = zeros(length(x),length(z));
           Ex_layer = zeros(length(x),length(z));
     end

     if ( layer_id(nl) == 1 )    % A grating layer
        if (dif_pol ~= 3)              % TE/TM
          c_p_m = [ I ; b_ai_X(:,:,nl)] * Tconv;
          c_plus = c_p_m(1:num_orders , : );
          c_minus = c_p_m(num_orders+1:size(c_p_m) , : );
        else                           % Conical
          c_p_m = [ I zero; zero I; b_ai_X(:,:,nl)] * Tconv;
          c1_plus = c_p_m(1:num_orders , : );
          c2_plus = c_p_m(num_orders+1:2*num_orders , : );
          c1_minus = c_p_m(2*num_orders+1:3*num_orders , : );
          c2_minus = c_p_m(3*num_orders+1:size(c_p_m) , : );
       end
       switch dif_pol
          case 1         % TE
             for zl = 1:1:length(z)
                cplus_exp = c_plus.*exp(-k0*diag(Q(:,:,nl))*zmDlm1(zl));
                cminus_exp = c_minus.*exp(k0*diag(Q(:,:,nl))*zmDl(zl));
                S_harmonic = W(:,:,nl)*(cplus_exp + cminus_exp);
                U_harmonic = V(:,:,nl)*(-cplus_exp + cminus_exp);
                for xl = 1:1:length(x)
                   xexp = exp(-i*kx*x(xl));
                   Ey_layer(xl,zl) = S_harmonic' * xexp';
                   Ey_0_layer(xl,zl) = S_harmonic(ord_0) * xexp(ord_0);
                   Ey_1_layer(xl,zl) = S_harmonic(ord_1) * xexp(ord_1);
                   Hx_layer(xl,zl) = (-i/Zee0)*U_harmonic' * xexp';
                end      % x loop

%  Temporary output of fields
                if (zl == 1)
                disp( ' Beginning of layer');nl
                Ey_m2 = S_harmonic(ord_0-2) * xexp(ord_0-2)
                Ey_m1 = S_harmonic(ord_0-1) * xexp(ord_0-1)
                Ey_0 = S_harmonic(ord_0) * xexp(ord_0)
                Ey_p1 = S_harmonic(ord_0+1) * xexp(ord_0+1)
                Ey_p2 = S_harmonic(ord_0+2) * xexp(ord_0+2)
```

```
       end


     end         % z loop
   case 2         % TM
      for zl = 1:1:length(z)
         cplus_exp = c_plus.*exp(-k0*diag(Q(:,:,nl))*zmDlm1(zl));
         cminus_exp = c_minus.*exp(k0*diag(Q(:,:,nl))*zmDl(zl));
         S_harmonic = V(:,:,nl)*(-cplus_exp + cminus_exp);
         U_harmonic = W(:,:,nl)*(cplus_exp + cminus_exp);
         for xl = 1:1:length(x)
            xexp = exp(-i*kx*x(xl));
            Hy_layer(xl,zl) = U_harmonic' * xexp';
            Ex_layer(xl,zl) = (i*Zee0)*S_harmonic' * xexp';
         end      % x loop
      end         % z loop
   case 3         % Conical
      for zl = 1:1:length(z)
         c1plus_exp = c1_plus.*exp(-k0*diag(Q1(:,:,nl))*zmDlm1(zl));
         c2plus_exp = c2_plus.*exp(-k0*diag(Q2(:,:,nl))*zmDlm1(zl));
         c1minus_exp = c1_minus.*exp(k0*diag(Q1(:,:,nl))*zmDl(zl));
         c2minus_exp = c2_minus.*exp(k0*diag(Q2(:,:,nl))*zmDl(zl));
         Sx_harmonic = W2(:,:,nl)*(c2plus_exp + c2minus_exp);
         Ux_harmonic = W1(:,:,nl)*(-c1plus_exp + c1minus_exp);
         Sy_harmonic = V11(:,:,nl)*(c1plus_exp + c1minus_exp) + ...
                       V12(:,:,nl)*(c2plus_exp + c2minus_exp);
         Uy_harmonic = V21(:,:,nl)*(c1plus_exp + c1minus_exp) + ...
                       V22(:,:,nl)*(c2plus_exp + c2minus_exp);
         for xl = 1:1:length(x)
            xexp = exp(-i*kx*x(xl));
            xyexp = exp(-i*(kx*x(xl) + ky*y));
            Ey_layer(xl,zl) = Sy_harmonic' * xyexp';
            Hx_layer(xl,zl) = (-i/Zee0)*Ux_harmonic' * xyexp';
            Hy_layer(xl,zl) = (-i/Zee0)*Uy_harmonic' * xyexp';
            Ex_layer(xl,zl) = Sx_harmonic' * xyexp';
         end      % x loop
      end         % z loop
end               % Polarization switch for grating layers

else       % A uniform layer
```

```
if (dif_pol ~= 3)              % TE/TM
   p_q = [ I ; b_ai_X(:,:,nl)] * Tconv;
   p = p_q(1:num_orders , : );
   q = p_q(num_orders+1:size(p_q) , : );
else                           % Conical
   p_q = [ I zero; zero I; b_ai_X(:,:,nl)] * Tconv;
   p1_plus = p_q(1:num_orders , : );
   p2_plus = p_q(num_orders+1:2*num_orders , : );
   q1_minus = p_q(2*num_orders+1:3*num_orders , : );
   q2_minus = p_q(3*num_orders+1:size(c_p_m) , : );
end
switch dif_pol
   case 1      % TE
      for zl = 1:1:length(zmDl)
         p_exp = p.* ...
             exp(-k0*diag(Gamma(:,:,Gmat_offset(nl)))*zmDlm1(zl));
         q_exp = q.* ...
             exp(k0*diag(Gamma(:,:,Gmat_offset(nl)))*zmDl(zl));
         S_harmonic = (p_exp + q_exp);
         U_harmonic = Gamma(:,:,Gmat_offset(nl))*(-p_exp + q_exp);
         for xl = 1:1:length(x)
            xexp = exp(-i*kx*x(xl));
            Ey_layer(xl,zl) = S_harmonic' * xexp';
            Ey_0_layer(xl,zl) = S_harmonic(ord_0) * xexp(ord_0);
            Ey_1_layer(xl,zl) = S_harmonic(ord_1) * xexp(ord_1);
            Hx_layer(xl,zl) = (-i/Zee0) * U_harmonic' * xexp';
         end    % x loop
     end       % z loop
   case 2       % TM
      for zl = 1:1:length(zmDl)
         p_exp = p.* ...
            exp(-k0*diag(Gamma(:,:,nGmat_offset(nl)))*zmDlm1(zl));
         q_exp = q.* ...
            exp(k0*diag(Gamma(:,:,Gmat_offset(nl)))*zmDl(zl));
         S_harmonic = Gamma(:,:,Gmat_offset(nl))*(-p_exp + q_exp);
         U_harmonic = (p_exp + q_exp);
         for xl = 1:1:length(x)
            xexp = exp(-i*kx*x(xl));
            Ey_layer(xl,zl) = S_harmonic' * xexp';
```

```
                      Hx_layer(xl,zl) = (-i/Zee0) * U_harmonic' * xexp';
                   end     % x loop
                end        % z loop
          end              % Polarization switch for uniform layers
      end                  % Grating vs. Uniform layer

      switch dif_pol
         case 1     %TE
            Ey_field = [ Ey_field Ey_layer(1:length(x), 1:length(z)) ];
            Ey_0_field = [ Ey_0_field Ey_0_layer(1:length(x), 1:length(z)) ];
            Ey_1_field = [ Ey_1_field Ey_1_layer(1:length(x), 1:length(z)) ];
            Hx_field = [ Hx_field Hx_layer(1:length(x), 1:length(z)) ];
         case 2    % TM
            Hy_field = [ Hy_field Hy_layer(1:length(x), 1:length(z)) ];
            Ex_field = [ Ex_field Ex_layer(1:length(x), 1:length(z)) ];
         case 3
            Ey_field = [ Ey_field Ey_layer(1:length(x), 1:length(z)) ];
            Hx_field = [ Hx_field Hx_layer(1:length(x), 1:length(z)) ];
            Hy_field = [ Hy_field Hy_layer(1:length(x), 1:length(z)) ];
            Ex_field = [ Ex_field Ex_layer(1:length(x), 1:length(z)) ];
      end   % Polarization switch for filling output matrix

      D_lm1 = D_l;
      Tconv = ai_X(:,:,nl) * Tconv;

  end      % number of layers loop

%  Calculate fields in exiting region

  z_max = D_l + dist_after;

  zII = (D_l+z_resolution):z_resolution:z_max;

  switch dif_pol
     case 1    % TE
%       Preallocate arrays for fields
        Ey_II_field = zeros(length(x),length(zII));
        Ey_0_II_field = zeros(length(x),length(zII));
        Ey_1_II_field = zeros(length(x),length(zII));
        Hx_II_field = zeros(length(x),length(zII));
```

```
%       Calculate each field point
        for zl = 1:1:length(zII)
           for xl = 1:1:length(x)
              Ey_II_field(xl,zl) = ...
                 T'*exp(-j*(kx*x(xl) + kIIz*(zII(zl) - D_l)))';
              Ey_0_II_field(xl,zl) = ...
                 T(ord_0)*exp(-j*(kx(ord_0)*x(xl) + ...
                              kIIz(ord_0)*(zII(zl) - D_l)));
              Ey_1_II_field(xl,zl) = ...
                 T(ord_1)*exp(-j*(kx(ord_1)*x(xl) + ...
                              kIIz(ord_1)*(zII(zl) - D_l)));
              Hx_II_field(xl,zl) = ...
                 (1/(k0*Zee0))*(kIIz.*T'*exp(-j*(kx*x(xl) + ...
                                                 kIIz*(zII(zl) - D_l)))');
           end   % x loop
        end      % z loop
%       Store to complete field matrix
        Ey_field = [ Ey_field Ey_II_field(1:length(x), 1:length(zII)) ];
        Ey_0_field = [ Ey_0_field Ey_0_II_field(1:length(x), 1:length(zII)) ];
        Ey_1_field = [ Ey_1_field Ey_1_II_field(1:length(x), 1:length(zII)) ];
        Hx_field = [ Hx_field Hx_II_field(1:length(x), 1:length(zII)) ];
     case 2    % TM
%       Preallocate arrays for fields
        Hy_II_field= zeros(length(x),length(zII));
        Ex_II_field = zeros(length(x),length(zII));
%       Calculate each field point
        for zl = 1:1:length(zII)
           for xl = 1:1:length(x)
              Hy_II_field(xl,zl) = ...
                 T'*exp(-j*(kx*x(xl) + kIIz*(zII(zl) - D_l)))';
              Ex_II_field(xl,zl) = ...
                 (Zee0/k0/index_II_2)*...
                 (-1*kIIz.*T'* exp(-j*(kx*x(xl) + kIIz*(zII(zl) - D_l)))');
           end   % x loop
        end      % z loop
%       Store to complete field matrix
        Hy_field = [ Hy_field Hy_II_field(1:length(x), 1:length(zII)) ];
        Ex_field = [ Ex_field Ex_II_field(1:length(x), 1:length(zII)) ];
     case 3    % Conical
%       Preallocate arrays for fields
```

```
        Ey_II_field = zeros(length(x),length(zII));
        Hx_II_field = zeros(length(x),length(zII));
        Hy_II_field= zeros(length(x),length(zII));
        Ex_II_field= zeros(length(x),length(zII));
%       Calculate each field point
        for zl = 1:1:length(zII)
           for xl = 1:1:length(x)
              ux = cpsi*ctheta*cphi - spsi*sphi;
              uy = cpsi*ctheta*sphi + spsi*cphi;
              Tx = Tp.*ctheta*cphi + Ts.*sphi;
              Ty = Tp.*ctheta*sphi + Ts.*cphi;
              Ey_II_field(xl,zl) = ...
                 Ty'*exp(-j*(kx*x(xl) + ky*y + kIIz*(zII(zl) - D_l)))';
              Hx_II_field(xl,zl) = ...
                 (1/(k0*Zee0)).*(kIIz.*Ty'*exp(-j*(kx*x(xl) +  ...
                                               ky*y + kIIz*(zII(zl) - D_l)))');
              Hy_II_field(xl,zl) = ...
                 (-1/(k0*Zee0)).*(kIIz.*Tx'*exp(-j*(kx*x(xl) + ...
                                                ky*y + kIIz*(zII(zl) - D_l)))');
              Ex_II_field(xl,zl) = ...
                 Tx'*exp(-j*(kx*x(xl) + ky*y + kIIz*(zII(zl) - D_l)))';
           end   % x loop
        end      % z loop
%       Store to complete field matrix
        Ey_field = [ Ey_field Ey_II_field(1:length(x), 1:length(zII)) ];
        Hx_field = [ Hx_field Hx_II_field(1:length(x), 1:length(zII)) ];
        Hy_field = [ Hy_field Hy_II_field(1:length(x), 1:length(zII)) ];
        Ex_field = [ Ex_field Ex_II_field(1:length(x), 1:length(zII)) ];
%       Temporary switch from field to phase
        Ey_field = angle(Ey_field);
        Hx_field = angle(Hx_field);
        Hy_field = angle(Hy_field);
        Ex_field = angle(Ex_field);
  end            % Polarization switch for exiting field calculations

  start = length(z_out)+1;
  z_out(start:(start+length(zII)-1)) = zII;
  if (dif_pol == 1)  %TE
     Ey_field_list = [ Ey_field ];
     h_menu_Ey = findobj(0, 'Tag', 'EyField');
```

```
     set(h_menu_Ey, 'UserData', Ey_field_list);

     Ey_0_field_list = [ Ey_0_field ];
     h_menu_Ey_0 = findobj(0, 'Tag', 'EyField_0');
     set(h_menu_Ey_0, 'UserData', Ey_0_field_list);

     Ey_1_field_list = [ Ey_1_field ];
     h_menu_Ey_1 = findobj(0, 'Tag', 'EyField_1');
     set(h_menu_Ey_1, 'UserData', Ey_1_field_list);

     Hx_field_list = [ Hx_field ];
     h_menu_Hx = findobj(0, 'Tag', 'HxField');
     set(h_menu_Hx, 'UserData', Hx_field_list);

%  Write field matrices in ASCII format

     fprintf(Eyfld_outf, '\t%g',z_out);
     fprintf(Eyfld_outf, '\n');
     for xl = 1:1:length(x)
        fprintf(Eyfld_outf, '%g\t', x(xl), Ey_field(xl,:));
        fprintf(Eyfld_outf, '\n');
     end
     save Ey_field;

     fprintf(Eyfld_0_outf, '\t%g',z_out);
     fprintf(Eyfld_0_outf, '\n');
     for xl = 1:1:length(x)
        fprintf(Eyfld_0_outf, '%g\t', x(xl), Ey_0_field(xl,:));
        fprintf(Eyfld_0_outf, '\n');
     end

     fprintf(Eyfld_1_outf, '\t%g',z_out);
     fprintf(Eyfld_1_outf, '\n');
     for xl = 1:1:length(x)
        fprintf(Eyfld_1_outf, '%g\t', x(xl), Ey_1_field(xl,:));
        fprintf(Eyfld_1_outf, '\n');
     end

     fprintf(Hxfld_outf, '\t%g',z_out);
     fprintf(Hxfld_outf, '\n');
```

```
     for xl = 1:1:length(x)
        fprintf(Hxfld_outf, '%g\t', x(xl), Hx_field(xl,:));
        fprintf(Hxfld_outf, '\n');
     end
     fclose(Eyfld_outf);
     fclose(Eyfld_0_outf);
     fclose(Eyfld_1_outf);
     fclose(Hxfld_outf);

  elseif (dif_pol == 2)  % TM

     Hy_field_list = [ Hy_field ];
     h_menu_Hy = findobj(0, 'Tag', 'HyField');
     set(h_menu_Hy, 'UserData', Hy_field_list);

     Ex_field_list = [ Ex_field ];
     h_menu_Ex = findobj(0, 'Tag', 'ExField');
     set(h_menu_Ex, 'UserData', Ex_field_list);

%  Write field matrices in ASCII format
     fprintf(Hyfld_outf, '\t%g',z_out);
     fprintf(Hyfld_outf, '\n');
     for xl = 1:1:length(x)
        fprintf(Hyfld_outf, '%g\t', x(xl), Hy_field(xl,:));
        fprintf(Hyfld_outf, '\n');
     end
     fprintf(Exfld_outf, '\t%g',z_out);
     fprintf(Exfld_outf, '\n');
     for xl = 1:1:length(x)
        fprintf(Exfld_outf, '%g\t', x(xl), Ex_field(xl,:));
        fprintf(Exfld_outf, '\n');
     end
     fclose(Hyfld_outf);
     fclose(Exfld_outf);

  else                    % Conical

     Ey_field_list = [ Ey_field ];
     h_menu_Ey = findobj(0, 'Tag', 'EyField');
     set(h_menu_Ey, 'UserData', Ey_field_list);
```

```
     Hx_field_list = [ Hx_field ];
     h_menu_Hx = findobj(0, 'Tag', 'HxField');
     set(h_menu_Hx, 'UserData', Hx_field_list);

     Hy_field_list = [ Hy_field ];
     h_menu_Hy = findobj(0, 'Tag', 'HyField');
     set(h_menu_Hy, 'UserData', Hy_field_list);

     Ex_field_list = [ Ex_field ];
     h_menu_Ex = findobj(0, 'Tag', 'ExField');
     set(h_menu_Ex, 'UserData', Ex_field_list);

%  Write field matrices in ASCII format
     fprintf(Eyfld_outf, '\t%g',z_out);
     fprintf(Eyfld_outf, '\n');
     for xl = 1:1:length(x)
        fprintf(Eyfld_outf, '%g\t', x(xl), Ey_field(xl,:));
        fprintf(Eyfld_outf, '\n');
     end
     fprintf(Hxfld_outf, '\t%g',z_out);
     fprintf(Hxfld_outf, '\n');
     for xl = 1:1:length(x)
        fprintf(Hxfld_outf, '%g\t', x(xl), Hx_field(xl,:));
        fprintf(Hxfld_outf, '\n');
     end
     fprintf(Hyfld_outf, '\t%g',z_out);
     fprintf(Hyfld_outf, '\n');
     for xl = 1:1:length(x)
        fprintf(Hyfld_outf, '%g\t', x(xl), Hy_field(xl,:));
        fprintf(Hyfld_outf, '\n');
     end
     fprintf(Exfld_outf, '\t%g',z_out);
     fprintf(Exfld_outf, '\n');
     for xl = 1:1:length(x)
        fprintf(Exfld_outf, '%g\t', x(xl), Ex_field(xl,:));
        fprintf(Exfld_outf, '\n');
     end
     fclose(Eyfld_outf);
     fclose(Hxfld_outf);
```

```
     fclose(Hyfld_outf);
     fclose(Exfld_outf);

  end

  field_spec_list = [ dist_before dist_after z_resolution ...
                     dist_along x_resolution dist_parallel y_resolution ...
                     z_max z_min x_max x_min y_max y_min z_out];
  set(h_menu_fieldspecs, 'UserData', field_spec_list);

%
%  Grating Display Calculations
%
   cum_thick = 0.0;
   num_index = ceil(((x_max - x_min)/grating_period)*2.)+2;
   xg = zeros(num_index, num_layers);
   zg = zeros(num_index, num_layers);

   for nl = 1:1:num_layers

      index = 1;
      xg(index,nl) = 0.0;
      if ( layer_id(nl) == 1 )    % A grating layer
         groove_width = grating_period - ridge_width(nl);
         if (grating_offset(nl) == 0)
            zg(index,nl) = cum_thick + thickness(nl);
            index = index + 1;
         elseif ((grating_offset(nl) > 0) & (grating_offset(nl) < groove_width))
            zg(index,nl) = cum_thick;
            index = index + 1;
            xg(index,nl) = xg(index-1,nl) + grating_offset(nl);
            zg(index,nl) = cum_thick + thickness(nl);
            index = index + 1;
         elseif ((grating_offset(nl) > 0) & (grating_offset(nl) > groove_width))
            zg(index,nl) = cum_thick + thickness(nl);
            index = index + 1;
            xg(index,nl) = xg(index-1,nl)+(grating_offset(nl) - groove_width);
            zg(index,nl) = cum_thick
            index = index + 1;
            xg(index,nl) = xg(index-1,nl) + groove_width;
```

```
            zg(index,nl) = cum_thick + thickness(nl);
            index = index + 1;
         end
         x_start = xg(index-1);
         for gl =  x_start:grating_period:x_max
            if (xg(index-1) + ridge_width(nl) < x_max)
               xg(index,nl) = xg(index-1,nl)+ridge_width(nl);
               zg(index,nl) = cum_thick;
               index = index + 1;
               if (xg(index-1) + groove_width < x_max)
                  xg(index,nl) = xg(index-1,nl) + groove_width;
                  zg(index,nl) = cum_thick + thickness(nl);
                  index = index + 1;
               else
                  xg(index,nl) = x_max;
                  zg(index,nl) = cum_thick + thickness(nl);
                  index = index + 1;
                  gl = x_max;
                  if (index > num_index)
                     index = num_index;
                  end
                  xg(num_index,nl) = xg(index,nl);
                  zg(num_index,nl) = zg(index,nl);
               end
            else
               xg(index,nl) = x_max;
               zg(index,nl) = cum_thick;
               gl = x_max;
               xg(num_index,nl) = xg(index,nl);
               zg(num_index,nl) = zg(index,nl);
            end              % 'for' loop over x range
         end              % 'for' loop over x range
      else                 % a uniform layer
         % play games to get all rows of xg to be same length
%         xg(1:num_index,nl) = (x_min + ((1:num_index)-1)*(grating_period/2))';
%         zg(1:num_index,nl) = cum_thick + thickness(nl);
      end                       %  grating vs. uniform layer
      cum_thick = cum_thick + thickness(nl);
   end                     % number of layers
```

```
layer_plot_list = [ xg zg];
set(h_menu_layers, 'UserData', layer_plot_list);


end       % Calculate fields



%------------------------------------------------------------------------------
%
%  Stop the stopwatch and get the time
%
toc

% The end
```

REFERENCES

[1] L. Solymar and D.J. Cooke, *Volume holography and volume gratings*, (Academic Press, New York, 1981).

[2] M.B. Fleming and M.C. Hutley, “Blazed diffractive optics,” Appl. Opt., **36**, 4635-4643 (1997).

[3] D.C. O’Shea and W.S. Rockward, “Gray-scale masks for diffractive-optics fabrication: II. Spatially filtered halftone screens,” Appl. Opt., **34**, 7518-7526 (1995).

[4] T.J. Suleski and D.C. O’Shea, “Gray-scale masks for diffractive-optics fabrication: I. Commercial slide imagers,” Appl. Opt., **34**, 7507-7517 (1995).

[5] W. Daschner, P. Long, R. Stein, C. Wu, and S.H. Lee, “Cost-effective mass fabrication of multilevel diffractive optical elements by use of a single optical exposure with a gray-scale mask on high-energy beam-sensitive glass,” Appl. Opt., **36**, 4675-4680 (1997).

[6] J.M. Miller, N. De Beaucoudrey, P. Chavel, J. Turunen, and E. Cambril, “Design and fabrication of binary slanted surface-relief gratings for a planar optical interconnection,” Appl. Opt., **36**, 5717-5727 (1997).

[7] Z. Zhou and T.J. Drabik, “Optimized binary, phase-only diffractive optical element with subwavelength features for 1.55 μm,” J. Opt. Soc. Am. A, **12**, 1104-1112 (1995).

[8] M.W. Farn, “Binary gratings with increased efficiency,” Appl. Opt., **31**, 4453-4458 (1992).

[9] M.C. Gupta and S.T. Peng, “Diffraction characteristics of surface-relief gratings,” Appl. Opt., **32**, 2911-2917 (1993).

[10] R.V. Johnson and A.R. Tanguay, Jr., “Stratified volume holographic optical elements,” Opt. Lett., **13**, 189-191 (1988).

[11] G.P. Nordin, R.V. Johnson, and A.R. Tanguay, Jr., “Diffraction properties of stratified volume holographic optical elements,” J. Opt. Soc. Am. A, **9**, 2206-2217 (1992).

[12] G.P. Nordin and A.R. Tanguay, Jr., “Photopolymer-based stratified volume holographic optical elements,” Opt. Lett., **17**, 1709-1711 (1992).

[13] F. Amzajerdian and M.J. Kavaya, “Development of solid state coherent lidars for global wind measurements,” Proceedings of the Ninth Conference on Coherent Laser Radar, Linkoping, Sweden, 1997.

[14] D.M. Chambers, “Modeling heterodyne efficiency for coherent laser radar in the presence of aberrations,” Opt. Ex., **1**(3), 60-76 (1997).

[15] J.A. Britten, S.M. Herman, B.W. Shore, H.T. Nguyen, L.J. Summers, S.N. Dixit, S.J. Bryan, and H.A. Cagle, “Tilted-groove transmission gratings for high efficiency diffraction at normal incidence and arbitrary polarization,” Technical Report UCRL-CR-135862 delivered by Lawrence Livermore National Laboratory under WFO contract L8636.1 to NASA Marshall Space Flight Center (1999).

[16] R.J. Collier, C.B. Burckhardt, and L.H. Lin, *Optical Holography*, (Academic Press, New York, 1971).

[17] W. Gambogi, K. Steijn, S. Mackara, T. Duzick, B. Hamzavy, and J. Kelly, “HOE imaging in DuPont holographic photopolymers,” Proc. SPIE, **2152** (1994).

[18] W.J. Gambogi, W.A. Gerstadt, S.R. Mackara, and A.M. Weber, “Holographic transmission elements using improved photopolymer films,” Proc. SPIE, **1555**, 256-267 (1991).

[19] W.K. Smothers, B.M. Monroe, A.M. Weber, and D.E. Keys, “Photopolymers for holography,” SPIE OE/Lase Conference Proceedings, Los Angeles, CA (1990).

[20] A.M. Weber, W.K. Smothers, T.J. Trout, and D.J. Mickish, “Hologram recording in DuPont’s new photopolymer materials,” SPIE OE/Lase Conference Proceedings, Los Angeles, CA (1990).

[21] H.J. Zhou, V. Morozov, and J. Neff, “Characterization of Dupont photopolymers in infrared light for free-space optical interconnects,” Appl. Opt., **34**, 7457-7459 (1995).

[22] F. Amzajerdian, “Analysis of measurements for solid state lidar development,” Technical Report delivered by The University of Alabama in Huntsville under Contract NAS8-38609 to NASA Marshall Space Flight Center (1995).

[23] J.T. Hall, D.M. Cook, S.M. Raffensperger, and A.B. O’Connor, “Holographic scanner applied to OASYS,” Proc. IRIS Active Systems, Vol. II, 155-170 (1993).

[24] P.F. McManamon, T.A. Dorschner, D.L. Corkum, L.J. Friedman, D.S. Hobs, M. Holz, S. Liberman, H.Q. Nguyen, D.P. Resler, R.C. Sharp, and E.A. Watson, “Optical phased array technology,” Proc. IEEE, **84**, 268-297 (1996).

[25] P.F. McManamon, E.A. Watson, T.A. Dorschner, and L.J. Barnes, “Applications look at the use of liquid crystal writable gratings for steering passive radiation,” Opt. Eng., **32**, 2657-2664 (1993).

[26] D.P. Resler, D.S. Hobs, R.C. Sharp, L.J. Friedman, and T.A. Dorschner, “High-efficiency liquid-crystal optical phased-array beam steering,” Opt. Lett., **21**, 689-691 (1996).

[27] A. Granger, L. Song, and R.A. Lessard, “Multiple beam generation using a stratified volume holographic grating,” Appl. Opt., **32**, 2534-2537 (1993).

[28] M.G. Moharam, E.B. Grann, D.A. Pommet, and T.K. Gaylord, “Formulation for stable and efficient implementation of the rigorous coupled-wave analysis of binary gratings,” J. Opt. Soc. Am. A, **12**, 1068-1076 (1995).

[29] M.G. Moharam, D.A. Pommet, E.B. Grann, and T.K. Gaylord, “Stable implementation of the rigorous coupled-wave analysis for surface-relief gratings: enhanced transmittance matrix approach,” J. Opt. Soc. Am. A, **12**, 1077-1086 (1995).

[30] L. Li, “Formulation and comparison of two recursive matrix algorithms for modeling layered diffraction gratings,” J. Opt. Soc. Am. A, **13**, 1024-1035 (1996).

[31] R.H. Morf, “Exponentially convergent and numerically efficient solution of Maxwell’s equations for lamellar gratings,” J. Opt. Soc. Am. A, **12**, 1043-1056 (1995).

[32] N. Chateau and J. Hugonin, “Algorithm for the rigorous coupled-wave analysis of grating diffraction,” J. Opt. Soc. Am. A, **11**, 1321-1331 (1994).

[33] S. Peng and G.M. Morris, “Efficient implementation of rigorous coupled-wave analysis for surface-relief gratings,” J. Opt. Soc. Am. A, **12**, 1087-1096 (1995).

[34] N.P.K. Cotter, T.W. Preist, and J.R. Sambles, “Scattering-matrix approach to multilayer diffraction,” J. Opt. Soc. Am. A, **12**, 1097-1103 (1995).

[35] G. Bao, D.C. Dobson, and J.A. Cox, “Mathematical studies in rigorous grating theory,” J. Opt. Soc. Am. A, **12**, 1029-1042 (1995).

[36] M.G. Moharam and T.K. Gaylord, “Rigorous coupled-wave analysis of planar-grating diffraction,” J. Opt. Soc. Am., **71**, 811-818 (1981).

[37] M.G. Moharam and T.K. Gaylord, “Diffraction analysis of dielectric surface-relief gratings,” J. Opt. Soc. Am., **72**, 1385-1392 (1982).

[38] L. Li, “Use of Fourier series in the analysis of discontinuous periodic structures,” J. Opt. Soc. Am. A, **13**, 1870-1876 (1996).

[39] S. Tibuleac and R. Magnusson, “Reflection and transmission guided-mode resonance filters,” J. Opt. Soc. Am. A, **14**, 1617-1626 (1997).

[40] M.V. Klein and T.E. Furtak, *Optics*, Second Edition, (John Wiley & Sons, Inc., New York, 1986).

[41] H. Kogelnik, “Coupled wave theory for thick hologram gratings,” Bell Syst. Tech. J., **48(9)**, 2909-2947 (1969).

[42] J.J. Jung, “Stratified volume holographic optical elements: analysis of diffraction behavior and implementation using InGaAs/GaAs multiple quantum well structures,” Ph.D. dissertation, University of Southern California (1994).

[43] C. Bungay, “IR_VASE Characterization of Thin Films, Contact: Diana Chambers, University of Alabama-Huntsville,” J.A. Woollam Co., Inc. Technical Report, April 2, 1999.

[44] C. Bungay, “IR_VASE Characterization of Bulk Glass, Contact: Diana Chambers, University of Alabama-Huntsville,” J.A. Woollam Co., Inc. Technical Report, May 7, 1999.

[45] Y. Torii and Y. Mizushima, “Theory of alignment monitoring by diffraction from superimposed dual gratings,” J. Opt. Soc. Am., **68**, 1716-1731 (1978).

[46] Y. Torii and Y. Mizushima, “Optical ultramicrometer technique utilizing a composite diffraction grating,” Opt. Comm., **23**, 135-138 (1977).

[47] D.C. Flanders, H.I. Smith, and S. Austin, “A new interferometric alignment technique,” Appl. Phy. Lett., **31**, 426-428 (1977).

[48] K. Kodate, T. Kamiya, and M. Kamiyama, “Double diffraction in the Fresnel region,” Jap. J. of App. Phy., **10**, 1040-1045 (1971).

[49] K. Kodate, T. Kamiya, H. Takenaka, and H. Yanai, "Double diffraction of phase gratings in the Fresnel region," Jap. J. of Appl. Phy., **14**, 1323-1334 (1975).

[50] S. Noda, N. Yamamoto, M. Imada, H. Kobayashi, and M. Okano, "Alignment and stacking of semiconductor photonic bandgaps by wafer-fusion," J. of Lightwave Tech., **17**, 1948-1955 (1999).

[51] *High Performance Diode Lasers*, Models 56IMS001, 56IMS005, and 56IMS009 Operator's Manual, Melles Griot.

[52] Personal communication with Melles Griot

[53] P. Lobl, M. Huppertz, and D. Mergel, "Nucleation and growth in TiO_2 films prepared by sputtering and evaporation," Thin Solid Films, **251**, 72-79 (1994).

[54] S. Astilean, P. Lalanne, P. Chavel, E. Cambril, and H. Launois, "High-efficiency subwavelength diffractive element patterned in a high-refractive-index material for 633nm," Opt. Lett., **23**, 552-554 (1998).

[55] P. Lalanne, S. Astilean, P. Chavel, E. Cambril, and H. Launois, "Design and fabrication of blazed binary diffractive elements with sampling periods smaller than the structural cutoff," J. Opt. Soc. Am. A, **16**, 1143-1156 (1999).

[56] D.A. Pommet, E.B. Grann, and M.G. Moharam, "Effects of process errors on the diffraction characteristics of binary dielectric gratings," Appl. Opt., **34**, 2430-2435 (1995).

[57] G.P. Nordin, J.T. Meier, P.C. Deguzman, and M.W. Jones, "Micropolarizer array for infrared imaging polarimetry," J. Opt. Soc. Am. A, **16**, 1184-1193 (1999).

[58] G.P. Nordin and P.C. Deguzman, "Broadband form birefringent quarter-wave plate for the mid-infrared wavelength region," Opt. Ex., **5**(8), 163-168 (1999).

[59] G.P. Nordin, J.T. Meier, P.C. Deguzman, and M.W. Jones, "Diffractive optical element for stokes vector measurement with a focal plane array," Proc. SPIE, **3754**, 169-177 (1999).

[60] H.J. Cole, S.N. Dixit, B.W. Shore, D.M. Chambers, J.A. Britten, M.J. Kavaya, "Rectangular relief diffraction gratings for coherent lidar beam deflection," Tenth Biennial Coherent Laser Radar Technology and Applications Conference, June 29-July 2, Mount Hood, OR (1999).

[61] H.T. Nguyen, B.W. Shore, S.J. Bryan, J.A. Britten, R.D. Boyd, and M.D. Perry, "High-efficiency fused-silica transmission gratings," Opt. Lett., **22**, 142-144 (1997).

[62] H.J. Gerritsen and M.L. Jepsen, "Rectangular surface-relief transmission gratings with a very large first-order diffraction efficiency (~95%) for unpolarized light," Appl. Opt., **37**, 5823-5829 (1998).

[63] G. Makosch and F.J. Schoenes, "Interferometric method for checking the mask alignment precision in the lithographic process," Appl. Opt., **23**, 628-632 (1984).

[64] G. Makosch and F. Prein, "Phase-locked interferometry for automatic mask alignment in projection printers," Appl. Opt., **26**, 2828-2835 (1987).

[65] D. Gregoris and V.M. Ristic, “Moire interferometric focusing system for optical microlithography,” Appl. Opt., **26**, 4475-4481 (1987).

[66] M. Nelson, J.L. Kreuzer, and G. Gallatin, “Design and test of a through-the-mask alignment sensor for a vertical stage x-ray aligner,” J. Vac. Sci. Tech. B, **12**, 3251-3255 (1994).

[67] G. Chen, J. Wallace, and F. Cerrina, “Experimental evaluation of the two-state alignment system,” J. Vac. Sci. Tech. B, **9**, 3222-3226 (1991).

[68] H. Zhou, M. Feldman, and R. Bass, “Subnanometer alignment system for x-ray lithography,” J. Vac. Sci. Tech. B, **12**, 3261-3264 (1994).

[69] B. Fay, J. Trote, and A. Frichet, “Optical alignment system for submicron x-ray lithography,” J. Vac. Sci. Tech., **16**, 1954-1958 (1979).

[70] S. Ishihara, M. Kanai, A. Une, and M. Suzuki, “A vertical stepper for synchrotron x-ray lithography,” J. Vac. Sci. Tech. B, **7**, 1652-1656 (1989).

[71] A. Moel, E.E. Moon, R.D. Frankel, and H.I. Smith, “Novel on-axis interferometric alignment method with sub-10 nm precision,” J. Vac. Sci. Tech. B, **11**, 2191-2194 (1993).

[72] E.E. Moon, P.N. Everett, and H.I. Smith, “Immunity to signal degradation by overlayers using a novel spatial-phase-matching alignment system,” J. Vac. Sci. Tech. B, **13**, 2648-2652 (1995).

[73] E.E. Moon, P.N. Everett, K. Rhee, and H.I. Smith, “Simultaneous measurement of gap and superposition in a precision aligner for x-ray nanolithography,” J. Vac. Sci. Tech. B, **14**, 3969-3973 (1996).